THEORETICAL AND NUMERICAL INVESTIGATION ON TRACTION FORCES FOR HIGH ADHESION LOCOMOTIVES

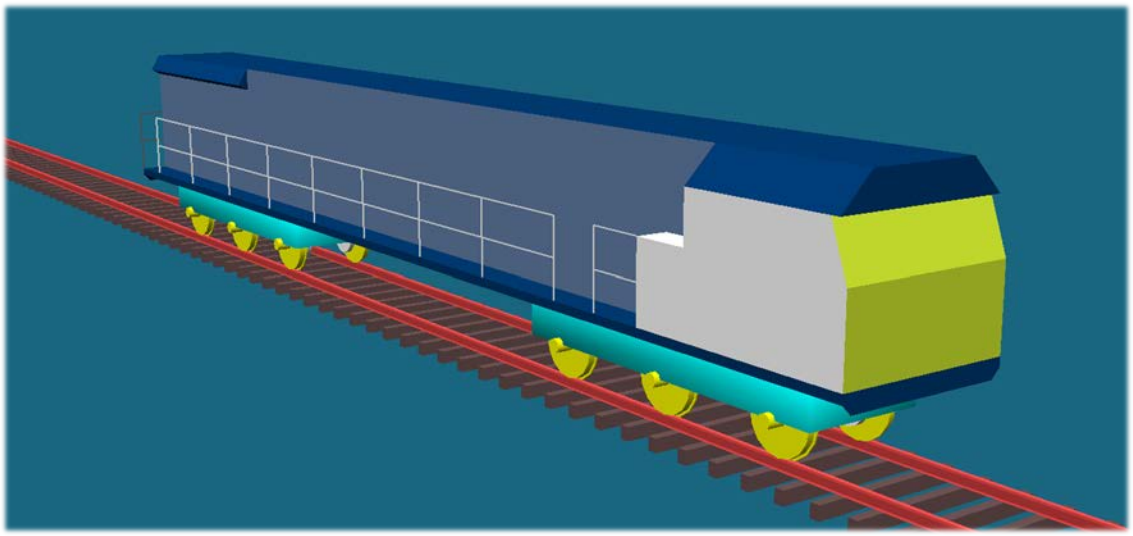

Andrew Liam George

Master of Engineering

Centre for Railway Engineering,
Central Queensland University Australia
Rockhampton, Queensland

School of Engineering and Technology

July 2015

Certificate of authorship and originality of thesis (declaration)

The work contained in this thesis has not been previously submitted either in whole or in part for a degree at any other tertiary institution in Australia or overseas. To the best of the author's knowledge the material presented in this thesis is original work except where due reference is made in text. Some research related to this thesis has been published in papers and presented to conferences as listed in the 'Publications' section.

Signed: _____

Date: 30 June 2014

Copyright statement

Signed: _____

Date: 30 June 2014

Abstract

High-adhesion AC-drive freight locomotives can exert 50% more traction force [1] for a given locomotive weight in comparison to older DC-drive units. One of the factors holding back widespread adoption in Australia, particularly on low-maintenance lines, is a lack of understanding of how locomotive adhesion forces contribute to track damage. So far most research on railway locomotive vehicle dynamics has been done using purely mechanical locomotive models that don't consider additional traction and/or in-train coupler forces.

This thesis presents a methodology for modelling locomotives as complex mechatronic systems so that wheel-rail forces and dynamic behaviour for locomotives under traction within trains can be simulated in detail. Three locomotive model types were created using the GENSYS simulation software [2]: Type AC1 (AC drive, rigid bogies), Type AC2 (AC drive, semi-steering bogies) and Type DC (DC drive, rigid bogies). The mechanical component of each locomotive model was a multi-body model that considered the locomotive, rails and track. Locomotive-specific Traction Control (TC) systems were modelled using simplified electronic controls within the GENSYS model codes. Approximated coupler force components based on results from a related study [3] could be used as input, with the approach allowing locomotives within a train to be analysed individually.

To help identify and mitigate any serious errors within the locomotive models, a Locomotive Model Acceptance Procedure (LMAP) was developed owing to the lack of existing validation procedures for locomotive models. Although the primary aim in this case was to evaluate the methodology, some LMAP case studies were performed to remedy any basic faults within the locomotive models. Tests performed on the final rigid bogie Type AC1 and DC models were successful, but a few minor errors were present in the semi-steering bogie Type AC2 model. Supplementary tests were conducted to validate bogie steering performance under rolling motion only (no applied traction forces) via comparison to an existing NUCARS study [4]. Angles of Attack (AoAs) between the GENSYS and NUCARS rigid bogie models were similar,

whereas the GENSYS semi-steering bogie model performed more like a rigid bogie than the NUCARS self-steering bogie model.

Once the GENSYS locomotive models were sufficiently tested, they were then run through a series of ‘worst case’ scenarios for conditions of small curve radii and high in-train coupler forces. Trains consisted of three locomotives of the same type powering at the head of 55 wagons, which were simulated to travel through test tracks consisting of right-handed curves with different radii. Locomotives travelled at minimum speed whilst exerting maximum continuous tractive effort, and both dry and wet rail head conditions were simulated.

During the analysis, lateral coupler forces were found to increase for locomotives along a train [3, 5], pulling locomotives toward the low rail [1]. For high lateral coupler forces, wheelsets were forced so far toward the low rail that most lateral (steering) wheel-rail forces were generated within gauge corner contact zones on low rail wheels. Longitudinal (traction) forces were influenced most by TC systems, with Type AC1’s per wheelset control obtaining higher adhesion levels than Type AC2’s per-bogie control, which in turn was followed by Type DC’s per-locomotive control. A fault was found in Type AC2’s semi-steering bogies during analysis, where the middle axle on the second bogie generated unusually high track-shifting forces toward the low rail in comparison to rigid bogie models. This will have to be fixed in future research, given improperly adjusted lateral clearances in the axle-boxes were thought to be the most likely reason. Despite this fault, AoAs for the two bogie types were found to be close when the locomotive models were under traction for varying curvatures and in-train positions. Traction forces were shown to deteriorate semi-steering bogie performance to that of the rigid bogies, mirroring findings in earlier research [6, 7]. More detailed phenomena are discussed within the remainder of this thesis.

Contents

List of figures

List of tables

List of equations

Publications

Conference proceedings:

- Spiryagin, M, George, A, Sun, YQ & Cole, C 2012, 'Locomotive model acceptance procedure based on international standards', *Proceedings of the IMSD2012 - The 2nd Joint International Conference on Multibody System Dynamics*, May 29 – June 1 2012, Stuttgart, Germany.
- Spiryagin, M, George, A, Ahmad, SSN, Rathakrishnan, K, Sun, YQ & Cole, C 2012, 'Wagon model acceptance procedure using Australian standards', *Proceedings of the Conference On Railway Engineering (CORE) 2012*, 10-12 September 2012, Brisbane, Australia, pp. 343-350.
- Spiryagin, M, Sun, YQ, Cole, C, George, A, Simson, S & Persson, I 2012, 'Influence of lateral components of coupler forces on the wheel-rail contact forces for hauling locomotives under traction', *Proceedings of the 13th Mini Conference on Vehicle System Dynamics, Identification and Anomalies (VSDIA) 2012'*, 5-7 November 2012, Budapest, Hungary.

Journal articles:

- Spiryagin, M, George, A, Sun, YQ, Cole, C, McSweeney, T & Simson, S 2013, 'Investigation of locomotive multibody modelling issues and results assessment based on the locomotive model acceptance procedure', *Proceedings of the Institution of Mechanical Engineers, Part F: Journal of Rail and Rapid Transit*, vol. 227, no. 5, pp. 453-468.

Acknowledgements

This thesis would not have been possible without the CRC for Rail Innovation (established and supported under the Australian Government's Cooperative Research Centres program) organising and funding research for Project R3.119 – Locomotive Adhesion. I am also grateful for the support offered by the Centre for Railway Engineering (CRE) and Central Queensland University (CQU), not to mention DEsolver for use of their GENSYS software for locomotive dynamics simulation in my research.

I must sincerely thank my advisor Maksym Spiryagin and co-advisor Colin Cole for their guidance throughout my research and thesis completion. They taught me how to adapt to the research environment, encouraged me to submit various papers for conferences and journals, and offered support with various items of work. Perhaps most importantly, given my tendencies toward perfectionism and setting overly ambitious goals, they encouraged me to make more realistic plans and to remain focused on the key tasks at hand. Maksym in particular helped me to become proficient with the GENSYS multi-body simulation software and for that I am grateful.

Other CRE staff and ex-staff I must acknowledge include Yan Sun (who provided Longitudinal Train Simulation data for use in this thesis), Scott Simson (whose GENSYS locomotive models formed the basis of those used in my research), Vicky Kreiser (who helped me with various conference and travel forms, amongst others) Tim McSweeney (for proof-reading several documents including this thesis) and Elise Crawford (who introduced me to Colin Cole at CORE 2010). There are various other CRE, CRC for Rail Innovation and CQU staff members who have offered their support, so for the sake of brevity I apologise for not mentioning their names explicitly.

Finally, I must thank my parents and immediate family for their considerable and much-needed support during the completion of my Master’s degree.

1. Introduction

High-adhesion locomotives with AC drive systems have been available and in use for several years on railway systems across the world. Advances in slip control systems enable high-adhesion locomotives to exert 50% more traction force than older DC-drive designs for the same engine power output, with maximum traction force exceeding 50% of locomotive weight in ideal conditions. This can allow trains of a given tonnage to be hauled with fewer locomotives, offering scope for reduced expenditure on new motive power [1]. Fewer locomotives with more robust AC drive equipment in relation to older DC drive technology [8] should also have the effect of reducing maintenance costs.

Despite this, there has been little research into the effects of locomotive traction forces on track infrastructure in general, let alone for high-adhesion locomotives. Recent tests at Cowan Bank showed that three high-adhesion locomotives at the head end of a 4500 tonne train exerted ~140 tonnes of drawbar force onto the track [9], which is considerably higher than the 100 tonnes that track engineers usually account for. Since high-adhesion locomotives allow more weight to be carried with less power, the train speed up gradients and through low radii curves is reduced, resulting in greater cant imbalance, increased wheel loading on the low rail and higher coupler forces [1]. Passively-steered locomotive bogies have been developed to improve steering and reduce wheelset angles of attack in curves, but they fail to do so when high traction forces are applied, effectively behaving like rigid bogies in this case [6].

Although track maintenance is not as much of a problem for dedicated heavy haul lines as opposed to routes with outdated infrastructure and suburban systems that allow little time for repair, questions regarding the effects of traction forces are effectively delaying the deployment of high-adhesion locomotive technology [1]. Reliable information regarding track damage in relation to locomotive traction is sought to resolve this situation and result in more effective and perhaps cheaper rail maintenance regimes.

1.1. Aims and objectives

The primary aims of this research are to:

- Develop a detailed simulation methodology for calculation of wheel-rail contact forces for locomotives under traction
- Perform theoretical and numerical investigations on locomotive traction forces for a wide variety of scenarios relevant to Australian practices

In order to meet these aims, the following objectives need to be met:

- Evaluate suitable wheel-rail contact models and solvers to choose the most suitable combination for modelling locomotive traction forces
- Find a means of simulating varying rail friction coefficients appropriate for multi-body vehicle simulation
- Create models of typical diesel-electric locomotives in use on Australian railways based on manufacturers' specifications
- Develop a Locomotive Model Acceptance Procedure (LMAP) to verify multi-body locomotive models that satisfies Australian Standards (AS) and other relevant Australian and worldwide standards
- Evaluate and improve the simulation process by first performing basic analyses
- Determine appropriate virtual track layouts to model the required geometry
- Obtain information on appropriate train consists and motive power arrangements, e.g. head-end and distributed power, typical of Australian practice

1.2. Scope

The research completed for this thesis was conducted as part of the broader Co-operative Research Centre (CRC) for Rail Innovation Project No. R3.119 "Locomotive Adhesion", which aims to quantitatively determine how increasing locomotive traction forces affect rail damage [1]. Project R3.119 is split into three separate project groups, being:

1. Locomotive Traction Force Analysis (CQU)
2. Locomotive Traction Control Modelling (UQ)
3. Rail and Track Stress Analysis (UoW)

This thesis is a summary of research undertaken by the author for the first project group, “Locomotive Traction Force Analysis”. It is concerned with quantitatively modelling wheel-rail forces for locomotives under traction using the GENSYS [2] Multi-Body Simulation (MBS) software. Although Longitudinal Train Simulation (LTS) was required to generate in-train coupler forces for use in multi-body locomotive models, it is outside the scope of this thesis. The simulated coupler forces were then used as input for Finite Element Analysis (FEA) conducted by the third project group “Rail and Track Stress Analysis”.

The focus is on the Australian railway freight industry as its practices are exceeding common practice overseas, with higher maximum locomotive adhesion coefficients and train mass to locomotive mass ratios in particular [1].

In order to conduct an extensive analysis of locomotive traction forces, several parameters had to be considered to reflect the various freight operations that occur in Australian railway practice. These include properties of locomotive classes, particularly drive and bogie types, train configurations, track layouts and rail surface conditions (namely wet or dry) being typical of current practice.

1.3. Thesis outline

The remainder of this thesis, except for the references section and appendix, is structured as follows:

- **Section 2:** Contains a review of current state-of-the-art literature on longitudinal train dynamics and railway vehicle dynamics. Topics related to vehicle dynamics include multi-body simulation, wheel-rail contact, friction and adhesion modelling, locomotive design and modelling, co-ordinate systems and traction control.

- **Section 3:** Details the three mechatronic locomotive models created for this thesis using the GENSYS [2] MBS software. Both common and model-specific parameters are outlined.
- **Section 4:** Describes the methodology for a Locomotive Model Acceptance Procedure (LMAP) designed to validate locomotive models using a series of tests derived from Australian and international locomotive dynamics standards. A few case studies are performed on the locomotive models detailed in Section 3 to a) show the methodology is sound, and b) help mitigate any major sources of error present in the models.
- **Section 5:** An additional test is conducted on the locomotive models to assess their bogie steering performance without traction and coupler forces applied. The results were compared to a related study [4] to provide a basis of comparison.
- **Section 6:** Presents a methodology for the simulation of locomotive models as complex mechatronic systems. In-train forces from LTS are fed to individual locomotive models to provide a detailed simulation of wheel-rail forces using MBS. Lateral coupler force magnitudes for the test tracks (right-hand curves) were approximated from data in a related study [3]. A variety of input parameters were considered in the simulations, particularly drive type (AC and DC), traction control systems, bogie type, in-train position, test track curve radius and rail head friction (dry/wet track). From these simulations, a detailed analysis of the resultant wheel-rail forces is conducted to determine how the input parameters affected the locomotive model's performance.
- **Section 7:** Conclusions for the research presented in this thesis.

2. Literature review

Simulating aggregate locomotive traction forces will require the analysis of entire trains in various configurations and operating scenarios on varying track alignments. This requires knowledge of several related fields that can be divided into two main categories:

- Longitudinal train dynamics – Simulation of train behaviour
- Vehicle dynamics – Simulation of railway vehicle behaviour using input from train simulation

Although most of the reviewed research centred on wheel-rail contact and adhesion modelling, knowledge of locomotive design, train simulation, multi-body simulation, traction control systems and basic concepts was required. Research relating to longitudinal train dynamics will first be discussed in the following subsections, followed by those for vehicle dynamics.

2.1. Longitudinal train dynamics

Longitudinal train dynamics is concerned with modelling forces and motions of connected railway vehicles along the track direction. Locomotives and wagons are modelled as lumped masses, with flexure modelled using stiffness elements, connected with coupling systems that account for inbuilt coupler slack and draft gear characteristics. Locomotive traction and dynamic braking, pneumatic (air) braking, gradients, curvature and retardation/drag forces are also considered in these analyses, along with knowledge of driving practices designed to maintain momentum and minimise fuel consumption [5]. For this project the software tool CRE-LTS, developed by the Centre for Railway Engineering (CRE) [10], was used to perform longitudinal train dynamics simulations, generating coupler forces for each locomotive and wagon in a train. These coupler forces were then applied to more detailed multi-body locomotive models in the vehicle analysis tool GENSYS developed and maintained by DEsolver [11].

Because of coupler slack, vehicles in a train can either bunch up or drag apart as a result of traversing undulations and gradients along the track and/or when traction and braking is applied.

Such actions are referred to as run-in and run-out behaviour respectively, which can result in high impact forces and accelerations within the train. To help prevent this, locomotive drivers often use a practice called “power braking” where trains are driven with minimum air braking on the wagons to stretch them out to reduce in-train vibrations when applying locomotive traction power. When normally braking a train, a set of wagon brakes near the locomotives are applied first so that the remaining wagons bunch together before more braking force is applied. General types of in-train forces that can occur include [5]:

- Steady: Caused by steady applications of power or drag, such as traction, braking, gradients, track curvature and rolling resistance
- Impact: Arise when more abrupt changes in traction/braking occur whilst negotiating track dips, turnouts and other irregularities, and during shunting
- Low-frequency oscillations [12]:
    - Sustained longitudinal vibration: An underdamped, sinusoidal vibration that occurs when a train is in a single stress state (run in/out); force magnitudes approach that of steady forces
    - Cyclic vibrations: Approximate square-wave vibrations that occur due to run ins/outs that can last for several seconds

As trains become larger, in-train forces correspondingly increase which can cause problems with vehicle stability and even cause derailment [5, 13]. Wheel unloading is one problem that is exacerbated with increased in-train forces, decreased curve radii and differing wagon lengths [5]. It is expressed as a percentage where 0% is static load, -100% is double static load and 100% is no load at all where derailment is considered likely to occur [13]. According to the Association of American Railroads (AAR) [14], wheel unloading beyond 90% is unacceptable. Pitching of vehicle bodies and bogies can also occur when subjected to longitudinal impacts and forces, where such behaviour may also compromise a locomotive’s ability to produce traction force. Bogie pitching occurs due to the transfer of longitudinal force from the wagon via the centre bowl connection at the top of the bogie assembly [13]. It is more likely to occur in empty wagons as the line of action at the couplers is close to the wagon centre of mass. As each bogie

comprises ~20% of an empty wagon's mass, wheel unloading of up to 50% can easily occur. When wagons are loaded, their centre of mass moves upward [5]. Hence, when longitudinal forces are applied at coupler level, they provide a moment about the centre of mass, causing the body to pitch [13]. A longitudinal force of ~380 kN is enough to cause wagon pitch and wheel unloading of 10% [15].

As mentioned earlier, railway vehicles are considered as lumped masses connected via coupling mechanisms where each vehicle (aside from the head and tail units) is modelled with couplers at each end [5]. A coupling system, of which a conceptual drawing is shown in Figure 1, consists of a draft gear unit connected to the vehicle chassis and a yoke. The yoke is separate from the chassis and is pin-connected to an auto-coupler assembly, consisting of a shank and knuckle, allowing rotation.

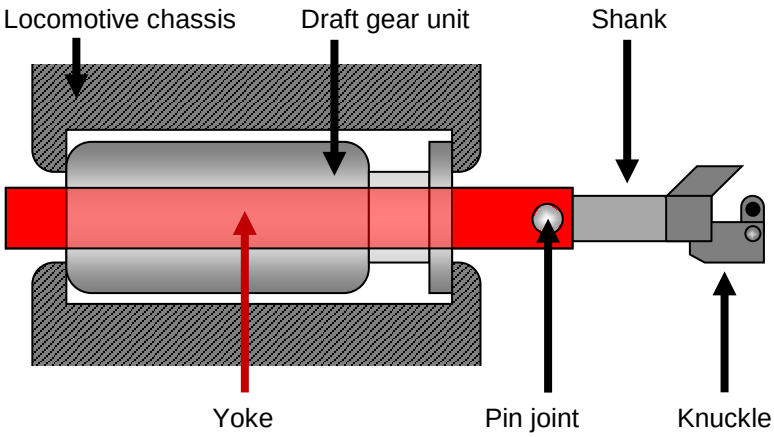

Figure 1: Conceptual drawing of a coupling system

When compressive or tensile longitudinal force is applied to the coupler, the yoke moves back and forth and compresses the draft gear assembly. A typical friction type draft gear unit is shown in Figure 2 [5]. When the rod contacts the friction wedges, it compresses a spring, typically made of steel or polymer.

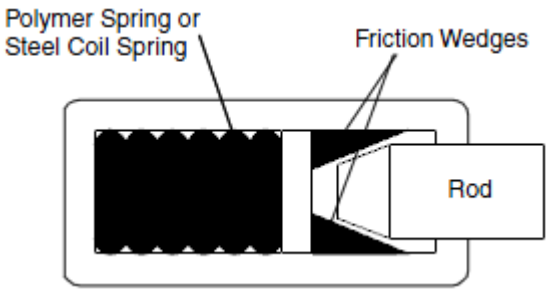

Figure 2: Friction type draft gear unit [5]

Depending on the friction coefficients and angles of the contacting surfaces, if enough force is applied to the draft gear, friction in the rod and wedges will cause the mechanism to seize, locking it into place until the applied force is reduced enough to free the mechanism again. Sustained longitudinal vibration can occur when draft gear units in a train are locked, with the corresponding stiffness required for this defined as the "locked stiffness". This is the series stiffness of locked draft gear, yoke, shank, knuckle, vehicle body stiffness and any "pseudo-linear" stiffness caused by bogie steering components and gravity [5].

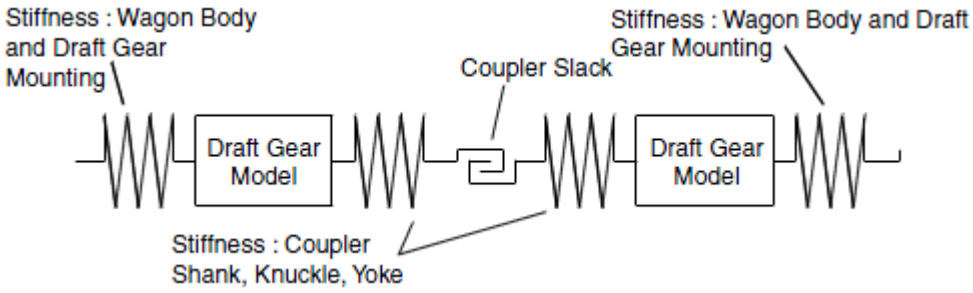

Figure 3: Components in a vehicle connection model [5]

Inter-vehicle coupling systems are typically modelled in longitudinal train dynamics simulations as shown in Figure 3 [5]. Alternate connection systems exist, such as slack-less coupling packages that contain mechanisms to compensate for wear and maintain small amounts of slack. These systems can reduce up to 96% of longitudinal accelerations and 86% of impact forces [16], but with less room for draft gear units they need to be designed for greater loads. Wagon body fatigue and impact-related failure can also be accelerated [5].

Some wagons have their draft gear directly connected via drawbars in place of separate coupling mechanisms, as in some recent coal wagons in Queensland that are permanently connected in pairs. These are modelled in a different manner as shown in Figure 4 [5].

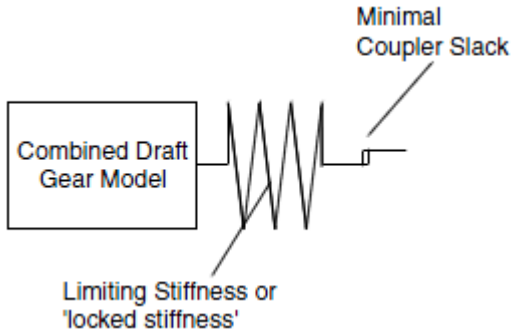

Figure 4: Wagon connection model for a drawbar coupled wagon [5]

Locomotive traction and dynamic braking forces are typically modelled from force-velocity plots provided in locomotive specification sheets. Understandably, the capabilities of older DC-drive locomotives in this area differ from recent DC-drive examples and the latest AC-drive high-adhesion locomotives. Dynamic brake capabilities vary between the three types as shown in Figure 5 [5], although the traction force-velocity curves for AC and DC locomotives are similar [8].

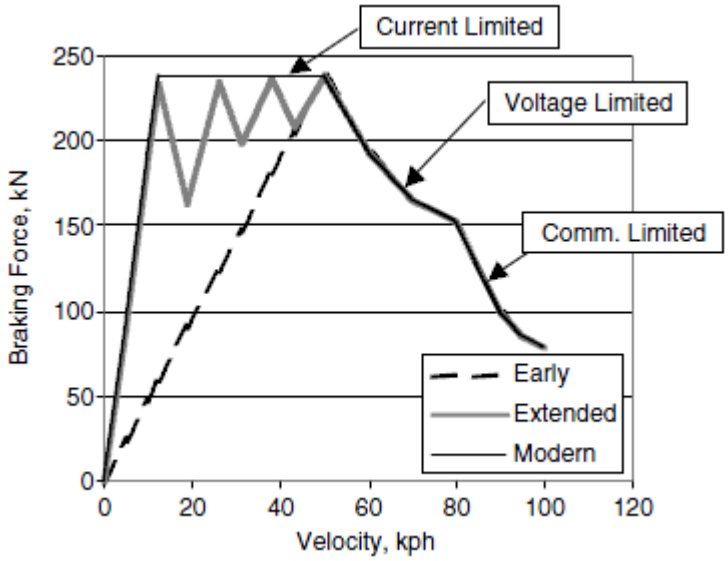

Figure 5: Typical dynamic brake characteristics [5]

Several other parameters have to be considered when modelling locomotive traction and dynamic braking, including [5]:

- Traction motor torque reduction as heat increases
- Friction coefficient of wheel/rail surfaces, which can be influenced by contaminants, roughness, etc.
- Traction control capabilities
- Limited power application controls (to reduce fuel use and pollution)

Pneumatic, or air, braking is another factor that needs to be considered in LTS, but only a brief description will be given here. Freight trains generally have train brakes controlled via the brake pipe where cylinders of pressurised air hold spring-loaded brake shoes off the wheelsets. A drop in air pressure, either from a locomotive control or because of a fault in the brake line, releases air from the cylinders so that the brake shoes are pressed onto the wheel rims. Pneumatic brakes will apply sequentially from the nearest exhaust air point(s), which are typically located at locomotives [5]. In other words, the further brakes are from an exhaust point, the longer it will take for them to apply.

Gravitational effects are simply calculated by resolving vehicle weight into tangential and normal components to the track gradient. Curving resistance is usually expressed in a form dependent on curve radius, as in Equation 1 [5, 17].

$$F_{cr} = 6116/R$$

Equation 1: Curving resistance dependent on curve radius [5, 17]

Where: F_{cr} = Curve resistance force (N per tonne of vehicle mass)
R = Curve radius (m)

Other forms of propulsion resistance are usually modelled using empirical formulae such as the Davis equation, which uses coefficients dependent on vehicle mass, number of vehicle axles, (flanging) friction and air resistance. Most of the other propulsion resistance formulae for freight rolling-stock mentioned by [5] seem to be dependent on velocity only – one simply

chooses the type of train closest to the one they are analysing and selects the appropriate equation. Because of these limitations it is recommended that more accurate means of estimating propulsion resistance should be devised. Amongst other parameters, bogie steering, wheel/rail profiles, vehicle warping stiffness and centre (bolster) bowl friction need to be considered [5].

Distributed locomotive power, where one or more groups of remotely controlled locomotives are placed part-way along a train, is one means of reducing coupler forces and the occurrence of train separation due to failed coupling units. As illustrated in Figure 6 [5], coupler forces increase down the length of a train amongst groups of locomotives and decrease down the length of groups of wagons.

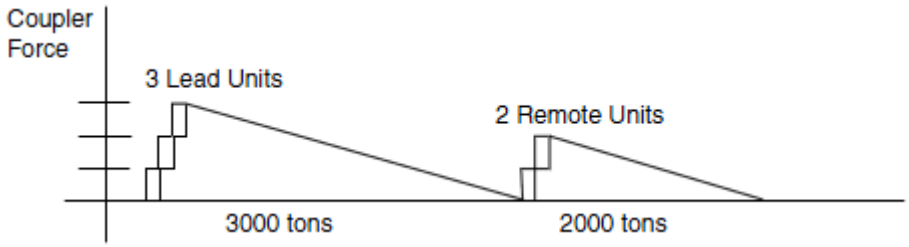

Figure 6: Coupler forces in a "two trains connected" configuration [5]

Figure 6 shows a "two trains connected" configuration, where a "node" of zero coupler force can be seen in front of the second locomotive group. The position of this node can move toward the front and back of a train during distributed power operation because of speed differences up to 8 km/h between locomotive groups [5, 18]. If the lead locomotives slow down relative to the remote group, the node moves forward and vice-versa. Appropriate remote locomotive control strategies need to be implemented, and these can be modelled in longitudinal train analysis to prevent excessive tension and/or compression coupler forces from damaging coupler units [5].

2.2. Vehicle dynamics

Vehicle dynamics is concerned with simulating the behaviour of an individual railway vehicle in response to track conditions. Locomotive models for analysis in multi-body software

packages are constructed from three-dimensional bodies connected with weightless elements such as springs and dampers at user-defined nodes [19].

The following subsections initially give an introduction to multi-body simulation packages and the co-ordinate systems used in vehicle simulations. As wheel-rail contact and modelling of friction and adhesion conditions are critical areas in locomotive traction simulation, the bulk of the reviewed research centres around these topics. Design and modelling of locomotive components, including bogies, is then covered before traction control systems are discussed.

2.2.1. Multi-body simulation

Railway application specific Multi-Body Simulation (MBS) packages are designed to model and test vehicles and rail in a virtual environment. These allow vehicle testing and optimisation of parameters such as suspension settings to be conducted quickly, easily and (relatively) cheaply, especially when compared to traditional analysis methods and empirical/experimental testing. The mathematical modelling used in these computer software packages is now mature and reliable, with modern versions incorporating easy-to-use graphical user interfaces and animation tools for program output [19].

Railway vehicle models are constructed from a series of masses, or bodies, connected to each other via flexible weightless elements to form a multi-body system. Each body is assumed to have six degrees of freedom, namely longitudinal, lateral and vertical translation and roll, yaw and pitch rotations, unless physical restraints are applied. Masses, moments of inertia and sometimes flexibilities need to be specified for each body, where external Finite Element Modelling (FEM) or Computer Aided Design (CAD) programs can be used to calculate these values if necessary. Nodes (or markers) are defined on each body to connect elements like springs, viscous and friction dampers, joints, links, and wheel-rail contact elements that can simply be selected from a library. Equations of motion can be automatically generated thanks to in-built scripts, although other equations may need to be defined by the user [19].

Inputs to the vehicle model, such as displacements/rotations arising from changes in track geometry and friction forces generated in wheel/rail contact patches, are usually applied to the wheelsets [19]. For this project, additional forces will also need to be modelled including traction (applied to wheelsets) and coupler forces (applied to the carbody) determined from longitudinal train dynamics simulation. This will require details of locomotive traction capabilities and locomotive electronics such as traction control systems. Fortunately it is possible to incorporate this data into a script for use in a MBS program. Most MBS packages are able to perform a variety of vehicle analyses to suit different requirements, with the main examples being [19, 20]:

- Eigenvalue analysis: A type of frequency analysis that determines a railway vehicle's modes of vibration. This can be used to detect natural frequencies responsible for body vibration, suspension oscillations such as bouncing, and unstable bogie hunting at high speeds. Only linear equations of motion are suitable for this analysis.
- Stochastic analysis: Similar to eigenvalue analysis and also requiring linear equations of motion, this type of frequency analysis is used to model a vehicle's vibrational response to track disturbances.
- Quasi-static analysis: Used to model effects of steady-state curving where vehicle bogies have adjusted to the track curvature after an initial disturbance. Vehicle speed and track radius is constant, whilst there are no track disturbances or other varying inputs.
- Time-stepping integration: Perhaps the most relevant for locomotive traction analysis, this powerful method fully solves the vehicle's equations of motion at discrete time steps. These equations of motion can incorporate nonlinearities and this method is well-suited for transient analysis. A wide range of numerical solvers, such as those based on Runge-Kutta techniques, are available for use in these simulations.

The MBS package used in this project will be GENSYS, with development starting on its component programs in 1971 by ASEA in Sweden according to the DEsolver [11] website. The first program was a linear frequency-domain utility and then development of a nonlinear time-

stepping integration program, where calculations are made for the model at small, discrete time steps, started in 1973. Consisting of two separate components to calculate lateral and vertical motions respectively, these were developed with the X15 high speed train. Further designs, including the Rc4 class locomotive in 1975 and the X2000 tilt train for ASEA and its successor ABB, were designed using these programs of which several revisions were made throughout the 1980s. In 1992 development started on a new three-dimensional simulation program and a new dynamics program, which were all transferred to a new company, DEsolver, along with other related programs for further development. The first version of the GENSYS railway vehicle analysis suite was then released in 1993, with DEsolver regularly releasing updated versions since then.

Section 2.4, clause 3 of AS 7509.1 [21] recognises the VAMPIRE, NUCARS and GENSYS software packages as suitable for dynamic behaviour simulation. NUCARS could not be considered since Central Queensland University (CQU) did not possess adequate licensing to use that program for this project, whilst VAMPIRE (as of early 2011) was not suitable for modelling longitudinal dynamics since:

- Velocities of 0 m/s could not be modelled
- The creepage expressions used assumed that only small amounts of wheelset pitch exists and its effects are ignored
- Although friction coefficients can be changed with respect to the track distance travelled, all wheel-rail contacts in the vehicle model were assumed to have identical friction coefficients at any time

For these reasons GENSYS was selected since CQU possessed licensing for it and the program was able to effectively model railway vehicle traction forces.

2.2.2. Co-ordinate systems

Figure 7 shows the sign convention used in railway vehicle simulation [22], with the vertical (z) axis facing downwards toward the ground. The longitudinal (x) direction faces toward the

direction of travel, whereas the lateral (y) axis points toward the right hand side of a body when facing in the direction of travel. Translational movement in the longitudinal, lateral and vertical axes is accompanied by roll, pitch and yaw rotations respectively.

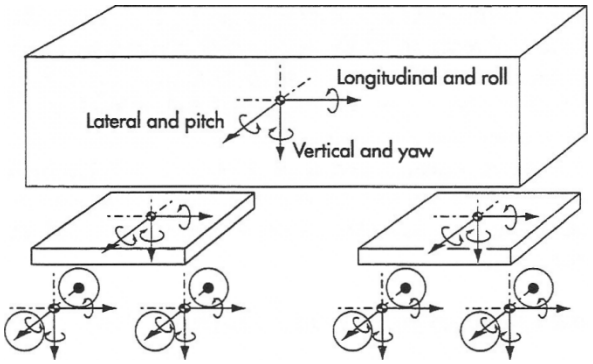

Figure 7: Vehicle/body co-ordinates [22]

Notice that each vehicle body in Figure 7 has its own co-ordinate system. These are usually tracked in multi-body simulation using a set of global co-ordinates [23] in one of the following manners:

- Absolute co-ordinates: Each body co-ordinate system (BCS) is described in terms of three absolute Cartesian co-ordinates from the global origin and by three independent rotations
- Trajectory co-ordinates: Each BCS is followed by an additional trajectory co-ordinate system (TCS) whose position and rotation are determined from their distance along the arc that defines the track centreline. BCSs maintain a fixed longitudinal distance from their TCSs but can move in all other directions (laterally, vertically, rolling, yawing and pitching). An example of this is shown in Figure 8 [23].

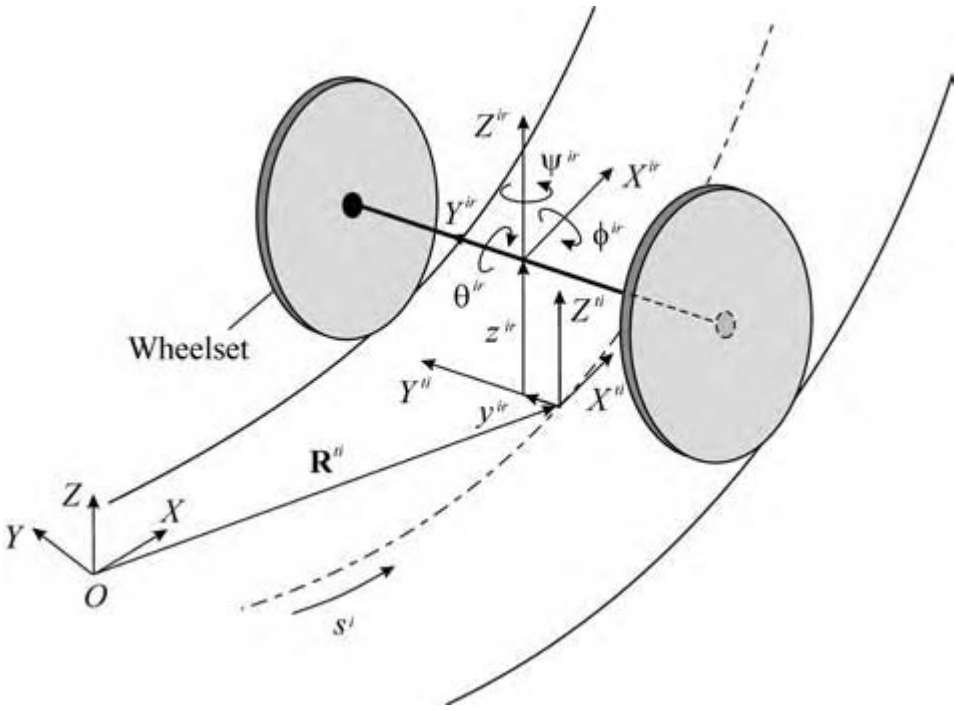

Figure 8: Trajectory co-ordinates [23]

To track the motions of bodies within a vehicle model, GENSYS uses the following dependent co-ordinate systems:

- fsys: A global, fixed co-ordinate system [24] in which the track trajectory is defined.
- esys: An Euler TCS that is related to fsys via trigonometric functions, making it suitable for large rotations and displacements [22, 24]. It follows track alignment and cant at the vehicle's nominal (or designed) speed [22]. Typically only one esys is required for each locomotive model because displacements of the bodies within it are small [24].
- lsys: A TCS that follows track alignment and cant, but is located at a fixed longitudinal distance from an esys. Related to an esys by linearised functions (small angle approximations), lsys is only suitable for small angles and displacements. They are typically used to track the motions of bodies within a locomotive model [22]. It is possible to use additional esys's to track bodies, particularly when they produce large rotations and/or displacements within a locomotive model, but this increases computing effort [24].

- bsys: A fixed BCS that describes a body's position relative to its lsys. In order to define a body, there must be an lsys (or body esys) for it to relate to which in turn requires an esys defined for the locomotive model [24].

Co-ordinate systems used for wheel-rail contact differ slightly from those used for vehicle/body motion. As shown in Figure 9 [25], the longitudinal (x) axis still points toward the direction of travel, but the vertical (z) axis points upwards, normal to the centre point of the contact patch (O). Likewise, the lateral (y) axis points left at a tangent to the contact patch centre point. (The surface curvatures A_1, B_1 and B_2 marked in Figure 9 relate to Hertz [26] theory.)

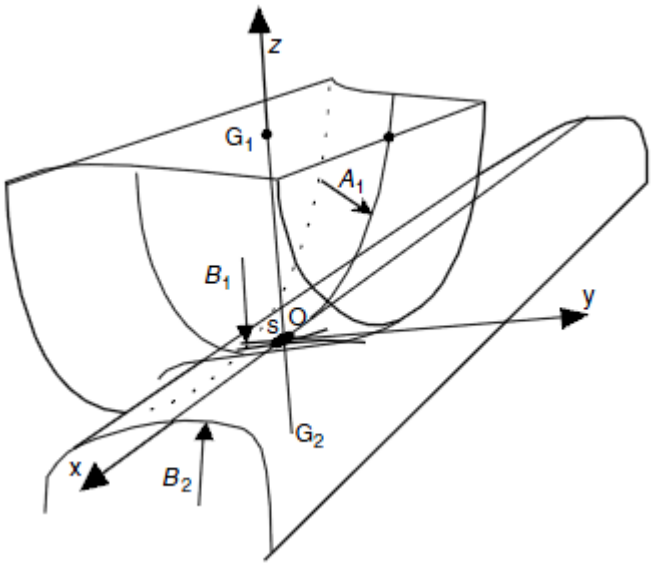

Figure 9: Wheel-rail contact patch co-ordinates [25]

2.2.3. Wheel-rail contact

Modelling interactions between railway wheels and rails is one of the critical areas in locomotive traction analysis. Forces and displacements are transferred between vehicles and track at each wheel-rail contact via small contact patches that have an area of roughly 1 cm^2 [27]. Despite their small size, wheel-rail contact patches are difficult to analyse partly because of the complex wheel and rail geometry involved, particularly as wheelsets move laterally and yaw as they travel along track [23, 25]. Further complications arise because of the highly concentrated stresses in contact areas, as well as the open nature of the system where contaminants like water, dust and even small stones can affect contact conditions [25].

When analysing wheel-rail contact, one of the first steps is to determine the shape, size, normal force on and pressure distribution within wheel-rail contact patches as determined from vehicle weight and wheel-rail geometry [28]. Point or non-conformal contact usually occurs between wheels and rails, but some combinations of new and/or worn wheel and rail profiles can result in conformal contact that occurs along a rail [23]. During flanging, or when a rail vehicle passes over a turnout, it is also possible for two or more contact patches to form at each wheel-rail interface [19]. Once the normal contact force and contact patch shapes have been found, the tangential force distribution within the contact patches can be calculated. Owing to distortion of wheel and rail surfaces and the rolling motion of wheelsets over track, areas of stick and slip form in contact patches; “stick” areas denote where the velocity of wheel and rail surfaces are identical, whilst “slip” occurs where there is a difference in wheel and rail surface velocity. Slip between the two bodies is referred to as creepage, which in turn gives rise to tangential creep forces that can be resolved into longitudinal and lateral creep forces respectively. Yaw rotations between contacting surfaces can also lead to the formation of ‘spin’ creep moments. As creepage increases within a contact patch, the stick area reduces as the contact patch becomes completely saturated with slip. Under full slip, the contact patch is transmitting the maximum amount of tangential force possible depending on available friction [23, 25, 29]. Slip in the contact patch can be increased when traction, braking and cornering forces are applied, which explains why locomotives cannot exert as much traction whilst cornering [9].

In light of this, wheel-rail contact modelling is an important part of locomotive traction analysis and vehicle dynamics in general, where several methods have been devised to model contact patch phenomena. The following subsections will first describe Hertz theory [26], which is widely used to calculate normal pressure distributions in the contact patch, and then related tangential creep-force laws such as those by Carter [30] and Kalker [31]. Complete wheel-rail modelling tools are then covered, namely CONTACT [32], finite-element modelling approaches and semi-Hertzian methods.

2.2.3.1. Normal contact (Hertz theory)

Non-conformal contact between two surfaces was first studied by Hertz [23, 26]. Two bodies in non-conformal contact, which are the wheel and rail in the railway case, are assumed to be elastic, frictionless half-spaces with continuous contact surfaces. These are loaded over an elliptical contact patch that is small in comparison to the dimensions and surface radii of the contacting bodies. Body surface curvatures are assumed to be constant in the contact patch, allowing the contact surface to be flat. The assumption of two half-spaces in non-conformal contact allows the resulting semi-ellipsoidal pressure distribution in the contact patch to be separately considered from the bodies' general stress state; in other words, stresses in the contact area vanish some distance away from it [23, 25].

The semi-axes *a* and *b* of the contact ellipse can be found with the following formulae in Equation 2 [23, 33].

$$a = m \cdot \sqrt[3]{\frac{3\pi \cdot N \cdot (k_1 + k_2)}{4 \cdot k_3}} \qquad b = n \cdot \sqrt[3]{\frac{3\pi \cdot N \cdot (k_1 + k_2)}{4 \cdot k_3}}$$

$$k_1 = \frac{1 - {\upsilon_R}^2}{E_W}, \qquad k_2 = \frac{1 - {\upsilon_W}^2}{E_R}, \qquad k_3 = \frac{1}{2}\left[\frac{1}{r_1} + \frac{1}{r_1'} + \frac{1}{r_2} + \frac{1}{r_2'}\right],$$

$$k_4 = \frac{1}{2} \cdot \sqrt[2]{\left(\frac{1}{r_1} - \frac{1}{r_1'}\right)^2 + \left(\frac{1}{r_2} - \frac{1}{r_2'}\right)^2 + 2\left(\frac{1}{r_1} - \frac{1}{r_1'}\right)\left(\frac{1}{r_2} - \frac{1}{r_2'}\right) cos2\psi},$$

$$\theta = arccos\left(\frac{k_4}{k_3}\right)$$

Equation 2: Hertz contact ellipse semi-axis formulae [23, 33]

Where: a, b = Contact ellipse semi-axes

k_1, k_2, k_3, k_4 = Coefficients based on wheel and rail material and geometric properties

m, n = Hertz coefficients, described in the following paragraph

N = Normal contact force

υ_R = Poisson's ratio for rail

υ_W = Poisson's ratio for wheel

E_R = Elastic modulus for rail

E_W = Elastic modulus for wheel

r_1 = Principal rolling radius of wheel at contact point

r_1' = Principal transverse radius of wheel profile curvature at contact point

r_2 = Principal rolling radius of rail at contact point, assumed to be infinite

r_2' = Principal transverse radius of rail profile curvature at contact point

θ = Angle between contacting planes

The m and n coefficients can be calculated using the following formulae in Equation 3 [25] allowing for the interval $0 < n/m < \infty$.

$$A = \frac{1}{2}\left(\frac{1}{r_1} + \frac{1}{r_2}\right), \qquad B = \frac{1}{2}\left(\frac{1}{r_1'} + \frac{1}{r_2'}\right), \qquad n\left(\frac{A}{B}\right) = m\left(\frac{1}{A/B}\right)$$

Equation 3: Hertz m & n coefficients [25]

Where: A = Rolling (longitudinal) curvature at contact point

B = Transverse (lateral) curvature at contact point

Alternatively, the *m* and *n* coefficients can be interpolated from Table 1, which contains data adapted from [25].

Table 1: Hertz coefficients for 0° ≤ θ ≤180° [25]

θ°	**0**	**5**	**10**	**30**	**60**	**90**	**120**	**150**	**170**	**175**	**180**
A/B	0	0.0019	0.0077	0.0717	0.3333	1	3.0	13.93	130.6	524.6	∞
n/m = b/a	0	0.0212	0.0470	0.1806	0.4826	1	2.0720	5.5380	21.26	47.20	∞
m	∞	11.238	6.612	2.731	1.486	1	0.7171	0.4931	0.311	0.2381	0

As the pressure distribution in the contact patch is semi-ellipsoidal, the contact pressure along the contact patch's longitudinal *x* and lateral *y* axes is as shown in Equation 4 [34].

$$p(x,y) = \frac{3 \cdot N}{2 \cdot \pi \cdot a \cdot b}\sqrt{1 - \left(\frac{x}{a}\right)^2 - \left(\frac{y}{b}\right)^2}$$

Equation 4: Semi-ellipsoidal contact patch pressure distribution [34]

Where: p = Contact pressure

x = Longitudinal contact patch axis

y = Lateral contact patch axis

Hertz theory is widely used today to estimate the size of and stress distribution within contact patches for use in vehicle dynamic analysis and many tangential contact algorithms, but there are a few drawbacks to consider when conducting more advanced simulations like traction modelling, flanging and vehicle response to turnouts. Although modifications can be made to detect multiple contact points, there are problems with modelling slender contact ellipses that occur, for example, when contact is made with the inside corner of the high rail whilst flanging occurs. As Hertz theory is concerned only with non-conformal contact and assumes an elliptical contact patch shape, it understandably cannot model conformal contact and has trouble modelling non-elliptical contact patches [25, 35-37].

2.2.3.2. Tangential contact

Slip between wheels and rail allows tangential (longitudinal and lateral) and spin creepages to form in the contact patch. The methods used to calculate creep forces will be briefly described by first referring to Figure 10 [23], which depicts a wheel rolling over a rail at the contact point P.

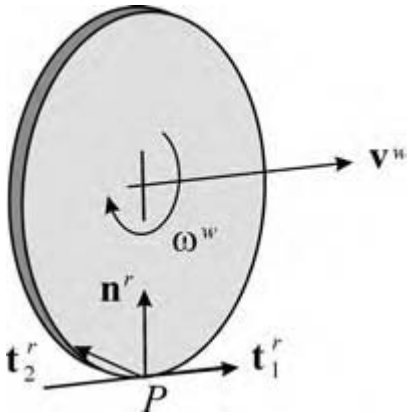

Figure 10: Wheel-rail contact frame [23]

Where: $\boldsymbol{v}^W$ = Wheel velocity

$\boldsymbol{\omega}^W$ = Wheel angular velocity

$\boldsymbol{n}^R$ = Unit normal to wheel/rail surfaces at contact point

$\boldsymbol{t}_1^R$ = Unit longitudinal tangent to wheel/rail surfaces at contact point

$\boldsymbol{t}_2^R$ = Unit lateral tangent to wheel/rail surfaces at contact point

P = Contact point

The longitudinal, lateral and spin creepages can now be defined as in Equation 5 [23].

$$\zeta_x = \frac{(\dot{\boldsymbol{r}}_P^W - \dot{\boldsymbol{r}}_P^R)\cdot \boldsymbol{t}_1^R}{V}, \qquad \zeta_y = \frac{(\dot{\boldsymbol{r}}_P^W - \dot{\boldsymbol{r}}_P^R)\cdot \boldsymbol{t}_2^R}{V}, \qquad \varphi = \frac{(\boldsymbol{\omega}^W - \boldsymbol{\omega}^R)\cdot \boldsymbol{n}^R}{V}$$

$$\boldsymbol{n}^R = \frac{\boldsymbol{t}_1^R \times \boldsymbol{t}_2^R}{|\boldsymbol{t}_1^R \times \boldsymbol{t}_2^R|}, \qquad V = \boldsymbol{v}^{W^T} \boldsymbol{t}_1^R$$

Equation 5: Longitudinal, lateral and spin creepage formulations [23]

Where: V = Magnitude of wheel velocity along the contact point longitudinal tangent

$\dot{\boldsymbol{r}}_P$ = Velocity vector at contact point

ζ_x = Longitudinal creepage

ζ_y = Lateral creepage

φ = Spin creepage

Superscripts: W = Wheel, R = Rail

In order to calculate contact patch forces, the true slip is first defined in terms of contact patch co-ordinates along the *x* and *y* axes. The formulation for this in Equation 6 [23] is based on pure rigid body kinematics for simplicity in the railway case.

$$\dot{\bar{\boldsymbol{w}}}(x,y) = \begin{bmatrix} \dot{\bar{\boldsymbol{w}}}_1 \\ \dot{\bar{\boldsymbol{w}}}_2 \end{bmatrix} = \begin{bmatrix} \dot{\boldsymbol{r}}_P^{WR} \cdot \boldsymbol{t}_1^R \\ \dot{\boldsymbol{r}}_P^{WR} \cdot \boldsymbol{t}_2^R \end{bmatrix}, \qquad \dot{\boldsymbol{r}}_P^{WR} = \dot{\boldsymbol{r}}_P^W - \dot{\boldsymbol{r}}_P^R$$

Equation 6: True slip in contact patch [23]

Where: $\dot{\bar{\boldsymbol{w}}}$ = True slip

$\dot{\bar{\boldsymbol{w}}}_1, \dot{\bar{\boldsymbol{w}}}_2$ = True slip components

$\dot{\boldsymbol{r}}_P^{WR}$ = Relative velocity at contact point

Tangential tractions in the contact patch can now be defined using Coulomb's law, along with the contact pressure *p* in Equation 7 [23].

$$|\boldsymbol{F}_T| = \left|\left[F_{Tx},\, F_{Ty}\right]^T\right| \leq \mu p \qquad \text{when} \quad \left|\dot{\tilde{\boldsymbol{w}}}\right| = 0 \qquad \text{(adhesion area)}$$

$$\boldsymbol{F}_T = \frac{\mu p \dot{\tilde{\boldsymbol{w}}}}{|\dot{\tilde{\boldsymbol{w}}}|} \qquad \text{when} \quad \left|\dot{\tilde{\boldsymbol{w}}}\right| \neq 0 \qquad \text{(slip area)}$$

Equation 7: Tangential tractions in contact patch [23]

Where: $\boldsymbol{F}_T$ = Tangential traction

F_{Tx} = Component along *x* axis

F_{Ty} = Component along *y* axis

μ = Coefficient of friction at wheel-rail interface

The above formulations now allow the tangential creep forces and spin creep moments to be defined as in Equation 8 [23].

$$F_x = \int\int F_{Tx}\, dx\, dy, \qquad F_y = \int\int F_{Ty}\, dx\, dy,$$

$$M = \int\int \left(xF_{Ty} - yF_{Tx}\right) dx\, dy$$

Equation 8: Tangential creep forces and spin creep moments [23]

Where: F_x = Longitudinal creep force

F_y = Lateral creep force

M = Spin creep moment

The distribution of tangential creep forces and spin creep moments in a contact patch depend on the normal force, creepages and dimensions of the contact ellipse [23], [34]. Several creep force laws have been devised to define the relationship between these creepages, with the first attempt being made by Carter in 1926 with a two-dimensional creep theory. Carter [30] assumed that the contact area was a 2D rectangular strip, wheels and rails could be represented by cylinders and thick plates respectively, and the wheel radius is larger than the contact patch length. This allows the contacting bodies to be considered as infinite elastic mediums, bounded by a plane with local tangential tractions and pressure distribution in the contact patch [23]. The tangential stress distribution in the contact area is assumed to be the difference between semicircular slip and adhesion profiles, with the latter starting at the leading edge where slip cannot occur as

shown by Cain [38]. A diagram of the superimposed slip and adhesion areas is shown in Figure 11 [29].

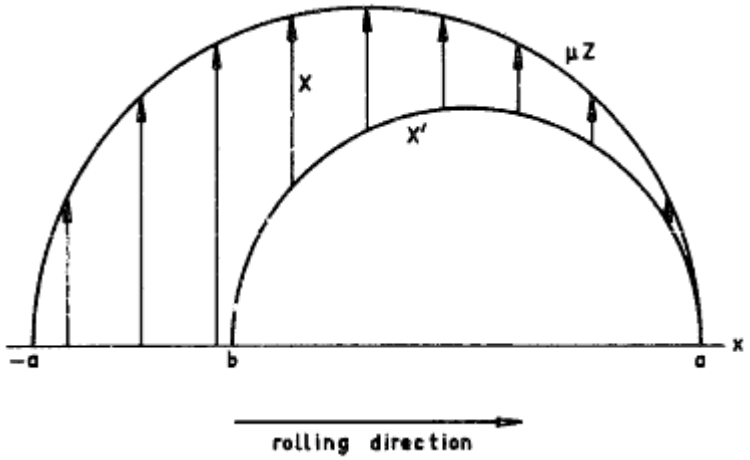

Figure 11: Contact patch slip and adhesion areas according to Carter theory [29]

The stress distribution in the contact area is obtained by subtracting the adhesion area from the slip area, giving the shape shown in Figure 12 [23]. When both slip and adhesion areas are present, the stress curve follows path ADCA', with points C and O moving further toward A as the adhesion area shrinks. If slip saturation occurs, the stress curve follows the upper limit curve ABCA', whereas in the case of pure rolling (adhesion area only) no slip exists in the contact patch [23, 29].

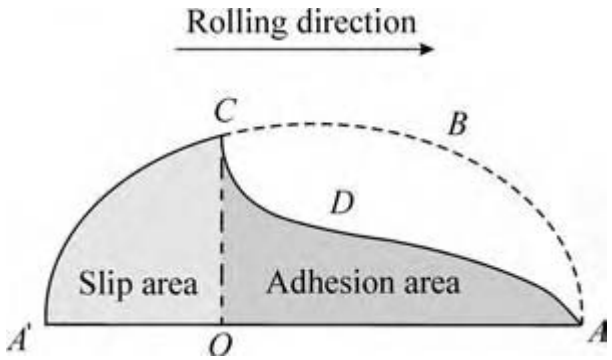

Figure 12: Contact patch stress distribution according to Carter theory [23]

Carter's longitudinal creepage and tangential force relation can be written as in Equation 9 [23, 39].

$$\frac{F_T}{\mu N_T} = \begin{cases} -k\zeta_x + 0.25k^2\zeta_x|\zeta_x| & k|\zeta_x| \leq 2 \\ -sign(\zeta_x) & k|\zeta_x| > 2' \end{cases} \quad \zeta_x = \frac{2(V_T+V_C)}{V_T+V_C}, \qquad k = \frac{4R_W}{\mu a}$$

Equation 9: Longitudinal creepage and tangential force (Carter theory) [23, 39]

Where: F_T = Tangential force per unit lateral length exerted at contact area on wheel

N_T = Total normal force per unit lateral length exerted on wheel

V_T = Tangential forward velocity

V_C = Tangential circumferential velocity

k = Carter's creepage coefficient

R_W = Wheel radius

These relationships define Carter's creep saturation law, which is compared to the linear Coulomb law in Figure 13 [23].

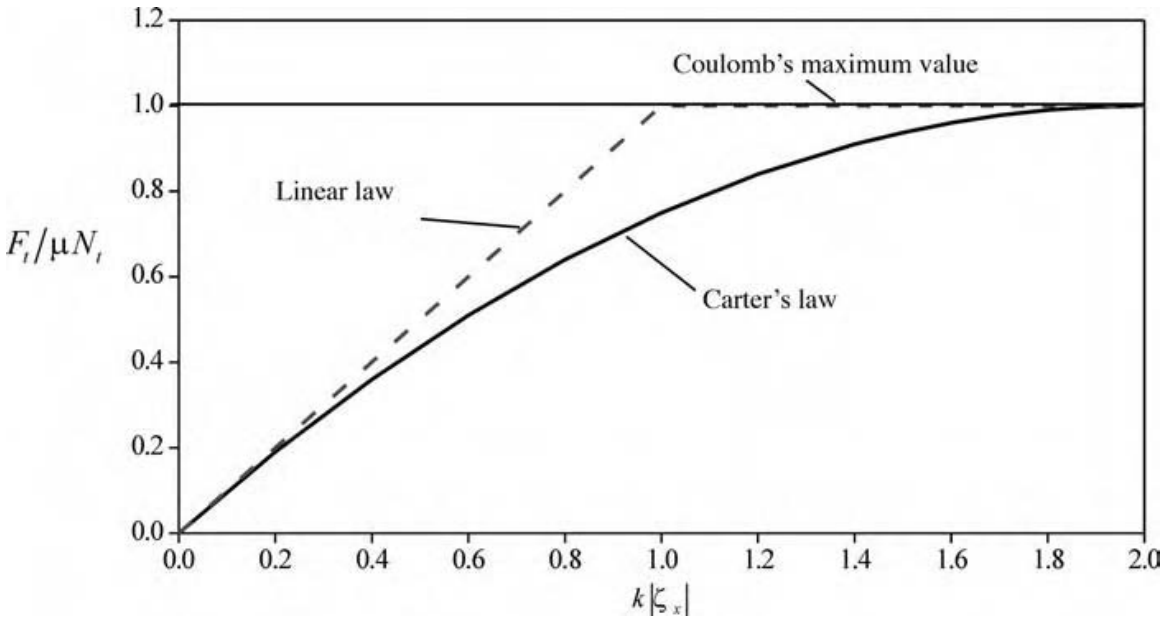

Figure 13: Comparison of Coulomb and Carter creep saturation laws [23]

Kalker devised a number of creep-force theories, the first being Linear Theory that was developed from 1957-1972 and introduced in Kalker's 1967 PhD thesis [34]. Linear Theory is concerned with modelling small creepages where the slip area is so small it can be ignored. As a result, the entire contact patch is assumed to be in adhesion and true slip vanishes completely, although the tangential contact condition is violated at its trailing edge. Hertzian contact conditions are assumed where the wheel and rail are half spaces with an elliptical contact

pressure distribution [23, 34]. The tangential creep forces and spin creep moment are obtained using the formulae in Equation 10 [23, 29].

$$\begin{bmatrix} F_x \\ F_y \\ M \end{bmatrix} = -Gab \begin{bmatrix} c_{11} & 0 & 0 \\ 0 & c_{22} & \sqrt{ab}c_{23} \\ 0 & -\sqrt{ab}c_{23} & abc_{33} \end{bmatrix} \begin{bmatrix} \zeta_x \\ \zeta_y \\ \varphi \end{bmatrix}, \qquad \frac{\nu}{G} = \frac{1}{2}\left[\frac{\nu^W}{G^W} + \frac{\nu^R}{G^R}\right]$$

Equation 10: Kalker's linear theory – Creep force and spin moment relation [23, 29]

Where: G = Average shear modulus of rigidity

G^R = Shear modulus of rigidity for rail

G^W = Shear modulus of rigidity for wheel

ν = Average Poisson's ratio

ν^R = Poisson's ratio for rail

ν^W = Poisson's ratio for wheel

$c_{11}, c_{22}, c_{23}, c_{33}$ = Kalker's creepage and spin coefficients

Values for Kalker's creepage and spin coefficients can be linearly interpolated from tables [29, 31, 40], or from a polynomial fit proposed by Ayasse & Chollet [25] from the contact ellipse semi-axes.

Carter's theory was extended to the 3D case of two spheres without spin by Johnson [41, 42], and then to smooth half-spaces without spin by Vermeulen & Johnson [43]. The latter theory assumes the contact area shown in Figure 14 [23] with elliptical adhesion and slip areas.

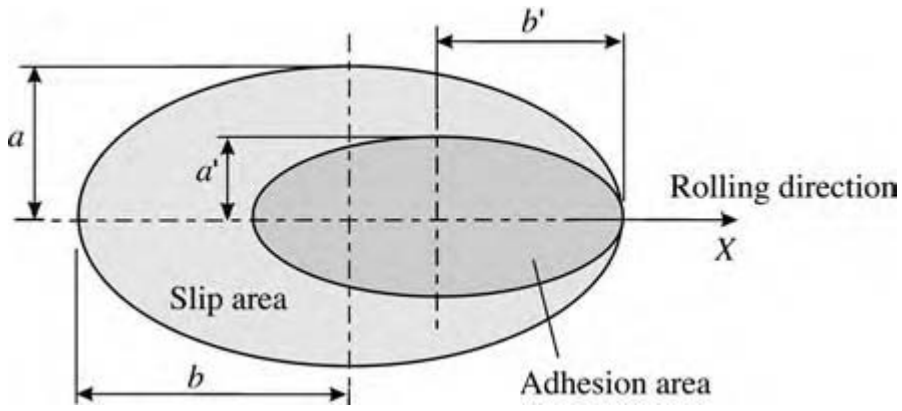

Figure 14: Contact area according to Vermeulen & Johnson [23]

Based on this assumed contact area and experimental data, Vermeulen & Johnson developed their creep-force law [31]. For brevity, only the expression for total creep force will be listed below in Equation 11; related equations are listed in the relevant literature [34].

$$\frac{\boldsymbol{F}}{\mu N} = [1 - (1 - \tau^3)]\boldsymbol{e}_1$$

Equation 11: Vermeulen & Johnson – total creep force [34]

Where: $\boldsymbol{F}$ = Total creep force vector
τ = Dimensionless total creep parameter
$\boldsymbol{e}_1$ = Unit longitudinal vector

Kalker improved Vermeulen & Johnson's creep-force law in 1968 by incorporating creepage coefficients, resulting in Kalker's Empirical Theory and a slightly different creep-force formulation as shown in Equation 12 [31, 34]. Related equations can be referred to in [34] along with those for Vermeulen & Johnson's formulation.

$$\frac{\boldsymbol{F}}{\mu N} = \begin{cases} f_1(\tau)\boldsymbol{e}_1 + f_2(\tau)\boldsymbol{e}_2 & \tau \leq 1 \\ \boldsymbol{e}_2 & \tau \geq 1 \end{cases}$$

Equation 12: Kalker's empirical theory – creep force [31, 34]

Where: $\boldsymbol{e}_2$ = Unit lateral vector

Figure 15 [31] compares Vermeulen & Johnson's experimental data (symbolled markers) and creep-force law (dashed line), along with Kalker's Empirical Theory (solid line), on a creep-force – creep plot.

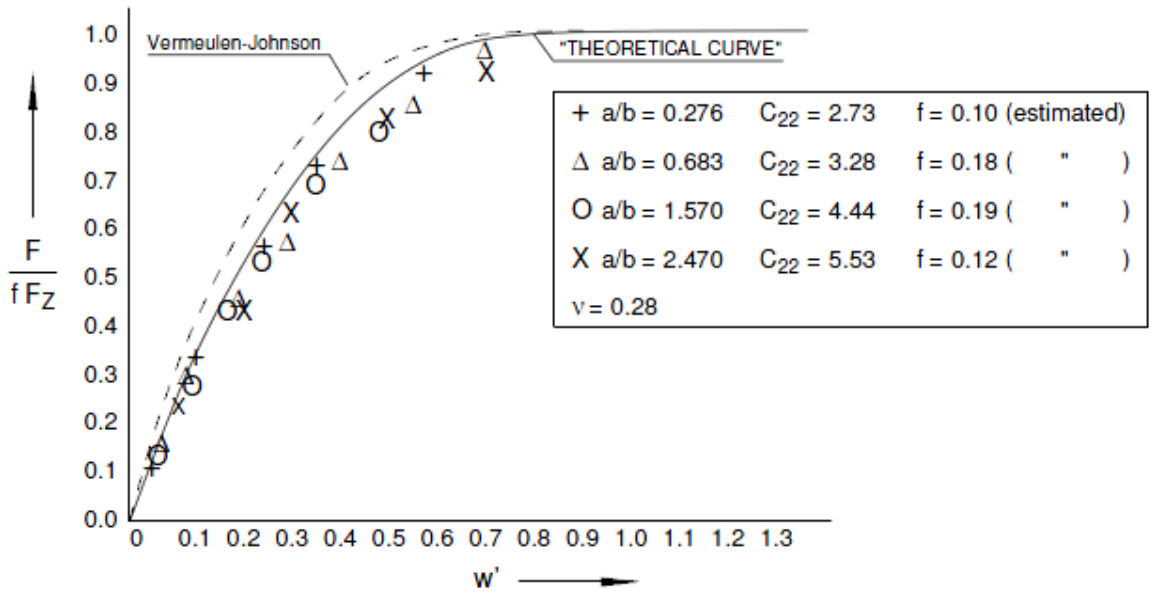

Figure 15: Comparison between Vermeulen & Johnson's experimental data and creep-force law, and Kalker's Empirical Theory [31]

Kalker's simplified theory assumes that, for quasi-identical bodies, the relationship between tangential surface displacement and traction can be approximated using compliant parameters [31, 34], as shown below in Equation 13 [23].

$$\boldsymbol{u}^{WR} = \boldsymbol{u}^{W} - \boldsymbol{u}^{R} = \left[L_x F_{tx,} \;\; L_y F_{ty}\right]^T$$

Equation 13: Kalker's simplified theory – approximate tangential surface displacement and traction [23]

Where: $\boldsymbol{u}^{WR}$ = Tangential surface displacement

$\boldsymbol{u}^{R}$ = Rail displacement

$\boldsymbol{u}^{W}$ = Wheel displacement

L_x, L_y = Longitudinal and lateral compliant parameters

F_{tx}, F_{ty} = Longitudinal and lateral surface tractions

Assuming Hertzian contact and no slip, the tangential creep forces obtained using the simplified theory are then compared with the equivalent expressions from the linear theory to derive expressions for the three compliance parameters [23, 31, 34].

$$F_x = \int_{-b}^{b}\int_{-a}^{a} F_{tx}\, dx\, dy = -\frac{8a^2 b\zeta_x}{3L_x} = -Gabc_{11}\zeta_x$$

$$F_y = \int_{-b}^{b}\int_{-a}^{a} F_{ty}\, dx\, dy = -\frac{8a^2 b\zeta_y}{3L_y} - \frac{\pi a^2 b\varphi}{4L_y} = -Gabc_{22}\zeta_y - G(ab)^{1.5}c_{23}\varphi$$

$$L_x = L_1 = \frac{8a}{3Gc_{11}}, \qquad L_{y1} = L_2 = \frac{8a}{3Gc_{22}}, \qquad L_{y2} = L_3 = \frac{\pi a^2}{4G\sqrt{ab}c_{23}}$$

Equation 14: Kalker's simplified theory – compliance parameters [23, 31, 34]

Where: L_1, L_2, L_3 = Compliance parameters

Analytical solutions using the simplified theory can only be performed for cases of no slip, so for more general wheel-rail contact situations a numerical method is required. In 1982 Kalker developed FASTSIM [32], a computer program that numerically determines creep forces using the simplified theory and is widely used in wheel-rail contact simulations today. To allow this, the contact patch is normalised to a circle with a radius of unity and the tangential creep force equations are converted to a dimensionless form [32]. The contact patch is then divided into longitudinal strips of equal thickness, although if a spin pole is detected within some strips the solution is refined by splitting these strips in half longitudinally. Each strip is then divided into the same number of elements as there are strips, where stress calculations are carried out from each strip's leading edge for each element with Kalker's coefficients assumed to be constant throughout the contact area [23, 25, 31, 34]. An example of output from FASTSIM can be seen in Figure 16 [31, 44] showing how the contact area is divided into strips (14 in this case) and elements. The arrows in each element represent the direction and magnitude of the tangential creep forces in each.

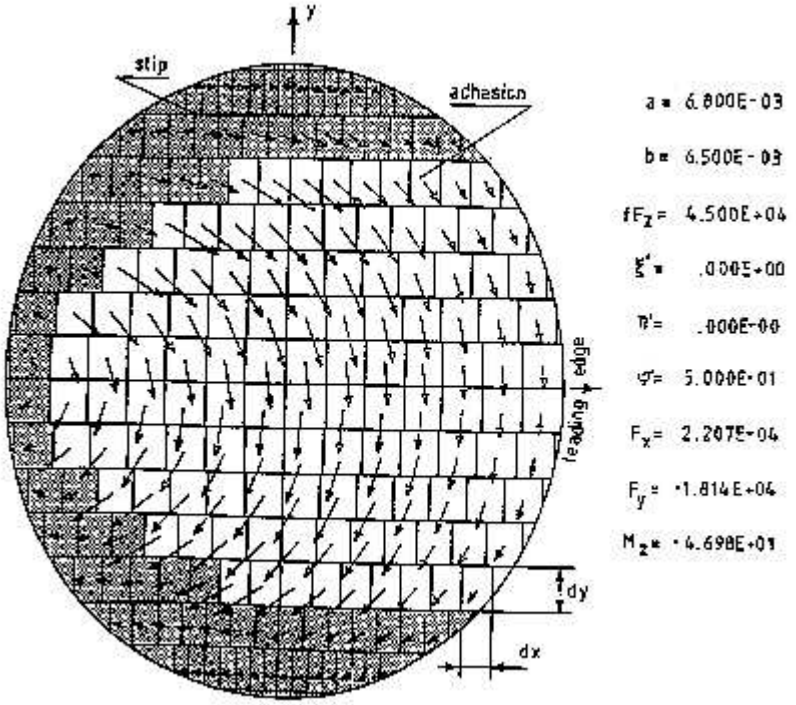

Figure 16: An example of output from FASTSIM [31, 44]

FASTSIM generally produces an error of roughly 10-15% [31], but this is suitable for most vehicle analyses especially when considering its quick solving time. Several modifications can be made to FASTSIM, including a method outlined by Zaazaa & Schwab [34] to help deal with wheel-rail interface contamination by adding an additional displacement to the tangential surface displacement and traction relationship. Ayasse & Chollet [25] report that FASTSIM can be modified to model non-Hertzian contact, whilst Alonso, Giménez, & Martín [45] created a FASTSIM-M version that was modified to incorporate a fourth compliance parameter in an effort to improve the calculation of spin moments. Compared with the original FASTSIM code, FASTSIM-M showed little difference in vehicle dynamics simulations although it can more accurately model dissipated energy in the wheel-rail contact area [45].

USETAB is a program written by Kalker [40] that calculates tangential creep forces and spin creep moments by linearly interpolating from pre-tabulated data [31]. It originally used results pre-tabulated by British Rail from Kalker's complete theory [36, 46], with an improved version being made in 1996 from Kalker's [47] CONTACT program. Contact ellipse semi-axis dimensions and creepages are required as program inputs along with the equivalent modulus of

rigidity and friction coefficient [23]. USETAB can be eight times quicker than FASTSIM and produce results with only ~1.5% error [23], but USETAB requires roughly ten times more memory to run than FASTSIM [31]. Like FASTSIM, USETAB is suitable only for Hertzian contact and quasi-identical bodies, but Poisson's ratio is set to a constant 0.28 which is the value for steel [31].

White et al. [48] and Shen, Hedrick & Elkins [23, 49], developed a non-linear "heuristic" theory that uses Vermeulen & Johnson's creep-force law and considers the effects of slip. The resultant tangential creep force in the contact area is obtained from Kalker's linear theory as shown in Equation 15 [23].

$$\begin{bmatrix} F_x^K \\ F_y^K \end{bmatrix} = -Gab \begin{bmatrix} c_{11} & 0 & 0 \\ 0 & c_{22} & \sqrt{ab}c_{23} \end{bmatrix} \begin{bmatrix} \zeta_x \\ \zeta_y \\ \varphi \end{bmatrix}$$

Equation 15: Kalker's linear theory – creep forces in contact area [23]

Where: F_x^K, F_y^K = Longitudinal and lateral creep forces calculated using Kalker linear theory

As the magnitude of the resultant tangential creep force cannot exceed the pure slip value μN according to the laws of Coulomb friction, Vermeulen & Johnson's theory is used to limit it with a nonlinear value [49] as defined in Equation 16 [23]:

$$\bar{F}_L = \sqrt{(F_x^K)^2 + (F_y^K)^2},$$

$$F_L = \begin{cases} \mu N \left[\left(\frac{\bar{F}_L}{\mu N} \right) - \frac{1}{3} \left(\frac{\bar{F}_L}{\mu N} \right)^2 + \frac{1}{27} \left(\frac{\bar{F}_L}{\mu N} \right)^3 \right] & \bar{F}_L \leq 3\mu N \\ \mu N & \bar{F}_L > 3\mu N \end{cases}$$

Equation 16: Kalker's linear theory – creep force limiting [23]

Where: $\bar{F}_L$ = Resultant linear creep force

F_L = Limiting nonlinear creep force

The resulting creep force model is then scaled by a creep-force reduction coefficient as shown in Equation 17 [23].

$$\begin{bmatrix} F_x \\ F_y \end{bmatrix} = \varepsilon \begin{bmatrix} \bar{F}_x \\ \bar{F}_y \end{bmatrix}, \qquad \varepsilon = \frac{F_L}{\bar{F}_L}$$

Equation 17: Kalker's linear theory – creep force reduction coefficient [23]

Where: $\bar{F}_x$, $\bar{F}_y$ = Longitudinal and lateral components of $\bar{F}_L$
ε = Creep-force reduction coefficient

According to Shen, Hedrick & Elkins [49], the heuristic model gives more realistic values for creep forces than Kalker's linear theory outside the linear creep range and it compares well with Kalker's simplified theory unless high values of spin are present [39], in which case the results are unsatisfactory [23].

Polach [50] has developed a method to calculate tangential forces and spin creep moments for Hertzian contact conditions that requires significantly less computing time than FASTSIM. At any arbitrary point in the contact patch, the maximum tangential stress is simply defined as in Equation 18 [50]

$$\tau_{MAX} = \mu\sigma$$

Equation 18: Polach theory – maximum tangential stress [50]

Where: τ_{MAX} = Maximum tangential stress
μ = Friction coefficient
σ = Normal stress

The normal and tangential stresses, along with the areas of adhesion and slip in the contact patch, are assumed to vary as shown in Figure 17 [50]. Notice how tangential stress is assumed to increase linearly in the adhesion area.

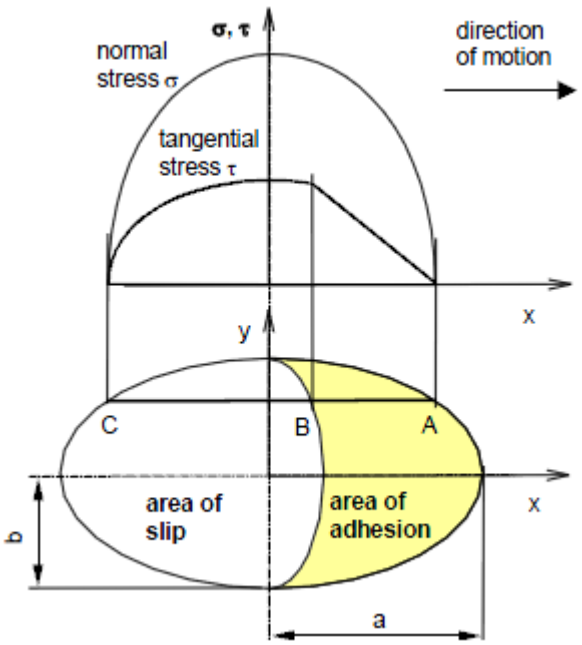

Figure 17: Assumed distribution of stresses in Polach's method [50]

Tangential forces and the relative creep spin moment in the contact patch are then calculated as in Equation 19 [50]:

$$F = \frac{2 \cdot Q \cdot \mu}{\pi}\left(\frac{\varepsilon}{1+\varepsilon^2} + \arctan \varepsilon\right), \qquad \psi = \frac{\omega \sin \gamma}{v} = \frac{\sin \gamma}{r}$$

Equation 19: Polach theory – tangential forces and relative creep spin moment [50]

Where: Q = Wheel load

ε = Gradient of tangential stress in adhesion area

ψ = Relative creep spin moment

ω = Wheel angular velocity

γ = Angle of contacting surfaces

v = Wheel tangential velocity

r = Wheel radius

Methods of resolving the tangential force into longitudinal and lateral components, calculating ε and adapting the formulations to allow use of Kalker's creepage and spin coefficients are contained in the relevant literature [50]. According to tests conducted for an ADAMS/Rail multi-body model, Polach's method gives similar results to FASTSIM, whilst tests in other programs show that calculation times are typically 3-8 and up to 17 times quicker depending on

the number of strips the contact patch is divided into in FASTSIM. Polach [51] has since modified this method to model wheel-rail friction forces more accurately.

A comparison between Kalker's linear theory, the Shen-Hedrick-Elkins Heuristic model and Polach's method was made by Pombo & Ambrósio [52] whilst modelling wheelset flange contact in low radii curves. A version of Hertz theory with hysteresis damping was used to model normal forces, whilst the simulation techniques adopted allowed multiple contact points to be analysed. Simulations using Kalker's linear theory resulted in derailments since it cannot effectively model creep saturation levels effectively, while the heuristic model, although giving similar results to Polach's model, was susceptible to error as a result of high spin creepages.

2.2.3.3. Non-Hertzian contact

The creep force-laws described earlier all assume Hertzian contact conditions, so alternative methods are required for the analysis of non-Hertzian contact such as in the case for contact "jumps" during flanging [25]. Perhaps the most well-known example is CONTACT, developed using Kalker's principle of virtual work and exact 3D rolling contact theory [34], which is often used to evaluate the accuracy of other wheel-rail contact models. Tangential and spin creepages in the contact area are considered [53] and, unlike FASTSIM and USETAB, it can evaluate non-quasi-identical bodies [31]. CONTACT first starts by defining a rectangular potential contact area split into a user defined number of rows and columns, with the actual contact area consisting of elements where the distance between the deformed contacting bodies is zero. NORM and TANG algorithms are then used to evaluate the normal and tangential contact conditions respectively for each element [31, 34]. Although CONTACT is accurate, it has a few drawbacks, particularly the fact that it is ~2000 times slower than FASTSIM. Part of the reason for this is because it uses a complex non-linear formulation that requires iterative procedures to calculate solutions [31]. Because of CONTACT's high computational time, it is rarely used in multi-body vehicle analysis programs [34]. Additional issues with CONTACT include [53]:

- Half-space assumption: Although acceptable for most cases where the contact area is small compared to surface dimensions and curvatures, this condition is violated near the gauge corner
- Elastic deformation: Plastic deformation cannot be modelled
- Friction coefficients: CONTACT can be modified to accept different formulations for friction coefficients, but Kalker [40] shows no possible means of how to do this
- Surface roughness: Solutions for 2D contact have been devised, but a 3D analysis using CONTACT has not yet been performed. This would require a potential contact patch with at least 200 x 200 elements.

The exact 3D rolling theory has also been extended to non-conformal contact by Li & Kalker [54, 55], and later Li [56], by decomposing the wheel and rail into quasi-quarter spaces for analysis using Finite Element Modelling (FEM). Similarities to CONTACT include analysing normal and tangential contact separately, the definition of a rectangular potential contact area and a lengthy computer time, exacerbated in this case since FEM is required [34]

Other wheel-rail contact approaches using FEM have been developed [53], but these are slow and require a lot of computing power. On the plus side, a range of nonlinearities such as surface roughness, temperature effects and plastic deformation can be modelled. Unlike most FEM analyses, the contact area is small compared to the size of the contacting bodies and the high rotational speed of the wheel also introduces difficulties. To increase the accuracy of results, a denser mesh of elements is needed near the contact area, but this increases computational time and effort. Constantly re-meshing the contact surfaces can reduce the element count, but it can fail when analysing rolling motion if changes to the wheel's circumference as a result of the re-meshing need to be corrected. Another method is the "ALE formation", where wheel and rail material is assumed to move within fixed meshes. After the contact patch is located, adhesion areas are simply determined by noting where the tangential velocity of the wheel and rail surfaces match. Knothe, Wille & Zastrau [53] performed a FEM analysis of a S1002-profile wheel loaded at 90 kN and travelling at 200 km/h over UIC60 rail at a 1/40 inclination, finding that its contact pressure outputs varied markedly from Hertz theory and even differed from

Kalker's [57] CONTACT algorithm. Further development has been made to FEM techniques since Knothe, Wille & Zastrau's paper in 2001, with Quost et al. remarking in their report [35] that they are now very precise, but still too slow for use in vehicle simulation.

In light of the long computational times required by CONTACT and FEM, "semi-Hertzian" methods, to use the terminology of Quost et al. [35], have been developed with the aim of offering comparable results with much lower computational effort, allowing them to be used effectively in multi-body simulation (MBS) packages. As implied by the name semi-Hertzian, these methods incorporate elements of Hertz theory, either using "multi-Hertzian" approaches based on interaction between multiple ellipses or the virtual interpenetration of wheel and rail surfaces [36].

Sauvage devised a method that could determine multiple Hertzian ellipses (up to seven in the computer code) from the interpenetration of rigid wheel and rail profiles, calculated from the Hertzian curvatures *A* & *B* as in Equation 20 [36].

$$\delta = r\sqrt[3]{\left(\frac{3}{2}N\frac{1-\nu^2}{E}\right)^2(A+B)}$$

Equation 20: Rigid wheel-rail interpenetration from Hertz curvatures [36]

Where: δ = Interpenetration
E = Elastic modulus
ν = Poisson's ratio

It is recommended to halve the interpenetration value δ for the next step so that the scaled value $h=\delta/2$, but Sauvage did not do this, leading to larger contact overlaps. In Figure 18 [36], an initial elliptical profile of height h_1 is subtracted from the rigid deflection and, if interpenetration still occurs, marked by h_2 in this case, an additional ellipse is formed.

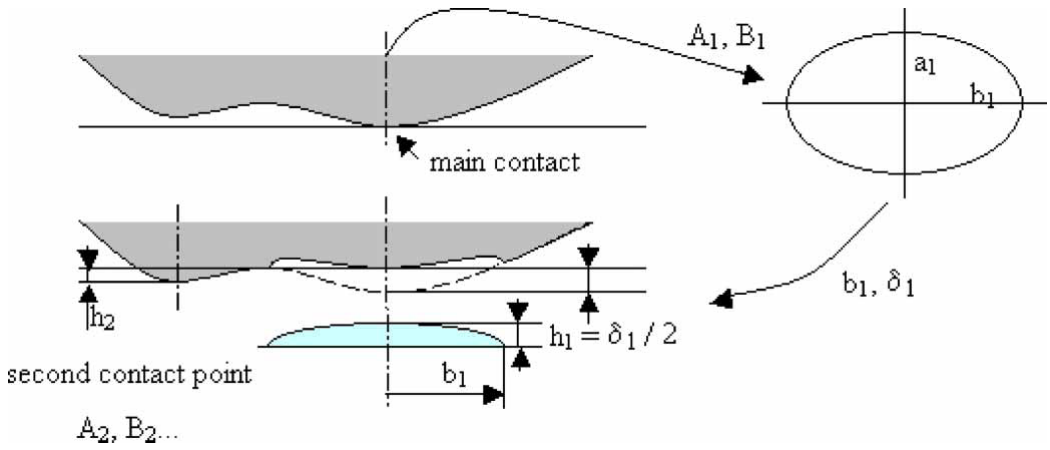

Figure 18: Determining a secondary contact ellipse using Sauvage's method [36]

Improvements can be made to this method by subtracting Boussinesq bell-curve deflections of the same height rather than elliptical deformations, avoiding the formation of secondary contact points. Sauvage used this theory in a code called DIPONT [36, 58], but it proved too slow for use in commercial MBS packages.

Pascal [59] devised an alternate method where multiple Hertzian contacts are found by quasi-statically applying lateral force to a wheelset at rail level whilst the normal load is kept constant. An equivalent ellipse is then formed from the multiple contacts with tangential forces evaluated using FASTSIM, making it valid only for vehicle dynamics simulations where Kalker's linear theory is adequate [36].

Ayasse's multi-Hertzian method included a number of simplifications to reduce computational effort so that the contact descriptions can be reduced to small pre-calculated tables from which data is interpolated in dynamic multi-body simulations. These simplifications include [36]:

- Wheelset roll during flanging: Instead of shifting the entire wheelset via longitudinal and roll displacements, profiles for left and right wheels are simply translated laterally and vertically in the transverse y-z plane. This assumption allows left and right wheels to be modelled independently and is reasonable for small wheelset roll angles, but errors will arise for large lateral displacements, roll angles and equivalent conicity differences between the left/right wheel profiles.

- Contact angle functions: Instead of directly recording track radii and wheel/rail profile curvatures as a function of lateral position, the radii of combined curvatures are recorded as piecewise linear functions. An example is shown in Figure 19 [36], where jumps in curvature are clearly visible.

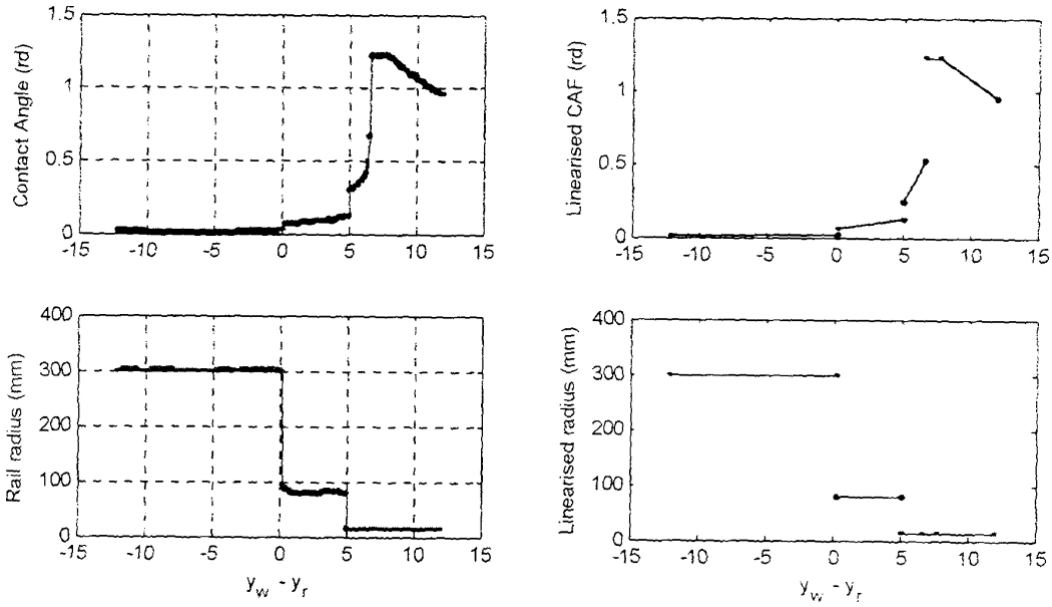

Figure 19: Wheel profile and track curvatures with associated contact angle functions [36]

Ayasse's code also includes provisions for detecting overlaps between separate Hertzian contacts on the rail face and gauge corner respectively during flange contact, with more details in [36]. Both Pascal's and Ayasse's methods have been validated in early MBS tests [60] of a CORAIL French passenger car at low speed, but the methods at the time only allowed three degrees of freedom per body. As MBS software improved, improvements were made to Ayasse's method which has since been renamed as the CAF (Contact Angle Function) method. Since this method was primarily developed as a means of determining jump overlaps quickly as opposed to determining the exact locations of multiple ellipses, there can be problems with changing rail profiles, for instance over turnouts, where identical ellipses can completely overlap each other [36].

Semi-Hertzian methods based on virtual penetration involve overlapping undeformed wheel and rail profiles in a contact zone by a distance δ_0 to form an interpenetration region as shown in Figure 20 [36].

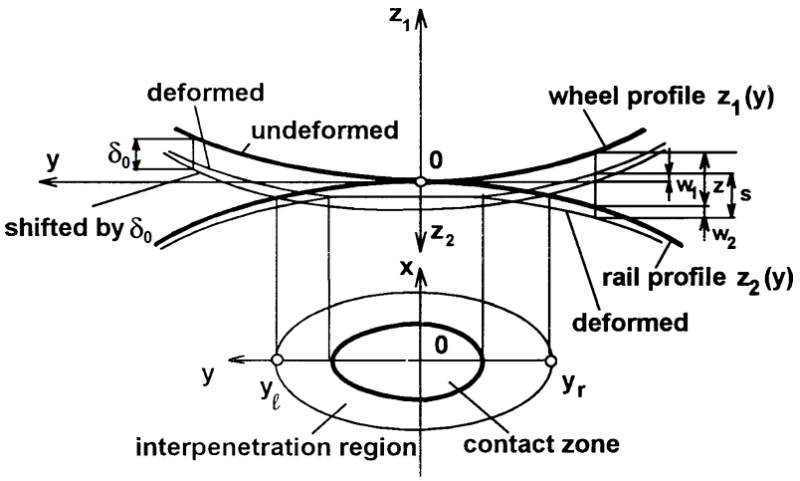

Figure 20: Interpenetration region and contact zone [36]

Linder's method involves discretising the contact area into longitudinal strips as shown in Figure 21 [36] where separate ellipses are generated from each strip.

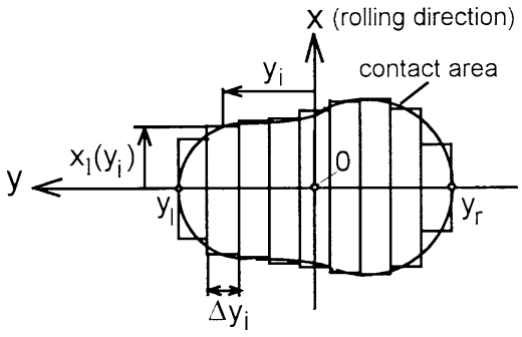

Figure 21: Discretisation of contact area in Linder's method [36]

A virtual interpenetration of $\delta_0 = 0.55\ \delta$ is used following numerical experiments carried out by Kik & Piotrowski [61] with CONTACT showing that this value is realistic. Creep forces in Linder's method are calculated using a modified version of FASTSIM to accept slightly different compliance (L) parameters and that assume a parabolic rather than elliptic normal stress distribution. Contact patches calculated using this method compare well to those from CONTACT except when multiple contact patches are encountered, although a direct comparison of creep forces has not yet been made [36].

Kik & Piotrowski's method assumes that the calculated contact area is quasi-Hertzian, meaning that it possesses some characteristics of Hertzian contact. The pressure distribution across the contact patch in this case is given in Equation 21 [36, 37]:

$$p(x,y) = \frac{p_0}{x_l(0)}\sqrt{x_l^2(y) - x^2}$$

Equation 21: Kik & Piotrowski's method – contact patch pressure distribution [36, 37]

Where: p_0 = Maximum normal pressure

Formulations for the maximum contact pressure and normal force distribution can be referred to in the related literature [36, 37]. Initial tests showed that the calculated contact patch shapes and maximum contact pressures somewhat differed from those calculated using CONTACT [37]. To improve those results, an algorithm was incorporated to correct the calculated contact patch shapes by stretching or contracting the initial profile longitudinally and/or laterally. Examples of the normal pressure distributions calculated by Kik & Piotrowski's method for (a) uncorrected and (b) corrected contact patches are compared with results from (c) CONTACT in Figure 22 [36] where a slight improvement can be seen when comparing (a) and (b) to (c). The differences between (a) and (b), at least visually, are slight. Notice how the maximum normal pressure for Kik & Piotrowski's method is lower than that for CONTACT, which is typical of semi-Hertzian methods.

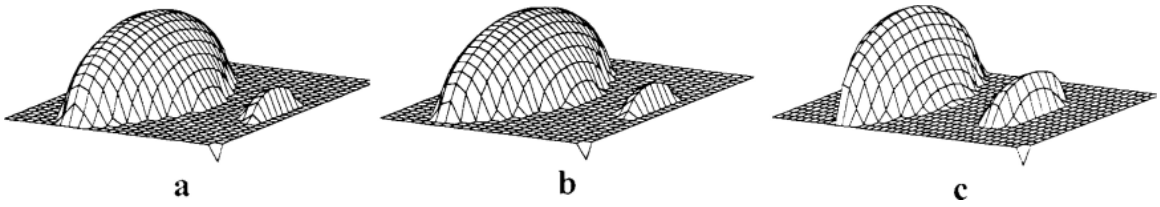

Figure 22: Normal contact pressure distributions calculated using (a) uncorrected and (b) corrected solutions compared to results from (c) CONTACT [36]

Tangential forces are calculated using a version of FASTSIM modified to analyse non-Hertzian contact patches. When used in combination with Kik & Piotrowski's method, the calculated tangential force distribution in the contact area is close to that of CONTACT, although significant changes can be noted in cases of pure spin because the semi-Hertzian method calculates elasticity parameters from an elliptical and consequently symmetrical area. Piotrowski & Kik [37] have also extended their method to model flange contact, wheelset travel over turnouts, wear simulation and wheel contact for corrugated rails.

From 1995-1996, Chollet developed a virtual penetration method where the contact area is divided into longitudinal strips, each with Hertzian characteristics, in a similar approach to those by Linder and Kik & Piotrowski. In order to more accurately model contact patch shapes, both the Hertzian *A* and *B* curvatures (described in Equation 3) are smoothed. The original STRIPES algorithm was used to determine an equivalent contact ellipse in a Simulink model, but despite performing well on the Manchester Benchmark [62] for vehicle analysis, it was much slower than Ayasse's multi-Hertzian FORTRAN code running in the VOCO MBS package. A project was then undertaken to adapt Chollet's semi-Hertzian contact description to Ayasse's faster code, along with changes to the Hertzian curvature smoothing procedures [36].

The improved STRIPES algorithm uses a modified form of FASTSIM to calculate tangential stresses in the contact area, with the Kalker (*c*) coefficients given as a function of the Hertzian *n* and *m* coefficients [36] and the slip being expressed in terms of the variation of longitudinal creepage between strips. Vehicle dynamics simulations by Ayasse & Chollet [63] using the VOCOLIN MBS software have shown little difference between wheelset forces calculated from STRIPES and Ayasse's multi-Hertzian method, but Piotrowski & Chollet [36] have remarked that STRIPES' physical interpretation appears to be more advanced. Further assessment of STRIPES was carried out by Quost et al. [35], who found that contact patches calculated using the method were close to that of FEM and Hertz theory in both Hertzian and non-Hertzian cases. Hertz theory, understandably, could not evaluate the latter condition. Because of fundamental differences between FASTSIM and CONTACT, such as the former assuming linear shear forces in the contact area, there were significant differences in the tangential forces calculated by STRIPES and CONTACT. Both parabolic and elliptical pressure distributions can be modelled in the contact patch by using the STRIPES P and STRIPES E algorithms respectively. Stresses calculated using SPRIPES P are less accurate, whereas STRIPES E may give false leading edges for the adhesion area.

2.2.4. Friction and adhesion coefficients

When two contacting surfaces under normal load are tangentially moved relative to each other, a friction force will be generated that opposes the direction of motion [27] because of deformations between microscopic asperities on the two surfaces. In some cases these asperities can weld together and break [64], or plough into others and remove them from the contacting surfaces [65]. The static friction force required to induce sliding motion between the two contacting surfaces is greater than the kinetic friction force required to maintain sliding motion once they are moving relative to each other [64]. In the railway case, both kinetic and static friction can occur in the contact patch as wheels roll over rail, even in the case of pure rolling. As the velocity difference between the wheel rim and rail surface increases when traction/braking torques or cornering forces are applied, creep levels increase and the contact patch transitions from a state of (almost) complete adhesion to full slip. At full slip, the amount of force that can be transferred by the contact patch is governed by the friction coefficient between the contacting surfaces [65]. For a constant friction coefficient, the frictional force (marked as “tractive force” in this case) increases with creep as shown in Figure 23 [27].

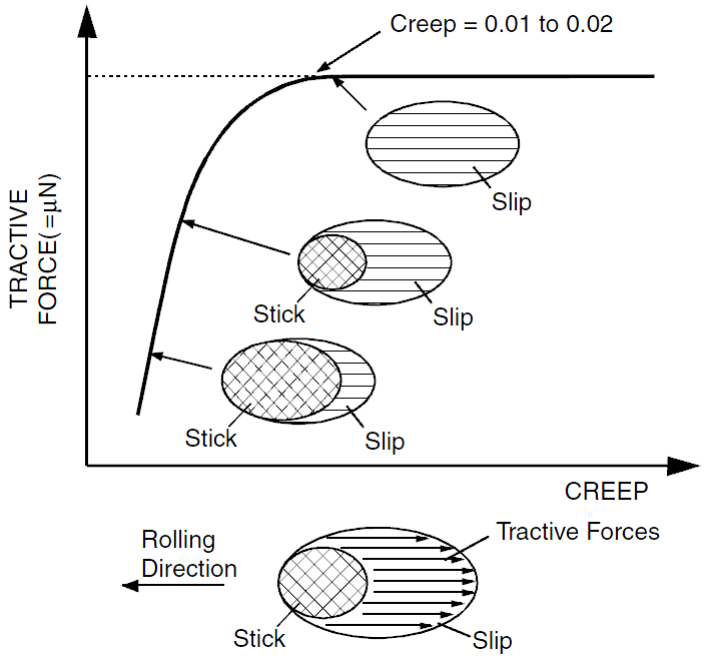

Figure 23: Relationship between traction and creep in the wheel – rail contact [27]

As the wheel-rail interface is open to the environment, surface contaminants such as water, dirt, oil and plant matter can deleteriously affect friction coefficients, whilst friction modifiers such as sand are often employed to help improve traction [27]. Friction coefficients are also affected by material properties, microscopic surface roughness and the amount of surface contamination present [66]. Typical values of friction coefficients for a variety of rail surface conditions measured from a hand-pushed rail tribometer are given in Table 2 [65].

Table 2: Friction coefficients [65]

Condition	**Coefficient of friction**
Sunshine dry rail, 19 °C	0.6-0.7
Recent rain, 5 °C	0.2-0.3
With a lot of grass on rail, 8 °C	0.05-0.1
Damp leaf film on rail, 8 °C	0.05-0.1

The tangential wheel-rail contact theories described earlier, namely those of Carter and Kalker [29], [67], Vermeulen & Johnson [31], Shen-Hedrick-Elkins [23] and Polach [50] assume a constant value for the coefficient of friction in the contact patch. Although this can describe the condition of the rail surface adequately, these models, being primarily designed for vehicle analysis, do not take traction and braking effects into consideration.

This requires the definition of another parameter, the adhesion coefficient, which is the ratio between the maximum tractive force a locomotive can exert onto the track and its weight. Unlike the friction force-creep relation shown in Figure 23, adhesion force-creep relations have a different form as shown from the recorded data by Lang & Roth [53, 68, 69] in Figure 24. According to Polach [69], the measurements were taken from a Siemens “S 252” locomotive travelling at 30 km/h on dry track, with Knothe, Wille & Zastrau [53] noting that they were recorded from an axle.

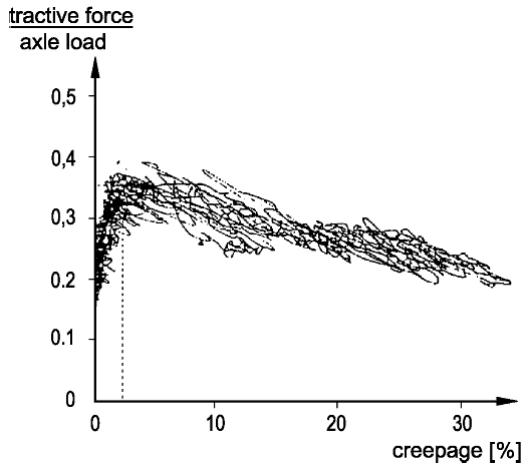

Figure 24: Model of creep forces based on measurements from Siemens locomotive S 252 (dry conditions, speed = 30 km/h) [53, 68, 69]

Despite a lot of scatter in the recorded data, it can be seen that tractive force increases until a creepage of ~1-2% is reached, from where it starts to decrease slightly as more creepage is applied. According to research by Knothe, Wille & Zastrau [53] and Polach [69], a likely reason for this is the increasing temperature in the contact area with slip, which has the effect of lowering the friction coefficient. Changes in track conditions can also alter adhesion force-creep curves as shown in Figure 25 [69]. These typical curves not only show a drop in the maximum adhesion force for wet rail in comparison to dry rail, but the peak adhesion force occurs at a higher creep level than for dry rail.

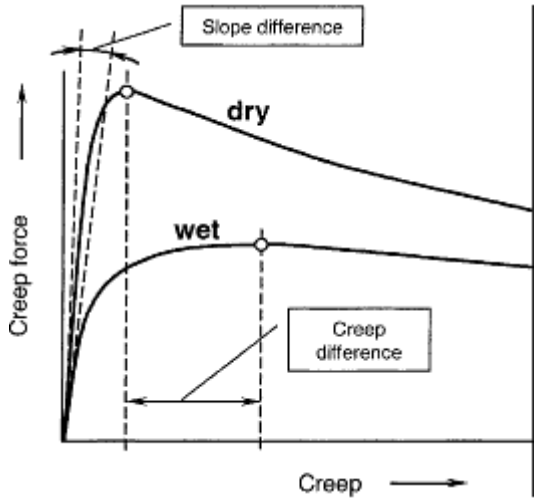

Figure 25: Typical adhesion force – creep curves for dry and wet rail [69]

Most tangential wheel-rail contact models are designed for use in vehicle dynamics simulations, which focus on evaluating vehicle behaviour such as responses to track disturbances and finding the critical speed. Since large creepages are rarely encountered in vehicle dynamics simulations, creep force – creep models with creep saturation characteristics similar to that in Figure 23 can be safely used in these analyses. For traction analysis where large creepages are present, different models that more accurately describe how creep force varies with creep are required [51].

2.2.4.1. Experimental findings

Some experiments have been undertaken to study the effects of factors such as surface contamination, vehicle velocity, axle load, friction modifiers and temperature on adhesion coefficients. Two notable examples are those by Zhang et al. [67] and Jin et al. [70] who seem to have used the same equipment consisting of a half-car model on a powered roller rig. Both tests monitored the effects of dry, water lubricated and machine oil lubricated surfaces whilst altering speed (0 – 260/280 km/h) and axle load (44 – 135kN). The test conducted by Zhang et al. [67] arrived at the following conclusions:

- For dry and clean wheels and rail, adhesion coefficients don't drop much after reaching a maximum as creep increases
- Machine oil contamination drops adhesion coefficients, but they don't fall much as speed increases
- With water contamination, adhesion coefficients decrease as speed increases and increases in track disturbance frequency decrease traction forces. (For dry wheels/rail, creepage rises and torque drops briefly during excitation, whilst for oil contamination, disturbances have little effect.)
- Increases in axle load lead to decreases in adhesion coefficients regardless of vehicle speed and track contamination

Zhang et al. [67] also observed an "interesting phenomenon" where wheelset torque increases as shown in Figure 26. Point B marks where creep saturation is reached after roller torque was

applied from point A. Wheelset torque decreased as expected through point C but, as roller torque was decreased at point D (at ~11% creep), the wheelset torque increased up to point E before decreasing to point B. This phenomenon might allow maximum locomotive traction forces to be increased further.

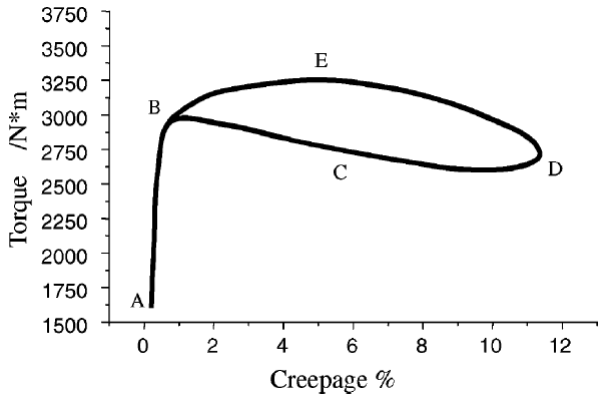

Figure 26: Variation of wheelset torque moment during test processes [67]

Tests by Jin et al. [70], excluding the wheelset torque phenomena noted by Zhang et al. [67], arrived at similar conclusions, but they found that the adhesion coefficient under oil-lubricated conditions increased with wheelset speed. The reason for this is not clear, with Jin et al. recommending further study using numerical and theoretical methods. Testing by Baek, Kyogoku & Nakahara [71] using a twin-disc roller rig found that, with water lubricated contact, maximum traction coefficients do not change much as contact pressure (axle load) increases, but they are reached at lower creep levels. Creep forces were also found to tail off more quickly as creep increases in this case. Chen et al. [72], who also used a twin-disc roller rig, found that raising the temperature of contaminating water (between 5-50° C) increases the adhesion coefficient, whilst increasing the wheel/rail surface roughness also (predictably) boosted adhesion in wet conditions.

Unfortunately, there has not been much research undertaken to date concerning the effects of sanding and traction modifiers on locomotive traction, with the underlying mechanisms currently understood poorly. So far the author has only found one article on the matter by Arias-Cuveas et al. [73], but since it is more concerned with comparing two proprietary friction-modifying compounds, not many general conclusions can be drawn save that friction modifiers

containing smaller particles (~10-100 μm) seem to provide better adhesion and cause less wheel/rail damage than compounds with larger particles (~0.5-2 mm).

During operation, a "third-body" layer can form between wheels and rail, consisting of worn material from the contacting surfaces and occasionally various contaminants from the environment. Niccolini & Berthier [74] have found that, for velocities below 0.1 m/s (tests were conducted on a roller rig at 0.03 m/s), the presence of this layer improves traction and wears preferentially to rail. As a result of third-body layer research, questions have been raised about the validity of Kalker's theoretical contact theories. But not all third-body layer formations are beneficial, for example where leaf litter on the rail surface can be compressed into a hard layer that can cause adhesion loss [27].

2.2.4.2. Modelling techniques

Polach [51] has developed an equation to calculate variable friction coefficients dependent on slip velocity for modelling the creep force – creep phenomena described earlier as shown in Equation 22 [51, 69].

$$\boldsymbol{\mu = \mu_0 \cdot [(1 - A) \cdot e^{-B \cdot w} + A]}, \qquad \boldsymbol{A = \frac{\mu_\infty}{\mu_0}}$$

Equation 22: Polach theory – Variable friction coefficient model [51, 69]

Where: μ = Friction coefficient

μ_0 = Maximum friction coefficient

μ_∞ = Limit friction coefficient at infinite slip velocity

B = Exponential friction decrease coefficient (s/m)

w = Slip velocity vector magnitude (m/s)

Modifications were also made to Polach's [51, 69] wheel-rail contact model, where the equation used to calculate tangential force (without spin) is modified using two reduction factors for adhesion and slip areas respectively as in Equation 23 [51, 69].

$$F = \frac{2 \cdot Q \cdot \mu}{\pi} \left(\frac{k_a \cdot \varepsilon}{1 + (k_a \cdot \varepsilon)^2} + \arctan(k_s \cdot \varepsilon) \right)$$

Equation 23: Polach theory – creep force (without spin) [51, 69]

Where: F = Tangential force (without spin)

Q = Wheel load

ε = Gradient of tangential stress in adhesion area

k_a = Reduction factor for adhesion area

k_s = Reduction factor for slip area

Typical values for some of these variables for dry and wet conditions are given in Table 3 [69], although in practice they are highly dependent on the type of locomotive being tested and need to be determined from experimental data.

Table 3: Typical model parameters for dry and wet conditions of wheel-rail contact [69]

Variable	Wheel-rail condition	
	Dry	Wet
k_a	1.00	0.30
k_s	0.40	0.10
f_0	0.55	0.30
A	0.40	0.40
B	0.60	0.20

As a result of these modifications to Polach's [51, 69] wheel-rail contact model, phenomena such as creep force reduction after creep saturation and adhesion reduction with velocity increases can be modelled with good agreement between simulated and measured data. Figure 27 [51] shows one example, where the creep force – creep curves for various surface contaminants calculated by Polach's model and from measured data (from adhesion tests for an SBB Re 460 locomotive at 20 km/h) are compared.

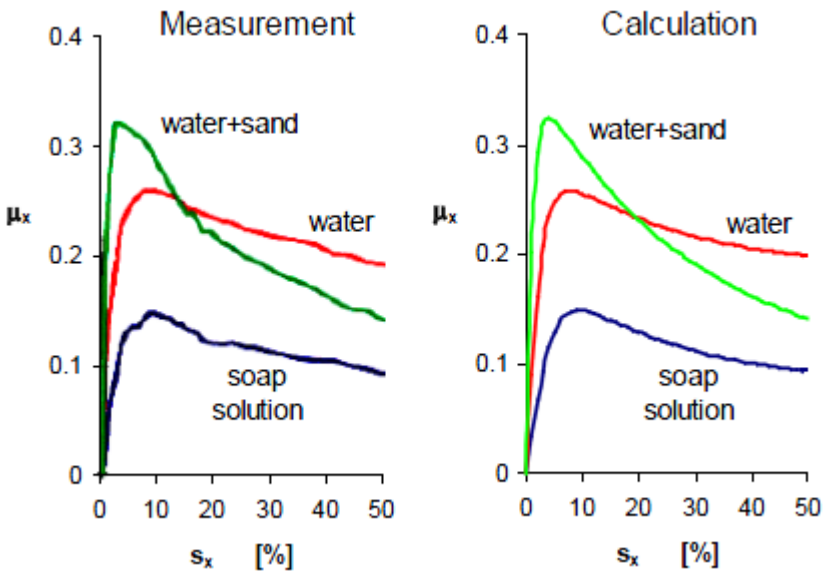

Figure 27: Modelling of various adhesion conditions using the friction coefficient as function of slip velocity between wheel and rail (measurement: adhesion tests with the SBB 460 locomotive, V = 20 km/h) [51]

The experimental data by Jin et al. [70] mentioned earlier was also compared with a numerical analysis that involved modification of Kalker's FASTSIM program to utilise variable friction coefficients. A modified version of Bochet's [75] experimental formula, as shown in Equation 24 [70], was developed to handle water and oil contaminated conditions more effectively.

$$f = \frac{f_s(v)}{1+\alpha v_r}$$

Equation 24: Improved Bochet formula for water and oil contaminated conditions [70]

Where: f = Kinetic friction coefficient

f_s = Static friction coefficient

v = Wheelset rolling speed (m/s)

v_r = Slip (mm/s)

α = Velocity-dependent parameter

Unfortunately, the formulae provided in the report [70] to calculate f_s and α are only applicable for a water-contaminated interface with 44kN of axle load, and it is not clear how they modified these from the general formulae. Both these values were dependent on vehicle velocity. Unlike Polach's [51] friction model, this approach [70] only looks to be capable of modelling wheel-rail interfaces with fluid contamination.

Jin et al. [70] claim that their model produced “reasonable” results in comparison to experimental data, the two often differing slightly as shown in Figure 28. The friction coefficient (μ) versus creepage (ξ) plot in this case is for 135kN of axle load and a water-contaminated interface, although similar deviations between numerical and experimental data are noted for lower axle loads. Dashed lines 1, 2, 3, 4, and 5 are numerical results for velocities of 140, 180, 220, 260 and 300 km/h respectively, whereas the symbolled curves ①, ②, ③ and ④ correspond to 140, 180, 220 and 260 km/h.

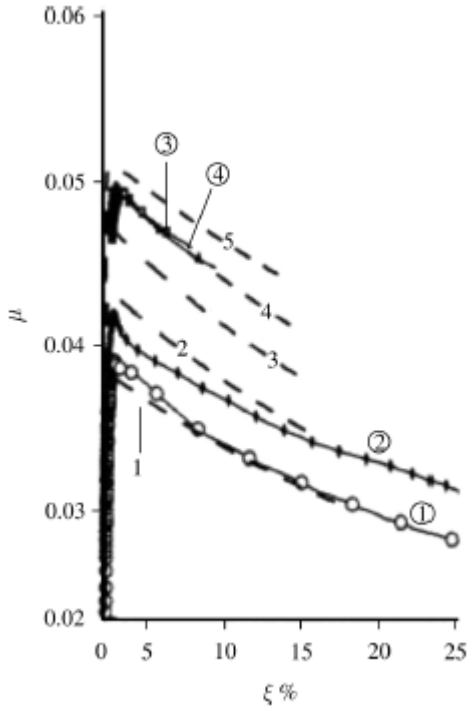

Figure 28: Adhesion-slip curve with water contamination and 135kN axle load [70]

Other variable friction models focus on wheel/rail surface roughness, in particular the microscopic asperity contacts that occur during dry and lubricated contact [76]. In the railway case, full hydrodynamic lubrication, where a fluid layer fully separates the contacting surfaces, never occurs. As a result, wheel-rail contact is limited to boundary lubrication, where only asperities are lubricated, and mixed lubrication where interfacial fluid can be trapped within asperity gaps [66].

One attempt to model and incorporate asperity contacts in dry and water-lubricated wheel-rail contact was devised by Chen et al. [76], where a previous model [77] is extended to take

lubricant shear forces into account. The effects of rolling velocity, axle load, slip, water temperature and surface roughness are also considered [76]. Asperity peaks are assumed to be parabolic and have the same curvature radius at their tips with their heights following a Gaussian distribution, allowing the mean asperity contact pressure to be calculated using a compliance relationship by Greenwood & Tripp [78] which is in turn based on a model by Greenwood and Williamson [79]. The adhesion coefficient is calculated using the dimensionless loads carried by the surface asperities and water film (if present) as shown below in Equation 25 [76].

$$\mu = \frac{\mu_h W_h + \mu_c W_c}{W}, \qquad W = W_h + W_c$$

Equation 25: Adhesion coefficient considering asperity contacts [76]

Where: μ = Adhesion coefficient

μ_h = Asperity contact adhesion coefficient

μ_c = Water film shear adhesion coefficient

W = Dimensionless total load per unit length

W_h = W carried by asperity contacts

W_c = W carried by water film

Although formulation of the W and μ coefficients will not be covered here, it is worth mentioning that the value of μ_c cannot be determined, at least mathematically. Chen et al. [76] assumed this value from Carter theory, meaning that slip saturation effects are not accounted for. In some cases, μ_c can also be assumed using fluidodynamic models and from Stribeck curves created from experimental data. As this model is mainly intended to qualitatively rather than quantitatively show how adhesion/friction coefficients change under varying contact conditions, a simplified line contact between wheels and rail is also assumed. Even though the numerical results seem to correspond reasonably well to experimental data, the model by Chen et al. [76] is suited more toward modelling adhesion characteristics at high speeds and low slip levels as opposed to the low speed and high slip situations this project is concerned with.

A more detailed and considerably more complex model has recently been devised by Tomberger et al. [66] that considers the volume occupied by metallic asperities on wheel and

rail surfaces. In this model, friction is described in terms of the maximum tangential shear stress over the real area of metallic contact, which is calculated from wheel/rail asperity contact and deformation. It is also capable of modelling both boundary and mixed lubrication in a contact zone, achieving this with a dependence on surface roughness instead of the relative wheel-rail velocity. To explain things simply, the model starts off by using Hertz theory, if appropriate, or Finite Element Modelling to model a nominal contact area and normal load. The nominal contact area is then divided into a grid of squares with equal area to form the computational domain. This and other input data is then processed by the wheel-rail contact model which contains four interdependent sub-models, or modules, which are explained briefly below [66]. Note that "local" values apply to each cell, whereas "global" values apply to the whole contact area:

- Micro-contact: Models microscopic surface asperities based on a method devised by Greenwood & Williamson [79], which in turn was extended to deal with combined elastic, plastic and elasto-plastic asperity deformation by Zhao, Maietta & Chang [80]. The reason for modelling elasto-plastic behaviour is to prevent load discontinuities at the elastic-plastic boundary [66]. Asperity heights are assumed to follow a Gaussian distribution, whilst the tips are assumed to be spherical. Surface roughness is expressed with a linear parameter, where values of 0 to 1 denote smooth and rough surfaces respectively. Using the local material properties (from the contact temperature module), surface roughness, nominal normal contact pressure and fluid pressure distribution, this module calculates wheel/rail separation, the asperity volume in each cell, and the metallic contact area.
- Contact temperature: Uses local normal loads, slip velocities and friction coefficients to calculate frictional power, which in turn influences the local temperature distribution and material properties. Instead of calculating asperity flash temperatures, a mean temperature distribution is assumed, along with wheels and rails being treated as half-spaces.

- Interfacial fluid: Calculates fluid volume and pressure in each cell, along with cell height and volume, based on the metallic asperity volume in each cell. Since interfacial fluid is said by Tomberger et al. [66] to pass through the contact zone roughly within a microsecond, fluid temperature and therefore viscosity effects are ignored. It is also assumed to be motionless on the rail surface.
- Tangential force: A modified version of FASTSIM [32] to allow varying friction coefficients in the contact area is used to calculate local tangential stresses and slip velocities using local friction coefficients as input. Local friction coefficients are defined by the ratio of tangential to normal force in each cell, from which the global friction coefficient can be calculated. Cells whose tangential contact stress exceeds the tangential adhesion limit, which is proportional to the bulk material yield stress, are deemed to be in the slip region. Likewise, cells in which this limit is not exceeded define the adhesion area. Damping effects are not considered for metallic contacts.

As can be seen above, there are a lot of interdependencies in the model as a result of having to model surface roughness, temperature and fluid effects on the wheel-rail interface. This and the level of detail required means that this method [66] cannot be used in real-time simulation. Another drawback is the use of some parameters that have to be determined indirectly as they cannot be directly measured, whilst the linear surface roughness parameter (mentioned along with the micro-contact model) needs to be calibrated from wheel/rail surface measurements. In future, the authors [66] hope to make further improvements to the model, in particular the contact temperature modelling that relies on discrete tangential contact stiffnesses so that FASTSIM can be used. Although the resulting errors are minor when calculating global traction coefficients, more detail is required to accurately model temperature phenomena within the contact area. The effects of third-body layers are also not presently considered as the authors [66] do not know of a suitable numerical model.

In spite of these drawbacks, the model by Tomberger et al. [66] gives results that are, qualitatively at least, consistent with experimental data such as the effects of surface roughness, velocity and normal load on dry and lubricated surfaces. Figure 29 below [66] shows a traction

coefficient – creep plot generated by the program, where two ‘peaks’ are present in the curve for dry contact at 30 m/s velocity.

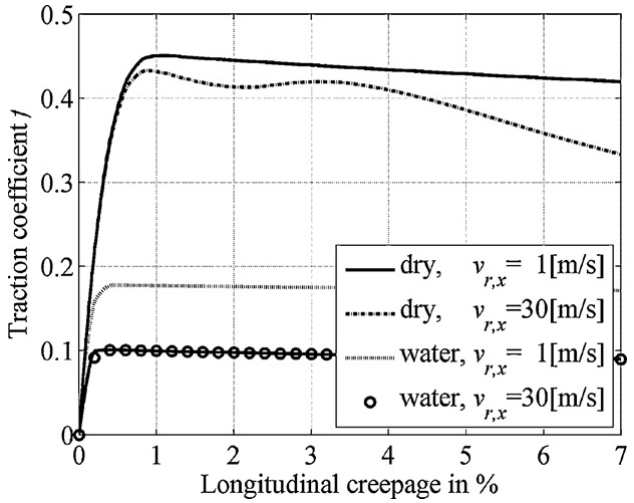

Figure 29: Computed traction-creepage curves for different rolling velocities under dry and water lubricated conditions [66]

This secondary peak is the result of an anomaly in the assumed variation of rail steel yield stress with temperature, as shown by the lower curve in Figure 30 [66].

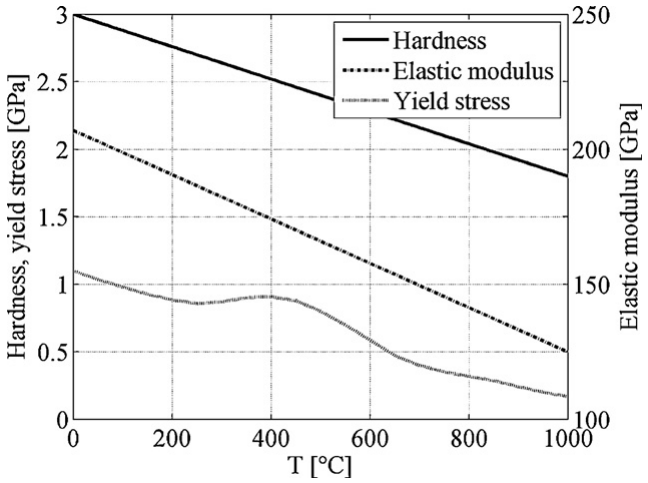

Figure 30: Assumed temperature variation of elastic modulus, hardness and yield stress [66]

The reason for the variation in rail steel yield stress between ~300-600°C is due to diffusion of dissolved carbon and nitrogen atoms, which has the effect of slowing down the mobility of any dislocations produced [66]. Such behaviour has been reported in experimental data [67] along with the other phenomena shown in Figure 29.

2.2.5. Locomotive design and modelling

Most diesel-electric locomotives have the same basic structure with the power generation equipment, driver cab(s), braking equipment and other ancillaries mounted on a chassis which in turn rests on two bogies that can rotate about a vertical axis, allowing the locomotive to negotiate changes in track curvature. A diesel engine is used to run a generator that provides electrical power to bogie-mounted traction motors which in turn are geared to powered wheelsets. Multiple locomotive types will be analysed in this project; variations in bogie structure, traction/dynamic brake characteristics and electrical aids such as traction control and delayed power application need to be considered when creating multi-body models for vehicle analysis.

In Australia, diesel-electric locomotives typically have a Co-Co wheel arrangement, although some Bo-Bo and A1A-A1A units are currently in use [81]. Early diesel-electric locomotives drove a generator to provide DC power for traction, which was replaced by an alternator in later DC-drive locomotives [82]. In the latter configuration, AC power from the alternator is converted to DC power for the traction motors using a rectifier, with traction motor/wheelset speeds regulated with either a DC 'chopper' or, in modern locomotives, a Gate Turn Off (GTO) thyristor circuit. The latest “high-adhesion” locomotives have AC traction motors in place of the traditional DC motors, where AC current from the alternator is fed to an inverter bank. Each inverter is able to provide three-phase AC current of varying voltage and frequency using Insulated Gate Bipolar Transistor (IGBT) technology in place of the GTO thyristors in early AC-drive locomotives [83]. In a ‘per-bogie’ drive configuration, separate inverters (usually two in total) supply power to all traction motors within each bogie, whilst ‘per wheelset’ setups go further by having separate inverters for each traction motor (usually six in total). Such setups allow for more precise traction control, compensation for varying wheel sizes in the case of per-wheelset control and the omission of commutator brushes in the traction motors, which has the effect of reducing maintenance costs and extending the useable life of wheelsets and traction motors [8, 84].

When modelling diesel-electric locomotives in Multi-Body Simulation (MBS) software, along with wagons for that matter, the chassis and body are usually considered as a lumped mass [19]. In light of this, most of the emphasis in creating multi-body models is directed toward the bogie structure, with traction, dynamic brake, pneumatic brake, traction control and delayed power application characteristics, amongst others, that can be modelled using additional scripts. Traction and dynamic brake performance can be determined from published tractive effort versus speed charts, whilst traction control can be adapted or reverse-engineered from existing algorithms.

Typical locomotive bogie components will be described with reference to Figure 31 [84] depicting a rigid-framed design for the UGL Rail Cv43ACi locomotive (based on their NR-class design).

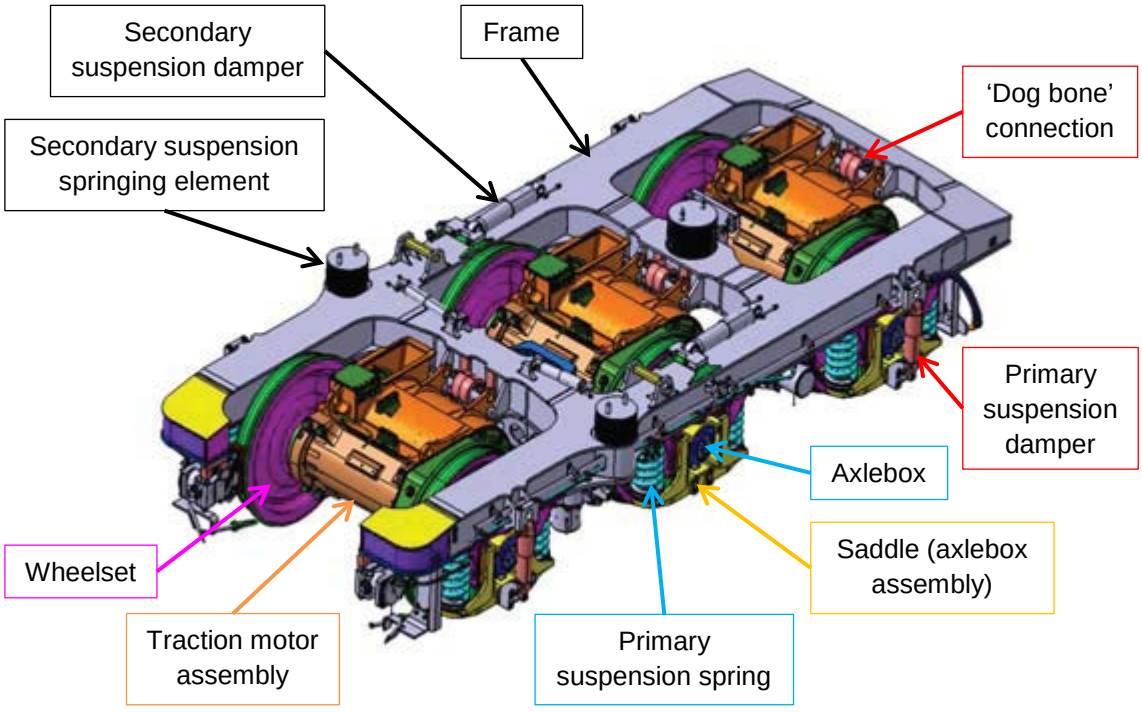

Figure 31: A rigid-framed bogie design (UGL Rail Cv43ACi locomotive) [84]

The frame rests on the wheelsets via the primary suspension, consisting of a saddle (or axlebox assembly) at the ends of each wheelset that secures the axleboxes and holds the primary springs in place. Except for the middle axle, dampers are also fitted, with traction motor assemblies being hinged to the frame with a "dog bone" connection. The secondary suspension consists of

three springing elements and two dampers (visible near the middle axle) on top of the bogie frame on which the locomotive body is attached. A centre pin and bowl (not pictured) are connected between the bogie frame and locomotive body to provide a point for the bogie to rotate around as the locomotive negotiates track curvature [85].

Multi-body locomotive models can be assembled from lumped masses and weightless elements such as springs and dampers. As previously mentioned, the body is a single lumped mass whilst the bogies consist of frame(s) and wheelsets, with nodes defined on each body for the attachment of any spring and/or damper units. Restraints can also be applied on the translational and rotational degrees of freedom of bodies and connection units. Traction components can be modelled in two ways, the first being that the mass of the traction motor and gearing assembly is incorporated into the bogie frame and wheelset assemblies as in this project. In this case, traction forces are modelled by applying torque directly to the powered wheelsets. Alternatively, the traction motor assemblies can be modelled as separate bodies connected to the wheelsets via a virtual gearing mechanism and connected to the frame via a spring/damper connection, allowing torque to be applied at the rotor shaft and geared down to the wheelsets. There is scope for traction torque, in either case, to be modelled from input power whilst also considering decreases in output power as traction motors heat up during operation. One example of a multi-body model, for a Japanese EH200 DC electric locomotive, is shown in Figure 32 [86] where, in this case, the traction motors have been modelled as separate bodies.

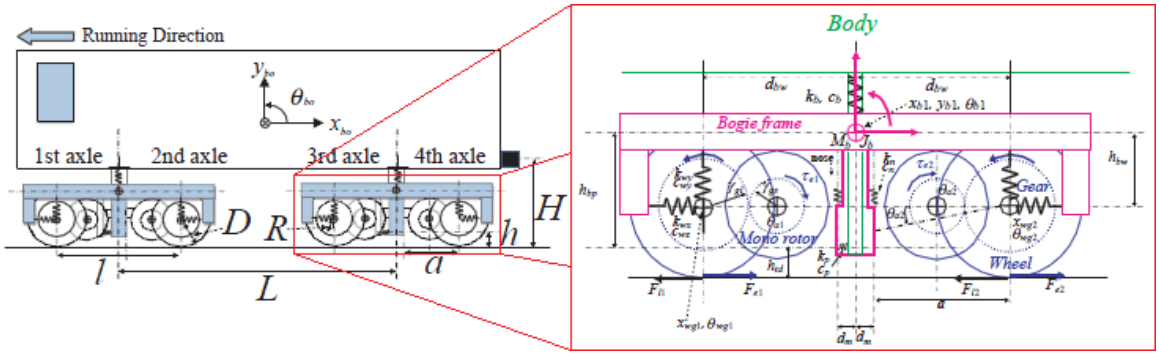

Figure 32: Multi-body model of an EH200 DC electric locomotive [86]

A more detailed depiction of individual traction motor and wheelset units by Pfleger [87] that incorporates flexible wheelset and traction motor shafts is shown in Figure 33.

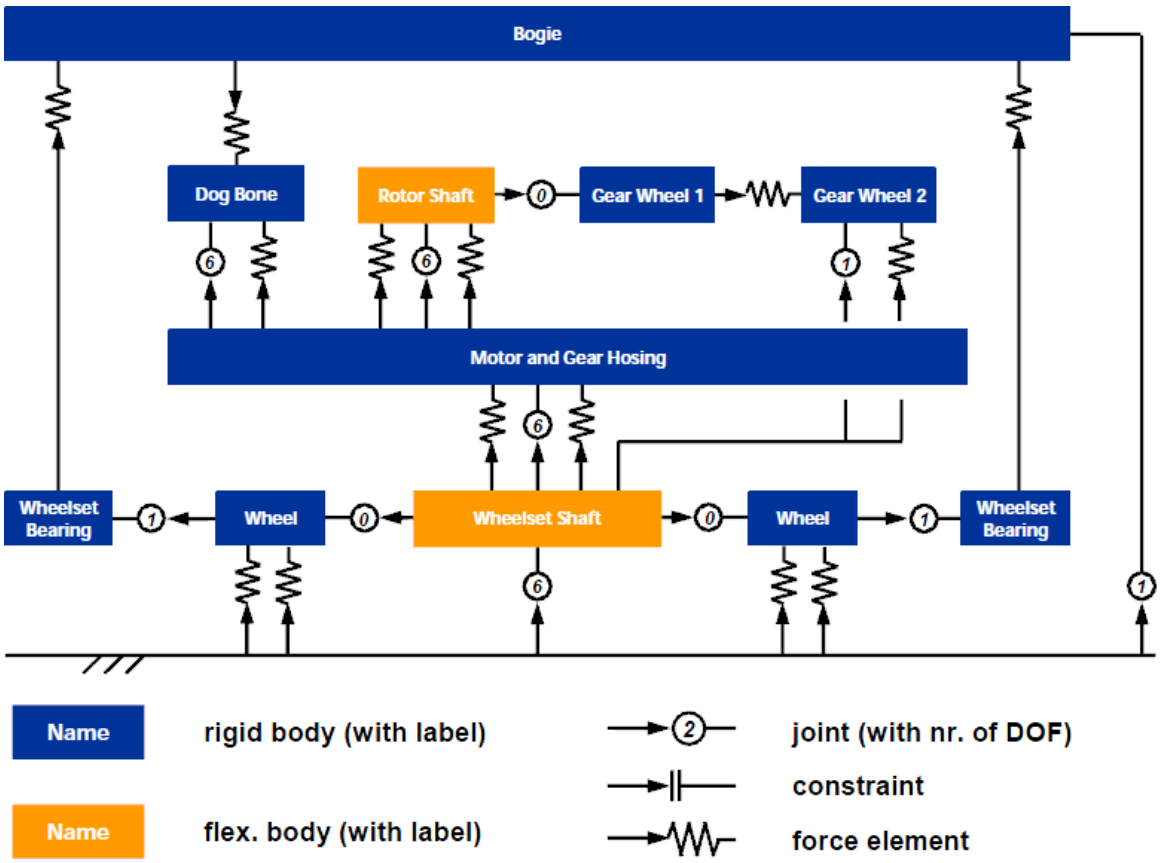

Figure 33: Multi-body model layout for individual traction motor and wheelset units [87]

2.2.5.1. Currently used bogie designs

The rigid bogie type has clearances in the primary suspension to give the wheelsets some side play in an effort to reduce cornering forces. To reduce wheelset angles of attack in curves, several bogie designs have been developed in an effort to allow wheelsets to conform to track curvature without deleteriously affecting stability [8, 88]. Typical bogie designs currently used on Australian locomotives are the rigid frame, semi-steering (yaw relaxation) and self-steering types [1] of which diagrams are shown in Figure 34 [9]. In this thesis the term ‘semi-steering bogie’ will be used instead of ‘yaw relaxation bogie’, following the terminology used by manufacturers [8, 89].

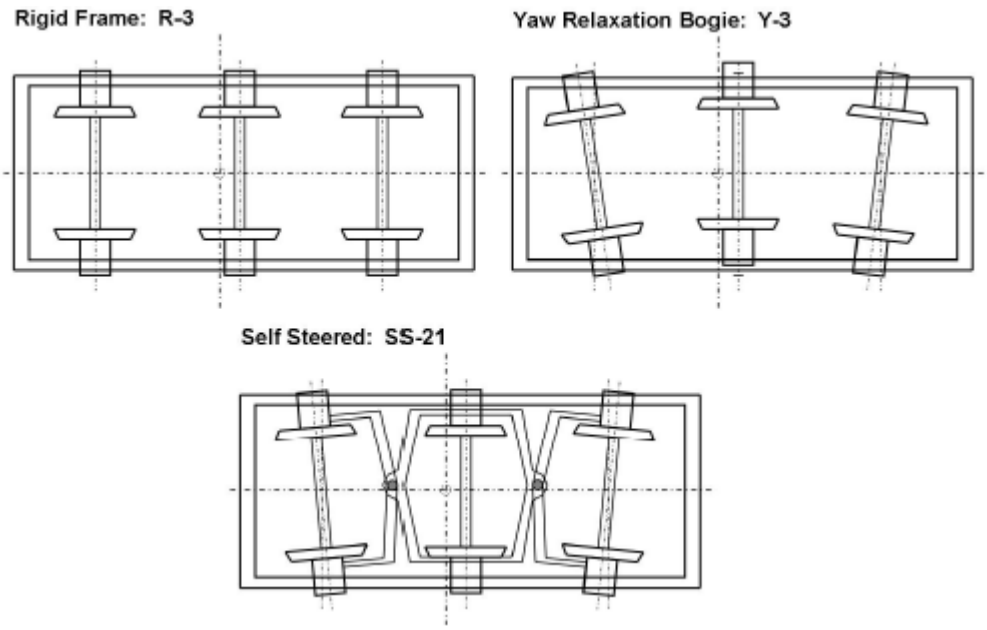

Figure 34: Typical bogie designs [9]

A plan view of Electro-Motive Diesel's (EMD) three-axle "radial" self-steering bogie design is shown in Figure 35 [90]. The steering beams visible in the centre of the drawing allows the end axles to yaw without being displaced longitudinally, with the effect of improving bogie curving and stability, whilst the centre axle is given 16mm of side play. Secondary suspension consists of rubber compression springs that are directly attached to the locomotive body [91]. Other locomotive builders have developed their own self-steering bogies, such as General Electric (GE) Transportation's [92] "HiAd" design.

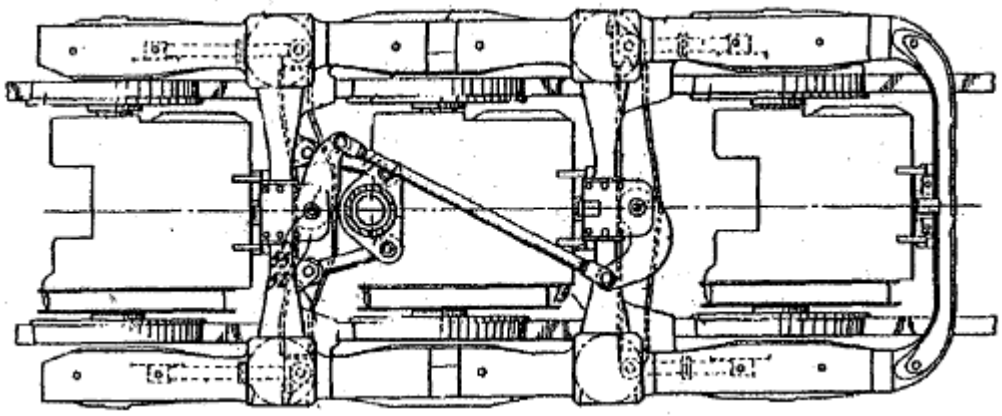

Figure 35: EMD three axle radial bogie [90]

The semi-steering bogie was developed by Downer EDi Rail, of whom EMD is a partner company, for the SCT-class locomotive in a bid to reduce maintenance and overhaul costs over the EMD radial self-steering bogies previously fitted to the Westrail Q class and QR 4000 class locomotives. Unlike the standard EMD design, the end-axles on the Australian versions are supported by swing axles with a rubber bush in the pivot allowing up to 10 mm of longitudinal displacement. Downer EDi's approach was to eliminate the steering beams, resulting in a bogie that was about a tonne lighter than the previous design. This also helped to offset the extra weight of the AC traction motors used in the SCT class. As a result, the end axles could move independently, but tests using the VAMPIRE software package showed that the design would be stable at speeds up to 130 km/h. An image of an SCT class semi-steering bogie can be seen in Figure 36 [8].

Figure 36: Semi-steering bogie as fitted to the SCT class locomotive [8]

2.2.6. Traction control

Early diesel electric locomotives relied purely on driver control to set the amount of power going into the traction motors, but as locomotive power and complexity increased, traction control algorithms were devised to maintain optimum power outputs for a variety of conditions. Creep forces in contact patches increase with slip up to a maximum value and then decrease as slip increases further. This creep force peak occurs at a value called the optimum slip level and it is the traction control system's job to detect and maintain optimum slip so that the maximum traction force can be exerted. Looking at the simplified diagram in Figure 37 [93], slip levels up to the adhesion optimum are within the "stable" region, whereas slip levels beyond this point lie in the "unstable" region where adhesion levels decrease with increasing slip. Notice how the

optimum slip level changes when track conditions are altered, being dependent on the adhesion-creep curve. This can also be affected by vehicle velocity [93].

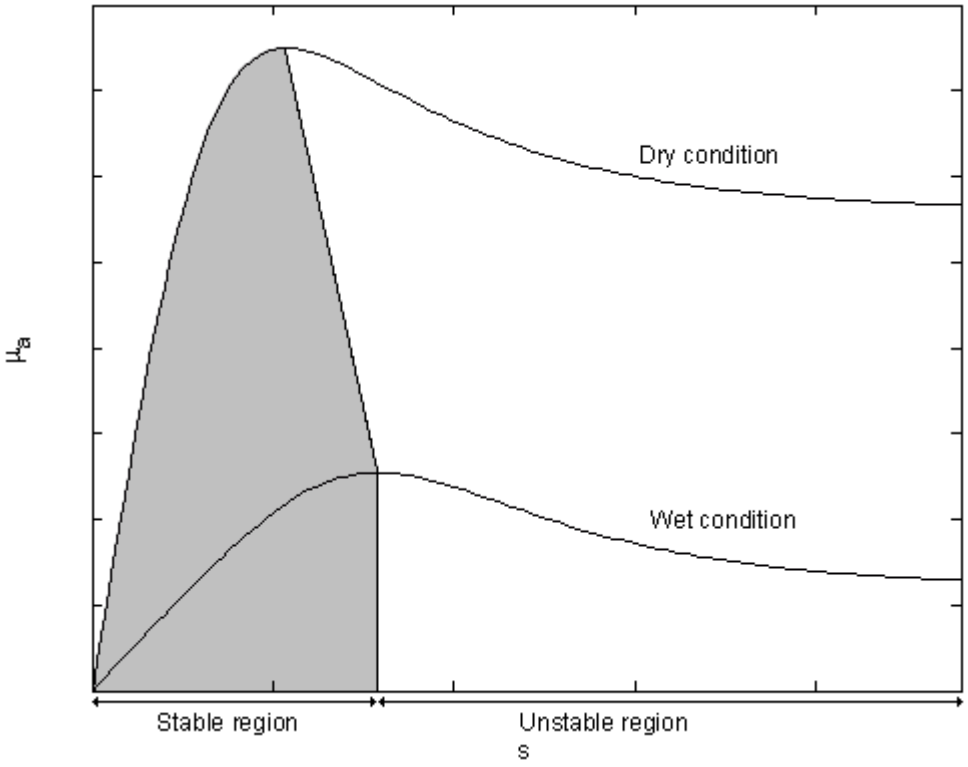

Figure 37: Stable and unstable adhesion regions for dry and wet conditions (simplified diagram) [93]

Several control strategies are available that detect the stable slip region and maintain the optimum slip levels within it. Some examples include [93]:

- Neural networks
- Diagnostic algorithms
- Detection of motor current differences without speed sensors
- Model based controllers, such as adhesion observers
- Hybrid method, based on the pattern control (a type of diagnostic algorithm) and speed difference (explained later) methods
- Steepest gradient method
- Fuzzy logic

Regardless of the control strategy adopted, the task of detecting optimum slip levels is difficult to carry out for two main reasons [93]:

- The wheel-rail friction coefficient varies with track conditions and cannot be measured directly, whilst the optimum slip level changes as a result
- Most traction control algorithms require an accurate measurement of vehicle speed.

When Frylmark & Johnsson [93] wrote their thesis, vehicle speed was usually recorded from axle-mounted units that detected a set number of electronic pulses per revolution. Recorded speeds in this case can be affected by wheel-slip caused by sudden applications of traction or braking, wheel unloading and variations in track contamination. One method to compensate for wheel slip effects on the recorded speed from axle-mounted recorders is the speed difference method proposed by Yasuoka et al. [93, 94], where speed sensors are attached to each axle and the locomotive speed is assumed to be the minimum recorded axle speed. Slip values for each axle are determined from their slip velocity, which is simply obtained by subtracting their tangential velocity from the minimum axle speed. Accuracy can be improved by taking measurements from an unpowered axle if one is present. Although the speed difference method was used widely, it had a few problems such as failing to detect long sections of track with low friction and high levels of wheel-slip amongst all axles at once [93]. More modern traction control systems such as EMD's Super Series control [95] use a Doppler radar gun located at the front of locomotives to measure track speed, which is compared to motor speeds so creep conditions can be modified.

Other kinds of traction control systems use differing forms of input, where the utilisation of multiple and varied inputs can improve system outputs to the drive system such as current and, in the case of some AC drive systems, frequency. One example is the QES-III system's [96] wheel slip/creep control module that consists of a speed-based control system that records axle speeds and a current-based system that monitors the generator and traction motors. If wheel-slip occurs, power to the traction motors is quickly cut then re-applied with a current just below the level that caused wheel-slip in the first case. Q-Tron [96] claim that this system can improve adhesion levels for poor rail conditions by 34%. Another system of note is ABB's [97] Direct

Torque Control that uses motor torque and magnetising flux as inputs. No modulators or speed sensors are required for this system, where traction motor torque response is typically ten times faster than other AC/DC drives and speed control is eight times more accurate. Spiryagin, Lee & Yoo [98] have developed a method that relies on recording the noise spectrum from the wheel-rail contact area using directional microphones in an effort to determine friction coefficients. Although simulations have been conducted, more research is required into the effects of track conditions on generated noise. A constant wheel radius is also assumed, so the system's performance may deteriorate as locomotive wheels eventually wear down. Using motor torque readings as input, Yamashita & Soeda [86] devised a system that accounts for axle weight transfer as a result of locomotive traction forces. When tested on a Bo-Bo EH200 type DC locomotive with water sprays on the driven axles, the system improved adhesion levels by ~10%.

3. Locomotive modelling

To allow detailed simulation of wheel-rail forces for locomotives under traction, mechatronic models of the considered locomotive types were created using the GENSYS Multi-Body Simulation (MBS) software. The mechanical component of these models was a multi-body model that considered the locomotive, rail and track. Simplified electronic controls realised within the GENSYS model codes were used to simulate locomotive-specific Traction Control (TC) systems. Approximate lateral coupler forces based on data obtained from Longitudinal Train Simulation (LTS) analyses could also be used as input, allowing the application of in-train forces to individual locomotive multi-body models for more accurate simulations.

In order to provide a comparison between high-adhesion AC and conventional DC drive systems, along with differing bogie structures, three locomotive types were modelled for this project:

- Type AC1 – AC drive, per-wheelset traction control, rigid bogies
- Type AC2 – AC drive, per-bogie traction control, 'semi-steering' bogies
- Type DC – DC drive, rigid bogies

These configurations are typical of modern Australian freight locomotives that run on its standard-gauge (1435 mm) network. Despite differing component dimensions, TC systems and bogie structures, the three locomotive models are largely similar. The subsections below first cover features common to all three locomotive models before describing individual model features in more detail.

3.1. Features/assumptions common to all locomotive models

All three of the locomotive types modelled have a Co-Co wheel arrangement, meaning that the car-body is connected to two three-axle bogies with each axle being independently driven by its own traction motor. The locomotive multi-body models were constructed from nine rigid bodies; one car-body, two bogie frames and six wheelsets. The masses (and moments of inertia)

of the traction motor assemblies were therefore incorporated into neighbouring wheelset and bogie frame bodies, as in earlier analyses by Simson [99-104] and Spiryagin et al. [105-110]. One-third of each traction motor assembly's mass (and moment of inertia) was added to their corresponding wheelsets (one traction motor per wheelset), with the remaining two-thirds added to the bogie frames (three traction motors per bogie). All bodies in the locomotive models were given six Degrees of Freedom (DOF).

Because axle boxes were not modelled, which would require additional bodies (two for each wheelset), further simplifications had to be made to the locomotive models:

- Any damping elements present in the primary suspension had to be placed along each wheelset's axis of rotation [111]
- Single equivalent springs were directly attached to the (left/right) ends of wheelsets for connection to the bogie frames [112]. Real-world locomotives typically have two springs at the end of each wheelset instead, which are connected between the bogie frames and axle boxes [85]. This approach to modelling primary suspension elements has been used previously by DeLorenzo [85] and Simson [99].
- Wheelset pitch angles had to be constrained to zero, otherwise the contact points on each wheel would move around its circumference as the pitch angle changes. This can result in contact patches on a wheel moving away from those on a rail, which is undesirable. For example, a pitch angle of ±π radians would result in the contact point(s) moving to the top of a wheel. Wheelset pitch velocity was kept free, however, to account for changes in the rolling radius of wheels such as when cornering. The initial value of wheelset pitch velocity is given in Equation 26 [111].

$$v_{k,axle} = \frac{V_0}{r_0}$$

Equation 26: Initial wheelset pitch velocity [111]

Where: $v_{k,axle}$ = Initial wheelset pitch velocity
V_0 = Initial locomotive velocity (m/s)
r_0 = (Initial) Wheel radius (m)

Each locomotive model had one Euler ‘esys’ co-ordinate system that followed track geometry defined in the GENSYS model code. The track geometry, in turn, was defined using the ‘fsys’ global co-ordinate system. Each rigid body within the model had a linear ‘lsys’ co-ordinate system related to the esys, allowing the motions of all bodies to be recorded. This also allowed the dynamic responses of the locomotive models to be assessed in more detail [106] as in modelling approaches used earlier by Simson [99-104] and Spiryagin et al. [105-110]. The locations of co-ordinate systems within a locomotive model are shown in Figure 38.

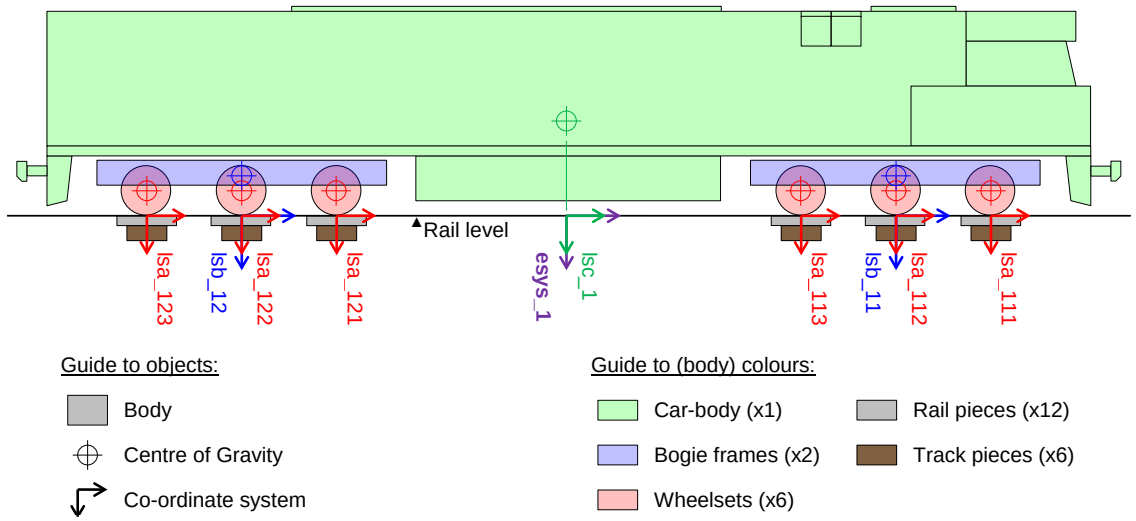

Figure 38: Co-ordinate system locations

Rails were modelled as separate weightless elements under each wheel, which could be connected with up to three wheel-rail contact points. Each contact point was assumed to have linear stiffness and damping [113] acting normal to the contacting wheel-rail surfaces. The two rails under each wheelset were connected to a body representing the track (sleepers) with lateral and vertical stiffness and damping units. The track bodies had mass and were constrained to move in the lateral and vertical directions and rotate in yaw, giving 3 DOF. These were in turn connected to the ground with a series stiffness-damping unit in the lateral direction and two pairs of stiffness and series stiffness-damping units, for the right and left sides of the track respectively, in the vertical direction [107]. A diagram of the connections between wheelset, rail and track bodies with the ground is given in Figure 39, with basic track model parameters given in Table 4.

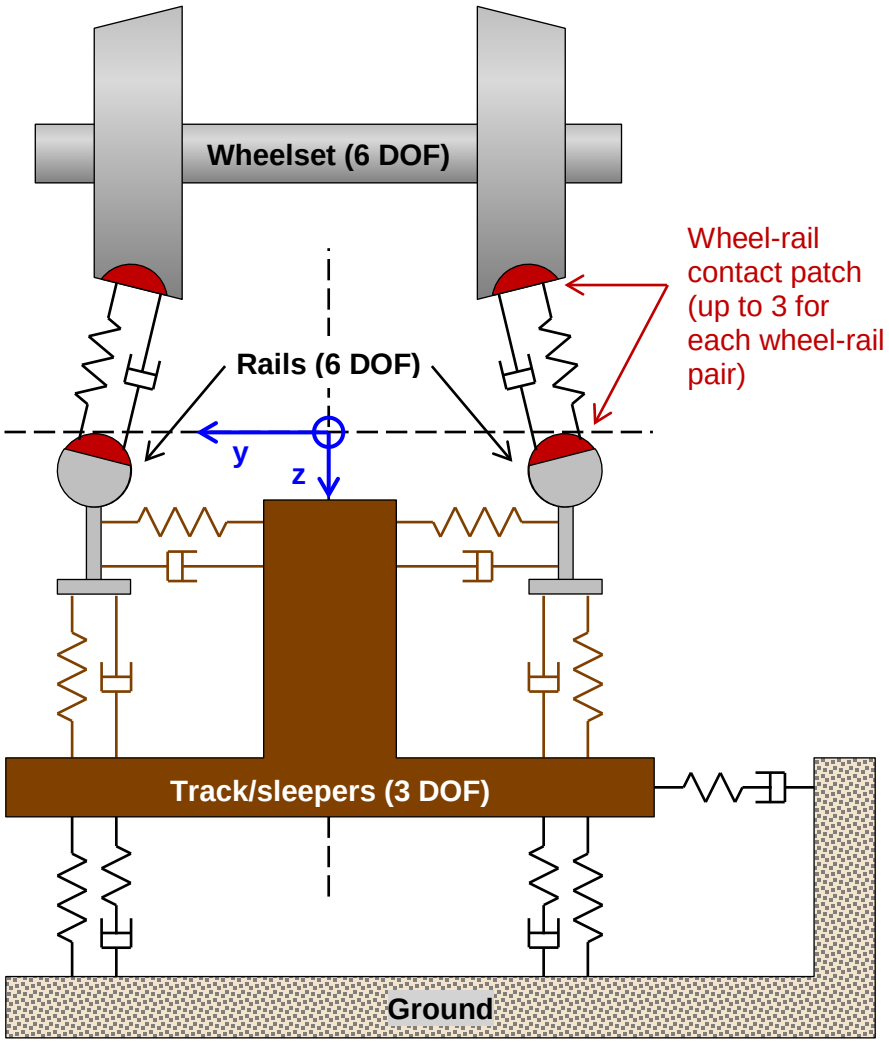

Figure 39: (Per) Wheelset – rail – track – ground connections

Table 4: Basic track model parameters

Wheel-rail connections (per contact patch)		
Normal contact stiffness	2.4×10^9	N/m
Normal contact damping	1.0×10^6	N.s/m
Rail-track connections		
Lateral stiffness	17×10^6	N/m
Lateral damping	10×10^3	N.s/m
Vertical stiffness	230×10^6	N/m
Vertical damping	50×10^3	N.s/m
Mass of track piece (under wheelset)	17×10^3	kg
Track-ground connections		
Lateral series stiffness	410×10^6	N/m
Lateral series damping	907×10^3	N.s/m
Vertical stiffness	220×10^6	N/m
Vertical shear stiffness	40×10^6	N/m
Vertical series stiffness	563×10^6	N/m
Vertical series damping	985×10^3	N.s/m
Data provided by researchers involved in CRC Project R3.119 – Locomotive Adhesion [1, 114]		

The GENSYS locomotive model code [115] is able to read differing wheel/rail profiles and track irregularities from external files. Track geometry, nominal track gauge and locomotive speed can also be defined in this manner but, in most cases (with simple designed track geometries, constant nominal track gauge and constant locomotive speed), these are written in the model code itself.

When performing simple simulations for which locomotive traction modelling was not required, such as model debugging and acceptance tests, it was sufficient to assume a constant coefficient of friction (μ) in the wheel-rail contact area. In these cases, creep forces in wheel-rail contact areas were interpolated from lookup tables generated by FASTSIM [113], with $\mu = 0.4$ for dry track. When considering locomotive traction forces, Polach's [51, 69] creep force formulations (see Section 2.2.4.2) were used instead, where friction coefficients within wheel-rail contact areas are dependent on slip velocity [110]. Table 5 shows the Polach contact model parameters used in this study for the AC and DC-drive locomotive models respectively for both dry and wet track. It was assumed that parameters for an EMD SD45X locomotive [69, 116] were suitable for the DC locomotive model.

Table 5: Polach contact model parameters for AC and DC-drive locomotive models

Locomotive drive type	Track surface condition	μ_0	A	B	k_A	k_S
AC*	Dry	0.47	0.44	0.70	0.60	0.15
	Wet	0.30	0.38	0.10	0.29	0.09
DC [69, 116]	Dry	0.40	0.44	0.60	0.68	0.14
	Wet	0.30	0.38	0.18	0.29	0.07
** Data provided by industry partners involved in CRC Project R3.119 – Locomotive Adhesion [1, 114]*						

The locomotive models allow for three wheel-rail contact patches to be modelled for each wheel/rail pair, corresponding to the wheel tread – rail head (contact patch 1), wheel/rail gauge corner (contact patch 2) and flanging (contact patch 3) contact zones respectively. This allows for different Polach contact model parameters to be used in each zone. For this study it was assumed that only the maximum friction coefficient (μ_0) changed between zones; other contact

model parameters (A, B, k_A and k_S) were left constant. Table 6 shows the maximum friction coefficients for each contact zone, using data from Olofsson [65] as guidance.

Table 6: Friction coefficients for different wheel/rail contact zones

Locomotive drive type	Track surface condition	Wheel tread – rail head (μ_0)	Wheel/rail gauge corner (μ_G) [65]	Flanging contact (μ_F) [65]
AC	Dry	0.47*	0.34	0.24
	Wet	0.30*	0.20	0.15
DC	Dry	0.40 [69, 116]	0.34	0.24
	Wet	0.30 [69, 116]	0.20	0.15
** Data provided by industry partners involved in CRC Project R3.119 – Locomotive Adhesion [1, 114]*				

Locomotive model TC systems were implemented as subroutines in their GENSYS codes, following the 'simplified approach' detailed in [117]. Although TC systems differed between locomotive models, namely with respect to the number of AC traction inverters or use of a DC rectifier and type of slip observers used, they were all based on the same feedback control strategy shown in Figure 40 [110].

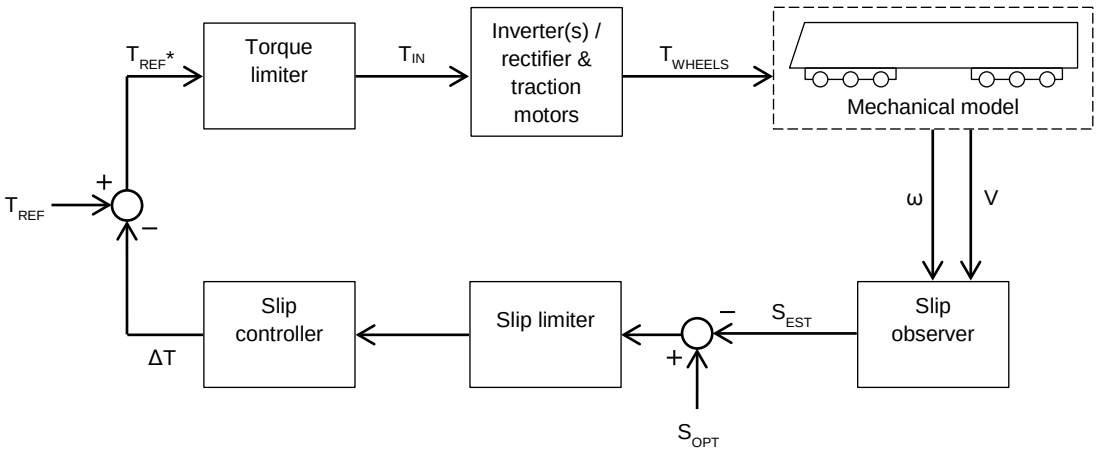

Figure 40: General traction control system [110]

Where: T_{REF} = Reference torque

T_{REF}*= T_{REF} generated by control system

T_{IN} = Input motor torque

T_{WHEELS} = Traction torque applied to wheelsets

ΔT = Torque reduction

ω = Wheelset angular velocity (pitch)

V = Locomotive velocity (longitudinal)

s_{EST} = Estimated longitudinal creep (slip level)

s_{OPT} = Optimum longitudinal creep

Estimated longitudinal creep (s_{EST}) was calculated using Equation 27 [105]. Although this is the expression for actual longitudinal creepage, it is considered to be an estimated value in this case because of some assumptions made in the locomotive models. Constraining wheelset pitch angles to zero simplifies the expressions for ω [23], whereas the assumption of rigid wheel and rail bodies affects the expressions of creep (longitudinal, lateral and spin) components [118].

$$s_{EST} = \frac{\omega \cdot r - V}{\omega \cdot r}$$

Equation 27: Estimated longitudinal creep [105]

Where: r = Wheel radius

With reference to Figure 41 [105], the optimum longitudinal creep has to be slightly below the slip level (s_{MAX}) that corresponds to the maximum longitudinal creep force ($F_{X,\,MAX}$) available in a creep-creep force curve. This is done to keep slip levels within the stable zone.

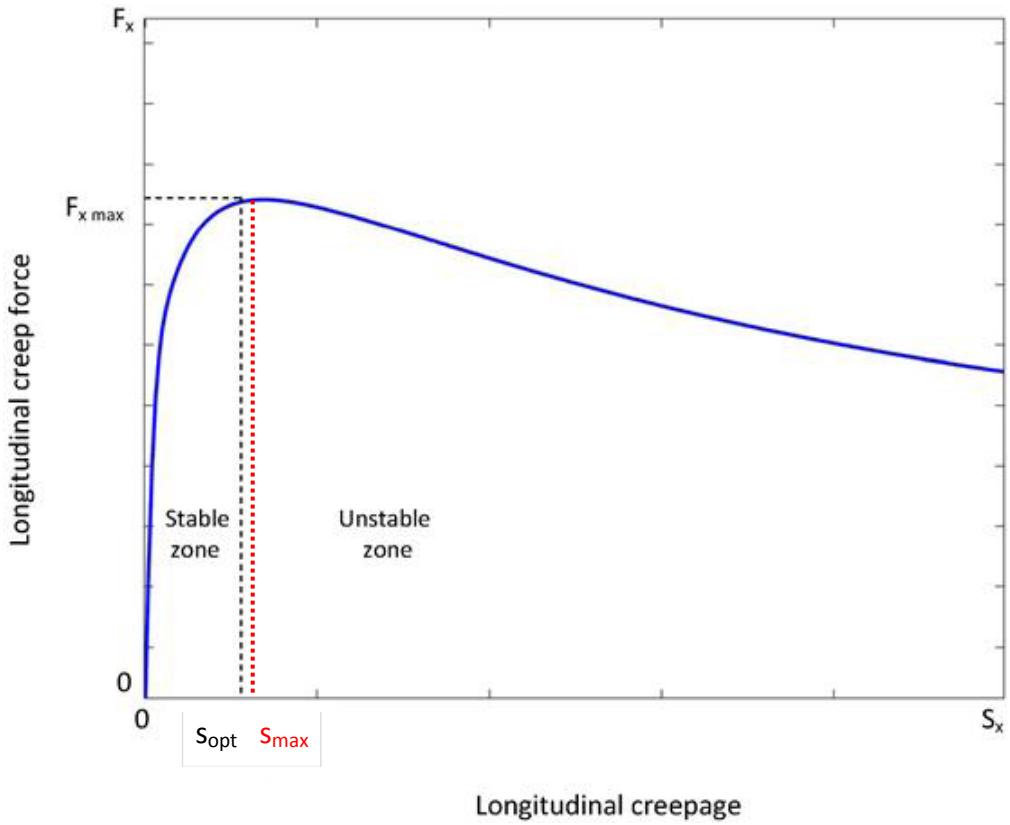

Figure 41: Longitudinal creep force versus longitudinal creep [105]

Torque limiters were contained in the TC systems so that the reference torque was not exceeded in traction modes. To avoid high levels of longitudinal creep and associated rail damage, slip limiters were incorporated with the limit value set to 20% as described in [119]. The slip controller was a Proportional-Integral (PI) type that used slip error as an input signal [110]. Motor/axle torques was processed using a second-order 15 Hz low-pass filter before input into the multi-body locomotive model. Traction-induced bogie and car-body pitching was also accounted for in the locomotive models, using the method described in [99].

This thesis is only concerned with modelling locomotive wheel-rail forces under maximum continuous tractive effort at constant speed, which is expected to represent the most extreme conditions in normal service. Instead of defining tractive effort curves for use in TC systems, it sufficed to include only the maximum continuous tractive effort ratings and the speed at which they occur. Maximum continuous tractive effort ratings for the modelled locomotive types are summarised in Table 7.

Table 7: Maximum continuous tractive effort ratings

Locomotive model	Maximum continuous tractive effort
Type AC1	453 kN @ 21 km/h*
Type AC2	500 kN @ 20 km/h [89]
Type DC	388 kN @ 23 km/h [120, 121]
** Data provided by industry partners involved in CRC Project R3.119 – Locomotive Adhesion [1, 114]*	

Values for optimum longitudinal creep were estimated from the creep-creep force-curves generated by each locomotive model at maximum continuous tractive effort for dry and wet track surfaces as part of acceptance testing in Section 4.3.3. These are summarised in Table 8, whilst the variable friction and estimated adhesion curves against slip for each locomotive model are shown in Figure 55 – Figure 57.

Table 8: Optimum longitudinal creep (s_{OPT})

Locomotive model	s_{OPT} (dry track)	s_{OPT} (wet track)
Type AC1	0.07	0.17
Type AC2	0.06	0.15
Type DC	0.07	0.14

Since coupler forces were provided in longitudinal and lateral components from LTS, coupler angling algorithms were not required, allowing forces to be applied at fixed points on the locomotive model body. These were located at each end of the locomotive model, laterally centred along the car-body, at a nominal coupler height above the track of 885 mm and at a distance of 11 m from the longitudinal centre-point. The latter corresponds to a distance of 22m between coupling centre lines, which is the same for all locomotive models tested. Rather than use coupler force components directly from LTS, which would require specific track layouts and are time-dependent, approximate distance-dependent coupler force components were used. These are easier to implement in the GENSYS model code and allow track layouts in MBS tests to differ from those used in the original MBS analyses. This approach has already been adopted in a previous analysis [109], where varying lateral coupler forces were applied to locomotives travelling within curves and transitions. Longitudinal coupler forces were assumed to be

constant in either case because a) their variation within curves was minor, and b) such variations would be nullified due the longitudinal speed control (consisting of a simple linear spring-damper system as described in [111, 115] for a Bo-Bo locomotive) and traction-induced bogie pitch modelling [99] adopted.

3.2. Locomotive model-specific features

Differences between the three locomotive models were mainly limited to:

- Basic dimensions (component lengths and masses)
- Primary and secondary suspension configurations (for rigid and semi-steering bogies)
- TC system configurations

The following subsections detail how the three locomotive models vary in these regards. A table of basic parameters for all three models is then given in a separate subsection.

3.2.1. Type AC1

The Type AC1 model represents one example of an Australian standard-gauge AC-drive freight locomotive. Each axle's traction motor was controlled by its own inverter (six in total), allowing wheelset slip levels to be controlled individually. Bogies were the conventional 'rigid' type with the wheelset and traction motor assemblies connected to a rigid frame, with the axles given some side-play so they could shift laterally in low radii curves. Each bogie had a central pin to allow bogie rotation in curves and transfer of longitudinal and lateral forces between the bogies and car-body. Total locomotive mass is 134 t, which is the maximum allowable for use on the Defined Interstate Rail Network (DIRN) [8], although it is possible for real-world locomotives to exceed this limit on suitable trackage by allowing more fuel to be provisioned [8, 84]. Basic dimensions of the Type AC1 model are given in Figure 42.

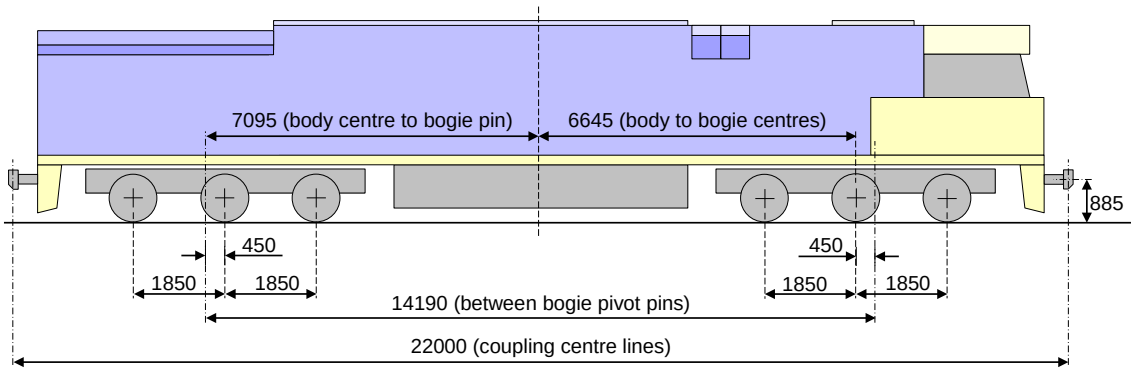

Figure 42: Type AC1 basic dimensions

Note that the bogie pivot pins were located 450 mm outwards from the mid-axles. An overall view of Type AC1's multi-body model, including the rail and track pieces, is shown in Figure 43.

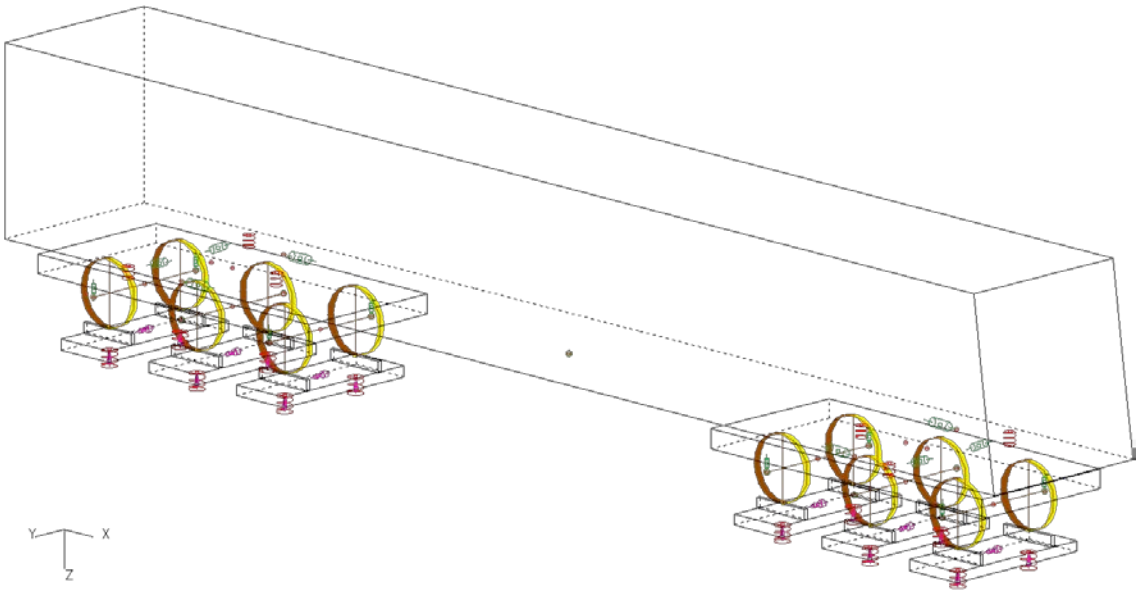

Figure 43: Type AC1 multi-body model

Figure 44 shows a close-up view of the lead bogie, with annotations for primary (below) and secondary (above) suspension elements.

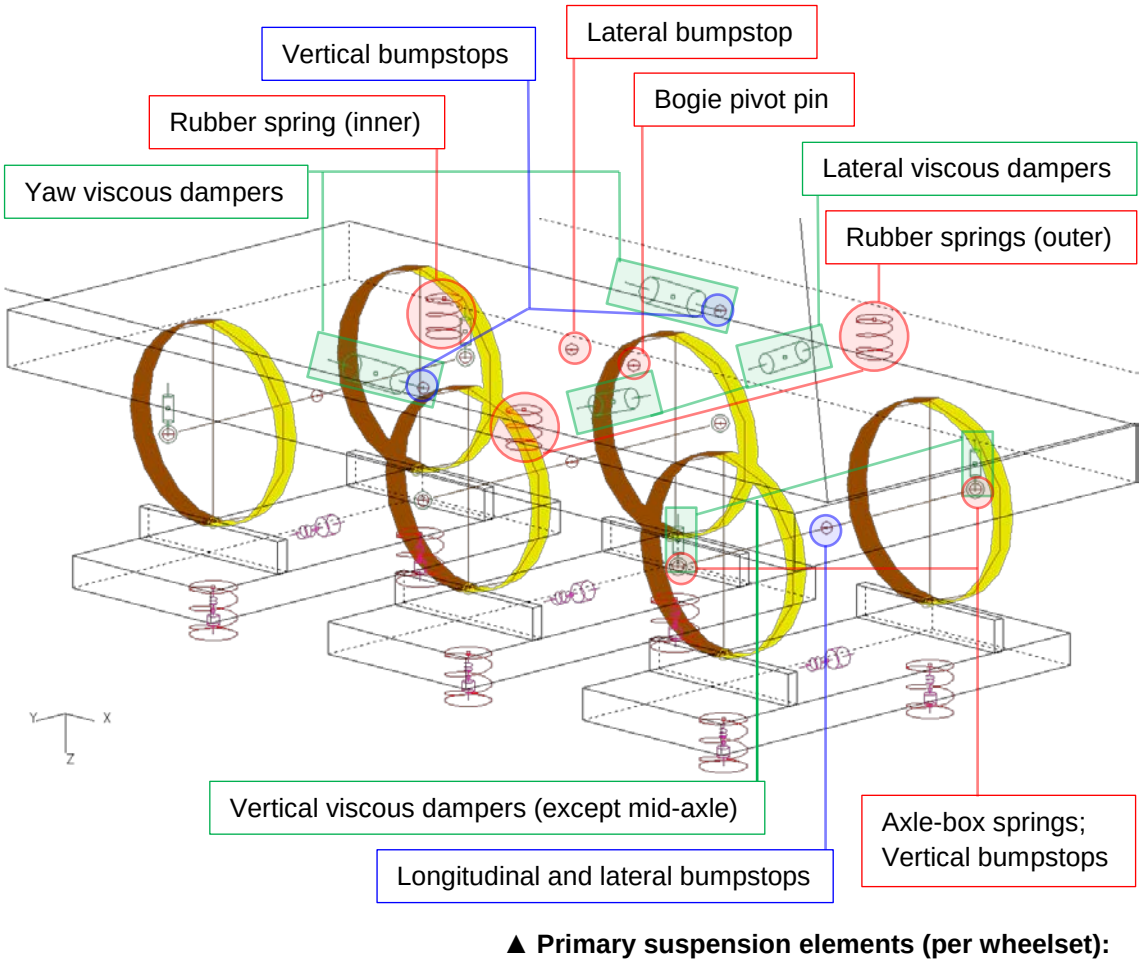

Figure 44: Rigid bogie connections (lead bogie)

Brief descriptions of suspension elements in the modelled rigid bogie are given below:

Secondary suspension elements:

- Rubber springs (linear): Each bogie had three rubber springs that the car-body rested on, with the inner spring being equivalent to both outer springs (twice the stiffness and vertical preload). Compressive stiffness was high to support car-body weight, whilst a low shear stiffness allowed bogie (yaw) rotation in curves [85].
- Yaw viscous dampers: These nonlinear blow-off dampers limit relative yaw between the bogie frames and car-body. In conjunction with the lateral viscous dampers, they help to control bogie hunting [85].

- Lateral viscous dampers (linear): These assist with controlling bogie hunting but have little effect on limiting relative yaw between the bogie frames and car-body [85].
- Lateral bumpstop: Limits relative bogie displacements [122] in the lateral direction at the bogie frame centre. 60 mm of side play was allowed (30 mm left/right from centre).
- Vertical bumpstops: Limit relative bogie displacements in the vertical direction on the left/right sides of the bogie frame. 50 mm of vertical travel was allowed (25 mm up/down from rest position).
- Bogie pivot pin: Transfers tractive effort (longitudinal) and cornering (lateral) forces from the bogie to the car-body [85]. These were modelled with two nonlinear springs constrained to move in the longitudinal and lateral directions respectively. 4 mm of free play (±2 mm from centre) was provided for in both directions.

Primary suspension elements:

Elements in the primary suspension, except for bump-stops, were assumed to be linear. This 'linearised/simplified stiffness' approach has been used previously by Grassie & Elkins [6, 7].

- Axle-box springs (linear): These were modelled as single springs, with parallel dampers, that were positioned at the ends of wheelsets (where axle-boxes would be on a real-world locomotive). Like the rubber springs in the secondary suspension, they have high compressive stiffness to support the car-body and bogie frame but are soft in shear to allow lateral and longitudinal wheelset movement [85].
- Vertical viscous dampers (linear): Provide additional damping to help control vertical wheelset movements in response to track irregularities [85]. These were only fitted to the lead and end axles in a bogie.
- Longitudinal bumpstops: Limited relative wheelset displacements in the longitudinal direction at the wheelset centres. 10 mm of longitudinal travel was allowed (5 mm front/back from centre).
- Lateral bumpstops: Located in the same positions as longitudinal bumpstops (one per wheelset). 22 mm of side play (11 mm left/right from centre) is allowed for the lead and end

axles, whilst mid-axles have 60 mm (30 mm left/right). Stiffness characteristics also differ between lead/end and mid-axle bumpstops.

- Vertical bumpstops: Limited relative wheelset displacements in the vertical direction on the left/right sides of wheelsets (where axle-boxes would be on a real-world locomotive). 50 mm of vertical travel was allowed (25 mm up/down from rest position).

Type AC1 used a 'per wheelset' TC system, where each of its six wheelsets is controlled by its own inverter. The TC system's slip observer calculates slip levels for each wheelset, allowing the application of wheelset (traction motor) torques to be individually controlled. A real-world advantage of per-wheelset TC is that it allows wheelsets of varying diameter, from new to fully worn, to be used on the same locomotive. Wheel diameters don't need to be matched when performing wheelset exchanges, although primary suspension springs might need to be packed to prevent wheel loads from deviating beyond prescribed limits [84]. For this thesis, however, wheel diameters in the locomotive models were kept constant.

3.2.2. Type AC2

The Type AC2 model represents a different design of AC-drive freight locomotive. Wheelset slip is controlled on a per-bogie basis, where all traction motors on a bogie are given the same input from their own inverter (two in total). Bogies were a bolster-less 'semi-steering' type with wheelsets connected to the bogie frames via swing-arms [8]. In comparison, lateral movement for wheelsets in rigid bogies is governed using horn guides, which are directly fixed to the bogie frame, with clearances to allow for some movement in low radii curves. For lead and end axles in the semi-steering bogie, the swing-arm pivots could displace longitudinally, allowing the wheelsets to passively steer in curves [8] in response to yaw moments being produced by the longitudinal creep forces generated in wheel-rail contact patches while cornering [99]. Traction rods are used to transfer longitudinal and lateral forces between the bogies and car-body[85], with the arrangement similar to that used in the bolster-less High Tensile Steel Cast (HTSC) bogies developed by EMD for their GT46MAC locomotive [123]. The total locomotive mass of

134t is identical to that of Type AC1 to comply with the same DIRN weight restrictions [8]. Basic dimensions of the Type AC2 model are given in Figure 45.

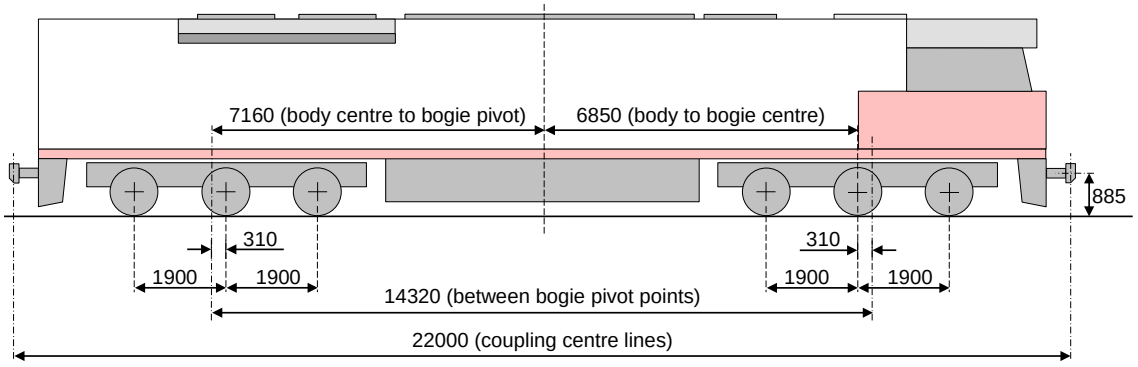

Figure 45: Type AC2 basic dimensions

An overall view of Type AC2's multi-body model, including the rail and track pieces, is shown in Figure 46.

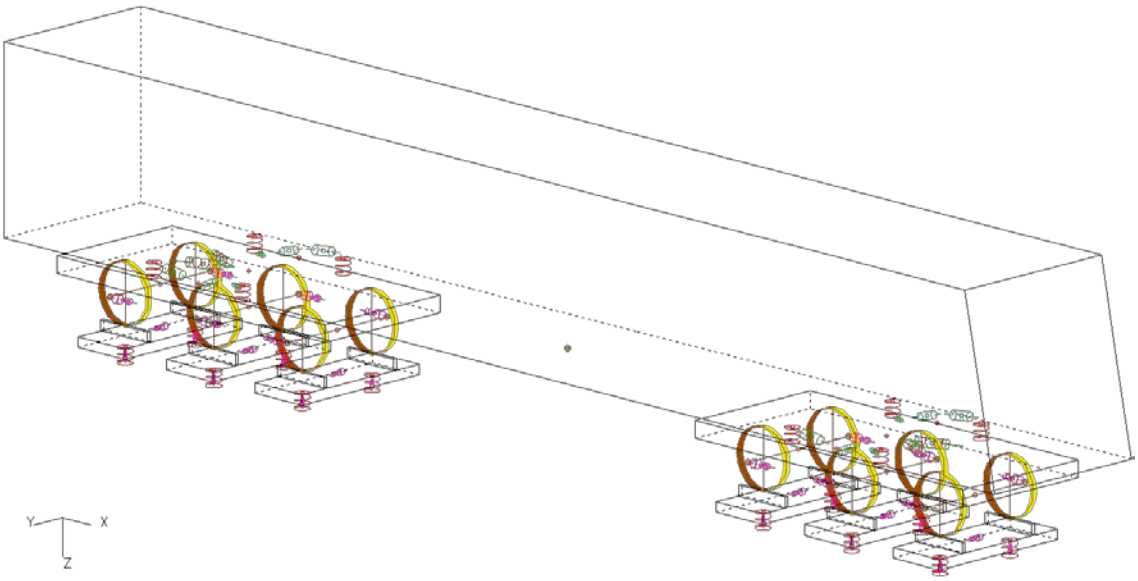

Figure 46: Type AC2 multi-body model

Figure 47 shows a close-up view of the lead bogie, with annotations for primary (below) and secondary (above) suspension elements.

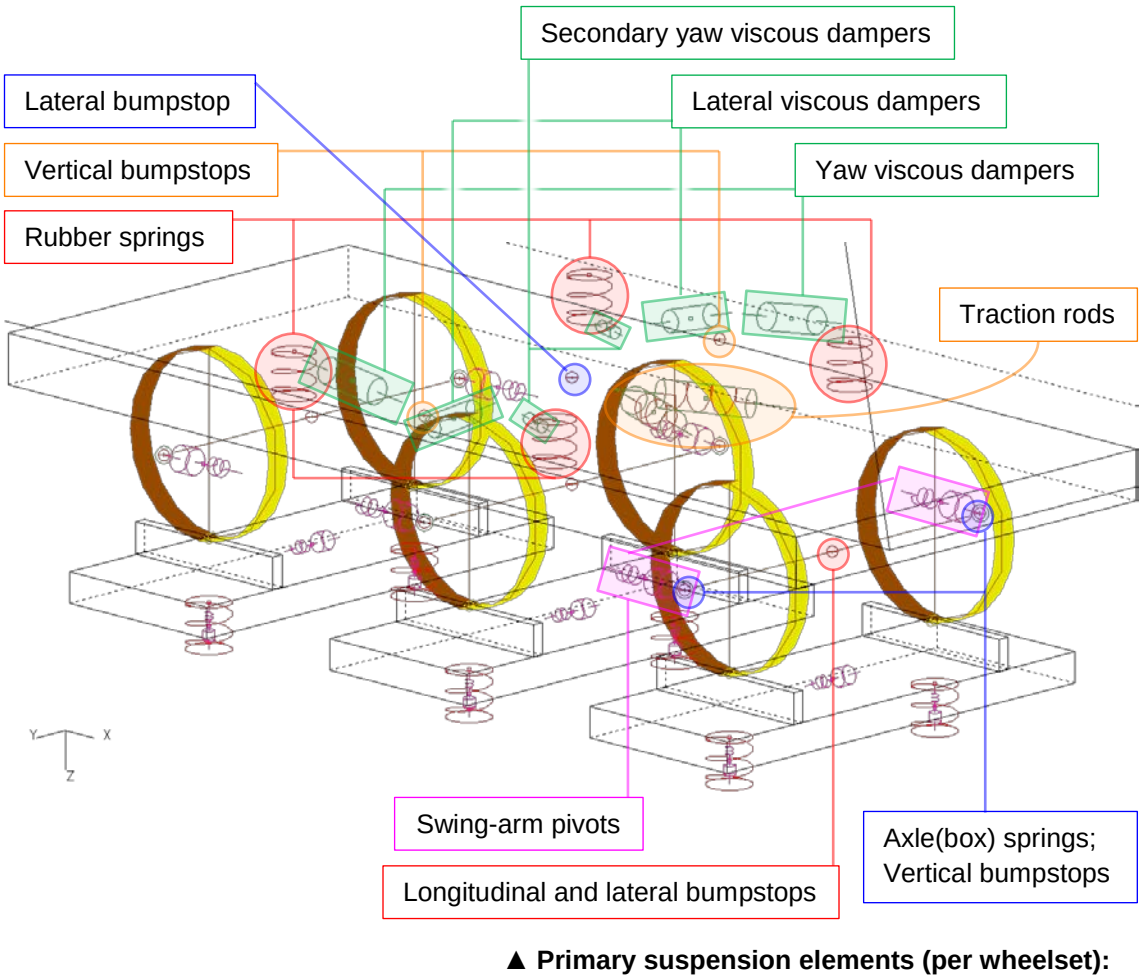

Figure 47: Semi-steering bogie connections (lead bogie)

Because the semi-steering bogie model was developed from the rigid bogie model, there are elements common to both models. Brief notes regarding suspension elements in the modelled semi-steering bogie are given below. Element types used in both the rigid and semi-steering bogie models are not underlined in these notes and their descriptions will not be repeated here (from Section 3.2.1).

Secondary suspension elements:

- Rubber springs (linear): Each bogie had four identical springs to support the car-body
- Yaw viscous dampers
- Lateral viscous dampers (linear)

- Secondary yaw viscous dampers (linear): This semi-steering bogie design features additional yaw viscous dampers, primarily because of the asymmetrical positioning (along the longitudinal axis) of the main blow-off dampers.
- Lateral and vertical bumpstops
- Traction rods (linear): Each of the two traction rods was modelled as a linear spring-damper unit. They were attached to the car-body over the bogie pivot point, with the ends of each rod attached to separate positions on the bogie frame. In the absence of a bogie pivot pin, these were responsible for transferring lateral and longitudinal forces between the bogie frames and car-body [85].

Primary suspension elements:

- Axle-box springs (linear): Same modelling as for rigid bogie (Type AC1) components, but with altered springing/damping rates
- Swing-arm pivots: These were modelled in a similar way to the traction rods used in the secondary suspension, consisting of a spring/damper unit. Their function is to transfer wheelset forces to the bogie frames [85].
- Longitudinal and vertical bumpstops
- Lateral bumpstops: Same modelling as for rigid bogie components, but springing rates have been altered and side-play reduced

Type AC2 used a 'per-bogie' TC system, with all three wheelsets in a bogie controlled by one inverter, giving two inverters in total. During development of Type AC2's TC system, it was found that the lead axles in each bogie experienced the highest wheelset slip levels when under traction, so these were treated as the reference axles for the TC system. This behaviour was to be expected given that traction-induced bogie and car-body pitching was accounted for in the locomotive model [99]. Wheelset slip levels are calculated by a slip observer for each bogie using input from the appropriate reference axles. These in turn are used to determine the wheelset (traction motor) torques for each bogie, with all wheelsets in a bogie given the same torque value. Although not as flexible as the per-wheelset traction control adopted in the Type

AC1 model, per-bogie traction control is adopted in real-world locomotives as a means of reducing part counts (and possible component failures) in a locomotive's drivetrain. For example, only two inverters are required for per-bogie TC, as opposed to six for per-wheelset TC. As wheelsets wear down in service, the difference in wheel diameters reduces when using per-bogie TC, whereas this increases for per-wheelset TC [124].

3.2.3. Type DC

Type DC was representative of a modern Australian standard-gauge DC-drive freight locomotive with rigid bogies. Modern DC-drive locomotives use rectifiers to convert AC electricity from the alternator into DC for traction motors, whose voltage/speed is regulated using a Gate Turn Off (GTO) thyristor circuit. Modern AC-drive locomotives, on the other hand, use inverters with Insulated Gate Bipolar Transistor (IGBT) circuits to convert AC from the alternator into variable frequency AC (higher AC frequency corresponds to increased motor speed) for traction motors [8, 82-84].

Except for variations in body weights, along with a reduction in total mass to 132 t, the multi-body model used for Type DC was identical to that of Type AC1. This means that Figure 42 – Figure 44 and their accompanying descriptions are applicable to both Type AC1 and Type DC.

Type DC's TC system has one rectifier, so all of its six wheelsets (traction motors) are given the same input torques. During development of Type DC's TC system, it was found that the highest wheelset slip levels occurred at the lead axle when under traction, so it was used as the reference axle for the slip observer.

3.2.4. Model parameters

Basic parameters for the three locomotive types modelled are given in Table 9. They were based on familiar parameters described in the GENSYS documentation [115] and those used in previous studies by Simson [99-104] and Spiryagin et al. [105-110].

Table 9: Locomotive model parameters

Category	Parameter	AC1	AC2	DC	Units
Dimensions	Coupler longitudinal distance from car-body CoG	22	22	22	m
	Nominal coupler height above rail level	0.885	0.885	0.885	m
	Bogie pivot longitudinal distance from carbody CoG	7.095	6.85	7.095	m
	Bogie pivot longitudinal distance (outwards) from bogie frame CoG	0.45	0.31	0.45	m
	Bogie semi-wheelbase	1.85	1.9	1.85	m
	New wheel diameter	1.067	1.016	1.016	m
	Total mass	134,000	134,000	132,000	kg
Car-body	CoG height above rail level	1.93	1.93	1.93	m
	Mass	91,600	90,000	91,742	kg
	Moment of inertia, roll	177,095	174,002	177,370	$kg.m^2$
	Moment of inertia, pitch	3,793,457	3,727,195	3,799,337	$kg.m^2$
	Moment of inertia, yaw	3,772,695	3,706,796	3,778,543	$kg.m^2$
Bogie frames	CoG height above rail level	0.733	0.733	0.733	m
	Mass	11,000	12,121	10,502	kg
	Moment of inertia, roll	4,826	5,318	4,608	$kg.m^2$
	Moment of inertia, pitch	33,585	37,007	32,064	$kg.m^2$
	Moment of inertia, yaw	37,234	41,029	35,548	$kg.m^2$
Wheel sets	CoG height above rail level = New wheel radius	0.5335	0.508	0.508	m
	Mass	3,400	3,209	3,293	kg
	Moment of inertia, roll = yaw	2,134	2,014	2,067	$kg.m^2$
	Moment of inertia, pitch	1.432	1,351	1,387	$kg.m^2$
Secondary suspension	Rubber springs - longitudinal distance from bogie frame CoG	0.925	0.95	0.925	m
	(Outer) springs:				
	Lateral distance from bogie CoG	1.272	1.078	1.272	m
	Longitudinal and lateral shear stiffness	188.4	188.4	188.4	kN/m
	Vertical stiffness	10	7.9	10	MN/m
	Inner/central springs:				
	Longitudinal and lateral shear stiffness	376.8	-	376.8	kN/m
	Vertical stiffness	20	-	20	MN/m
	Traction rods:				
	Stiffness	-	5	-	MN/m
	Damping coefficient	-	20	-	kN.s/m
	Bogie centre pins:				
	Stiffness at 2 mm displacement (expansion/compression)	0	-	0	kN/m
	Stiffness at 40 mm displacement	60	-	60	kN/m
	Stiffness from 41 mm displacement	1	-	1	GN/m
	Lateral viscous dampers:				
	Longitudinal distance from bogie CoG	0.925	0.275	0.925	m
	Damping coefficient	40	40	40	kN.s/m
	Yaw viscous dampers:				
	Lateral distance from bogie CoG	1.078	1.24	1.078	m
	Series stiffness	45	45	45	MN/m
	Damping coefficient (at 32 mm expansion/compression)	4,600	4,600	4,600	N.s/m
	Blow-off point (at 1.032 m expansion/compression)	6,800	6,800	6,800	N.s/m
	Secondary yaw viscous dampers - Damping coefficient	-	40	-	kN.s/m
Primary suspension	(Axlebox) Lateral position from wheelset CoG	1.078	1.078	1.078	m
	Coil springs:				
	Longitudinal shear stiffness	45	45	45	MN/m
	Lateral shear stiffness	2.25	2.25	2.25	MN/m
	Vertical stiffness	782	288.5	782	kN/m
	Damping coefficient	10	10	10	kN.s/m
	Vertical viscous dampers (except mid-axle)	60	-	60	kN.s/m
	Traction rods:				
	Stiffness	-	44	-	MN/m
	Damping coefficient	-	100	-	kN.s/m

4. Locomotive Model Acceptance Procedure (LMAP)

Before locomotive models can be used for detailed simulation, basic tests need to be performed to validate their static and dynamic behaviour. These tests should define criteria for acceptable model performance so that any significant errors present can be identified and mitigated. Although several standards exist worldwide to govern the dynamic behaviour of real-world locomotives, there is a lack of documentation regarding the validation of multi-body locomotive models.

In light of this, a Locomotive Model Acceptance Procedure (LMAP) was developed for use in this project. In this case its specific purpose was to evaluate models of Australian freight/heavy-haul locomotives, which required the LMAP to satisfy relevant Australian Standards (AS) [21, 125, 126] as discussed in previous publications [108-110]. Given test data from real-world locomotives was not available, the main focus of this section is to evaluate the methodology behind the proposed LMAP. With a sound methodology, it should be easier to adapt the LMAP to suit other types of locomotive models in future work. This methodology was also adapted to form a Wagon Model Acceptance Procedure [127] which was presented at the Conference On Railway Engineering (CORE) in September 2012.

Various Australian and international standards applicable to locomotive dynamic behaviour, along with Multi-Body Simulation (MBS) software manuals [2, 128], were first reviewed to determine a list of tests along with the most suitable parameters to use for each. A number of these tests were then carried out on the locomotive models discussed in Section 3 in order to remedy any serious faults present and to get a basic idea of how they respond to certain on-track situations, which will help to form project conclusions later. Only some of the tests contained in the LMAP were conducted for this thesis because:

- Results from some tests, namely those related to gauging and pneumatic/dynamic braking, are not particularly relevant to this thesis' outcomes
- The main focus of this section is to evaluate the LMAP's methodology, for the reasons stated earlier

- Developing a LMAP is not the primary focus of this thesis. Presenting results from every test, along with using data from real-world locomotives to validate/improve locomotive models as proposed in [108-110], would require a thesis in itself.

4.1. Background

Several standards exist worldwide to assess the dynamic behaviour of railway locomotives. These typically contain a range of static and dynamic tests, conducted on either laboratory equipment, test tracks or operating rail lines, to determine locomotive performances such as the ability to negotiate sharp curves and susceptibility to hunting. Locomotives that are new, substantially modified, or have been relocated to a new location with significantly different track parameters need to undergo physical testing so that their dynamic performance can be assessed [21, 125, 126], which can be both time consuming and expensive for rail operators. In the case of slightly modified or relocated locomotives, it is possible to reduce the time and resources required for dynamic behaviour testing via the use of virtual multi-body locomotive models in place of actual locomotive testing. Several verified MBS packages are available for this purpose, with the underlying mathematical modelling theory now considered to be mature and reliable [19, 20]. It may also be advantageous to use multi-body models, along with additional scripts to model systems such as traction and pneumatic/dynamic braking, in the early design phase of new locomotives [110].

Although some standards allow simulation in place of specified physical tests, namely from Standards Australia [21, 125, 126], British/European Standards [129, 130] and Rail Corporation New South Wales (RailCorp) [131, 132], few acceptance procedures currently exist to validate the multi-body locomotive models required for virtual testing. Additionally, few standards contain information on testing locomotive traction and braking (dynamic and air) capabilities. Of the currently researched papers, only the RailCorp and superseded Railways of Australia (ROA) [133] standards detail traction and braking tests. Some braking tests were also mentioned in a Request For Purchase (RFP) by Virginia Railway Express (VRE) [134] for new diesel-electric passenger locomotives.

Documentation relating to validation of multi-body locomotive models is also scarce. Although the Manchester Benchmarks developed by the Manchester Metropolitan University's Rail Technology Unit (RTU) [135-137] are (relatively) well known, they are instead concerned with using 'benchmark' vehicles to evaluate the performance of MBS packages. However, the RTU and Intec Dynamics Ltd. [138] developed a very similar framework to the LMAP discussed in this thesis using SIMPACK MBS software. Their framework allows the use of simulation for the replacement of real-world testing, along with verification of multi-body models using real-world data if available, whilst adhering to UK standards. Similar frameworks have been presented by Siemens [139] and Stadler Rail [140] that adhere to UIC standards, although, like the RTU's example, these appear to be limited to passenger locomotives and rolling stock. At CORE 2012, Interfleet Technology presented a validation procedure [141] for passenger cars and freight wagons that adhered to AS 7508 and 7509. Tests were performed on real world wagons to provide data for validating multi-body models in VAMPIRE, with the validated models then tested to simulate data that could not be easily measured (such as wheel L/V ratios) in the physical tests.

Work on (freight) locomotive simulation and validation appears to be more limited. ENSCO [142] developed a VAMPIRE model in conjunction with the BNSF railway for validation purposes. A real-world SD70MAC locomotive was run over a given track section, with the locomotive and track geometry recreated in the VAMPIRE MBS software. Using both real-world and virtual results, the (mechanical) multi-body model was tuned to emulate the performance of its real-world equivalent. Jönsson et al. [143] have used the GENSYS MBS software to perform a similar analysis for a Swedish Rc7 class locomotive over a 40 km track section in accordance with UIC 518 [130] requirements, although in this case no changes were made to the tested locomotive model.

A recent review of the state-of-the-art in vehicle model validation procedures has been conducted by Polach and Evans [144], who remark that multi-body simulation is being increasingly used in rolling-stock design. A key concern is the lack of qualitative measures available for the validation of model behaviour using real-world vehicle data, with the approval

of test outcomes being determined subjectively by assessors. In response to this, the European Dynotrain research project proposed a framework for validating railway vehicle models utilising a) dynamic test criteria from EN 14363, b) subjective assessments by project partners and invited experts, and c) a series of quantitative measures or ‘validation metrics’ to compare data (with respect to time) between real-world locomotives and virtual models.

Table 10: Test categories contained in proposed LMAP

Country/region/category:		***Australia***					***Europe***	***International***	***U.S.A***		***MBS manuals***	
Organisation:		Australian Standards			ROA	RailCorp	BS/EN	UIC	AAR	VRE	DEsolver	DeltaRail
Standard/software:		**AS 7507.1**	**AS 7508.1**	**AS 7509.1**	**ROA Section 13**	**Various**	**BS EN 14363:2005**	**UIC 518 (2005)**	**AAR MSRP Section C part II**	**RFP 08-004 Division 6**	**GENSYS**	**VAMPIRE**
References:		[125]	[126]	[21]	[133]	[131, 132]	[129]	[130]	[145]	[134]	[2]	[128]
Stage 1 - Locomotive model checking/debug												
Automatic error checking	S										R	R
Visual check	S										R	R
Quasistatic analyses (vertical & lateral)	S										R	
Zero speed modal (eigenvalue) analysis	S										R	Incapable
Time-stepping analysis - numerical instabilities	D										R	R
Critical speed	D										R	
Stage 2 - Tests currently included in Australian Standards												
Locomotive (candidate) outlines												
Static outline	S	X				X						
Basic kinematic sway	S, D	X				AS 7507.1	X					
Swept kinematic outline	D	X				AS 7507.1						
Track forces and stresses												
Gross vehicle mass, wheel/axle/vertical loads	S		X			X	X		X		UIC 518	
P/D ratio	S		X			X						
P2 forces	D		X			X						
Lateral track-shifting forces	D		X								UIC 518	
Lateral wheel-rail forces	D		X					X				
Dynamic behaviour												
Hunting	D			X	X				X			
Base ride accelerations (ride quality)	D			X	X	X		X		I	UIC 518	X
Horizontal and vertical (constant) curve negotiation	D			X			X		X		UIC 518	X
Vehicle-vehicle clearance	D			X		X						
Vehicle-bogie clearance	D			X		X						
Transition curve negotiation (spiral)	D			X					X			
Twist test	S			X		X	X				I	
Bogie rotational resistance	S, D			X			X					
Rollover	D			X							I	
Isolated track irregularities (vertical and lateral)	D			R		X						
Cyclic track irregularities:	D			R					X			
Pitch and bounce	D			R		X			X			
Harmonic roll (Twist and roll?)	D			R					X			
Curve entry irregularity (dynamic curving)	D			R					X			
Longitudinal forces in curves	D			X					X			
Stage 3 - Tests from other researched standards/documents												
Traction												
Gradient starting	D				I							
All weather adhesion limit	D					X						
Tractive effort-speed for dry/wet rail	D					X						
Continuous tractive effort for dry/wet rail	D					X						
Balance speed acceleration test	D				I							
Braking												
Stopping distances	D				X	X				X		
Gradient parking	D				X	X						
Static test	S				X	X						
Deceleration rates	D					X						

KEY TO SYMBOLS: S = Static, D = Dynamic, X = Mandatory, R = Recommended, Underlined = Simulation presently allowed, I = Implied/supplementary

Table 11: Brief descriptions of proposed LMAP tests

		Test	Description
Stage 1: Basic locomotive model checking/debugging		1. Automatic syntax error checking	Locomotive model code is checked using an automatic syntax checking program such as RUNF_INFO (GENSYS) [146, 147]
		2. Visual model check	Create a 3D plot of the locomotive model to observe any geometry errors (not observable by syntax checking programs) [147]
		3. Quasistatic analyses: a) Vertical car-body displacement b) Lateral car-body displacement	Observe effects on suspension components, bogie movements and wheel loads when applying a) downward and b) rightward displacements on the car body [147]
		4. Modal (eigenvalue) analysis	Calculate eigenvalues at zero speed for the locomotive model. Errors include negative damping and high absolute eigenvalues (~5000 rad/s) [128, 147].
		5. Time-stepping analysis – numerical instabilities	Run the locomotive model at high speed and check for unexpected motions. Check effects of altering time-step on instabilities [147].
		6. Critical speed	Apply an initial car-body disturbance and decelerate the locomotive from a high speed to determine when hunting stops [147]
Stage 2: Tests currently included in Australian Standards	A. Rolling stock outlines	1. Static suspension heights	Measure locomotive suspension response in the maximum and minimum static height conditions [125, 148, 149]
		2. Basic kinematics – sway a) Cant test rig b) On-track test c) Stationary on max. Installed cant	Determine the body roll relative to the wheelset plane and lateral translation relative to the wheelset centreline by a) raising to maximum cant on both sides, b) running the locomotive at maximum speed and cant deficiency or c) when stationary on maximum installed cant [125, 129, 148, 149]
	B. track forces and stresses	1. Axle loads and P/D ratios a) Static test b) Dynamic test	Axle loads can be measured when the locomotive is a) static or b) travelling at 10 km/h on straight track. The P/D ratio is simply wheel load divided by wheel diameter [126, 129, 148, 150]
		2. P2 force	Can be obtained from an equation or by running the locomotive over a dipped rail weld [126, 148]
		3. Lateral track-shifting force	Cannot exceed the calculated limit when running through a curve at maximum speed and cant deficiency [126]
		4. Lateral wheel-to-rail force	Bogie side L/V (Y/Q, lateral/vertical force) ratios cannot be exceeded when a) running through various curve radii or b) on straight track with a sinusoidal lateral irregularity [126, 145]
	C. Dynamic behaviour	1. Hunting	Measurement of lateral and vertical accelerations at bogie centres at 110% design speed on smooth, straight track [21, 133, 145, 149, 151]
		2. Base ride accelerations	Evaluation of ride quality on rough track [21, 128, 129, 133, 134, 149, 151, 152]
		3. Horizontal and vertical curve negotiation	Negotiation of minimum-radius horizontal curves and vertical humps/dips [21, 149, 152]
		4. Transition curve negotiation a) Twist test b) Bogie rotational resistance c) On-track assessment	Wheel unloading is to be measured when a) static on a twisted test track or when c) travelling through a specified exit transition after a curve. Bogie rotational resistance is also measured to determine its dimensionless 'X-factor' [21, 149, 152]
		5. Rollover	Determines if the locomotive can negotiate curves above the posted speed limit without rolling onto its side about the high rail [21]
		6. Isolated track irregularities a) Flat hump b) Curved dip c) Curve kink	Vertical and lateral bogie centre accelerations, wheel unloading and axle L/V ratios are measured through a, b) vertical disturbances on straight track and c) a lateral disturbance in a curve [21, 149]
		7. Cyclic track irregularities a) Pitch and bounce b) Harmonic roll c) Curve entry irregularities	Similar criteria for testing isolated track irregularities. Deals with vertical track disturbances in a) the track centreline and b) staggered between the high and low rail, along with c) cant imbalance in a curve [21, 145, 149]
		8. Longitudinal forces in curves	Determination of buff and draft forces on the locomotive when cornering between other rolling stock. (This test is optional since additional longitudinal train dynamics simulation is required) [21, 149]
Stage 3: Traction and braking		1. Traction testing	Evaluates the locomotive's ability to start a train of given mass on a gradient in dry and wet conditions [133, 151-153]
		2. Braking	Time taken to stop the locomotive on dry track for a variety of speeds [133, 134, 149, 151, 152, 154-156]

4.2. Methodology

When developing the proposed LMAP for heavy-haul locomotives, a review of relevant worldwide standards and MBS software manuals was first conducted to determine the tests

required and the most suitable parameters to use for each test. In order to thoroughly test locomotive models, it was decided to include a wide variety of tests to identify and solve as many problems as possible that could potentially arise. As the proposed LMAP is intended for use in Australia, the terminology is based on that used in the Rail Industry Safety & Standards Board (RISSB)/Australian Standards [21, 125, 126]. Test categories covered in the proposed LMAP are outlined in Table 10 along with the standards and MBS manuals that were referred to. The derived list of tests, including brief descriptions of the tests, is then given in Table 11. The proposed LMAP has been split into three main 'stages', or categories, which are explained in the following subsections.

4.2.1. Stage 1 – Basic locomotive model checking/debugging

Stage 1 consists of tests to ensure that the model code used is free of errors and that the multi-body model behaves as expected when basic (static and dynamic) analyses are performed. As the RISSB/Australian Standards [21, 125, 126] do not contain provisions for the debugging of multi-body locomotive models, the tests adopted in Stage 1 were based mainly on the GENSYS online documentation [146, 147, 157] with some input from the VAMPIRE (version 4.32) user manual [128]. The procedures and acceptance criteria for Stage 1 tests can be summarised as follows:

1. Automatic syntax error checking [128, 146, 147, 157]: *Procedure:* Run the model code as input to an automatic code checking program such as RUNF_INFO in GENSYS. *Acceptance criteria:* No syntax/coding errors or extremely soft/stiff connections should be found in the model code.
2. Visual model check [128, 147]: *Procedure:* View the model in a 3D plotting program. *Acceptance criteria:* All bodies and connections should be correctly placed and dimensioned.
3. Quasistatic analyses [147]:
    a. Vertical car-body displacement: *Procedure:* Constrain vertical car-body movements and displace it 5 cm in the negative direction (downwards). *Acceptance criteria:*

Both bogies should deflect symmetrically whilst wheel loads should increase linearly in proportion to total primary and secondary suspension stiffness.

b. Lateral car-body displacement: *Procedure:* Constrain lateral car-body movements and displace it 5 cm in the positive direction (right). *Acceptance criteria:* Both bogies should deflect symmetrically, having negative roll displacements relative to the track.

4. Modal (eigenvalue) analysis [128, 147]: *Procedure*: Perform a modal analysis on the locomotive model at zero speed. Look for basic modes/eigenvalues. *Acceptance criteria:* Errors such as negatively damped and overly high eigenvalues (upwards of ~5,000 rad/s) should not be present.
5. Time-stepping analysis – Numerical instabilities [128, 147]: *Procedure:* Perform two time-stepping analyses on the locomotive model, with both fine and coarse time steps, at high speed (~100% design). *Acceptance criteria:* There should be no unexpected motions in the model. Initial disturbances should stabilise at the same time regardless of the time step value.
6. Critical speed estimation [21, 147, 158]: *Procedure:* Perform a time-stepping analysis with the locomotive at very high speed (~300 km/h). Instabilities are initiated with an initial excitation. Wheelset hunting stops near ±10 km/h of the locomotive's critical speed. *Acceptance criteria:* The approximate critical speed should be >110% of the locomotive's design speed.

4.2.2. Stage 2 – Tests currently included in Australian Standards

Stage 2 consists of static and dynamic tests that are presently included in the RISSB/Australian Standards for freight rolling stock, namely AS 7507.1 [125] for rolling stock outlines, AS 7508.1 [126] for track forces/stresses and AS 7509.1 [21] for dynamic behaviour. A review of equivalent standards from RailCorp [131, 132], the (now superseded) Railways of Australia (ROA) Manual [133, 159], the Association of American Railroads (AAR) Manual of Standards and Recommended Practices [145], British Standards [129] and the International Union of Railways (UIC) Leaflet 518 [130] showed that few augmentations needed to be made to the

Australian Standards test requirements. The VAMPIRE user manual [128] and a Request For Purchase (RFP) for new diesel-electric passenger locomotives by Virginia Railway Express (VRE) [134] gave only supplementary or implied information, whereas the relevant test requirements contained in the online GENSYS manual were largely based on UIC Leaflet 518 [130]. Procedures and acceptance criteria for Stage 2 tests can be summarised as follows:

Stage 2A – Rolling stock outlines:

- Static suspension heights [125, 148, 149]: *Procedure:* Perform quasistatic analyses on the locomotive for both maximum and minimum operational weights to find the maximum/minimum static heights. *Acceptance criteria*: No part of the locomotive should infringe its applicable static (cross-sectional) outline.
- Basic kinematics – sway [125, 129, 148, 149, 152]: These tests are used to determine body roll and lateral translation relative to the wheelset centreline when the locomotive is tilted (e.g., when cornering). *Acceptance criteria:* No part of the locomotive should infringe its applicable basic kinematic (cross-sectional) outline.
    a. Cant test rig: *Procedure:* Raise the locomotive in multiple increments up to its maximum applicable cant on one side, then lower back to zero cant. Do the same to the other side to get a hysteresis curve of lateral and roll movements versus applied cant.
    b. On-track test (dynamic): *Procedure:* Perform a time-stepping (or quasistatic) analysis with the locomotive curving at maximum cant deficiency as close to maximum speed as possible.
    c. On-track test (static): *Procedure:* Perform a quasistatic analysis of the locomotive at maximum cant when stationary.

Stage 2B – Track forces and stresses:

1. Test 1 – Axle loads and P/D ratios [126, 129, 148, 150]: *Procedure:* Wheelset loads can be obtained either from a quasistatic analysis at 0 km/h or a quasistatic/time-stepping analysis

at 10 km/h. The P/D ratio is simply wheel load divided by wheel diameter. *Acceptance criteria:* Wheelset/axle loadings and P/D ratios cannot exceed prescribed limits.

2. Test 2 – P2 forces [126, 148]: *Procedure:* This is simply obtained using the equation described in [21]. *Acceptance criteria:* P2 forces cannot exceed prescribed limits.
3. Test 3 – Lateral track-shifting forces [126]: *Procedure:* Perform time-stepping analyses for situations (if any) where the locomotive will experience unbalanced lateral acceleration $\geq$0.72 m/s^2 (for 1435 mm gauge) in curves. *Acceptance criteria:* The sum of lateral wheelset forces on each axle cannot exceed limits defined in [21].
4. Test 4 – Lateral wheel-to-rail forces [126, 145]: *Procedure:* Run the locomotive through various curves whose speed, cant and radius result in an unbalanced lateral acceleration of 0.73 m/s^2 using time-stepping analyses. *Acceptance criteria:* Lateral wheel-rail forces (L or Y) cannot exceed limits defined in [21].

Stage 2C – Dynamic behaviour (Time-stepping analyses are required unless otherwise noted):

1. Hunting [21, 133, 145, 149, 151]: *Procedure:* Run the locomotive model over a $\geq$2 km stretch of smooth, straight track at 110% of design speed. *Acceptance criteria:* Lateral and vertical acceleration limits at the bogie centres cannot be exceeded. Significant hunting motions of the wheelsets cannot occur during the test.
2. Base ride accelerations [21, 129, 133, 134, 149, 151, 152]: *Procedure:* Run the locomotive over track that represents the roughest encountered in service. Straight track will suffice. *Acceptance criteria:* Lateral and vertical acceleration limits at the bogie centres cannot be exceeded along with applicable ride index/comfort limits.
3. Horizontal and vertical curve negotiation [21, 149, 152]: *Procedure:* Measure displacements of locomotive bodies when traversing the minimum radius horizontal and vertical curves encountered in service (at low speeds). *Acceptance criteria:* Clearances between the car body, bogie frames and wheelsets should allow the locomotive to traverse the track geometry without derailing or becoming damaged. Suspension elements/parameters and wheel/rail profiles may also have an effect.
4. Transition curve negotiation [21, 149, 152]:

a. Twist test: *Procedure:* The static locomotive model is placed on a cant ramp designed to impart (underframe) twisting forces. Wheelsets of interest, in this case the lead wheelset of the first bogie, are then incrementally raised and lowered on both sides in a similar manner to stage 2A, test 2a to obtain a hysteresis curve showing wheel unloading versus applied wheelset cant. *Acceptance criteria:* The average wheel unloading for the analysed wheelset cannot exceed 60%.

b. Bogie rotational resistance: *Procedure:* Determine the torque required to rotate the bogies relative to the car-body by either a) running the model through a minimum-radius curve at a speed typical of in-service operation, or b) rotating one bogie while the locomotive is static. *Acceptance criteria:* The X-factor calculated for the bogie should be less than 0.1.

c. Alternate on-track assessment: *Procedure:* Run the locomotive model at 10 km/h through a minimum radius curve with a prescribed cant irregularity in the exit transition. *Acceptance criteria:* Limits on maximum axle (sum) L/V (Y/Q) ratios and wheel L/V ratios sustained for 50 ms cannot be exceeded.

5. Rollover [21]: *Procedure:* Perform time-stepping analyses for situations (if any) where the locomotive will experience unbalanced lateral acceleration ≥ 0.72 m/s^2 (for 1435 mm gauge) in curves. *Acceptance criteria:* The vertical unloading for wheels on the low rail cannot be greater than 60%

6. Isolated track irregularities [21, 149]: *Procedure:* Run the locomotive at a range of speeds up to 110% of design speed over the following irregularities: a) flat hump (vertical), b) curved dip (vertical), and c) curve entry irregularities (lateral). *Acceptance criteria:* Prescribed limits for maximum lateral/vertical accelerations, vertical wheel-rail forces and sum axle L/V (Y/Q) ratios cannot be exceeded.

7. Cyclic track irregularities [21, 145, 149]: *Procedure:* Run the locomotive at a range of speeds up to 110% of design speed for the following cases: a) pitch and bounce (vertical parallel rail disturbances), b) harmonic roll (vertical staggered rail disturbances), and c) curve entry irregularities (variations in cant imbalance). *Acceptance criteria:* Prescribed

limits for maximum lateral/vertical accelerations, vertical wheel-rail forces and sum axle L/V (Y/Q) ratios cannot be exceeded.

8. Longitudinal forces in curves [21, 149]: *Procedure:* Calculations are first carried out to determine wheel unloading limits and if they will be breached for a locomotive experiencing longitudinal buff/draft forces in a small-radius curve. If the calculated limit is not exceeded but the calculated wheel unloading is greater than 90%, a time-stepping analysis is required. The locomotive is simulated to run in a small-radius curve with either separate rolling stock models coupled to it to provide buff/draft forces, or by applying coupler forces to the locomotive model determined using Longitudinal Train Simulation (LTS). *Acceptance criteria:* The calculated wheel unloading limit should not be exceeded. Any wheel lift during simulations results in failure.

4.2.3. Stage 3 –Tests not included in Australian Standards (traction and braking)

Locomotive traction and braking tests are contained in Stage 3 since they are not covered in the Australian Standards. In addition to a mechanical multi-body model, these require modelling of traction and/or braking systems, such as the simplified Traction Control (TC) code described in Section 3. Another alternative, outside the scope of this thesis, is the 'open' GENSYS-Simulink co-simulation method proposed by Spiryagin et al. [106] where various locomotive subsystems can be modelled separately in Simulink and communicating with a GENSYS mechanical model via a network. Out of the researched standards, only those from RailCorp [149, 151-155] supplied detailed instructions for traction and braking tests, with the ROA Manual [133] and the VRE RFP [134] providing only supplementary or implied information. A brief summary of the tests in Stage 3 is given below:

Stage 3A – Traction tests:

1. Gradient starting [133, 152]: *Procedure:* Determine the longitudinal coupler force exerted on the locomotive when hauling the heaviest permissible train up a given gradient. Apply this coupler force to the locomotive model and have it start from rest on straight, level track

(since the locomotive model can only start on straight track in GENSYS). *Acceptance criteria:* The locomotive (and train) should be able to accelerate to balance speed without exceeding the traction equipment's short-time (thermal) rating.

2. All-weather adhesion limit [153]: *Procedure:* Start the locomotive and train (the latter simulated with applied longitudinal coupler forces) at line speed on dry, level straight track before climbing a 1 km incline. 500 m up the incline track, friction will change from dry to wet to simulate the application of water sprays on the locomotive. *Acceptance criteria:* The test is failed if a) speed drops below 10 km/h, b) excessive uncontrolled wheel-slip occurs, and/or c) the traction equipment's short-time rating is exceeded.
3. Tractive effort-speed for dry/wet rail [152]: *Procedure:* Run the locomotive and train from rest on straight track up to balance speed. The rail can be on a gradient, but level track will suffice. Record tractive effort, speed, throttle reading, wheel-slip, sanding applications and the time taken to accelerate to balance speed during the test. *Acceptance criteria:* Excessive wheel-slip is not allowed.
4. Continuous tractive effort for dry/wet rail [152]: *Procedure:* Starting at balance speed, run the locomotive on straight track. The rail can be on a gradient, but level track will suffice. *Acceptance criteria:* The locomotive must be able to maintain its balance speed without excessive wheel-slip.
5. Balance speed acceleration test [133]: *Procedure:* Similar to Test 1, although the object is to record the time taken for the locomotive to accelerate to balance speed with its given gradient and load. *Acceptance criteria:* Those mentioned in Test 1, with the additional requirement that the time taken to accelerate to balance speed should be similar to data provided by the locomotive manufacturer (although this is not strictly a criterion for failure).

Stage 3B – Braking tests:

1. Stopping distances [133, 134, 151, 152, 155]: *Procedure:* A locomotive and train is to be tested on dry, straight track. It is preferred to have level track, but constant gradients can also be used. Shortly after the train has started at speed, apply the

(emergency/dynamic/pneumatic) brakes and record the distance and time elapsed whilst the train slows to a stop. Multiple speeds should be tested. *Acceptance criteria:* Excessive wheel-slip cannot occur and the train must be able to slow to a complete stop. Braking time and distance (with the train) should be similar to data provided by the locomotive manufacturer (although this is not strictly a criterion for failure) and within limits imposed by the locomotive operator.

2. Gradient parking [133, 149]: This test should only be considered if parking brake mechanisms are being tested. *Procedure:* Start the locomotive at rest on a 1:30 gradient with the parking brake on. *Acceptance criteria:* The parking brake should be strong enough to secure the locomotive indefinitely. No movement is allowed.
3. Static test [133, 149, 156]: Consider this test only if pneumatic braking is modelled. *Procedure:* Apply the locomotive air brakes when it is at rest. Simulation of the air brakes alone (rather than the multi-body model) should suffice. *Acceptance criteria:* The air brakes should function properly, with appropriate air pressures, apply/release times and brake block forces.
4. Deceleration rates [151, 154]: *Procedure:* Dovetailed out of Test 1. Deceleration rates can either be recorded directly or calculated from the deceleration times and distances recorded earlier. *Acceptance criteria:* Braking deceleration rates should be similar to data provided by the locomotive manufacturer (although this is not strictly a criterion for failure) and within limits imposed by the locomotive operator.

4.3. Simulated case studies for locomotive model validation

During development of the Type AC1, AC2 and DC locomotive models, a range of LMAP tests were conducted in GENSYS to help identify and mitigate any major errors that could negatively affect model performance. As stated earlier, it would be impractical to complete all LMAP tests since the results of some would be not particularly relevant to and/or beyond the scope of this thesis. Although the main point of these case studies was to evaluate the LMAP's methodology, they had the secondary benefit of (partially) validating locomotive models for use in further simulation. Owing to the lack of available data from real-world testing, and quantitative

measures for verifying the locomotive models using that data [144], it was assumed that compliance with standards referenced in the LMAP constituted successful test outcomes. This assumption is reasonable because similar real-world locomotives are accredited to run on Australia's Defined Interstate Rail Network (DIRN) [8, 84]. Generally, however, a locomotive model should accurately replicate the capabilities of its real-world counterpart; if a real-world locomotive fails an acceptance test then so should its equivalent virtual model. For brevity, only results from the finalised locomotive models will be reported; results from earlier models and the changes made to them will not be covered in depth here.

All of the checking/debugging tests in Stage 1 were carried out except for the 'modal (eigenvalue) analysis' because the locomotive models used in this thesis contain nonlinear elements. Although GENSYS' MODAL calculation program [160] can automatically linearise nonlinear elements, doing so in this case introduced further problems such as some modes being calculated to have negative eigenfrequencies. The 'hunting' and 'pitch and bounce' tests in Stage 2 were performed, but none of the Stage 3 tests mentioned in the LMAP methodology were carried out since they required model capabilities that would not be used in further simulations. However, a 'TC system debugging' test was subsequently created to ensure that the locomotive model TC systems worked, to fine tune parameters for the Polach friction model [51, 69] and to determine the optimum longitudinal creep values for TC system slip limiters mentioned earlier in Table 8. Detailed parameters, procedures and acceptance criteria are explained in each subsection before test outcomes for all three locomotive models are given. These are mainly written to suit the GENSYS multi-body modelling software, although the basic principles can be applied to other suitable software suites.

In all tests that required time-stepping analysis (in GENSYS's TSIM program), the 'heun_c' two-step Runge-Kutta solver with step-size control was used with output results written every 10 ms. Except for the TC system debugging test in Stage 3, a constant coefficient of friction in the wheel-rail contact area is assumed, being 0.4 for dry track, with creep forces interpolated from lookup tables generated by FASTSIM [113].

4.3.1. Stage 1 – Basic locomotive model checking/debugging

4.3.1.1. Automatic syntax error checking

GENSYS uses a program called RUNF_INFO to check for syntax errors in locomotive model 'runf' files. A user's manual can be referred to in [146].

Parameters:

- New (ANZR1) wheel and (AS60) rail profiles
- Analysis type = Built-in code checking (RUNF_INFO)
- Locomotive speed = 0 km/h
- **Test track = 1-1.** Geometry: 25 m of straight, level, ideal (no irregularities) track with 25 m of over-run at each end (75 m total). The over-runs ensure that the locomotive model is in contact with track at all times.

Procedure:

- A 'runf_infof' file will need to be created to read the locomotive model 'runf' file. This is usually achieved by creating and modifying a master runf_infof file [161].
- Run the .runf_infof file to check the locomotive model file [147]. Warnings will be printed in its 'genterm' (GENSYS terminal output) window, along with the locations of any output files.
- Although [128] recommends that vehicle models should always be automatically checked for errors before analyses are performed, practical experience showed that this was not always necessary because of the extra processing effort involved. This was particularly the case when working with multiple copies of the same locomotive model file where only 'outside' parameters like track geometry and wheel/rail friction conditions (as opposed to 'inside' parameters like masses and connections within the locomotive multi-body model itself) were changed.

Acceptance criteria:

The test has been passed if no syntax/coding errors or extremely soft/stiff connections have been found by RUNF_INFO (i.e., there are no warnings printed in its 'genterm' window).

Test outcomes:

All locomotive models passed. No syntax/coding errors or extremely soft/stiff connections were present in the final model codes.

4.3.1.2. Visual model check

Parameters:

- New (ANZR1) wheel and (AS60) rail profiles
- Analysis type = Visual inspection (GPLOT)
- Locomotive speed = 0 km/h
- Test track = 1-1

Procedure:

- Create a 3D plot of the vehicle model. In GENSYS, the GPLOT post-processing program is used for this purpose [147, 162].
- Visually check that all couplings within the locomotive model are properly mounted. More information on couplings can be obtained in GPLOT by left-clicking on them to bring up an information window. If there are multiple couplings/elements in the same place, multiple information windows will open [147]. It may be worth checking the model code for dimensioning errors (such as body masses) that cannot be displayed in GPLOT.
- Examples of geometry errors to look out for include [128]:
    - Incorrect units (element sizes, stiffnesses, etc. too large/small)
    - Incorrect sign (elements face the wrong way or are misplaced)
    - Elements connected to the wrong side of bodies/wheelsets

Acceptance criteria:

All masses and couplings in the locomotive model should be correctly placed and dimensioned.

Test outcomes:

All locomotive models passed. No bodies and connections in the final locomotive models were incorrectly placed and/or dimensioned. A GPLOT screenshot applicable to the Type AC1 and Type DC models can be seen in Figure 43, whereas one for the Type AC2 model is in Figure 46.

4.3.1.3. Quasistatic analyses

This section consists of two tests (per locomotive model) to determine model behaviour in response to simple disturbances [147]. GENSYS performs quasistatic analyses using the QUASI calculation program [160]

Parameters:

- New (ANZR1) wheel and (AS60) rail profiles
- Analysis type = Quasistatic (QUASI)
- Locomotive speed = 0 km/h
- Test track = 1-1

Procedure [147]:

- Vertical car-body displacement: Constrain vertical (z) motion in the car-body, move its centre of mass 5 cm in the positive direction (down) and perform a new quasistatic analysis.
- Lateral car-body displacement: Constrain lateral (y) motion in the car-body, move its centre of mass 5 cm in the positive direction (right) and perform a new quasistatic analysis.

Acceptance criteria [147]:

- Vertical car-body displacement: Vertical wheel/rail contact forces should increase in proportion to the total stiffness in the primary and secondary suspension. These should be symmetric for both bogies.
- Lateral car-body displacement: Both bogies should have a negative roll angle relative to the track

Test outcomes:

All locomotive models passed. Figure 48 shows front views of the Type AC1 model with positive vertical (left image) and lateral (right image) car-body displacements applied. Deformations are amplified by five times, with responses for the Type AC2 and DC models being practically identical to Type AC1.

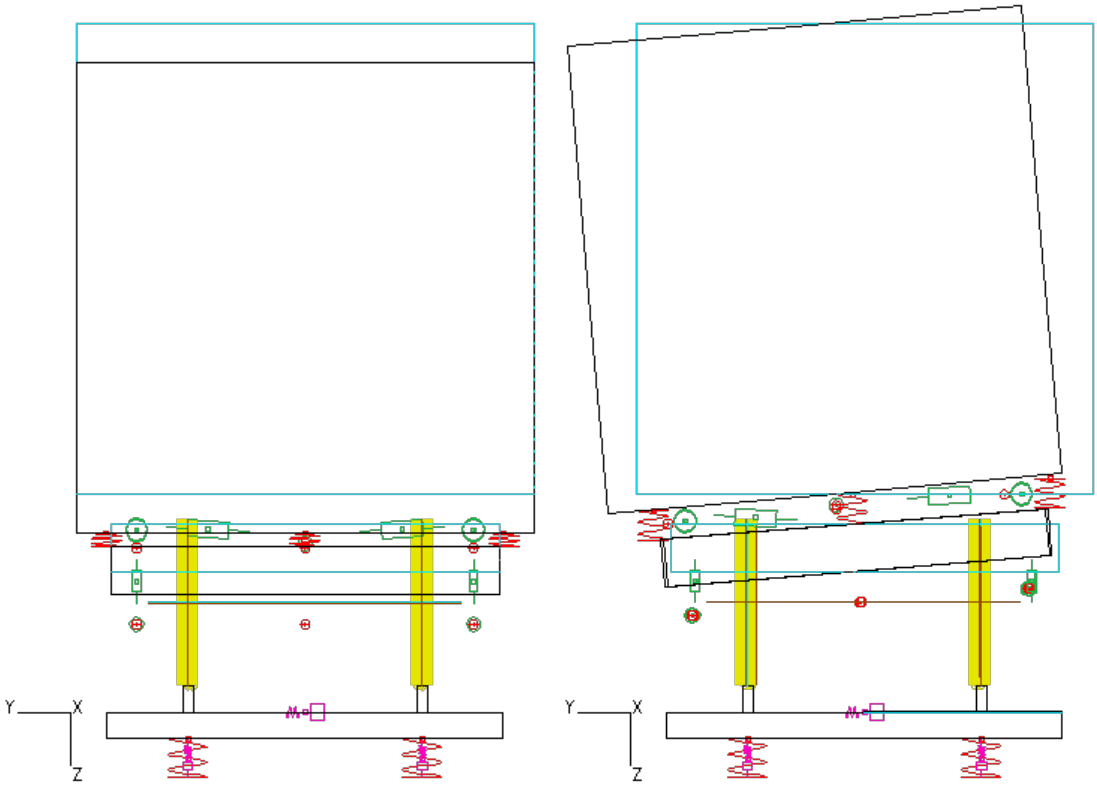

Figure 48: Front views of Type AC1 model undergoing vertical (left) and lateral (right) car-body displacements (5x deformation scale)

With vertical car-body displacements applied to all locomotive models, the car-body and bogie frames were displaced downward as expected, with no longitudinal movement of the bogie frames (and consequently wheelsets). Vertical wheel-rail contact forces had increased in response to the car-body displacement and were equal across all wheels. Making reference to Figure 48, it can be seen that the lateral car-body displacement causes additional roll displacements in the car body and bogie frames (along with the wheelsets and track pieces to a lesser extent) since car-body roll movements were not constrained. It is apparent that the secondary suspensions for all three locomotive models were much stiffer compared to their primary suspensions. Significant bogie frame displacements were only noted in the lateral and roll directions and were symmetrical for all locomotive models.

4.3.1.4. Time-stepping analysis – numerical instabilities

GENSYS performs time-stepping analyses using the calculation program TSIM [160]. Initial instabilities that occur during time stepping analyses should quickly dissipate, even with varying time steps [128] and locomotive speeds.

Parameters:

Constant:

- New (ANZR1) wheel and (AS60) rail profiles
- Analysis type = Time-stepping (TSIM)
- **Test track = 1-2.** Geometry: 1000 m of straight, level, ideal track with 25 m of over-run at each end (1050 m total).

Variable:

- Time steps = Fine (0.1 ms) and coarse (1 ms)
- Locomotive speeds:
    - At maximum continuous tractive effort (approx.) = 20 km/h
    - Typical maximum operating speed = 70 km/h

- Maximum design speed = 115 km/h

Total number of tests required for each locomotive model = 6

Procedure:

- Perform separate time-domain simulations [147] for each combination of:
  - (Constant) Locomotive speed [147]
  - Time step (fine and coarse) [128]
- View the results in GPLOT and set the deformation scale to 300-400 times. Animate the simulation and look for any unexpected motions [147].
- Check displacements (x, y, z) and rotations (f, k, p) of model bodies in MPLOT
- Check variations in normal wheel-rail contact patch force (cp1_$1r.Fn and cp1_$1l.Fn)

Acceptance criteria:

- There should be no unexpected motions in the model [147]. Possible sources of instability may include numerical noise or a rough longitudinal displacement control [108].
- The model should stabilise at both fine and coarse time steps. One method of countering model instabilities is to use finer time steps [128]

Test outcomes:

Type AC1 and DC passed, whereas Type AC2's performance was satisfactory. It was assumed that the locomotive models became stable once all vertical wheel-rail forces had stabilised. These were determined graphically as shown in Figure 49 for the Type DC model at 70 km/h.

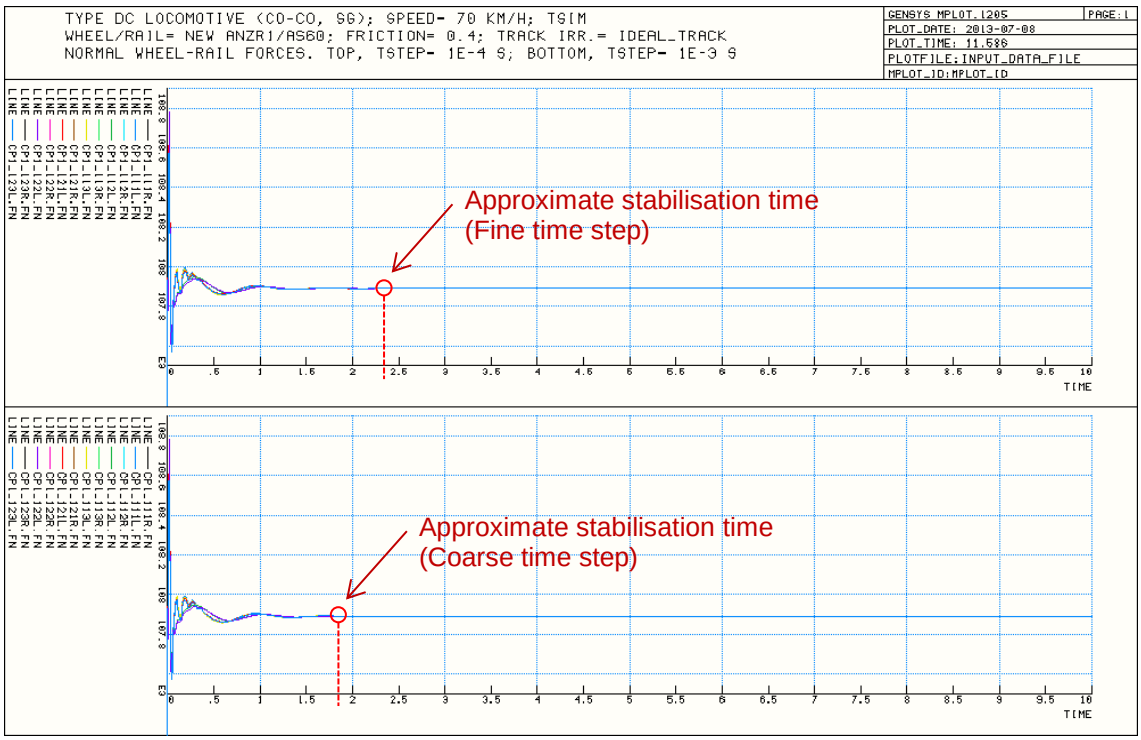

Figure 49: Determining model stabilisation times graphically (Type DC, 70 km/h)

Approximate stabilisation times for all locomotive models, speeds and solver time steps are summarised in Table 12.

Table 12: Approximate locomotive model stabilisation times

Locomotive model	Time step	20 km/h	70 km/h	115 km/h
Type AC1	Fine (0.1 ms)	2.3 s	2.3 s	2.3 s
	Coarse (1 ms)	1.8 s	1.8 s	1.8 s
Type AC2	Fine	6.1 s	7.1 s	7.1 s
	Coarse	6.6 s	6.6 s	6.6 s
Type DC	Fine	2.3 s	2.3 s	2.3 s
	Coarse	1.8 s	1.8 s	1.8 s

Stabilisation times for the Type AC1 and DC models did not vary with speed, but they seemed to increase when decreasing the time step, the opposite of what was expected to happen [128]. Type AC2 meanwhile took a much longer time to completely stabilise than the other models. This is most likely the result of using a different bogie model (semi-steering as opposed to rigid) and some additional fine-tuning may be required for future work.

Some minor differences were also noted when analysing body motions. For the rigid bogie Type AC1 and DC locomotive models, small initial vibrations in the range of 1 mm ($1x10^{-3}$ m) were noted in the longitudinal (x) and vertical (z) directions in all bodies. For the car-body and bogie frames, some minor initial pitch (p) vibrations in the range of 1 μrad ($1x10^{-6}$ rad) were also detected. The initial vertical disturbances occur as the locomotive model settles on its suspension, whereas the longitudinal disturbances are due to the longitudinal speed control, which consists of a spring-damper system, stabilising the locomotive velocity. These longitudinal and vertical vibrations would in turn induce minor pitching in the car body and bogie frames.

Similar behaviour is noted in the semi-steering bogie Type AC2 model at 20 km/h, although such vibrations take a longer time to settle. At and above 70 km/h, minor lateral (y) vibrations in the range of 1 μm ($1x10^{-6}$ m) are noted in all bodies, whereas minor roll (f) vibrations in the range of 1 μrad ($1x10^{-6}$ rad) appeared in the car-body and bogie frames. It is most likely that lateral vibrations in the wheelsets are inducing lateral and roll vibrations in the bogie frames and car-body. Although this seems to have only a minor effect on locomotive model dynamics, the stabilisation time is increased, but for the purposes of this thesis performance of the Type AC2 model is still satisfactory.

4.3.1.5. Critical speed estimation

A quick method of estimating the critical speed of a railway vehicle model is to start it off at high speed with an initial disturbance applied to the car-body and have it decelerate at a fixed rate until hunting motions in the wheelsets stop [147]. Although ‘ramping’ vehicle speed downward in this manner allows for a quicker analysis than separately testing stepwise increases/decreases in vehicle speed (e.g., 160, 155, 150 km/h), it is inaccurate because the lower bound of the critical speed can be overshot [158]. In light of this, critical speeds estimated using this method are accurate to within ± 10 km/h.

Parameters:

- New (ANZR1) wheel and (AS60) rail profiles
- Analysis type: Time-stepping (TSIM)
- Time step: Fine (1 ms)
- Initial locomotive speed: 300 km/h (based on 115 km/h design speed)
- Locomotive deceleration = 5 km/h/s
- **Test track = 1-3.** Geometry: 2600 m of straight, level, ideal track with 25 m of over-run at each end (2650 m total).

Procedure:

- Start the simulation at high speed (above the locomotive's critical speed) and have it gradually reduced. The speed variable 'vkmh' can be defined as follows [147]:

```
func operp vkmh= 300 - 5 * time
```

- To initiate instability modes, apply an initial excitation to the car-body. An example is given in [147]:

```
initval set_var  car_1.vy= .15
initval set_var  car_1.vp= .15
```

- To make the vehicle follow the co-ordinate systems, apply negative forces to all its masses. One way to do this is shown below (for a deceleration of 5 km/h per second) [147]:

```
force rel_lsys1  retard_car_1    car_1   0 0 -hccg_1   -mc_1*5/3.6  0. 0.  0. 0. 0.     # Apply redardation 5[km/h/s]
force rel_lsys1  retard_bog_11   bog_11  0 0 -hbcg_11  -mb_11*5/3.6 0. 0.  0. 0. 0.     # as external forces
force rel_lsys1  retard_bog_12   bog_12  0 0 -hbcg_12  -mb_12*5/3.6 0. 0.  0. 0. 0.
force rel_lsys1  retard_axl_111  axl_111 0 0 -ro_111  -(ma_111+Jka_111/ro_111^2)*5/3.6 0. 0.  0. 0. 0.
force rel_lsys1  retard_axl_112  axl_112 0 0 -ro_112  -(ma_112+Jka_112/ro_112^2)*5/3.6 0. 0.  0. 0. 0.
force rel_lsys1  retard_axl_121  axl_121 0 0 -ro_121  -(ma_121+Jka_121/ro_121^2)*5/3.6 0. 0.  0. 0. 0.
force rel_lsys1  retard_axl_122  axl_122 0 0 -ro_122  -(ma_122+Jka_122/ro_122^2)*5/3.6 0. 0.  0. 0. 0.
```

- Given the locomotive's 300 km/h initial speed and 5 km/h/s deceleration, it should stop before the test track length of 2.6 km is reached. The following methods can be used to prevent the locomotive from accelerating in reverse:
    - Limit the simulation time 'tstop' to 60s (corresponds to 0 km/h)
    - Limit the simulation distance 'Xtrac_stop' to 2500 m

- Insert the following code to stop simulation when speed 'vkmh' = 0:

```
if_then vkmh .eq. 0
 func print06_char_all " "
 func print06_char_all " Execution interrupted due to vkmh = 0"
 func print06_char_all " -------------------------------------"
 func stop
endif
```

- Plot lateral axle movements (axl_$1.y) in MPLOT. The point where hunting motions cease can be taken as an approximate critical speed accurate to ±10 km/h

Acceptance criteria:

The approximate critical speed should be above 110% of a locomotive's design speed [21]. Given that the design speed of all modelled locomotives is 115 km/h [81], their approximate critical speed should be above 126.5 km/h (115 km/h x 1.1).

Test outcomes:

Type AC1 and DC passed, whereas Type AC2's performance was satisfactory. The time where wheelset hunting motions stopped was found graphically as shown in Figure 50 for the Type AC1 model. Since deceleration was linear, the corresponding speed could then be found using Equation 28.

$$v_{CRIT,APPROX.}\ km/h\ = 300\ km/h - \left(5\ km/h/s \times t_{CRIT,APPROX.}\ s\right)$$

Equation 28: Approximate critical speed from time where wheelset hunting stops

Where: $v_{CRIT,APPROX.}$ = Approximate critical speed (km/h)

$t_{CRIT,APPROX.}$ = Time where wheelset hunting stops (s)

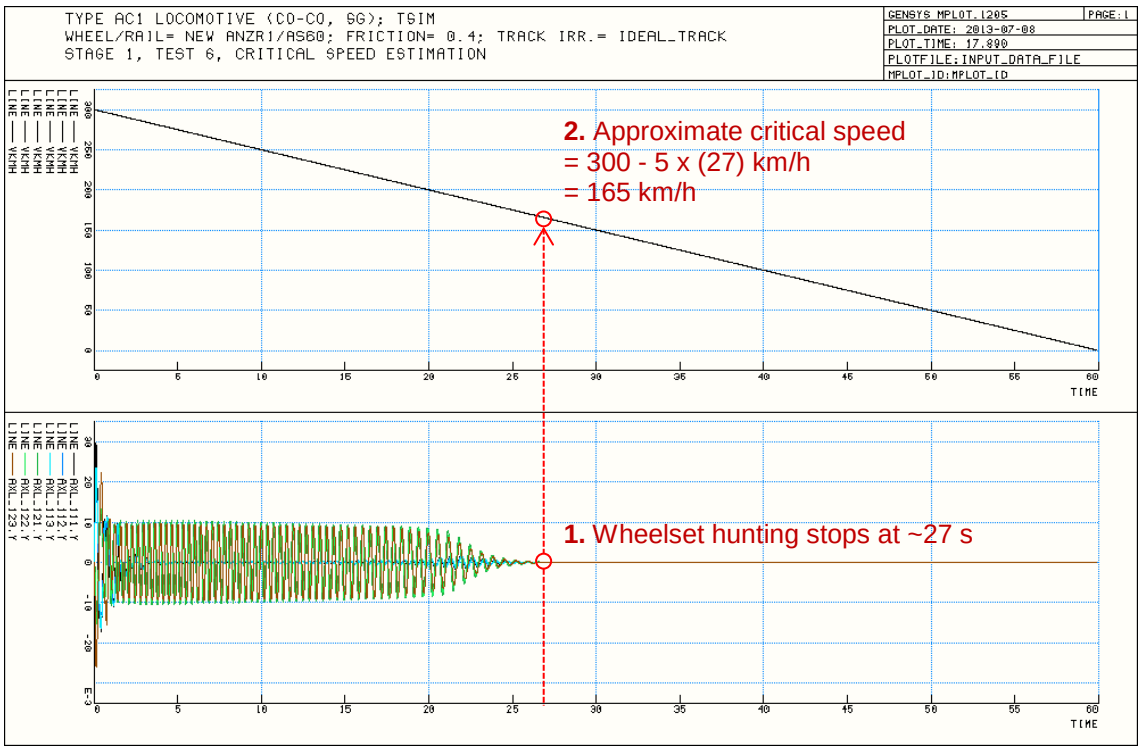

Figure 50: Determining approximate critical speed (Type AC1)

Type DC's approximate critical speed and wheelset hunting behaviour is the same as that shown for Type AC1 in Figure 50. This was expected since the mechanical model for Type DC has the same layout as for Type AC1, albeit with altered body and connecting element properties. Wheelset hunting motions for Type AC2 did not end as abruptly as for the other models, where most vibrations stopped at one point with minor vibrations continuing until a subsequent second point. This is illustrated in Figure 51.

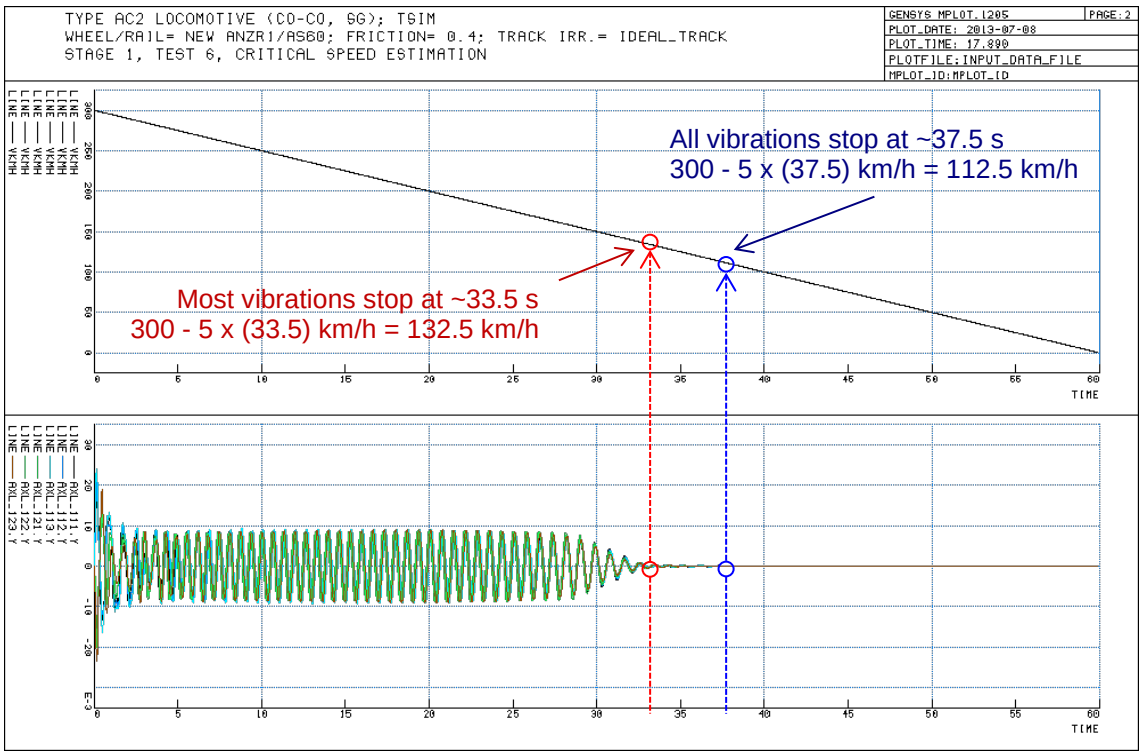

Figure 51: Approximate critical speed data for Type AC2

Given that the approximate critical speed occurs when *all* wheelset hunting motions stop, Type AC2 fails this criterion since this occurs at 112.5 km/h, below the required minimum of 126.5 km/h. As in the numerical instability tests done earlier, this implies that the semi-steering bogies in the Type AC2 model may need further fine-tuning, particularly with regard to connection (spring and damper) parameters. However, for the purposes of this thesis, where most simulations will be conducted at low speed (~20 km/h) and maximum continuous tractive effort, this is not a significant issue. Approximate critical speeds for all modelled locomotive types are summarised in Table 13.

Table 13: Critical speed approximations

Locomotive model	Time wheelset hunting stops (s)	Approximate critical speed (km/h)	Outcome
Type AC1	27	165	Passed
Type AC2	33.5 – 37.5	132.5 – 112.5	Satisfactory
Type DC	27	165	Passed

4.3.2. Stage 2 – Tests currently included in Australian Standards

4.3.2.1. Hunting

This test determines if a locomotive model is susceptible to hunting motions at high speed. Although it mainly draws from the hunting test in AS 7509.1 Section 3 [21], it was decided to augment the test by evaluating maximum car-body lateral and vertical accelerations at the bogie centres using the limits prescribed in AS 7509.1 Section 4 [21] and RailCorp document ESR 0001 – 200 Section 26 (Ride Performance Test – RSU 288) [149].

Parameters:

- Analysis type: Time-stepping (TSIM)
- Time step: Fine (1 ms)
- Speed = 110% design [21] = 126.5 km/h for all locomotive models
- Dry weather conditions [21], (minimum) $\mu = 0.4$ [145]
- Travelling as a single vehicle in tare (empty) condition [21, 149]
- The vehicle should be in a Simulated Service Worn condition, with worn dampers and a Worn Wheel Test Profile [21, 149].
    - Neither worn damper data nor quantitative definitions of the Simulated Service Worn condition were available, so as-new damping was used instead
    - Two ANZR1 wheel profiles with flange wear and some tread wear were supplied by the CRE and converted into GENSYS format. During each test, all wheels on the locomotive models had the same worn wheel profile (1 or 2).
- The gauge corner of the rail profile should have minimal grinding [21]. In this case new AS60 rail was used since suitable worn profiles weren't available.
- **Test track = 2-1.** Designed geometry: 3000 m of straight, level track with 25 m of over-run at each end (3050 m total).
    - According to AS 7509.1 Section 4 [21], the test track should be ≥2 km of straight, level track. RailCorp [149] recommends at least 3 km, so this length was chosen.

- Smooth track irregularities [21]. FRA Class 6 or better is recommended in [145]. FRA track spectra, generated by the CRE in a VAMPIRE script and converted to GENSYS format, were used throughout this thesis as it was the only track irregularity data available at the time. Properties of the generated FRA Class 6 track used are given below in Table 14 [163].

Table 14: Properties of generated FRA Class 6 track irregularity data [163]

	Centreline deviation (mm)		**Gauge (mm)**	**Cant (mm)**
	Lateral	Vertical		
Max.	6.86680	7.37876	1440.06114	5.06114
Min.	-7.43427	-9.13506	1430.39155	-4.60845

Total number of tests required for each locomotive model = 2

Procedure:

- Accelerations should be measured on the vehicle body at the leading and trailing bogie centres of rotation [21, 145, 149]
- Measured signals should be recorded with a sampling frequency of ≥50 Hz [21] and filtered with a 10 Hz cut-off. [21, 149]

Acceptance criteria:

- Lateral vehicle body accelerations measured at the bogie centres that are greater than 0.5 Hz and 0.35 g sustained for 10 s or longer constitutes sustained hunting [149, 151]. If the locomotive model experiences sustained hunting during the test, it has failed.
- Limits for accelerations recorded at bogie centres [21, 149]:
    - Maximum lateral acceleration = ±0.5 g
    - Average lateral acceleration = ±0.35 g
    - Maximum vertical acceleration = ±0.8 g
    - Average lateral acceleration = ±0.5 g
- For soft lateral suspension, wheel L/V ratios sustained for 2 m should not exceed 1.0 [21]. Although the tested locomotive models did not appear to have soft lateral suspensions, this criterion was still evaluated.

Test outcomes:

All models passed. Results from the hunting tests are summarised in Table 15 and Figure 52, where, out of the worn wheel profiles tested, profile 2 is more heavily worn than profile 1.

Table 15: Hunting test results

Locomotive model:		**Type AC1**		**Type AC2**		**Type DC**	
Worn wheel profile:		**1**	**2**	**1**	**2**	**1**	**2**
Acceptance criteria [21, 149]	**Limit**						
Maximum lateral bogie centre accelerations	±0.5 g	±0.03690	±0.04510	±0.11873	±0.10045	±0.03688	±0.04487
Average lateral bogie centre accelerations	±0.35 g	±0.00897	±0.01022	±0.02845	±0.02529	±0.00894	±0.01013
Maximum vertical bogie centre accelerations	±0.8 g	±0.26685	±0.26638	±0.07683	±0.07733	±0.26098	±0.26053
Average vertical bogie centre accelerations	±0.5 g	±0.01781	±0.01780	±0.01228	±0.01227	±0.01758	±0.01758
Maximum wheel L/V ratio	≤1.0	0.12075	0.14424	0.22764	0.19963	0.11750	0.14439

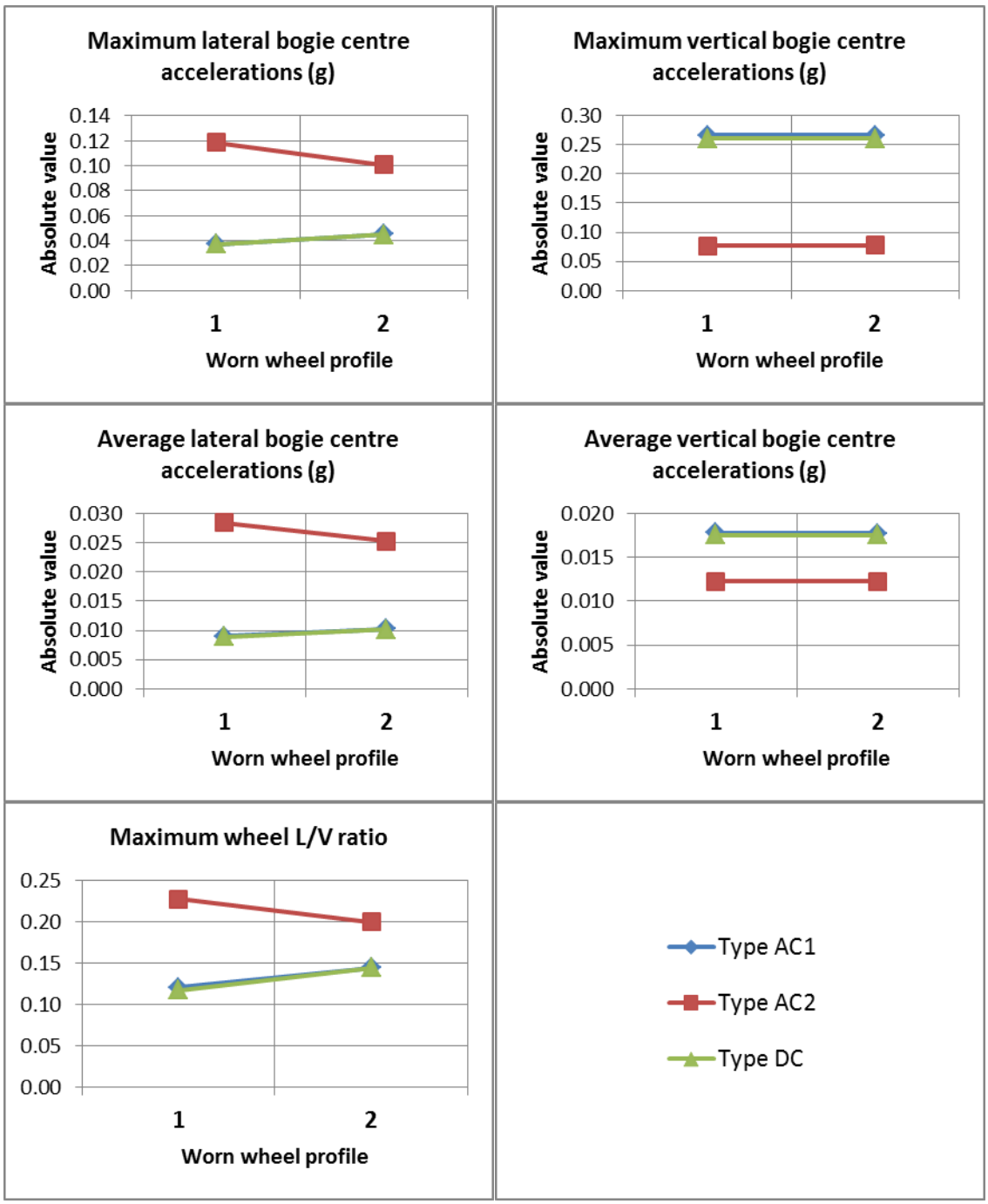

Figure 52: Hunting test results against worn wheel profiles

Performances of the rigid-bogie Type AC1 and DC models were similar. In comparison, the semi-steering bogie Type AC2 model produced significantly higher (i.e., undesirable) maximum lateral bogie centre accelerations and wheel L/V ratios, but on the positive side, significantly lower maximum vertical bogie centre accelerations were simulated. When Types AC1 and DC were tested with the more heavily worn wheel profile 2, they showed slightly higher maximum

lateral bogie centre accelerations and wheel L/V ratios than with the less worn wheel profile 1. In Type AC2's case, this outcome was reversed, with those performances improving.

4.3.2.2. Cyclic track irregularities – Pitch and bounce

In this test, locomotive models are run over a test track with cyclic vertical track centreline disturbances, representing conditions where rail joints have dipped during service, to induce pitch and bounce oscillations [21, 145]. Suspensions in the locomotive models should be able to control these oscillations adequately [149]. Other examples of isolated and cyclic track irregularities, tests of which are conducted in a similar manner, are described in Section 4.2.2.

Parameters:

Constant:

- Analysis type: Time-stepping (TSIM)
- Time step: Fine (1 ms)
- Dry weather conditions [21], (minimum) μ = 0.4 [145]
- Travelling as a light engine [21] in tare condition
- New ANZR1 wheel and AS60 rail profiles
- **Test track = 2-2.** Designed geometry: 1000 m of straight, level track with 25 m over-runs at each end (1050 m total). Three vertical track centreline disturbances were located 275 m after the start point (0 m). Although the exact geometry isn't specified in AS 7509.1 [21] or Section 28 (RSU 290) of RailCorp document ESR 0001 – 200 [149], the bump height H = 20 mm and wavelength L = 13.7 m were defined. In this test the vertical bumps were assumed to have a sinusoidal shape, as shown in Figure 53 [21, 149].

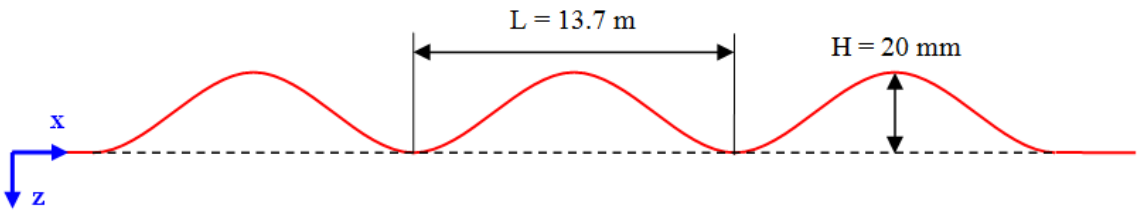

Figure 53: Vertical track disturbance geometry for pitch and bounce test [21, 149]

- FRA Class 5 or better track is recommended [145]. FRA Class 6 track will be used in this case since high-speed test track passes will be made. These irregularities are superimposed over the entire test track (including the designed vertical track centreline disturbances).

Variable:

It is recommended to test a range of locomotive speeds up to 110% design speed [21, 149]. In this case, increments of 20, 40, 60, 80, 100 and 110% design speed were tested. To minimise simulation time for lower locomotive speeds, the start and end points were placed closer to the track irregularities (test track 2-2). Table 16 shows the range of speeds tested and the corresponding start/end points.

Table 16: Locomotive speeds and start/end points for test track 2-2

Locomotive speed:						
% of design	20	40	60	80	100	110
km/h	23	46	69	92	115	126.5
Test track start and finish points (m from start):						
Start point	225	175	125	75	25	0
End point	460	580	700	820	940	1000

Total number of tests required for each locomotive model = 6

Procedure:

Accelerations should be measured on the vehicle body at the leading and trailing bogie centres of rotation and filtered using a low-pass filter with a 10 Hz cut-off frequency [21, 149]

Acceptance criteria:

- Maximum lateral acceleration allowed = ±0.5 g [21, 149]
- Maximum vertical acceleration allowed = ±0.8 g [21, 149]
- Maximum wheel unloading over 50 ms ≤ 90% [21, 149]
- Maximum sum axle L/V ratio over 50 ms ≤ 1.5 [21]

Test outcomes:

All locomotive models passed. Results from the pitch and bounce tests are summarised in Table 17 and Figure 54.

Table 17: Pitch and bounce test results

% design speed		20	40	60	80	100	110
Speed (km/h)		23	46	69	92	115	126.5
Type AC1:							
Acceptance criteria	**Limit**						
Maximum lateral bogie centre accelerations	±0.5g	±0.00822	±0.00793	±0.01575	±0.02702	±0.02702	±0.03855
Maximum vertical bogie centre accelerations	±0.8g	±0.01010	±0.05273	±0.12951	±0.13618	±0.15431	±0.16658
Maximum wheel unloading	≤90%	38.131%	39.942%	45.417%	47.191%	48.901%	49.297%
Maximum sum axle L/V ratio	≤1.5	0.08907	0.08881	0.08737	0.08708	0.08630	0.08596
Type AC2:							
Acceptance criteria	**Limits**						
Maximum lateral bogie centre accelerations	±0.5g	±0.00608	±0.03514	±0.01619	±0.03737	±0.02702	±0.08626
Maximum vertical bogie centre accelerations	±0.8g	±0.01221	±0.22897	±0.07716	±0.06468	±0.06303	±0.06152
Maximum wheel unloading	≤90%	36.434%	72.909%	44.228%	38.801%	41.773%	44.785%
Maximum sum axle L/V ratio	≤1.5	0.08772	0.08687	0.08649	0.08631	0.08493	0.08451
Type DC:							
Acceptance criteria	**Limits**						
Maximum lateral bogie centre accelerations	±0.5g	±0.00815	±0.00788	±0.01569	±0.02718	±0.02702	±0.03867
Maximum vertical bogie centre accelerations	±0.8g	±0.01011	±0.05248	±0.12931	±0.13703	±0.15448	±0.16659
Maximum wheel unloading	≤90%	38.208%	39.985%	45.448%	47.339%	48.769%	49.438%
Maximum sum axle L/V ratio	≤1.5	0.08837	0.08813	0.08669	0.08658	0.08628	0.08575

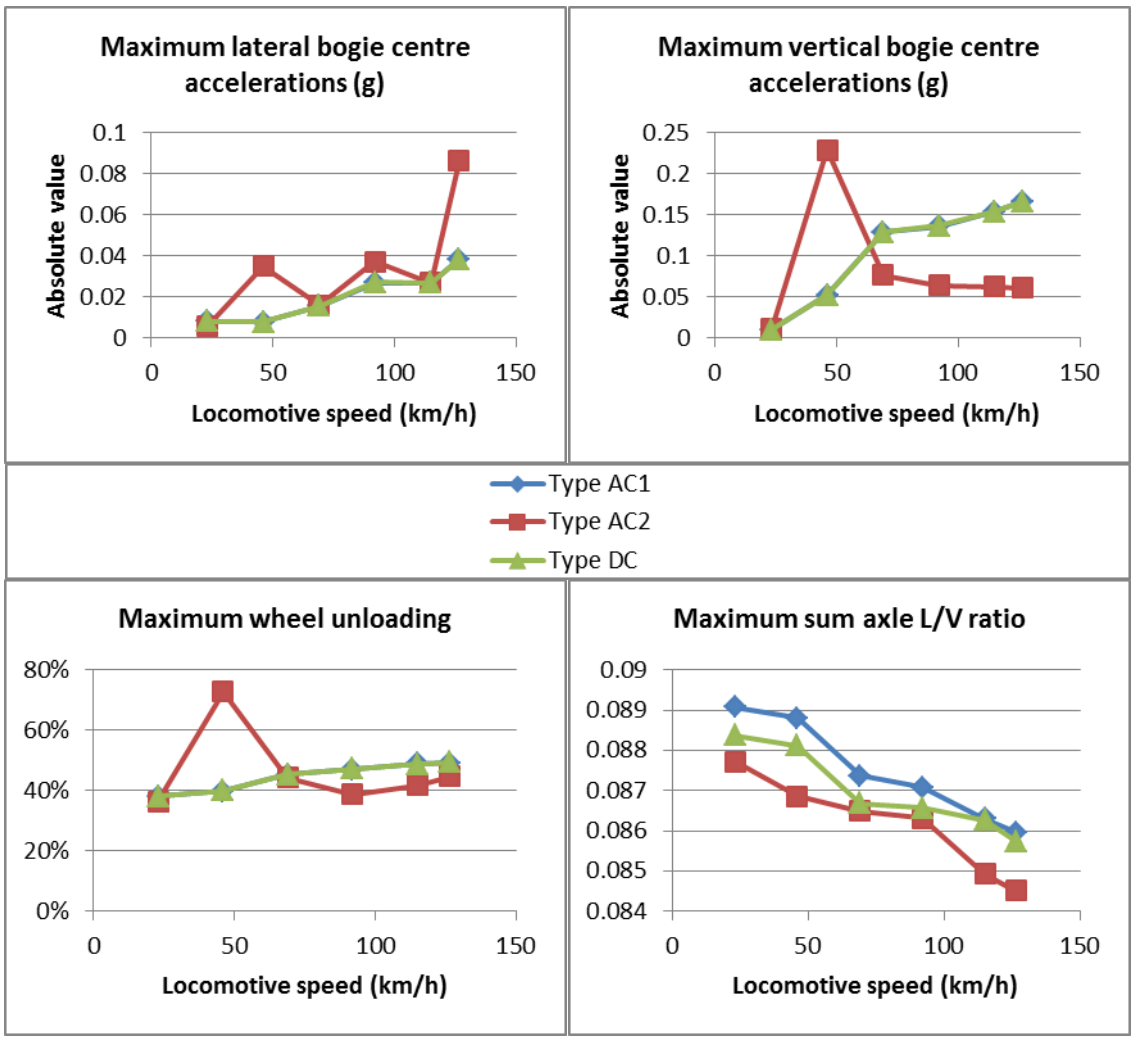

Figure 54: Pitch and bounce test results against locomotive speed

In comparison to the rigid-bogie Type AC1 and DC models, maximum lateral bogie centre accelerations for the semi-steering bogie Type AC2 model were generally greater in magnitude, while the variation with increasing speed appears to be more erratic. The spike in lateral accelerations at 126.5 km/h (110% design speed) for Type AC2 may be the result of minor hunting motions, since in Section 4.3.1.6 (Stage 1, Test 6) hunting was found not to completely stop until ~112.5 km/h. As in Section 4.3.2.1 (Stage 2, Test 1), maximum vertical bogie centre accelerations were generally lower for Type AC2 than for Types AC1 and DC, but a high reading was recorded for 46 km/h (40% design speed) for Type AC2. Maximum wheel unloading for Type AC2 also spiked at this speed. At first glance such behaviour appeared to be the result of a natural frequency being crossed, so a check was made to see if any vertical modes matched/approached the track disturbance frequency at this speed, which is:

Speed = 46 km/h; Disturbance wavelength = 13.7 m

46 km/h / 3.6 = 12.778 m/s

Track disturbance frequency = 12.778 m/s / 13.7 m = 0.933 Hz

Unfortunately no vertical modes were found to have eigenfrequencies close to 0.933 Hz, indicating that there must have been another fault in the Type AC2 model causing these disturbances. Unlike the other tabled data (with the possible exception of maximum vertical bogie centre accelerations), maximum sum axle L/V ratios were found to decrease with locomotive speed, with little variance between locomotive models.

4.3.3. Stage 3 –Tests not included in Australian Standards (traction and braking) – TC system testing

This is somewhat of a 'debugging' exercise to ensure that the variable friction modelling and TC system in the locomotive models works properly. Results were used to select the optimum longitudinal creep values summarised earlier in Table 8 for each locomotive model at maximum continuous tractive effort for dry and wet track surfaces.

Parameters:

Constant:

- Analysis type: Time-stepping (TSIM)
- Time step: 0.1 ms
- New (ANZR1) wheel and (AS60) rail profiles
- Creep/slip range to be simulated = 0-30%
- Rate of creep increase = 0.1% per second
- Total simulation time = 300 s
- **Test track = 3-1.** Designed geometry: 2000 m of straight, level, ideal track with 25 m of over-run at each end (2050 m total).

Variable:

- Test both dry and wet track conditions. Polach contact model parameters for the tested locomotive models are mentioned earlier in Table 5
- Maximum continuous tractive effort ratings (obtained) for the locomotive models tested can be referred to in Table 7.

Total number of tests required for each locomotive model = 2

Procedure:

- Run analyses for both dry and wet track conditions for each locomotive type at their rated maximum continuous tractive effort ratings
- Plot the following data against creep/slip:
  - Variable friction coefficient μ
  - (Approximate) Adhesion coefficient
  - Measured adhesion coefficients (if available)

Adhesion coefficients for each wheel are approximated using Equation 29. It is assumed that wheel-rail contact will only occur at the wheel tread/rail head during this test.

$$\mu_{EST,WHEEL} = \frac{Fx_{WHEEL}}{Fn_{WHEEL}}$$

Equation 29: Estimated adhesion coefficient (per wheel)

Where: $\mu_{EST,WHEEL}$ = Estimated adhesion coefficient per wheel

Fx_{WHEEL} = Longitudinal contact patch creepage (N)

Fn_{WHEEL} = Contact patch normal force (N)

Acceptance criteria:

- No uncontrolled wheel-slip or other TC system malfunctions should occur over the tested creep/slip range
- No significant interference/vibrations should be present in the plotted data

Test outcomes:

All locomotive models passed. Variable friction and estimated adhesion curves are plotted against slip for the tested locomotive models in Figure 55 – Figure 57.

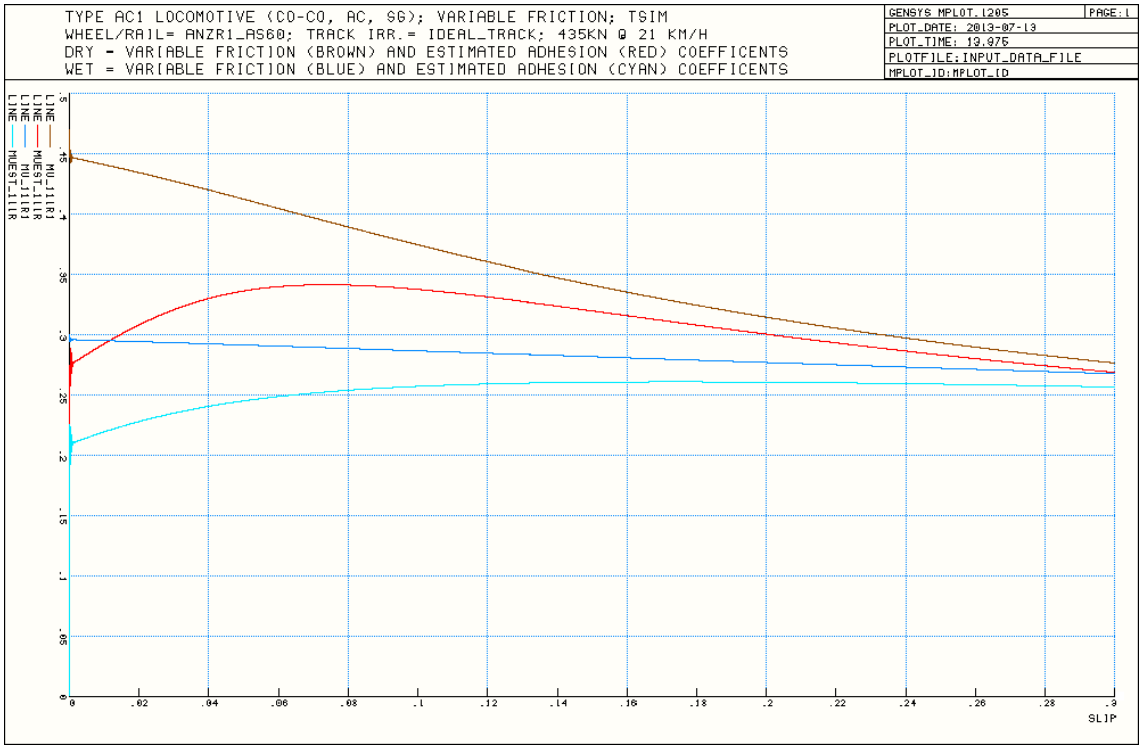

Figure 55: Variable friction and estimated adhesion curves for Type AC1

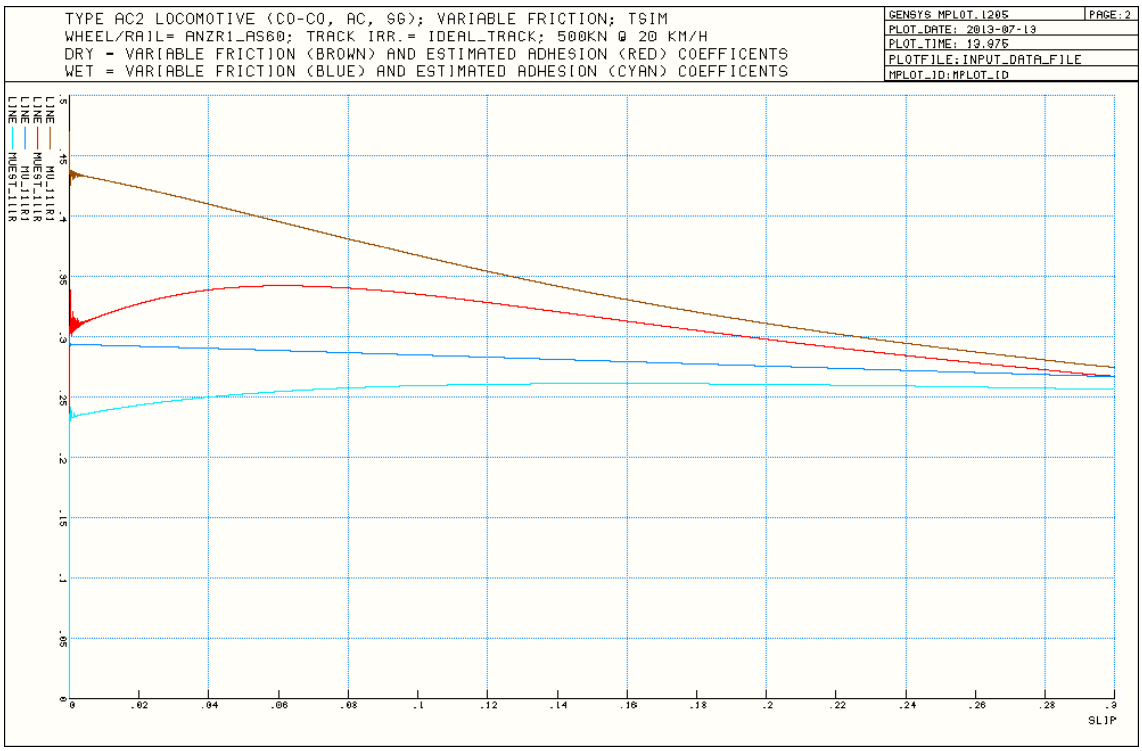

Figure 56: Variable friction and estimated adhesion curves for Type AC2

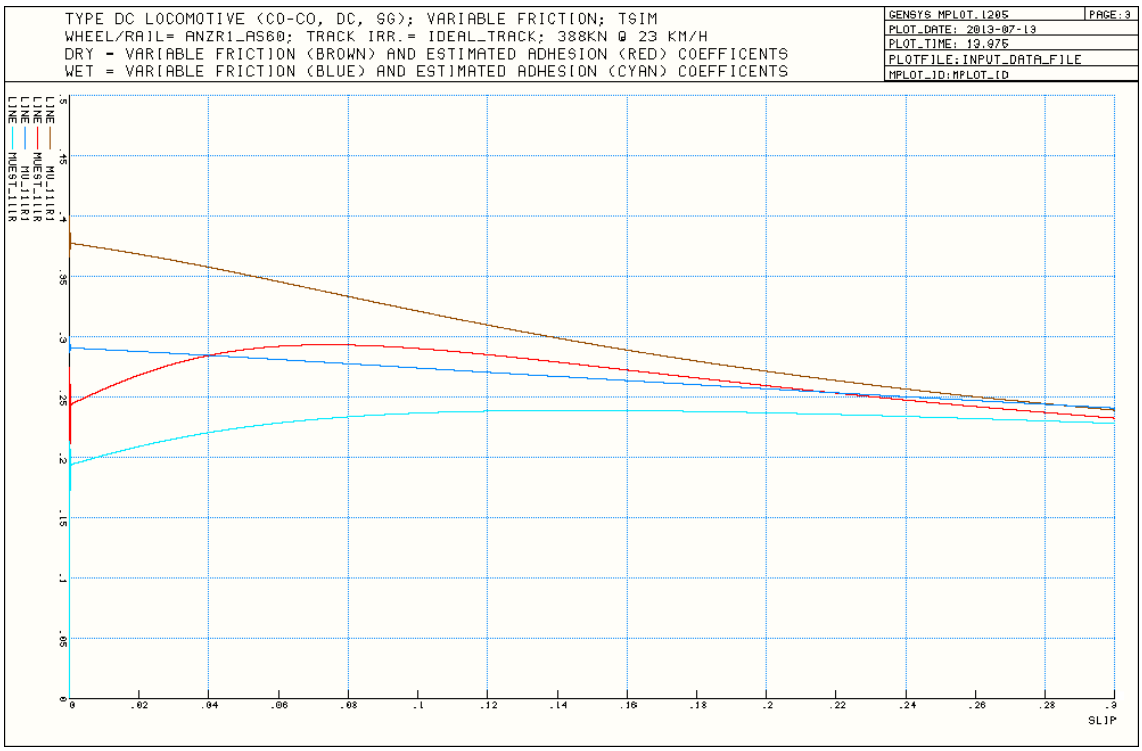

Figure 57: Variable friction and estimated adhesion curves for Type DC

Type AC2 seems to suffer more from initial disturbances than the other models, although they are still minor. This can be attributed to its longer stabilisation time as discussed in Section 4.3.1.5 (Stage 1, Test 5).

Table 18 summarises the maximum estimated adhesion coefficients and the peak slip values at which they occur for each locomotive model. Note that the optimum longitudinal creep values used in locomotive model TC systems, described earlier in Table 8, are close to (but below) the peak slip values obtained for each locomotive model.

Table 18: Maximum estimated adhesion coefficients

Locomotive model	Dry track	Wet track
Type AC1	0.341 @ 7.354% slip	0.261 @ 17.419% slip
Type AC2	0.343 @ 6.129% slip	0.261 @ 15.742 % slip
Type DC	0.293 @ 7.419% slip	0.239 @ 14.710% slip

Type DC produced the lowest adhesion in both dry and wet track conditions, which was expected because it generates the lowest maximum continuous tractive effort at the highest speed and the simplest TC system. Of the AC-drive locomotives, Type AC2 produced higher adhesion levels on dry track than Type AC1, most likely because it generates the highest maximum continuous tractive effort at the lowest speed. However, it reaches peak adhesion for both dry and wet track at lower peak slip levels than Type AC1. This would most likely be due to Type AC2's TE capabilities and simpler per-bogie TC system (as opposed to Type AC1's per-wheelset TC system). There is also a possibility that the Polach contact model parameters used for Type AC2 in this thesis may need to be tweaked in future work.

4.4. Discussion

A proposed LMAP has been developed for use in MBS software, with sample tests having been conducted using various locomotive models in GENSYS. These simulated case studies show that simulation of locomotive dynamic behaviour in MBS software is not only possible, but can identify issues with a locomotive model that can otherwise be overlooked.

Although the main objective of performing case studies on locomotive models throughout work related to this thesis was to evaluate the proposed LMAP's methodology, it had the secondary benefit of improving such models despite only having access to acceptance criteria from researched standards. In this case, performance of the locomotive models tested was generally satisfactory. A few minor issues were noted with Type AC2's semi-steering bogies, where (small) lateral vibrations in the wheelsets took longer to settle than in Type AC1 and DC's rigid bogies. This possibly had flow-on effects with the modelled semi-steering bogies resulting in a lower critical speed and being more susceptible to hunting motions, particularly above Type AC2's design speed (115 km/h). On the other hand, the modelled semi-steering bogies were able to handle vertical vibrations more effectively. Such minor issues are not expected to have a major impact on this thesis' outcomes, although tweaks to the locomotive models are suggested for further analyses.

Future work involves the completion of all tests contained within the proposed LMAP. This will help locate any significant sources of error so that locomotive models, and arguably the LMAP itself, can be properly debugged. The simplified TC models used in this thesis can be adapted for further traction simulations, but it is hoped to use more suitable algorithms for modelling traction and braking forces for completion of all Stage 3 LMAP tests, such as the 'open' GENSYS-Simulink co-simulation interface described by Spiryagin et al. [106].

In order to validate locomotive model results from the LMAP, they will then be compared to experimental data from equivalent real-world locomotives. Physical tests are expected to be similar to those described in RISSB/Australian Standards [21, 125, 126], although some augmentations from the LMAP may be incorporated. Comparing the simulated and experimental locomotive data will enable the accuracy of the locomotive model to be determined and can provide a basis for implementing further adjustments to the multi-body code if required. The primary goal is to obtain a virtual locomotive model that accurately replicates the behaviour of its real-world counterpart. Similar model validation work in an automotive application using experimental data has been covered by Pastorino [164] in his PhD thesis.

Over time, further validated locomotives of different types and wheel arrangements will be created. It is hoped to use validated locomotive models in future to perform a greater share of locomotive acceptance testing, particularly with regard to modifications and new designs. Approaches using validated locomotive models offer scope to reduce the time, cost and effort involved with physical locomotive (type) testing. The use of validated locomotive models may also be used to advantage in the early design phase [110].

5. Angle of attack testing (without traction)

In addition to case studies performed from the proposed Locomotive Model Acceptance Procedure (LMAP) in Section 4, a further supplementary test was carried out to ensure that the modelled rigid and semi-steering bogies performed as expected whilst cornering with no traction forces applied. The procedure is very similar to that in a report by Ahmadian [4] that compared the steering capabilities of rigid and self-steering bogies for heavy freight locomotives modelled in NUCARS. This allows Ahmadian's [4] data to be used as a basis of comparison when determining whether or not cornering performance of the locomotive types modelled for this project are satisfactory.

As mentioned earlier, locomotive types AC1 and DC are fitted with rigid bogies and Type AC2 with semi-steering bogies. These were run in GENSYS with no applied traction forces through the two test tracks defined in [4] so that wheelset Angles of Attack (AoAs) could be compared. Since Type AC2 has semi-steering bogies [8] instead of the self-steering bogies modelled by Ahmadian [4, 165], wheelset AoAs simulated for the semi-steering bogies should lie between those of the rigid and self-steering types. Wheelset AoAs for Types AC1 and DC should also be similar given that their only major difference (except for traction control systems, which are not modelled in this case) is overall mass (Type DC is 2 t lighter than Type AC1).

5.1. Background

Whilst cornering, lateral and yaw wheelset movements in railway vehicles are restricted by their suspension systems. As track curvature (the inverse of curve radius), bogie wheelbase and primary yaw suspension stiffness increase, wheelsets need to produce greater longitudinal forces to align radially with track curvatures [20]. If the forces required to steer a wheelset become greater than what could be transmitted with the available adhesion, where its wheel/rail contact points are at full slip [23, 25, 29], the wheelset cannot completely align to the track curvature. In this case, the wheelset will produce an Angle of Attack (AoA), where the track curve angle and the wheelset yaw angle differ [20]. This is illustrated in Figure 58 [4]. Increasing wheelset

AoAs can worsen wheel/rail wear and, in severe cases, can lead to flanging contact, wheel climb and derailments [4, 20, 88].

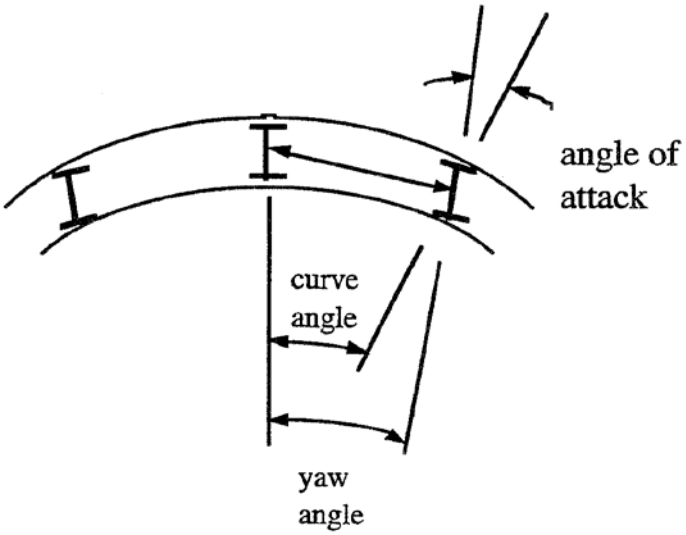

Figure 58: Angle of Attack at wheel/rail interface [4]

5.2. Procedure

Following the procedure in [4], the GENSYS locomotive models were run through two test tracks with curvatures of 7.5 and 10 US degrees, equating to curve radii of 233 and 175 m respectively. Both test tracks had 3" (76.2 mm) of track cant along with the basic geometry detailed in Table 19 [85]. Within entry/exit transitions, both curve radius and cant increased/decreased linearly with track distance.

Table 19: Basic test track geometry [85]

Distance from start		Track section
ft	m	
50	15.24	50' (15.24 m) tangent track
150	45.72	100' (30.48 m) entry transition
1050	320.04	900' (274.32 m) right curve
1150	350.52	100' (30.48 m) exit transition
1250	396.24	100' (30.48 m) tangent track

Locomotive speeds through the test tracks were equal to the balance speed through each curve, calculated using Equation 30 [4].

$$V_b = \sqrt{\frac{C}{6.9 \times 10^{-4} \times R}}$$

Equation 30: Balance speed for US curvatures [4]

Where: V_b = Balance speed (mph)

C = Track cant (inches)

R = Curve radius (US degrees)

For curve radii of 7.5 and 10 US degrees with 3" of track cant, the balance speeds for each curve were 24.077 and 20.851 mph (39.748 and 33.556 km/h) respectively. The test tracks had zero gradient, ideal track (no track irregularities) and new AS60 rail profiles, whilst the locomotives had new ANZR1 wheel profiles. It is not specified in [4] or [85] what wheel/rail profiles were used, but the effective wheel/rail conicities appear to be similar.

As in previous GENSYS time-stepping analyses detailed in Section 4, the 'heun_c' two-step Runge-Kutta solver with step-size control was used with output results written every 10 ms. Since locomotive traction forces are not modelled, it was sufficient to assume a constant coefficient of friction of 0.4 [85] in wheel/rail contact areas with creep forces interpolated from lookup tables generated by FASTSIM [113].

5.3. Simulation results

To allow comparison with the test results presented in Section 6.4, the sign conventions and body naming structure will follow those mentioned earlier in Section 2.2.2 and [2]. Clockwise wheelset and bogie yaw rotations relative to the track will therefore result in positive AoAs (which is the opposite sign convention to that used in [4]). Bogies/bogie frames and axles/wheelsets are numbered in their order of appearance from the leading ends of the locomotive models. For example, Bogie 1 is located at the leading end of the locomotive and rests on Axles 1-3, whereas Bogie 2 is at the trailing end and rests on Axles 4-6.

5.3.1. GENSYS model testing

To begin with, all wheelset and bogie frame AoAs for the GENSYS models will be compared to see if Type AC2's semi-steering bogies show any steering improvement over the rigid-framed Type AC1 and DC models. Simulated AoAs (measured from diagrams) for the 7.5 and 10 US degree (233 and 175 m radii) curves are shown in Figure 59 and Figure 60 respectively. Note that, in all cases, the bogie frame AoAs are close to that of (being slightly below) their corresponding mid-axles.

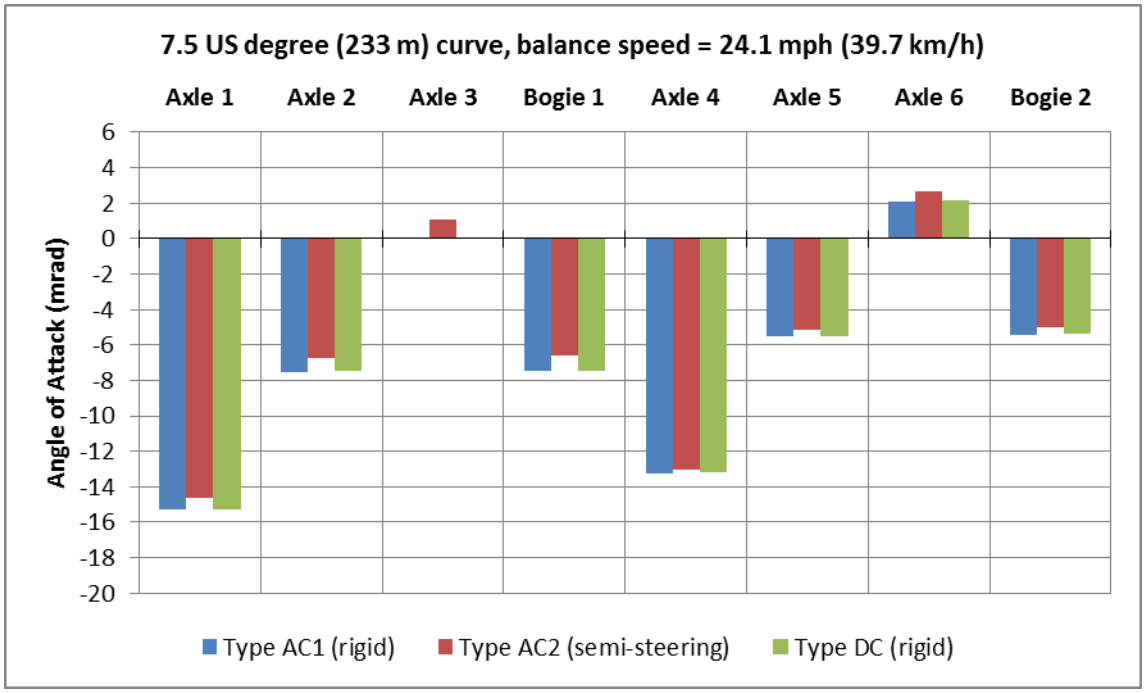

Figure 59: Axle and bogie Angles of Attack in a 7.5 US degree (233 m radius) curve

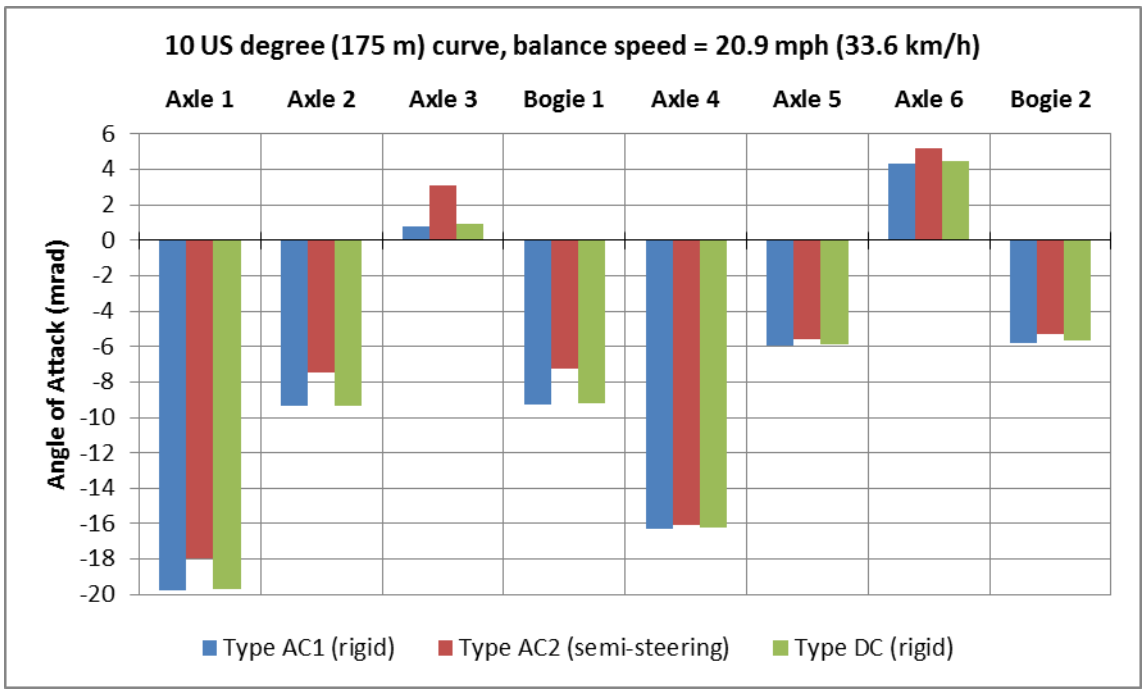

Figure 60: Axle and bogie Angles of Attack in a 10 US degree (175 m radius) curve

As expected, wheelset and bogie AoAs barely differed between the rigid-bogie locomotive types AC1 and DC. Type AC2's semi-steering bogie setup showed improvements in wheelset AoAs for the first two axles in each bogie, although the trailing axles didn't conform to track curvatures as well as the rigid bogies with higher positive AoAs. This was exacerbated, particularly for the lead bogie, as the track radius decreased.

5.3.2. Comparison with NUCARS simulations

To ensure that the cornering performance of the GENSYS models was satisfactory, simulated AoAs were compared to those obtained for the NUCARS models in [4] for which data of only the lead bogie and its wheelsets were published. Wheelset and bogie frame AoAs (measured from diagrams) within the 7.5 and 10 US degree (233 and 175 m) curves are summarised in Table 20 and Table 21, and displayed graphically in Figure 61.

Table 20: Lead bogie Angles of Attack for a 7.5 US degree (233 m radius) curve

Locomotive model	Bogie type	Axle 1	Axle 2	Axle 3	Bogie 1
NUCARS model [4]	Rigid	-13.542	-4.792	0.417	-5.625
Type AC1	Rigid	-15.314	-7.551	0.000	-7.498
Type DC	Rigid	-15.314	-7.498	0.053	-7.446
NUCARS model [4]	Self-steering	0.026	-2.684	-0.684	-1.895
Type AC2	Semi-steering	-14.627	-6.759	1.109	-6.601

Table 21: Lead bogie Angles of Attack for a 10 US degree (175 m radius) curve

Locomotive model	Bogie type	Axle 1	Axle 2	Axle 3	Bogie 1
NUCARS model [4]	Rigid	-18.250	-6.795	1.447	-7.051
Type AC1	Rigid	-19.788	-9.365	0.794	-9.259
Type DC	Rigid	-19.683	-9.312	0.899	-9.206
NUCARS model [4]	Self-steering	0.327	-5.102	-1.333	-3.958
Type AC2	Semi-steering	-17.683	-7.460	3.122	-7.249

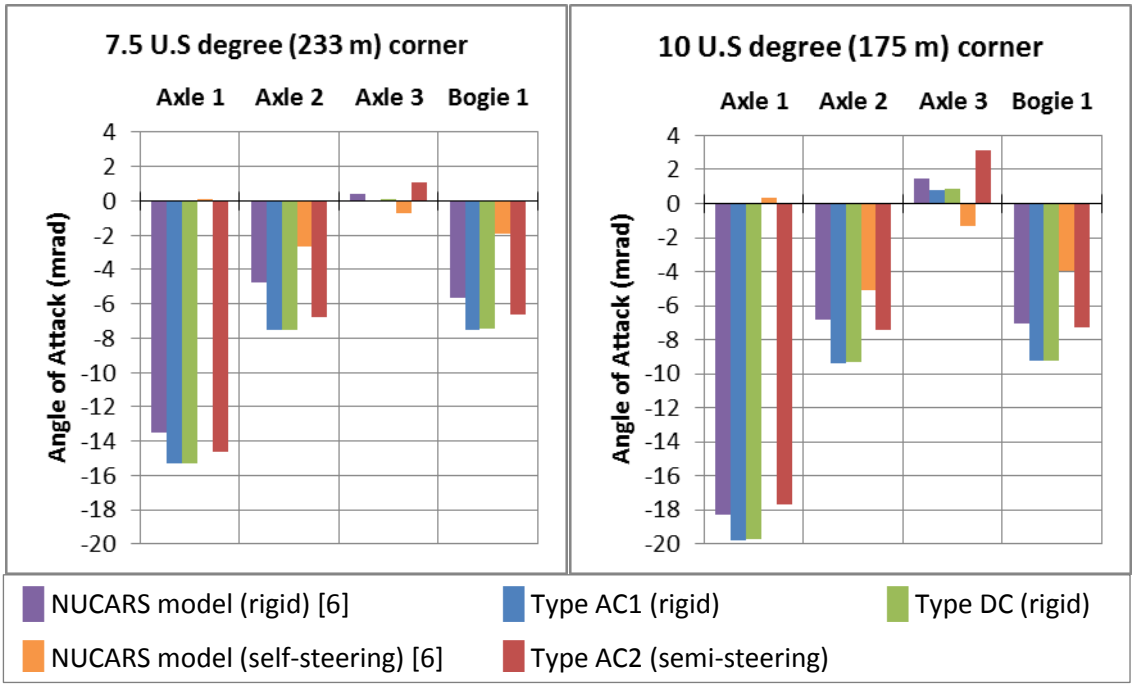

Figure 61: Lead bogie Angles of Attack (both curvatures)

Both the GENSYS (Types AC1 and DC) and NUCARS [4] rigid bogie models produced similar AoAs in both curvatures for the lead bogies. AoAs for Axles 1 and 2 were respectively ~1 and ~2 mrad higher for the GENSYS model, but Axle 3 had AoAs ~0.5 mrad lower (in magnitude).

Type AC2's semi-steering bogies meanwhile showed cornering behaviour much closer to the rigid-bogie models, at least in terms of AoAs, than the NUCARS self-steering bogie model. Real-world tests have shown that semi-steering bogies can only align radially to a minimum curve radius of 400 m [8], so for the sharper curve radii of 233 and 175 m tested, flanging occurs. The self-steering bogies modelled in NUCARS, which adopt steering links between the leading and trailing axles [165], are said to radially steer to curve radii down to 116 m (15 US degrees). In this case, given non-flanging contact, mid-axles produce the highest AoAs as they are constrained longitudinally to the bogie frame as in a rigid bogie design [4].

5.4. Discussion

The locomotive cornering tests in this section were conducted to:

- Show whether or not Type AC2's semi-steering bogies produced lower AoAs than the rigid bogies in Type AC1 and Type DC when no traction forces are applied
- Determine whether or not cornering performance of the GENSYS locomotive models was satisfactory compared to NUCARS models [4] in similar tests
- Provide a basis of comparison for further tests that are under traction discussed in Section 6

Even though Type AC2's semi-steering bogies were in flange contact because of the tight track curvatures tested (radius < 400 m), there were notable AoA improvements in comparison to the rigid bogies in Types AC1 and DC. AoAs for Axles 1 and 2 in the semi-steering bogie showed the biggest improvements, being ~1 mrad lower than in the rigid bogies for the 7.5 US degree (233 m radius) curve and ~2 mrad lower for the 10 US degree (175 m radius) curve. Conversely, trailing axles in the semi-steering bogies steered less effectively, with Axles 3 and 6 having AoAs ~1 mrad higher (in magnitude) in the 10 US degree curve. In the 7.5 US degree curve, Axle 6 gave AoAs ~1 mrad higher, whereas for Axle 3 the increase was ~2 mrad. Despite not having any suitable data for comparison, performance of the semi-steering bogie model is deemed to be satisfactory. Other factors that could have influenced the semi-steering bogie model's steering performance in comparison to the rigid bogie models are a greater bogie

wheelbase (wheelsets are 1900 mm apart instead of 1850 mm) and a bogie pivot point located closer to the mid-wheelsets (310 mm longitudinal distance outwards instead of 450 mm).

AoAs generated by the GENSYS rigid bogie models were close to those of the NUCARS rigid bogie model [4], so their performance is deemed satisfactory. In both 7.5 and 10 US degree (233 and 175 m radii) curvatures, the GENSYS rigid bogies had AoAs ~1.5 mrad higher for Axle 1 and ~2.5 mrad higher for Axle 2. Axle 3 however steered more effectively by ~0.5 mrad in the 7.5 US degree curve and by ~1 mrad when the curvature increased to 10 US degrees. Several factors could be responsible for these small differences, particularly differing wheel-rail profiles and creep-force models, neither of which were specified in [4, 85]. Component dimensions and parameters, particularly the bogie structures, would also have differed between the GENSYS (Australian) and NUCARS (US) locomotive models; compared to Australian heavy-haul freight locomotives, the US equivalents are generally heavier and built to a larger loading gauge.

6. Simulation of locomotive wheel-rail forces when cornering under traction

The vehicle dynamics of railway locomotives has been extensively studied with regard to mechanisms like wheel-rail contact and self-steering bogie designs in multi-body software packages. Since most of this research has been done using purely mechanical locomotive models, there is little information available on modelling locomotives as mechatronic systems with traction (and braking) capabilities. Progress on using results from longitudinal train dynamics simulations as input to multi-body locomotive models for more detailed simulation has also been limited.

To meet the aims stated earlier in this thesis, a methodology was developed to allow the simulation of aggregate locomotive traction forces, requiring locomotives to be modelled as complex systems. The basic methodology [109], presented to the 13th Mini Conference on Vehicle System Dynamics, Identification and Anomalies (VSDIA) in November 2012, involves the simulation of:

- In-train forces using the CRE-LTS [10] longitudinal train dynamics software
- Individual locomotive dynamics in GENSYS using mechatronic locomotive models and input of approximated longitudinal and lateral coupler force components from CRE-LTS

By applying in-train coupler forces from Longitudinal Train Simulation (LTS) to a multi-body locomotive model, with additional input from a Traction Control (TC) system, it is possible to analyse wheel/rail forces in detail for individual locomotives within a train. Since only one locomotive at a time needs to be analysed in the multi-body simulations, the processing time and complexity of simulations is reduced.

A range of 'typical' scenarios relevant to Australian rail freight operations were defined before conducting any simulations, considering a wide range of parameters such as locomotive type, train configuration, test track geometry and rail friction conditions whilst minimising the

number of simulation cases required. The longitudinal train dynamics simulations were performed in a related study by Sun [3] using CRE-LTS, where trains with three locomotives of the same type powering at the head of 55 wagon trains were simulated to traverse a hypothetical uphill test track with a 1:30 gradient and several curves. In both the CRE-LTS and GENSYS simulations, locomotives were travelling at minimum speed (20-23 km/h) whilst exerting their maximum continuous tractive effort. From the CRE-LTS data, approximate distance-dependent expressions for lateral coupler force components within each curve section were defined for use in the GENSYS multi-body locomotive models described in Section 3. This approach allowed locomotive models in the GENSYS simulations to travel through simplified test tracks, each consisting of a right-handed curve with entry/exit transitions and with shorter curve lengths than those in the hypothetical CRE-LTS test track. Data from the GENSYS simulations was then analysed to see what effect locomotive (drive and bogie) types, in-train positions (increasing lateral coupler forces down the length of the locomotive group), curve radii and rail friction conditions (dry and wet rail heads) have on axle forces, wheel/rail contact patch forces and wheel/rail contact patch creepages.

6.1. Methodology

In order to evaluate the effect of lateral coupler forces on locomotives cornering when under traction, a methodology was developed to allow locomotives to be simulated as complex systems. The proposed methodology consists of three inter-linked stages, a flowchart of which is shown in Figure 62 [109].

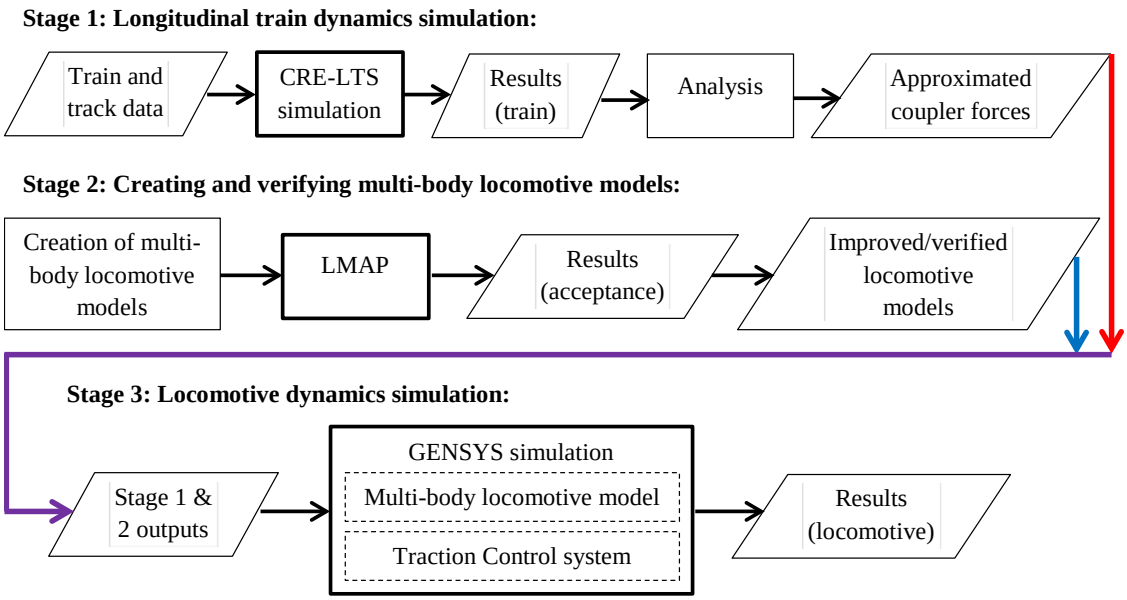

Figure 62: Simulation methodology flowchart [109]

Stage 1 involves the simulation of entire trains using longitudinal train dynamics software in order to provide in-train coupler forces for use in further analyses. In this case, analyses were performed using CRE-LTS in a separate study [3] by CQUniversity as part of the broader CRC for Rail Innovation Project No. R3.119 [1]. From the simulated data, approximate relationships for lateral coupler force versus locomotive distance along track were formed for use in GENSYS multi-body model simulations. Longitudinal coupler forces were assumed to be constant throughout the test track, for reasons explained in Section 1.3.

Stage 2 more-or-less summarises what's already been covered in Sections 3-5. Multi-body locomotive models, based on typical Australian freight locomotives, were tested using a Locomotive Model Acceptance Procedure (LMAP) to identify and mitigate any serious errors present within the model codes. In this thesis, an additional cornering test (Section 5) was also performed and compared to existing published data [4] to verify the models' performance.

Stage 3 involves the tested locomotive models from Stage 2 being run through test tracks with applied approximate lateral coupler forces from Stage 1 to obtain detailed wheel-rail forces whilst cornering under traction for a variety of conditions. In this case, locomotive TC systems were modelled using simplified electronic controls within the GENSYS model codes as detailed in Section 3.1. More complex methods such as co-simulation between GENSYS and

MATLAB/Simulink [106] to model locomotive (electrical and pneumatic) subsystems can also be accommodated by this methodology in further study.

6.1.1. Defining simulation cases

A primary aim of this thesis was to investigate the aggregate effects of locomotive traction forces for a wide variety of scenarios relevant to Australian rail freight practice. This required a multitude of parameters relating to locomotives, trains and track to be taken into account. Understandably, one of the first steps undertaken by CRC Project R3.119 staff was to devise a list of typical 'worst case' scenarios that considered as wide a range of relevant parameters as possible whilst reducing the time and effort required for primary simulations. The simulation cases chosen for this thesis were selected to dovetail with those of the broader project, particularly the CRE-LTS analyses [3].

It was decided that four main independent parameters be assessed in the GENSYS simulations:

- Locomotive model types = 3 (AC1, AC2 and DC)
- In-train locomotive positions = 3 (head, mid and end of locomotive group)
- Curve radii = 4 (240, 300, 400 and 600 m)
- Rail-head friction conditions = 2 (dry and wet)

Therefore, the total number of simulations required was 3 x 3 x 4 x 2 = 72.

With regard to locomotive type, there are two dependent parameters that are expected to noticeably impact locomotive model dynamic behaviour:

- Bogie type:
    - Rigid (Types AC1 and DC)
    - Semi-steering (Type AC2)
- TC systems:
    - Per-wheelset control (Type AC1)
    - Per-bogie control (Type AC2)

- Per-locomotive control (Type DC)

Other dependent simulation parameters are detailed in Section 1.3.

6.2. Approximating lateral coupler forces from CRE-LTS data

Because performing simulations using CRE-LTS is beyond the scope of this thesis, coupler force data was obtained from a related LTS study conducted by Sun [3]. Since coupler forces were supplied from the CRE-LTS analyses in longitudinal and lateral components, it was not necessary to use coupler angling algorithms as in previous research by Simson [99]. This allowed longitudinal and lateral coupler force components to be applied at fixed points on the locomotive models, over the coupler centre lines, as described in Section 3.1.

Instead of using the simulated CRE-LTS coupler force data directly, approximate expressions for longitudinal and lateral coupler forces were created for the GENSYS locomotive models as in previous work [109]. This reduced simulation complexity and allowed curve lengths in test tracks to differ. For example, curve lengths of 1 km were used in the CRE-LTS simulations [3], whereas 200 m was suitable for GENSYS analyses [109]. Approximating coupler forces and reducing test track lengths in the GENSYS locomotive models offered reductions in simulation time without significantly affecting dynamic behaviour.

With three locomotives powering at the head end of the train, the (net) longitudinal coupler force applied to each locomotive equalled one third of the weight of all wagons in its train. A constant value was assumed to be satisfactory because the minor variations of longitudinal coupler force within curves would have been nullified by the simple longitudinal speed control [111, 115] and traction-induced bogie pitch modelling [99] adopted. Lateral coupler forces also had to be assumed equal for all three locomotive types because suitable CRE-LTS data for an Australian DC freight locomotive was unavailable for use in the GENSYS simulations. Because all locomotive types had the same length between coupler centre lines and similar total mass, it was assumed that there would be no significant impact on Type DC's dynamic behaviour when lateral coupler forces from AC locomotives were used. Since Types AC1 and AC2 have similar

continuous tractive effort capabilities, lateral coupler forces wouldn't have varied much between them so it is acceptable to use the same values.

As part of the related LTS study [3], a train consisting of three AC locomotives (similar to Type AC1) at the head of 55 wagons traversing a hypothetical uphill test track was simulated in CRE-LTS, to obtain in-train lateral coupler forces for the locomotive couplers amongst other data. Elevation and curvature of the 40 km long hypothetical uphill test track is described in Figure 63 [3].

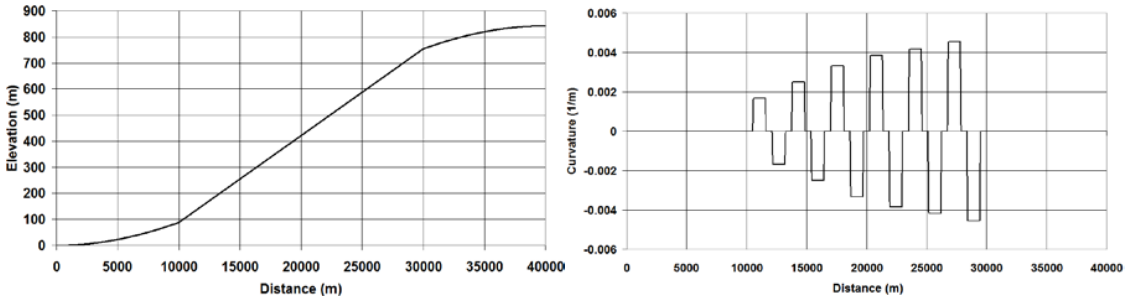

Figure 63: Elevation (left) and curvature (right) of a hypothetical uphill test track [3]

From 10-30 km, the track gradient is a constant 1 in 30 uphill. Within this section are 12 curves, alternating between right and left-handed directions, of 600, 400, 300, 260, 240 and 220 m radii. When going uphill, there is first a 600 m radius right curve, followed by a 600 m radius left curve, a 400 m radius right curve and so on. Each curve is 1 km long, including entry/exit transitions each of 55 m length [3]. Lateral coupler forces obtained in CRE-LTS for locomotives within the 600 m radius left and 400, 300 and 240 m radii right curves are shown in Figure 64 [3].

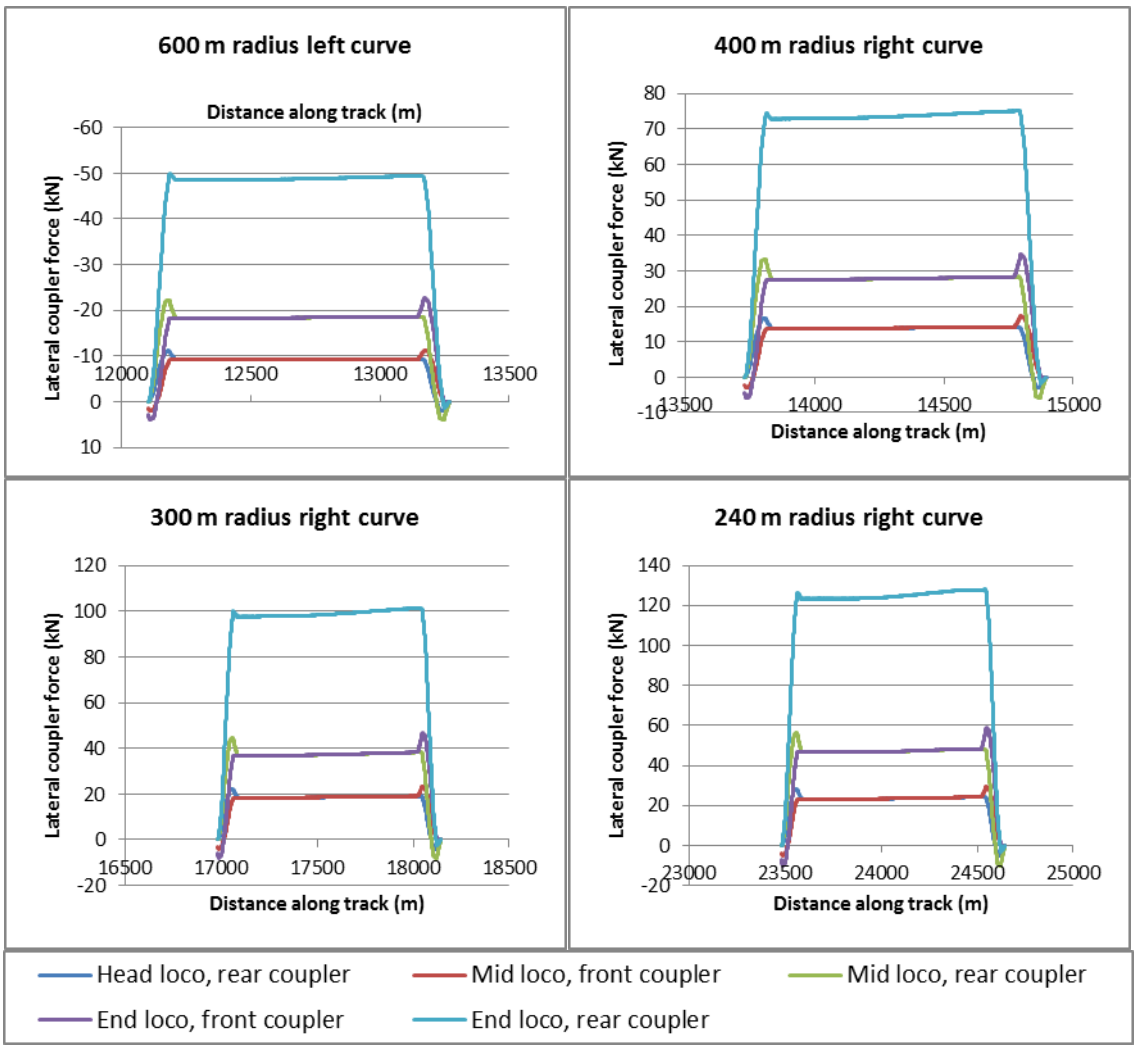

Figure 64: Locomotive lateral coupler forces simulated using CRE-LTS [3]

As expected, lateral coupler force magnitudes within curves increased down the length of the group of locomotives in the train [5] and further increased when curve radius decreased. Those between adjacent locomotives (e.g., rear coupler of the head (leading) loco and front coupler of the middle loco) are equal. The lateral coupler forces between the middle and end (trailing) locomotives are roughly twice those between the head and middle locomotives as shown in the previous VSDIA study [109]. A greater jump is noted between the end locomotive and lead wagon because of the wagon's shorter length between coupling centres. It can be seen in Figure 64 [3] for low train speeds that lateral coupler forces tend to pull vehicles toward the low rail [1]. Since their magnitudes within left and right curves were practically equal, data from right curves was used to approximate lateral coupler forces for the GENSYS simulations except for the 600 m radius curve. In this case, as shown in Figure 65 [3], the train was still slowing down

from 43.6 to 21.4 km/h within the 600 m radius right curve. Lateral coupler forces increased with the decline in train speed and there were some rather large impact forces present between 11-11.2 km. These impact forces could have been the result of run-out behaviour in the train causing draft gear assemblies in the vehicles to lock [5], or possible stability issues with coupler models used in the CRE-LTS analyses.

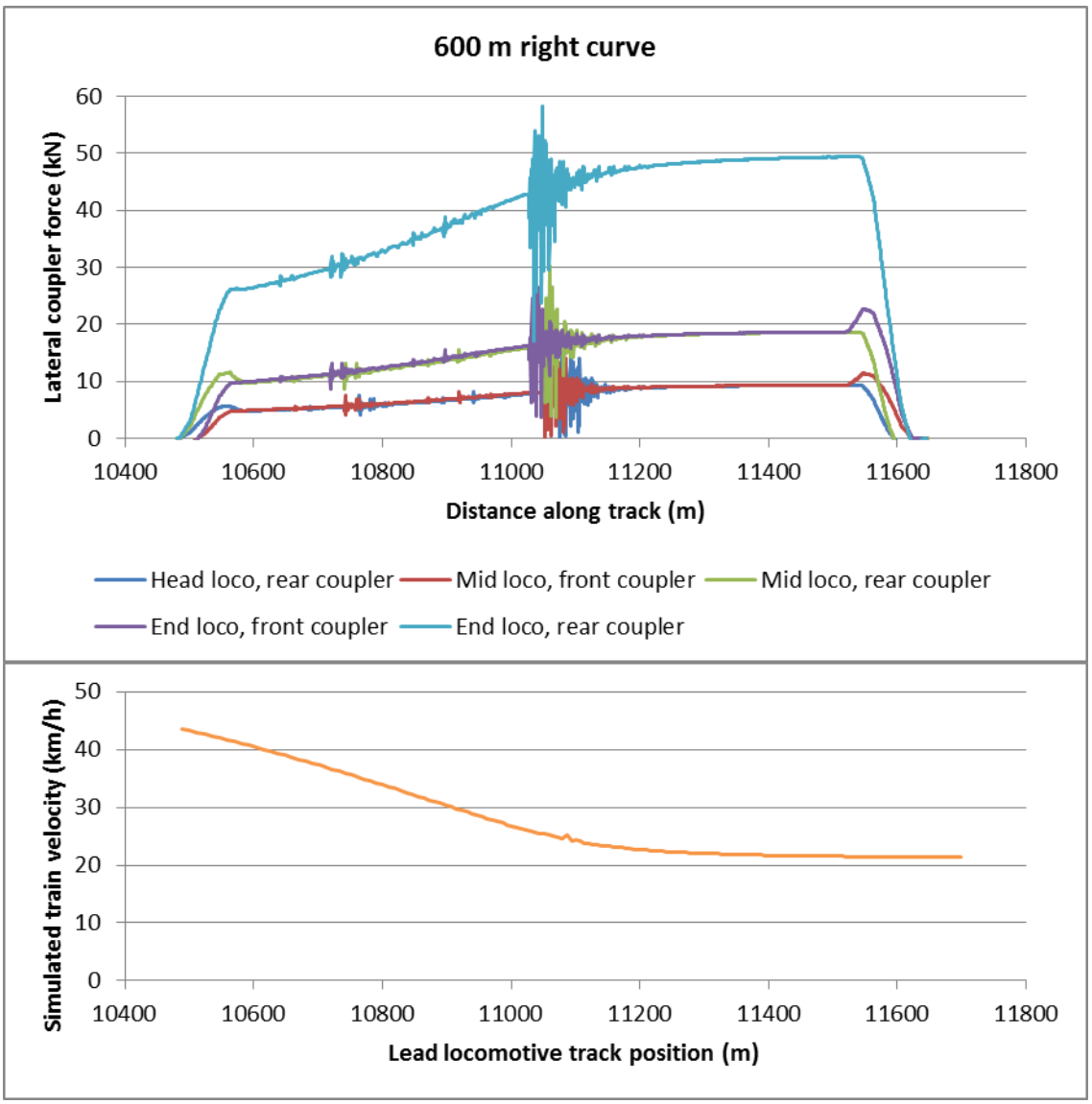

Figure 65: Lateral coupler forces (top) and train velocity (bottom) in 600 m radius right curve [3]

In GENSYS simulations, lateral coupler forces were approximated using the same approach as in the VSDIA paper [109]. They were assumed to be constant in curves and increase/decrease linearly in curve entry/exit transitions. An example is shown in Figure 66 for the middle

locomotive in a 300 m radius right curve. Note how the rear coupler forces are applied 22 m (the length between coupler centre lines) after the front coupler forces.

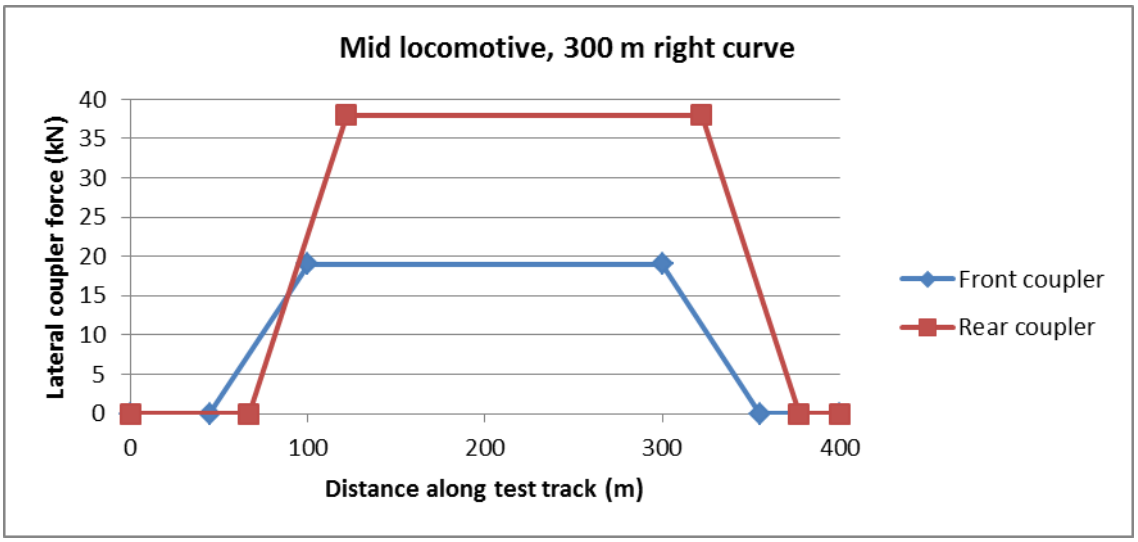

Figure 66: Example of approximated lateral coupler forces in GENSYS test track

Referring to Figure 64 [3], the maximum lateral coupler force magnitudes occurred toward the end of a curve, just before the start of the exit transition. These values, summarised in Table 22 [3], were used in the approximate lateral coupler force formations.

Table 22: Maximum lateral coupler forces in curves [3]

Curve radius (m)	Head loco – mid loco (kN)	Mid loco – end loco (kN)	End loco – head wagon (kN)
600	9.3	18.6	49.5
400	14.1	28.2	75.0
300	19.0	38.0	101.5
240	24.0	48.0	128.0

6.3. Train and test track parameters for GENSYS simulations

Parameters relating to the GENSYS multi-body locomotive models were detailed in Section 3. In summary, the three locomotive types modelled were representative of modern Australian freight locomotives with differing drive, traction control and bogie types. Key parameters relevant to this section are summarised in Table 23.

Table 23: Basic locomotive model parameters

	Type AC1	Type AC2	Type DC
Drive type	AC	AC	DC
Traction control	Per-wheelset (six inverters) [84]	Per-bogie (two inverters) [8]	Per-locomotive (one rectifier)
Bogie type	Rigid	Semi-steering	Rigid
Maximum continuous tractive effort	453 kN @ 21 km/h	500 kN @ 20 km/h [89]	388 kN @ 23 km/h [120, 121]
Total mass	134 t [84]	134 t [8, 89]	132 t [120, 121]

Since the GENSYS simulations were essentially an extension of the CRE-LTS simulations [3], the train configurations were identical whilst test track parameters were similar to those of the hypothetical test track. Trains consisted of three locomotives, all of the same type, powering at the head of 55 wagons. Because the AC locomotives could exert greater maximum continuous tractive effort than the DC locomotives, wagons in trains hauled by AC locomotives were more heavily loaded. This was done in the CRE-LTS analyses [3] to slow trains down so they would be travelling at minimum speed and exerting maximum tractive effort onto the track. Wagon weights for trains hauled by AC and DC locomotives are given in Table 24.

Table 24: Train masses

Locomotive drive type	**AC**	**DC**
Individual loaded wagon mass [3]	80 t	72 t
Total wagon mass (55 wagons)	4400 t	3960 t
Individual locomotive mass	134 t	132 t
Total locomotive mass (3 locos)	402 t	396 t
Total train mass [3]	4802 t	4356 t

The GENSYS locomotive models were run through right curves of 240, 300, 400 and 600 m radii with the basic track geometry given in Table 25. Curve cant was 65 mm [109] for all radii, whilst the track gauge was widened by 8 mm (from 1435 mm) to 1443 mm. Although it is possible to vary gauge widening in GENSYS as with curve cant (with a constant value in curves, linear increases/decreases in curve transitions, and none on straight track), in this case it greatly increased simulation time with a barely noticeable impact on results, so a wider gauge

was used throughout the test tracks. Within entry/exit transitions, both curve radius and cant increased/decreased linearly with track distance.

Table 25: Basic designed track geometry

Distance from start (m):	Track section:	Curve cant (mm):
0	Starting point	0
45	45 m tangent track	0
100	55 m entry transition	65
300	200 m right curve	65
355	55 m exit transition	0
400	45 m tangent track	0

Also evident in Table 25 is the absence of any uphill sections in the test tracks. Even though the VSDIA [109] and CRE-LTS [3] analyses considered uphill curves, it was decided to conduct the tests for this thesis on level track in an effort to reduce simulation time and complexity. Performing uphill analyses would have required an additional vertical transition (and more track length) in the test tracks because the GENSYS locomotive models could only start on level track [109]. It was assumed that the lateral coupler force magnitudes experienced on level track and on a 1:30 uphill gradient were similar.

FRA Class 5 track irregularities, the properties of which are given in Table 26 [166], were superimposed over the test track geometries. As in Sections 4 and 5, new ANZR1 wheel and AS60 rail profiles were used owing to the lack of publically available worn wheel/rail profiles.

Table 26: Properties of generated FRA Class 5 track irregularity data [166]

	Centreline deviation (mm)		Gauge (mm)	Cant (mm)
	Lateral	Vertical		
Max.	10.29513	18.34322	1442.91410	7.91410
Min.	-11.14593	-22.70929	1427.30847	-7.69153

Dry and wet rail head friction conditions were both considered in this analysis. Friction coefficients for the wheel tread / rail head, gauge corner and flanging contact zones have been described in Table 6, with the corresponding Polach contact model parameters for AC and DC locomotive models described in Table 5.

For these simulations, time-stepping analyses were conducted using GENSYS's TSIM calculation program [160]. The 'heun_c' two-step Runge-Kutta solver with step-size control was used with output results written every 10 ms.

6.4. Simulation of axle and wheel/rail contact patch forces in GENSYS

The simulations undertaken for this thesis were essentially an extension of those completed for the VSDIA paper [109], with a larger set of input and output parameters considered. Individual locomotives were run through four test tracks with curve radii of 240, 300, 400 and 600 m and the basic geometry in Table 25. Differing lateral coupler forces were applied to the locomotives depending on their position in the train. The locomotives were running at the minimum speeds and maximum tractive efforts summarised in Table 23 on both dry and wet rail head conditions. Recalling from Section 6.1.1, 72 simulations in total were performed for each combination of:

- Locomotive model types = 3 (AC1, AC2 and DC)
- In-train locomotive positions = 3 (head, mid and end of locomotive group)
- Curve radii = 4 (240, 300, 400 and 600 m)
- Rail-head friction conditions = 2 (dry and wet)

A primary aim of this thesis is to determine how variations of these parameters affect the dynamic behaviour of locomotives in a train when cornering under traction. To achieve this aim, a wide range of output parameters from the simulations was considered, being split into the three categories described below:

- Net wheelset forces:
    - Longitudinal (traction) force X
    - Lateral track-shifting force S
    - Vertical axle load V
    - Approximate per-wheelset adhesion coefficient X/V
    - Sum wheelset L/V ratio
    - Wheelset and bogie Angles of Attack p

- High (left) rail forces:
    - Longitudinal contact patch forces Fx (wheel traction)
    - Lateral contact patch forces Fy (wheel steering)
    - Vertical contact patch forces Fz (wheel load)
    - Approximate per-wheel adhesion coefficient X/V
    - Wheel L/V ratio
    - Longitudinal contact patch creepages nux
    - Lateral contact patch creepages nuy
- Low (right) rail forces: As for high rail forces

More detailed descriptions of, and formulations for, these parameters are contained in Appendix A. The naming scheme for wheelset/axle and bogie (frame) bodies in the locomotive models is the same used in Section 5.3. When presenting these results, average values for in-curve and tangent track sections will be considered; entry and exit transition behaviour is beyond the scope of this thesis. Results for dry and wet rail head friction conditions will be described separately in Sections 6.4.1 and 6.4.2, each split into subsections for the output parameter categories mentioned above.

6.4.1. Results for dry rail head conditions

6.4.1.1. Net wheelset forces

Figure 67 shows the net longitudinal force exerted by each wheelset onto the track, where forces acting forward are considered positive. For each combination of locomotive type (rows) and position (columns), X forces for each wheelset are plotted against track curvature. Note that curvature is the inverse of curve radius; zero curvature denotes tangent track (infinite radius), whilst increasing curvatures denote decreasing curve radii.

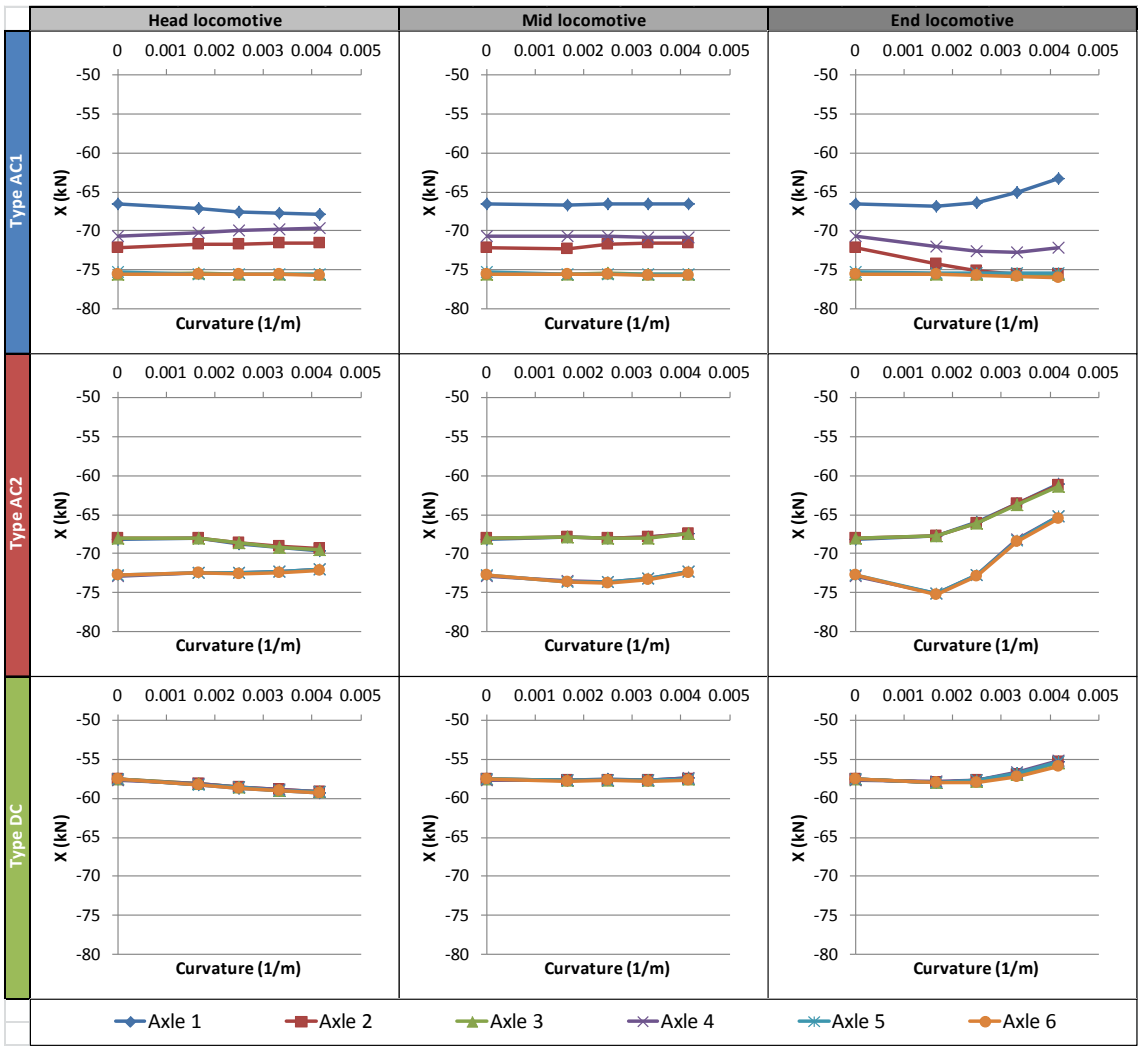

Figure 67: Longitudinal wheelset forces X (dry track)

Looking at Figure 67, it can be seen how each locomotive model's TC system affected the net longitudinal forces exerted by wheelsets, particularly in response to traction-induced car body and bogie (frame) pitching (modelled using the method described in [99]). Since Type DC had one rectifier supplying the same input torque to all traction motors, X forces across all wheelsets were similar. Type AC2's TC system had two inverters, each supplying power to a bogie; hence, as weight shifted to the back of the locomotives when under traction, more X force could be exerted by Bogie 2 (Axles 4-6) than by Bogie 1 (Axles 1-3) before adhesion limits were reached. For Type AC1, which had individual wheelset control, Axles 3, 5 and 6 exerted the most traction force followed by Axles 2, 4 and 1. The variation of X forces across wheelsets with increasing curvature differed across locomotive positions within the train. In general, it appears that less longitudinal force could be exerted by wheelsets as the lateral coupler forces

applied to locomotives increased. This was most apparent with Type DC; X forces increased slightly with increasing curvature for the head locomotive, remained relatively constant for the mid locomotive, and slightly decreased with increasing curvature for the end locomotive. Similar behaviour was noted for Type AC2, particularly Bogie 2, but X forces for the end locomotive were more badly affected by decreasing curve radii. In Type AC1's case, X forces didn't change much with curvature variation for the head locomotive, with the mid locomotive showing very similar behaviour. For the end locomotive, only Axle 1's longitudinal force worsened with increasing curvature; X forces for Axle 4 reached a peak in the 300 m radius curve, whilst the force exerted by Axle 2 converged with Axles 3, 5, and 6 as curvature increased. It appears that Type AC1 was best able to exert high per-wheelset longitudinal forces in conditions with high lateral coupler forces and track curvature (on dry track), followed by Types AC2 and DC.

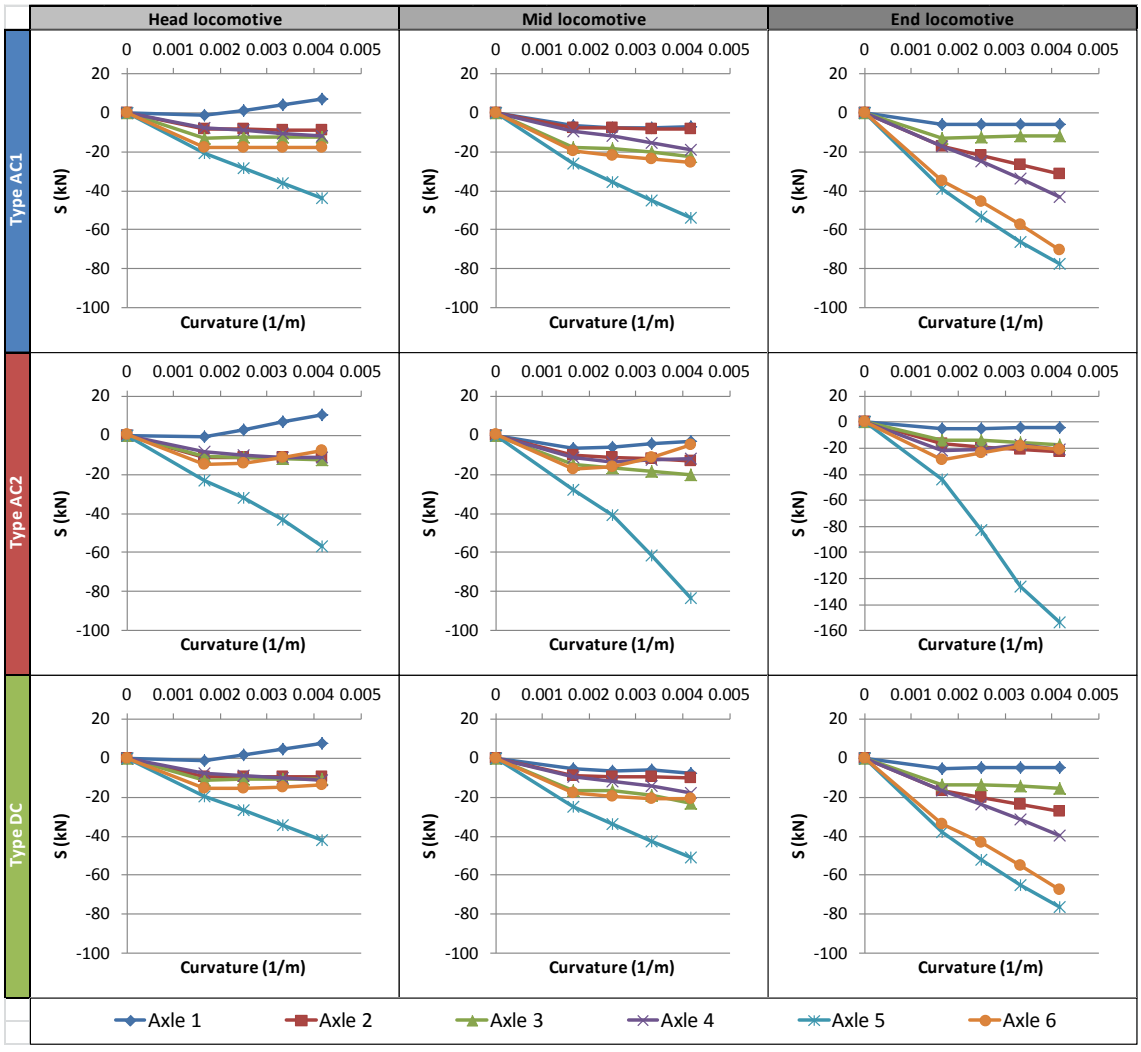

Figure 68: Lateral track-shifting forces S (dry track)

Figure 68 shows lateral track-shifting force S for each wheelset, where track is forced left of the centre line within curves for positive S. Only Axle 1 on the head locomotives seemed to be pushed toward the high (left) rail; in all other cases axles were pulled toward the low (right) rail. This was most likely because of applied lateral coupler forces pulling locomotives toward the low rail as mentioned in [1]. Types AC1 and DC, both fitted with rigid bogies, produced similar track-shifting forces across different curvatures and in-train positions. As both curvature and lateral coupler forces increased, so did the simulated S forces, with axles in Bogie 2 exerting greater S forces than Bogie 1. Type AC2's semi-steering bogies behaved differently in two main areas. First, for all locomotive types and positions, Axle 5 was pushed the hardest toward the low rail, but in Type AC2's case the S forces produced by Axle 5 were far higher than for the rigid bogie locomotive models. For end locomotives in the 240 m radius curve, Axle 5's S forces for Types AC1 and DC were 77.5 kN and 76.0 kN respectively, whereas for Type AC2 it was roughly double that at ~154 kN. This indicates a fault within the modelled semi-steering bogies that will need to be remedied in future work. It is most likely that lateral clearances in the axle boxes, at least for mid-axles, need to be adjusted. Secondly, the remaining axles in Type AC2's semi-steering bogie models appeared to produce lower S forces than for the rigid bogie models in Types AC1 and DC. This is particularly evident for the end locomotives. With the rigid bogie models, S forces for all axles in all curves (thus excluding tangent track sections) lie between 4.67 – 76.0 kN. For Axles 1-4 and 6 in the semi-steering bogie models, this range drops to 1.38 – 22.7 kN.

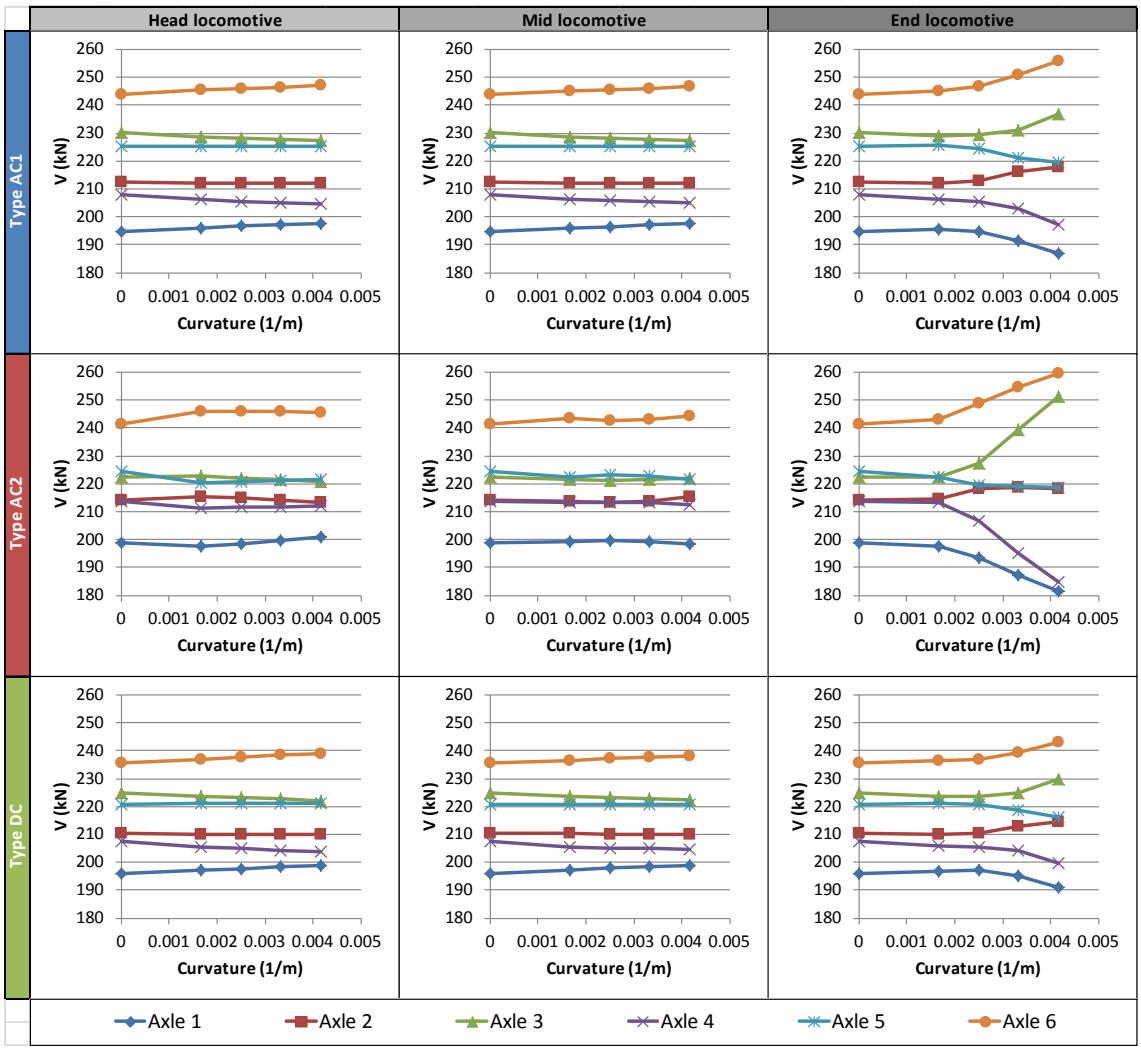

Figure 69: Vertical axle loads V (dry track)

Vertical axle loads V are shown in Figure 69, where downward acting forces are positive. Clearly visible are variations in axle load caused by car-body and bogie frame pitching when the locomotive models were under traction. For all locomotive types, behaviour of the head and mid locomotives was similar, with axle loads not changing much as curvature increased. Curvature had a marked effect on axle loads for the end locomotives, with greater load imbalances experienced within bogies as the radii of curves decreased. V forces for Axles 1 and 4 decreased, those for Axles 3 and 6 increased, whereas Axles 2 and 5 converged in the middle. If the end locomotives were run through curves of lower radii, with corresponding increases in lateral coupler forces, V forces for these axle pairs might have eventually converged as maximum levels of traction-induced bogie frame pitching were reached. This was particularly evident for Type AC2. Behaviour for the rigid bogie Type AC1 and DC locomotives was

similar, with slightly lower axle loads for Type DC because of its lower overall mass. For the head and mid locomotive positions, Type AC2's semi-steering bogies produced axle loads for Axles 2-5 that were closer together (toward a median axle load) than the rigid bogie locomotive models.

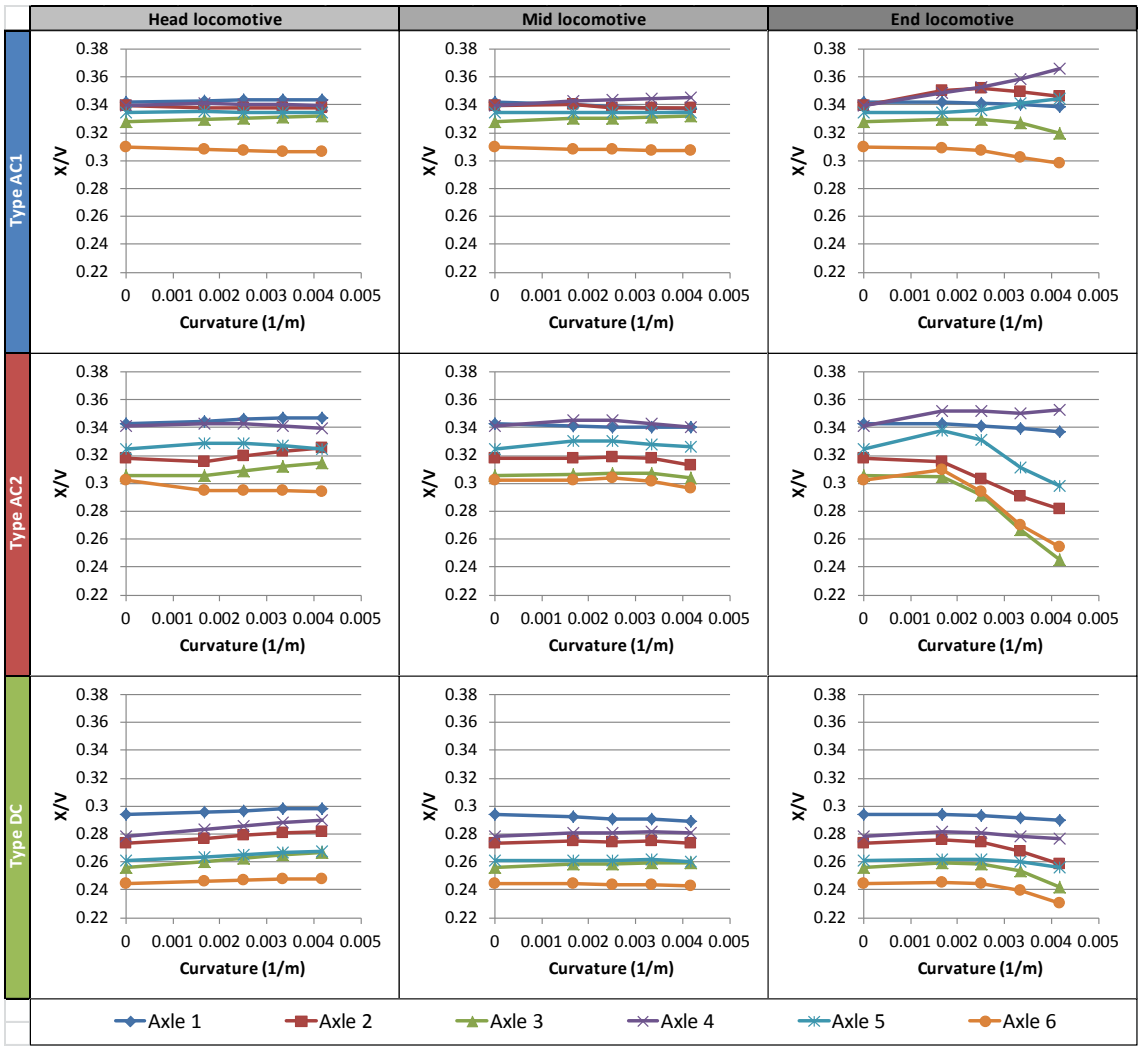

Figure 70: Approximate per-wheelset adhesion coefficients X/V (dry track)

Figure 70 shows the approximate per-wheelset adhesion coefficients obtained by dividing per-wheelset longitudinal X forces by per-wheelset vertical V forces. In general there were small changes in X/V from the head to mid locomotives, with increasing curvature having the greatest effect on end locomotives. Type AC1 appeared to generate the highest adhesion coefficients, particularly in the head and mid locomotive positions where X/V for Axles 1-5 lay between 0.328 – 0.345. For Axle 6 meanwhile, X/V was between 0.306 – 0.310. At the end locomotive position, X/V for Axles 2, 3 and 6 worsened with increasing curvature, remained relatively

constant for Axle 1 and improved for Axles 4 and 5. In the 240 m radius curve, X/V for Type AC1 lay between 0.298 – 0.366. In Type AC2's case, adhesion coefficients varied more between wheelsets, within the range of 0.294 – 0.347 for head and mid locomotives. Adhesion coefficients slightly decreased with increasing curvature for mid locomotives, with a rapid decrease noted for end locomotives, especially Axles 2, 3, 5 and 6. In the 240 m radius curve, X/V for Type AC1 lay between 0.246 – 0.353. For Type DC, X/V slightly improved with increasing curvature for the head locomotive position, mostly remained constant for the mid locomotive and decreased for the end locomotive. Adhesion coefficients were noticeably lower for Type DC in comparison to the AC locomotive models, ranging between 0.230 – 0.299 across all test track curvatures and locomotive positions.

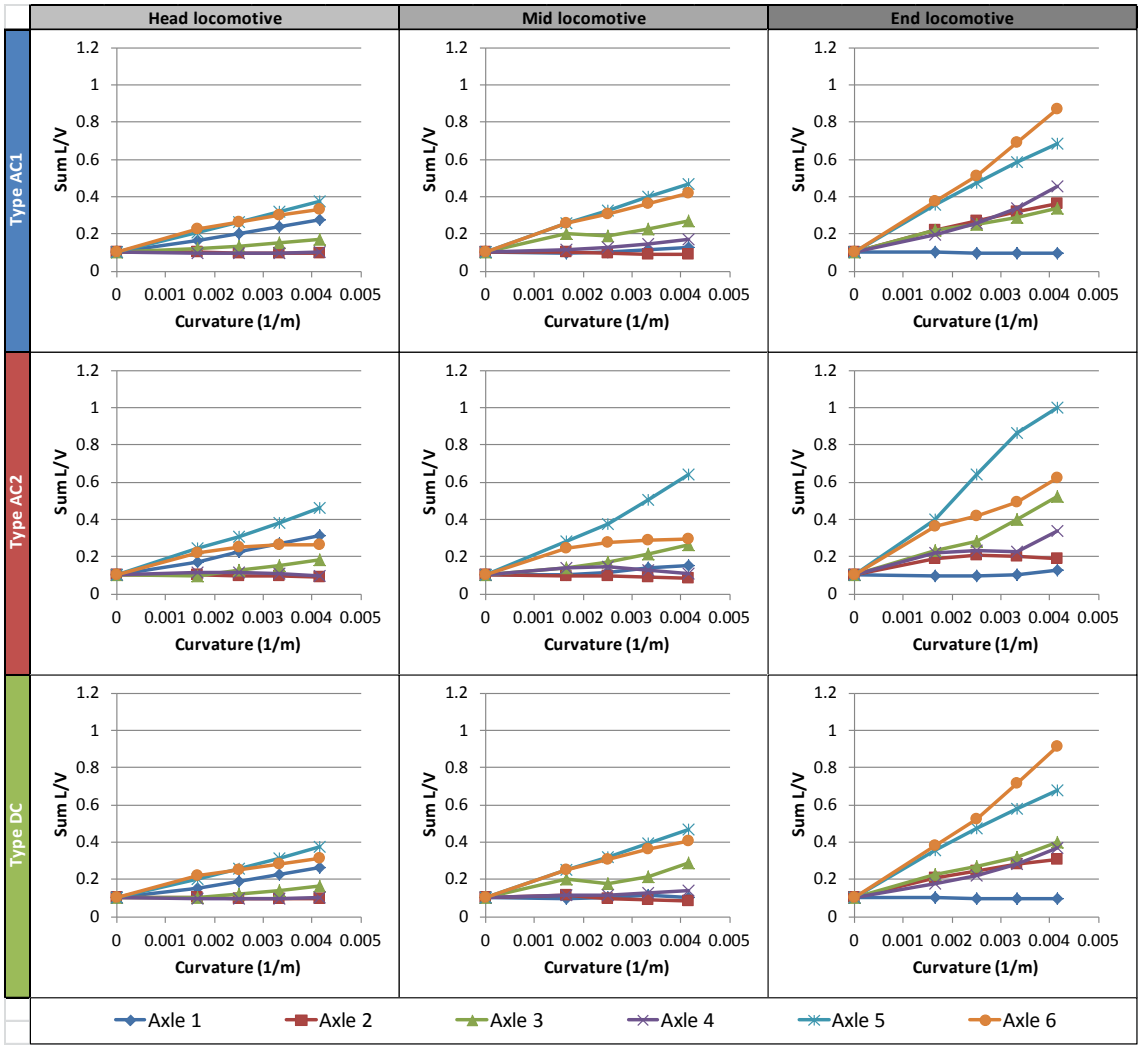

Figure 71: Sum wheelset L/V ratios (dry track)

Simulated sum wheelset L/V ratios are shown in Figure 71, with none equalling or exceeding the limit of 1.5 recommended in AS 7509.1 [21]. Across all locomotive types, sum wheelset L/V ratios typically increased with both curvature and applied lateral coupler forces. Axle 1 appeared to be an exception; as lateral coupler forces increased, L/V changed less with increasing curvature. Sum wheelset L/V ratios for the rigid bogie Types AC1 and DC were similar. The maxima calculated for end locomotives in a 240 m radius curve were 0.874 and 0.915 respectively at Axle 6. For the same locomotive position and test track curvature, Type AC2 reached a maximum of 1.000 at Axle 5. A high L/V (of 0.640) was also noted for Axle 5 in the mid locomotive position, which might be related to the same bogie modelling error that resulted in the high lateral track-shifting forces seen earlier in Figure 68.

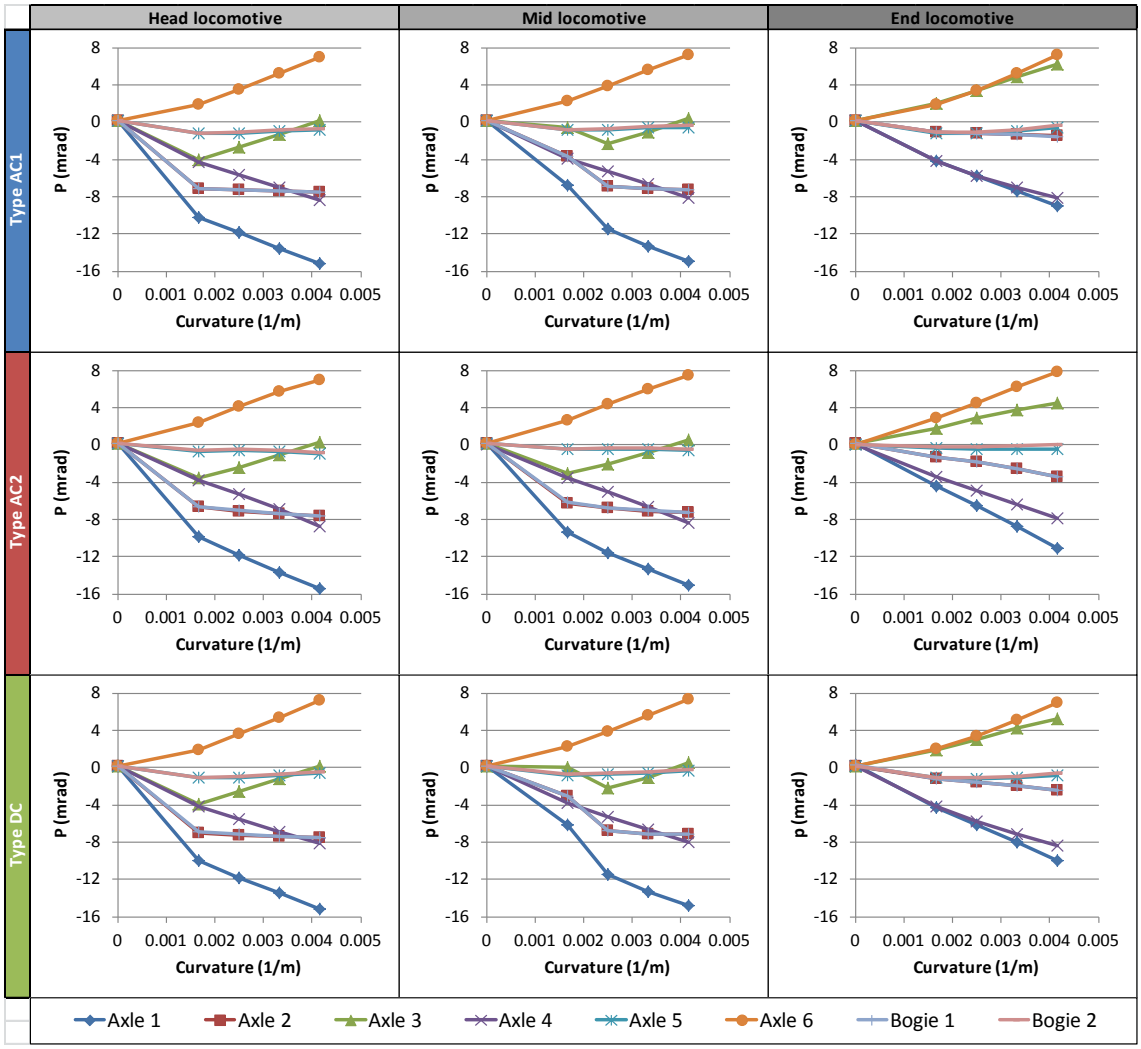

Figure 72: Wheelset and bogie Angles of Attack p (dry track)

Comparing the wheelset and bogie Angles of Attack (AoAs) in Figure 72 and results from the rolling (without traction and applied coupler forces) tests in Section 5, a few similarities can be noticed. In both cases, AoAs worsened as curvature increased, whilst bogie AoAs were close to those of their mid-axles (Axles 2 and 5). For all locomotive types, AoAs for Bogie 2 barely changed with respect to increasing lateral coupler forces down the locomotive groups; only Bogie 1's steering was noticeably affected. Bogie type mainly determined how the locomotive models steered. For the rigid bogie locomotive models Type AC1 and DC, AoAs for head and mid locomotives were similar except for mid locomotives in the 600 m radius curve where AoAs for Axles 1-3 improved ~4 mrad. For end locomotives, Bogie 1 was rotated slightly anticlockwise compared to Bogie 2, improving Axle 3's AoA but worsening those for Axles 1 and 2. The Type AC2 locomotive model showed little difference in AoAs between the head and mid locomotive positions, whilst Bogie 1 was rotated further anticlockwise for the end locomotive position than for the rigid bogie locomotive models.

It was stated in Section 5.4 that results from the AoA tests for rolling locomotives could be used as a basis of comparison for evaluating the effects of applied traction and coupler forces on bogie steering. The 7.5 US degree (233 m radius) curve used in Section 5 is close to the 240 m radius curve used in this set of simulations, so it is most suitable to compare AoAs for those cases. Perhaps the most significant difference between the two tests is locomotive speed; all locomotives travelled at 39.7 km/h (24.1 mph) in the 233 m radius curve, which is almost twice the 20-23 km/h speeds travelled in the 240 m radius curve. The absence of superimposed track irregularities in the 233 m radius curve is of little concern; even if they were applied, the simulated AoAs would still oscillate around a mean value. AoAs for the rolling locomotives tested in Section 5 are compared to those for head, mid and end powering locomotives in the Section 1 tests from Figure 73 through to Figure 75.

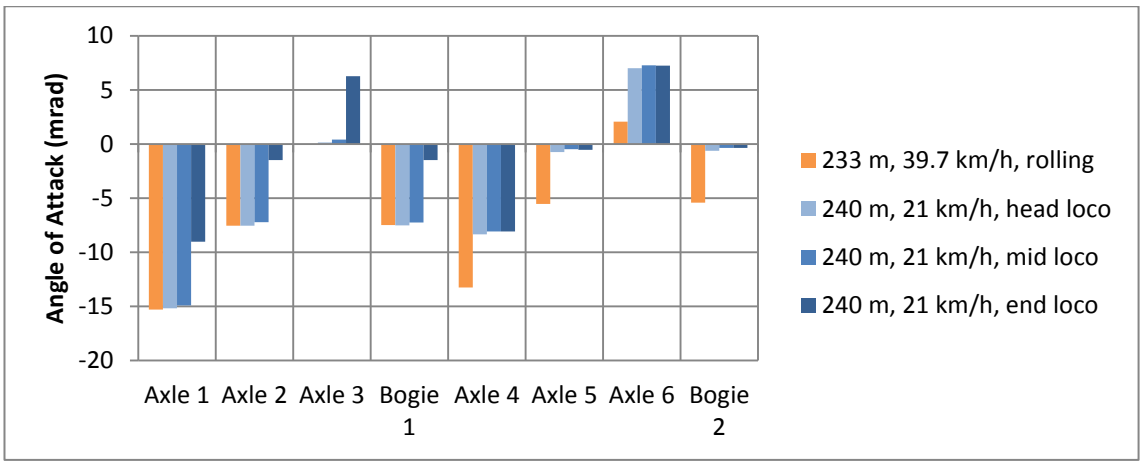

Figure 73: AoA comparison – Type AC1

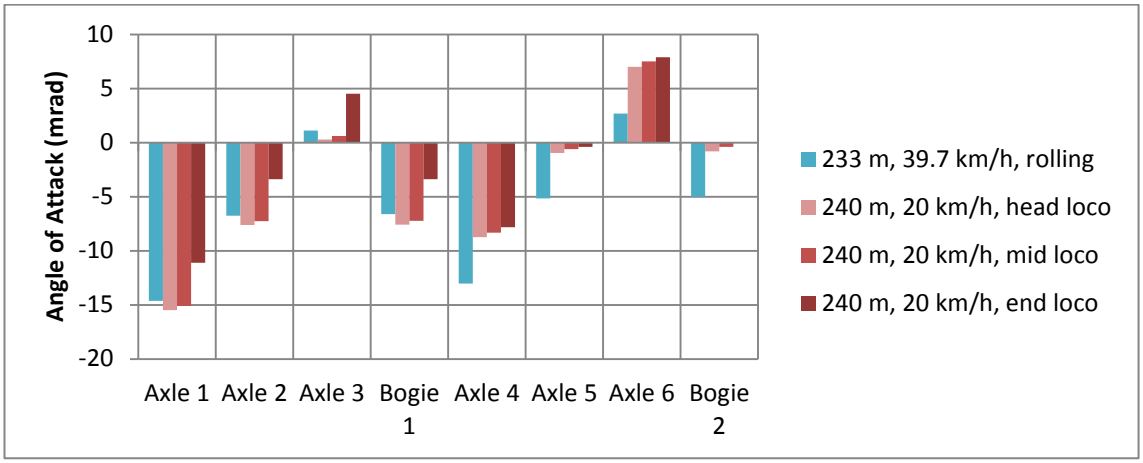

Figure 74: AoA comparison – Type AC2

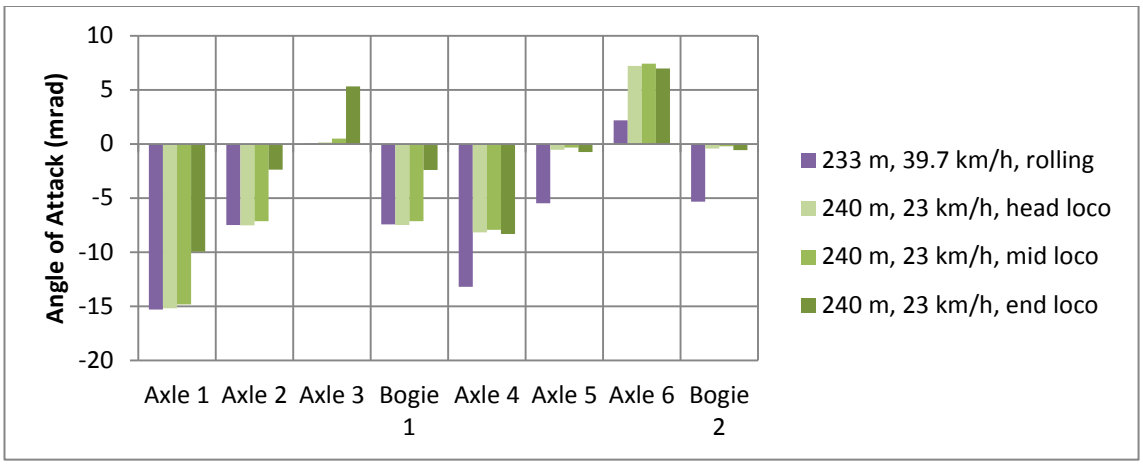

Figure 75: AoA comparison – Type DC

For all locomotive types, AoAs for Bogie 1, including Axles 1-3, across rolling and powering locomotives were similar except for the end powering locomotives. In that case, Bogie 1 was rotated further clockwise by ~6 mrad for Type AC1, ~4 mrad for Type AC2 and ~ 5 mrad for Type DC. This resulted in AoAs improving for Axles 1-2, but worsening for Axle 3. For Bogie 2, AoAs across powering locomotives were similar. For rolling locomotives, Bogie 2 was rotated further anticlockwise by 4-5 mrad for Type AC2 and 5-6 mrad for Types AC1 and DC. In this case AoAs worsened for Axles 4-5 and improved for Axle 6.

6.4.1.2. High (left) rail forces

When analysing contact patch forces for high rail wheels, two-point contact was found to occur within curves for the first axle in the head and mid locomotive positions. In these cases there was contact between the wheel tread / rail head (contact patch 1 / cp1) and wheel/rail gauge corner (contact patch 2 / cp2). Two-point contact at Axle 1 occurred within all curves for head locomotives, whereas only the Type AC2 mid locomotive experienced two-point contact in the 600 m radius curve. Following on from the analysis of lateral track-shifting forces in Section 6.4.1.1 (see Figure 68), these look to be the only cases where wheelsets are being pushed toward the high rail. In most cases, wheelsets were pulled toward the low rail because of high applied lateral coupler forces and low train speeds [1].

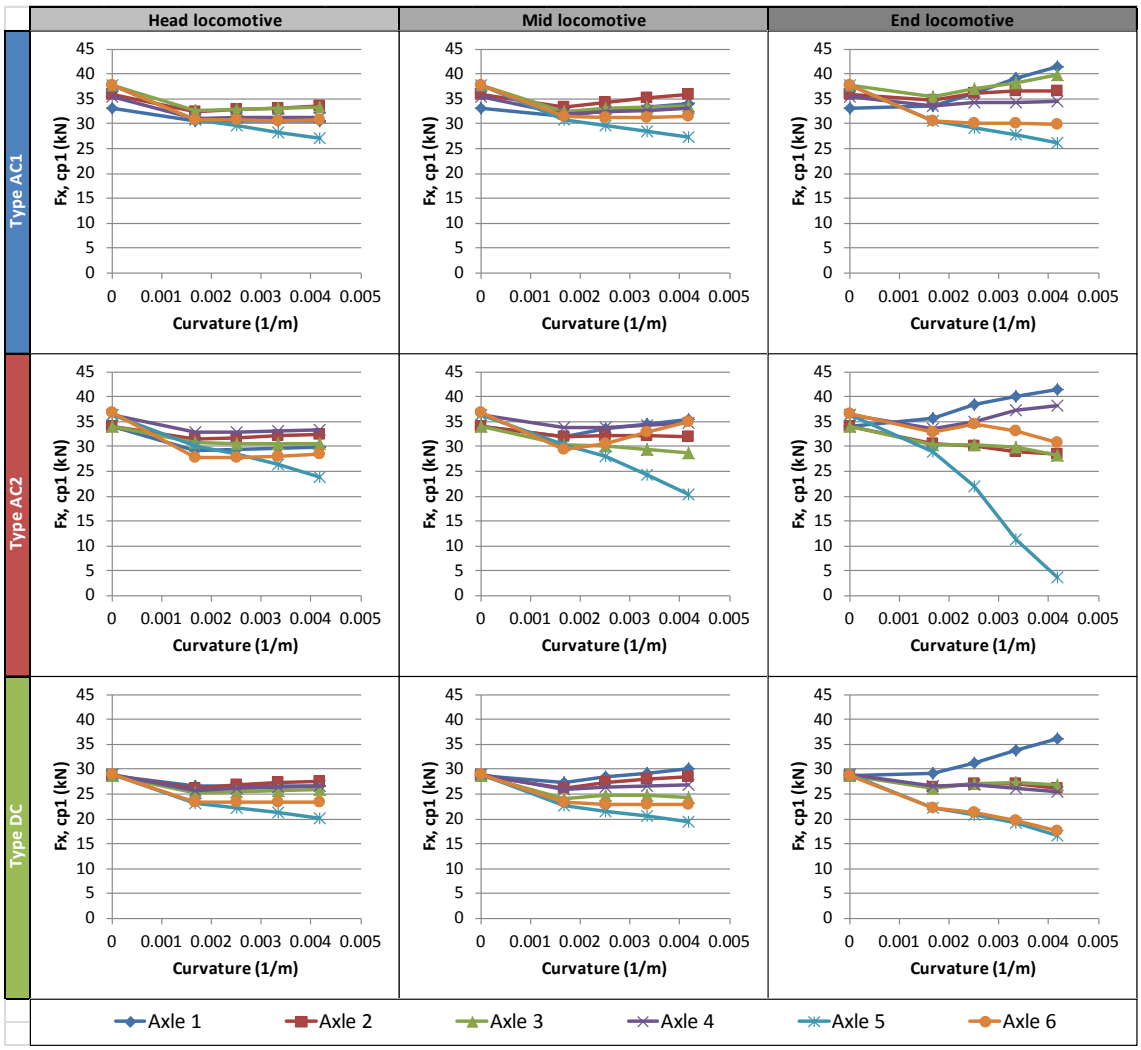

Figure 76: Rail head contact patch longitudinal forces Fx, cp1 (high rail, dry track)

Figure 76 shows the simulated longitudinal contact patch forces Fx, cp1 within rail head contact patches, where forward acting forces are positive. Unlike the net wheelset forces described earlier in Section 6.4.1.1, this section concerns reaction forces generated by the (high) rail that act in the opposite direction. There was generally a drop in Fx, cp1 from tangent track to 600 m radius curves, then longitudinal forces amongst each wheel's rail head contact patch diverged further as curvature continued to increase. High (left) rail wheels in Bogie 1 tended to exert more Fx, cp1 in curves than did Bogie 2's wheels, which was the opposite of the trend evident for the left side wheels on tangent track (zero curvature). As lateral coupler forces increased, Fx, cp1 for Axle 1's high rail wheel improved the most with increasing curvature, whereas the opposite was noted for Axle 5. For Type AC2, Axle 5's Fx, cp1 dropped severely as both curvature and lateral coupler forces increased. This was particularly evident for the end

locomotive position, where Fx, cp1 was only 3.65 kN in the 240 m radius curve. Axle 6 in the end locomotive appeared to be impacted by Axle 5's performance (most likely because of a bogie model fault) as Fx, cp1 dropped for the high rail wheel when curvature tightened below 400 m radius.

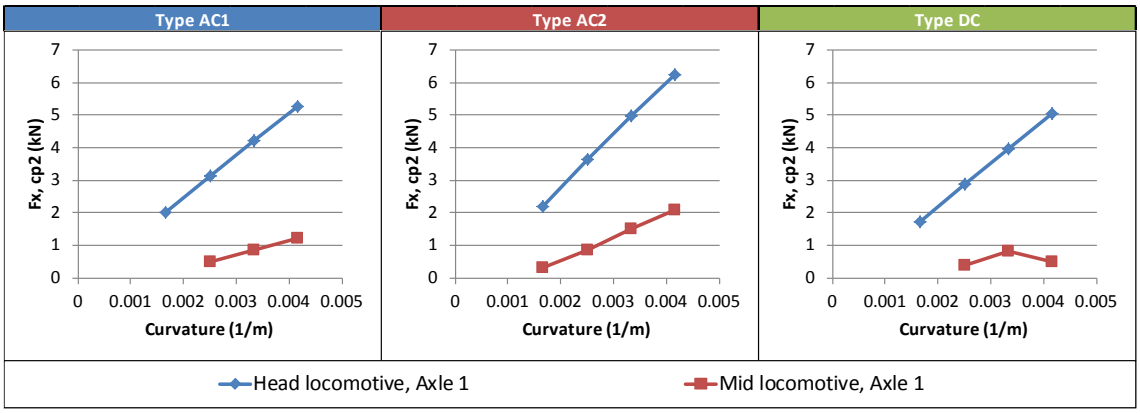

Figure 77: Gauge corner contact patch longitudinal forces Fx, cp2 (high rail, dry track)

Magnitudes of the longitudinal forces in gauge corner contact patches, denoted by Fx, cp2 and plotted in Figure 77, were low in comparison to the Fx, cp1 forces described earlier (in Figure 76). As lateral coupler forces increased from the head to mid locomotive positions, Fx, cp2 was considerably reduced, whereas no two-point contact occurred for the end locomotive position. In other words, increasing lateral coupler forces pulled Axle 1 further away from the high rail. Increases in curvature, however, generally resulted in an increase of Fx, cp2 forces, indicating that Axle 1 was pushed harder toward the high rail as curvature increased. An exception occurred for the Type DC mid locomotive where, instead of continually increasing with curvature, Fx, cp2 hit a peak in the 300 m radius curve and decreased in the 240 m radius curve. As will be shown later, similar behaviour also occurred when analysing lateral (Fy, cp2) and vertical (Fz, cp2) forces in high rail gauge corner contact zones. Aside from this, the rigid bogie locomotive models produced similar Fx, cp2 forces, whilst those for Type AC2 (semi-steering bogie) were higher.

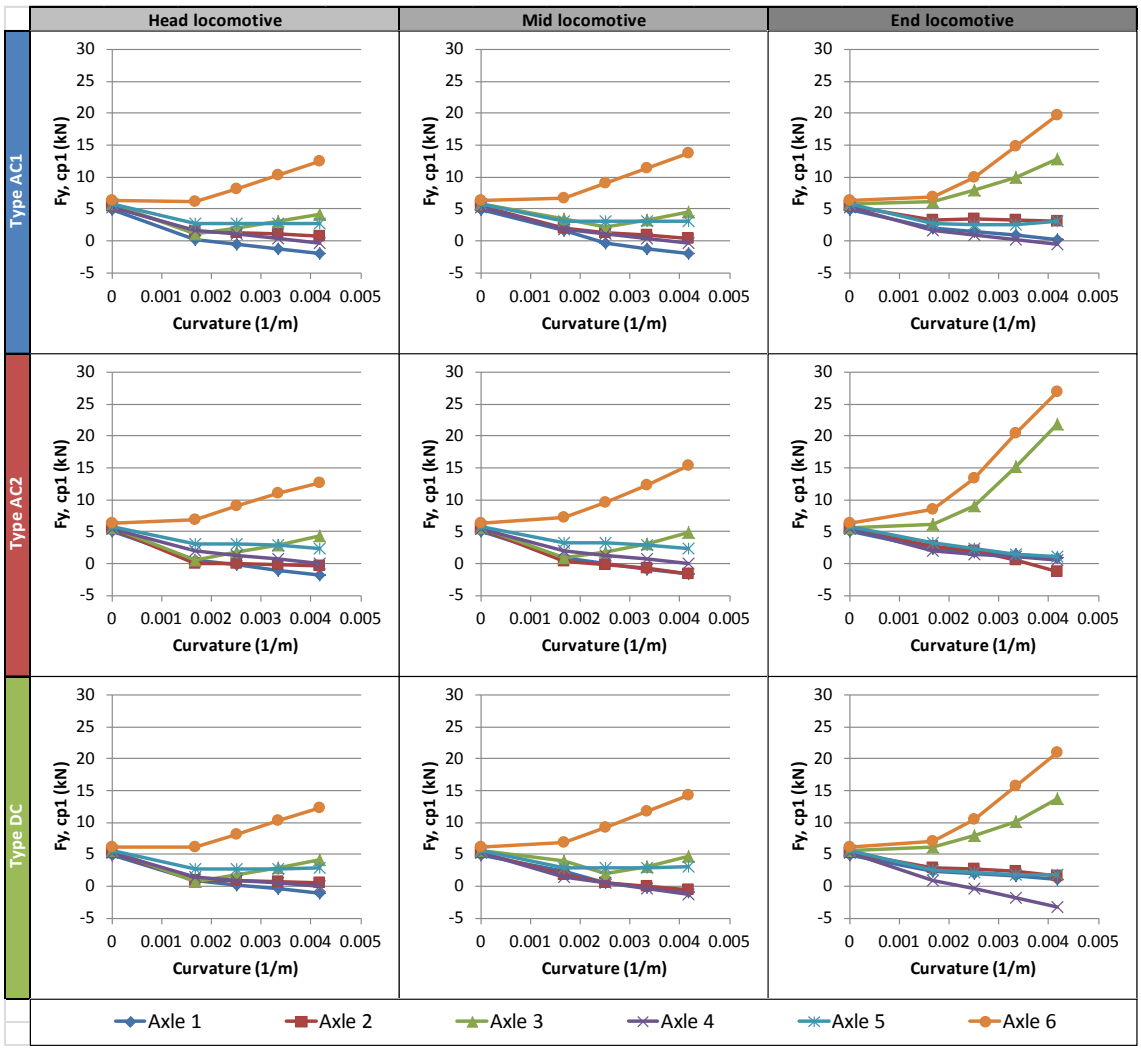

Figure 78: Rail head contact patch lateral forces Fy, cp1 (high rail, dry track)

Simulated lateral forces Fy, cp1 for rail head contact patches are shown in Figure 78, where right acting forces are positive. All locomotive types behaved similarly in the head and mid locomotive positions, with only significant changes in Fy, cp1 noted for end locomotives. For head and mid locomotives, Fy, cp1 for Axles 1-5 within curves were lower than for tangent track. Taking the gauge corner contact patch lateral forces Fy, cp2 in Figure 79 into account, it seems that Axles 2-5 were being pulled away from the high rail within curves. Axle 6 meanwhile was being pushed toward the high rail in curves, with Fy, cp1 increasing in response to both applied lateral coupler forces and curvature. For end locomotives, Axle 3 was forced almost as far onto the high rail in curves as Axle 6, especially for Type AC2. Fy, cp1 forces at Axles 3 and 6 were highest for Type AC2, followed by Type DC and AC1.

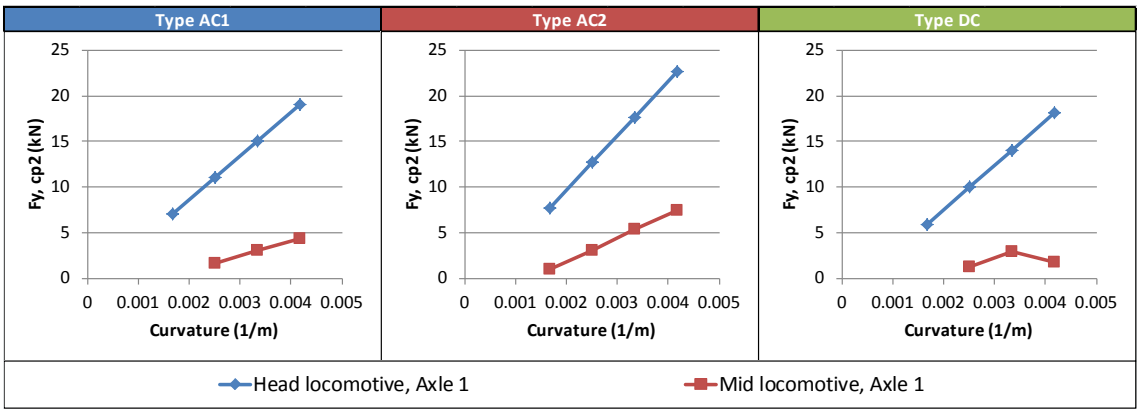

Figure 79: Gauge corner contact patch lateral forces Fy, cp2 (high rail, dry track)

Figure 79 shows Fy, cp2 for gauge corner contact patches, with similar magnitudes to the Fy, cp1 forces described earlier in Figure 78. Axle 1 was pushed hardest toward the high rail when there were low radii curves and low lateral coupler forces. The distribution of Fy, cp2 across curvature, locomotive type and locomotive position was similar to that of Fx, cp2 (Figure 77).

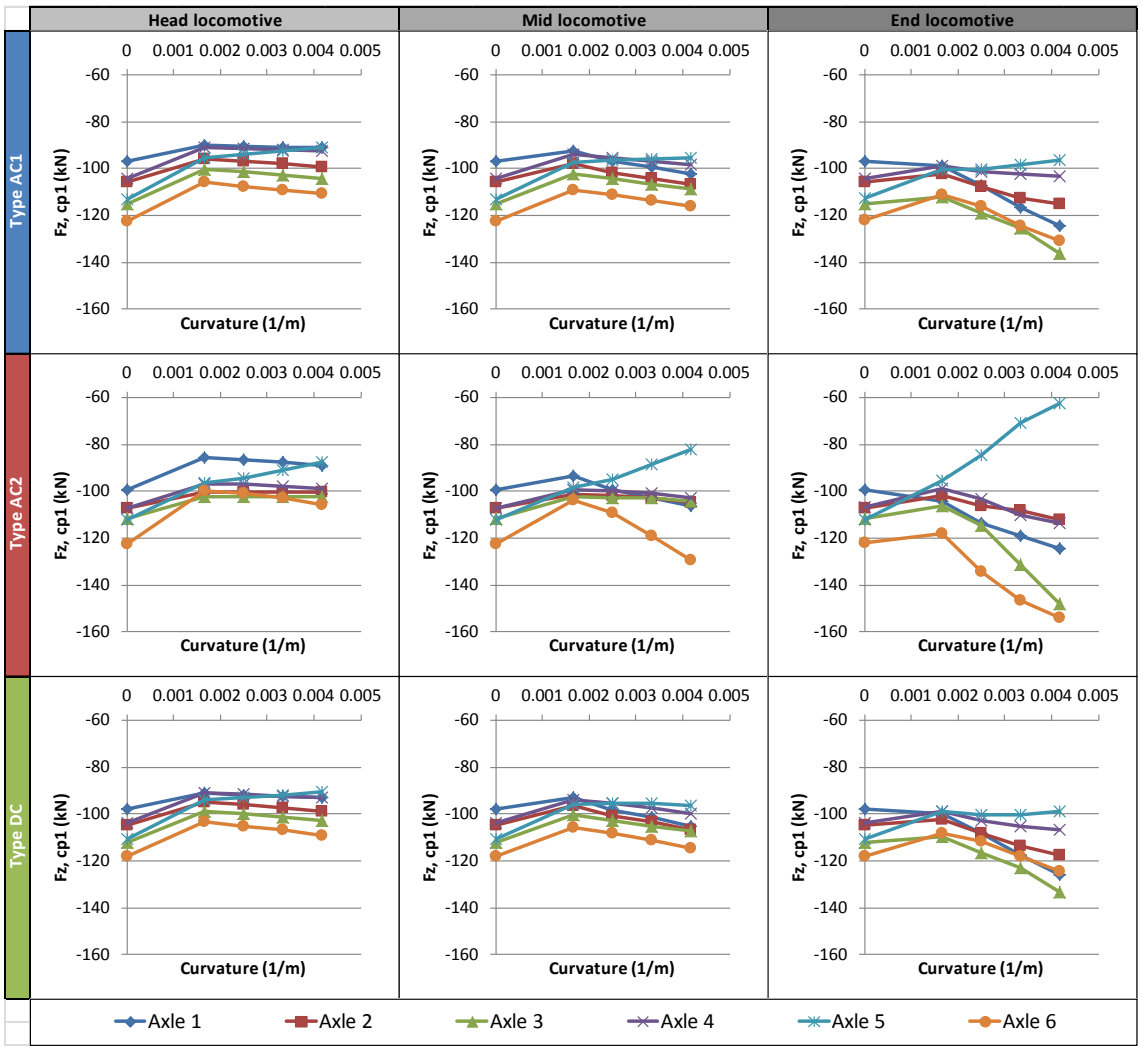

Figure 80: Rail head contact patch vertical forces Fz, cp1 (high rail, dry track)

Figure 80 shows vertical forces Fz, cp1 for rail head contact patches, where downward acting forces are positive. Fz, cp1 generally seemed to drop across high rail wheels from tangent track to the 600 m radius curve, then increased as curvature increased, with increasing lateral coupler forces exacerbating the problem. The rigid bogie Type AC1 and DC models behaved similarly, where Fz, cp1 for high rail wheels on Axles 4-5 were the most stable in response to curvature and coupler load variations. Type AC2's behaviour differed markedly, particularly with dropping vertical load on Axle 5's wheel as lateral coupler forces and curvature increased. This appears to have impacted Fz, cp1 for Axle 6's high rail wheel, which may have increased in response to Axle 5's high unloading.

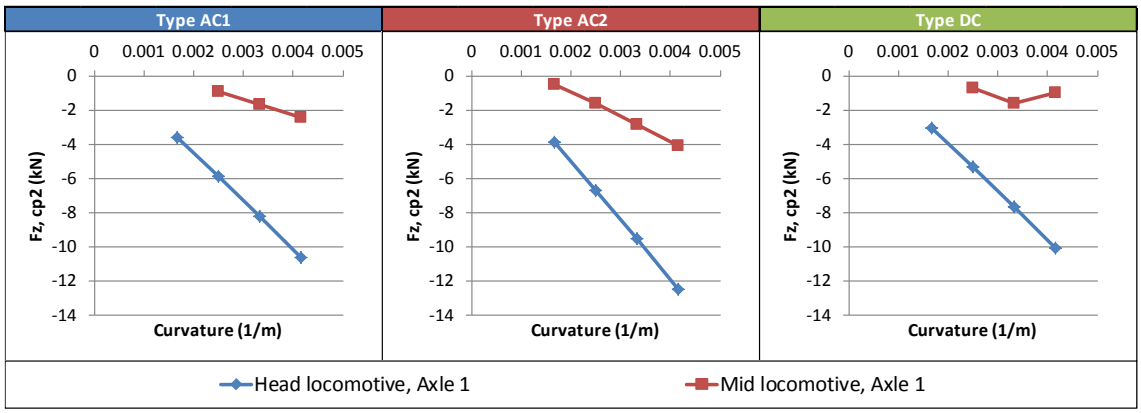

Figure 81: Gauge corner contact patch vertical forces Fz, cp2 (high rail, dry track)

Vertical forces Fz, cp2 for gauge corner contact patches are shown in Figure 81. These forces were small compared to Fz, cp1 for Axle 1, whilst overall behaviour was similar to Fx, cp2 (Figure 77) and Fy, cp2 (Figure 79).

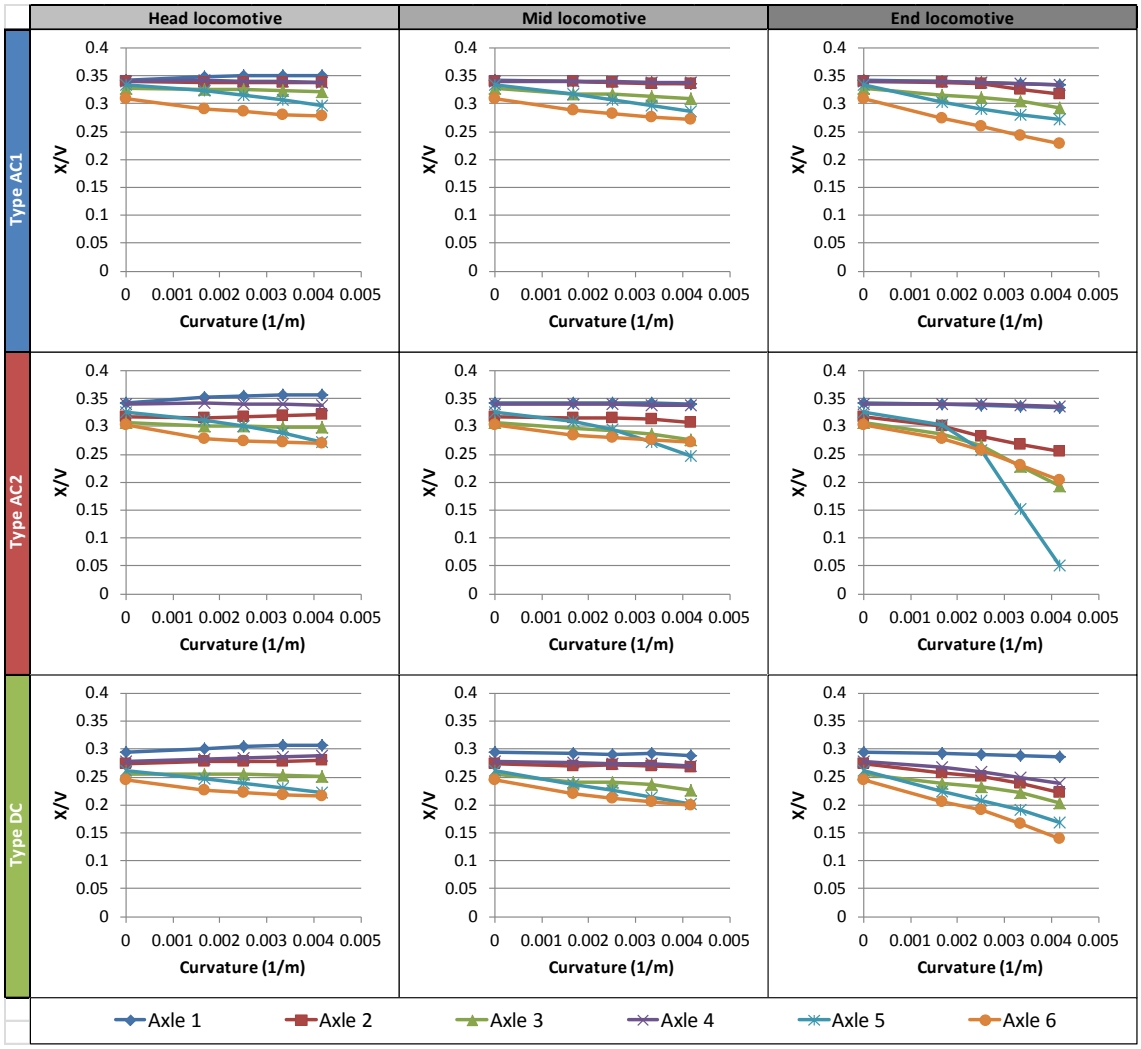

Figure 82: Approximate wheel adhesion coefficients X/V (high rail, dry track)

Approximate adhesion coefficients X/V for high rail wheels are plotted in Figure 82, where behaviour across all locomotive types was similar. As lateral coupler forces increased, X/V across high rail wheels decreased further with increasing curvature. As for the per-wheelset adhesion coefficients (Figure 70), Type AC1 produced the highest X/V coefficients for high rail wheels and Type DC the lowest. Problems with Axle 5 for Type AC2 are visible, where X/V dropped to a minimum of 0.0508 for the end locomotive in the 240 m radius curve. It appears that high unloading occurred for Axle 5's high rail wheel under conditions of high lateral coupler forces and curvatures, which is most likely a symptom of Axle 5 being forced toward the low rail in these conditions

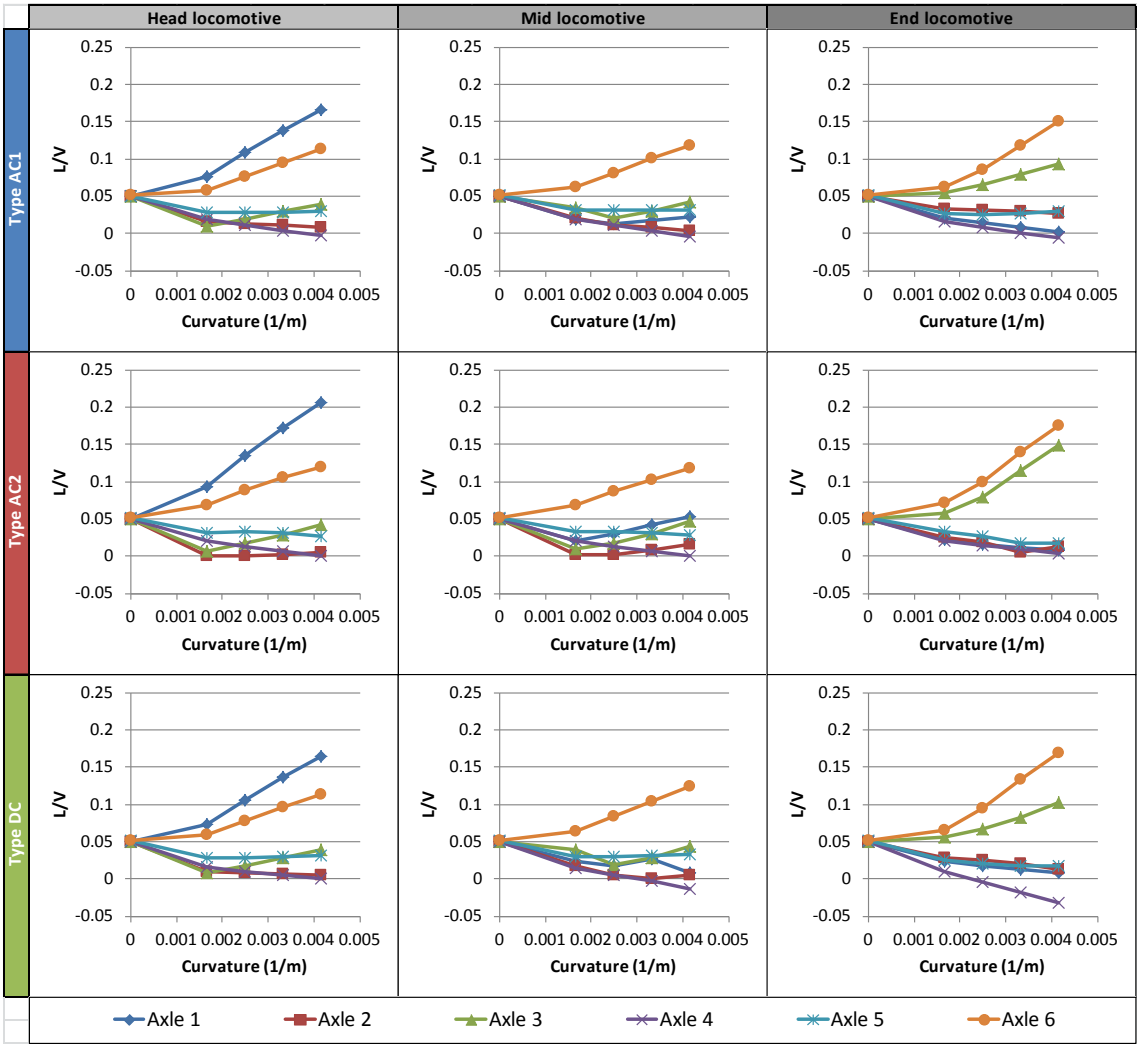

Figure 83: Wheel L/V ratios (high rail, dry track)

L/V ratios for high rail wheels, as shown in Figure 83, had a similar distribution with respect to curvature and locomotive position as the Fy, cp1 forces summarised earlier in Figure 78. The

key difference between the two parameters was Axle 1's performance for head and mid locomotives, noting that lateral and vertical forces for all contact patches are considered in the wheel L/V ratio (as described in Appendix A). This resulted in the high rail wheel on Axle 1 reaching relatively high L/V ratios for head locomotives, indicating that Axle 1 was being pushed toward the high rail. In some cases, L/V ratios for high rail wheels were negative, particularly for Axle 4 in the Type DC end locomotive for curve radii lower than 600 m. This means that the wheels were being pulled toward the centre of the curve, rather than being pushed away from it (and getting into gauge corner and/or flanging contact) as for positive L/V ratios.

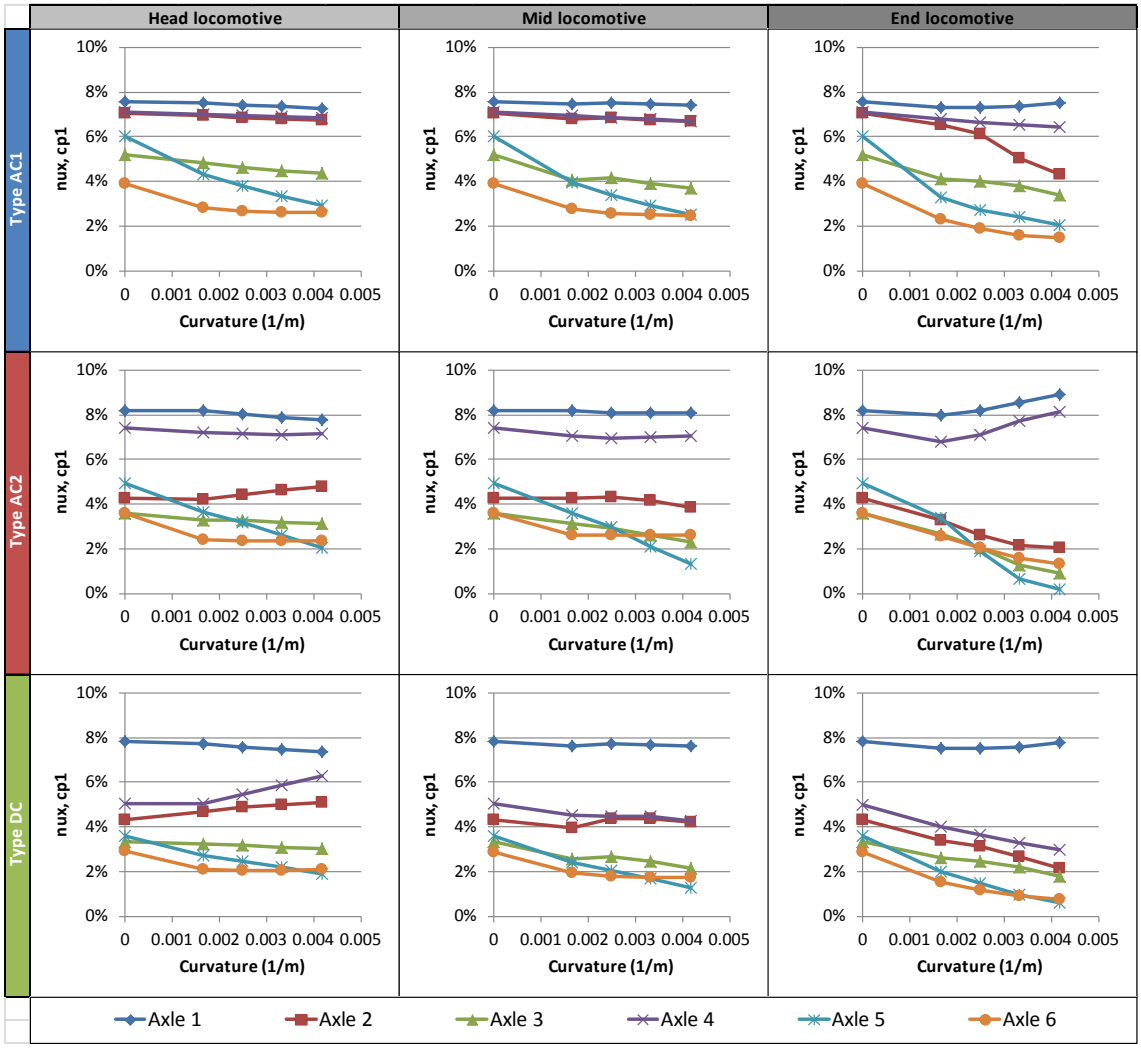

Figure 84: Rail head contact patch longitudinal creepages nux, cp1 (high rail, dry track)

Figure 84 shows longitudinal creepages for the rail head contact patch nux, cp1, which seemed to be impacted most by the TC systems used in each locomotive model type. Looking at Type

AC1, nux, cp1 for Axles 1, 2 and 4 changed little with increasing curvature and lateral coupler forces, although Axle 2's creepage for the end locomotive worsened as curvature increased. Longitudinal creepages for Axles 3, 5 and 6 worsened in response to increasing curvature and lateral coupler forces, especially when compared to tangent track conditions, but not to the same extent as for other locomotive model types. For Type AC2, high creepages were maintained for Axles 1 and 4, which actually seemed to improve with increasing curvature as lateral coupler forces increased. In contrast, creepages for Axles 2, 3, 5 and 6 (which were not monitored by Type AC2's TC system) generally worsened under these conditions, particularly in low radius curves for the end locomotive. In Type DC's case, high creepages were only maintained for Axle 1, which was the sole reference axle for its TC system, across different locomotive positions and curvatures. Creepages for Axles 4 and 2 were the most affected by increasing lateral coupler forces; nux, cp1 increased with increasing curvature for the head locomotive, remained somewhat constant in the mid locomotive and decreased for the end locomotive.

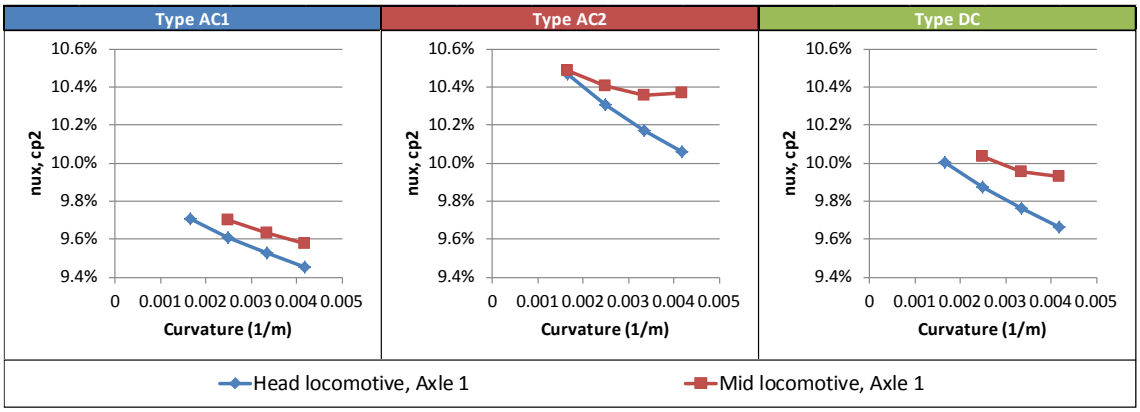

Figure 85: Gauge corner contact patch longitudinal creepages nux, cp2 (high rail, dry track)

Longitudinal creepages for the gauge corner contact patch nux, cp2, plotted in Figure 85, were higher than the nux, cp1 creepages discussed earlier (in Figure 84). Creepages for mid locomotives were higher than for head locomotives, but in both cases nux, cp2 decreased as curvature increased. The highest nux, cp2 occurred for Type AC2, followed by Types DC and AC1.

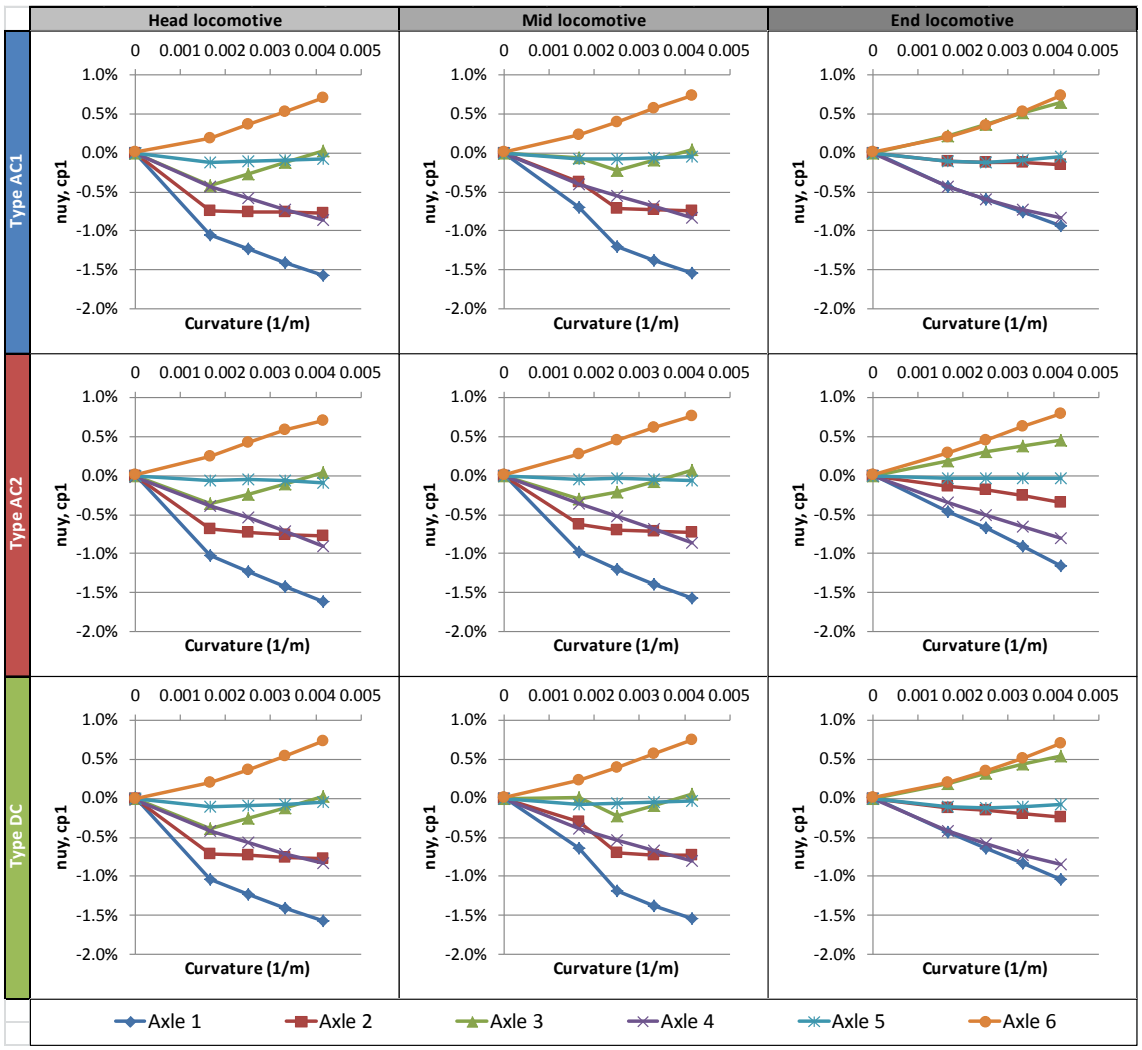

Figure 86: Rail head contact patch lateral creepages nuy, cp1 (high rail, dry track)

Lateral creepages nuy, cp1 for the rail head contact patch are shown in Figure 86. The variation of nuy, cp1 with curvature, locomotive type and locomotive position was just about identical to the Angle of Attack p described earlier in Figure 72. The magnitudes of nuy, cp1 were typically much lower than for nux, cp1; hence, in most cases (except for some high coupler force and curvature conditions), locomotive traction forces were having the biggest influence on rail head contact patch creepages on the high rail.

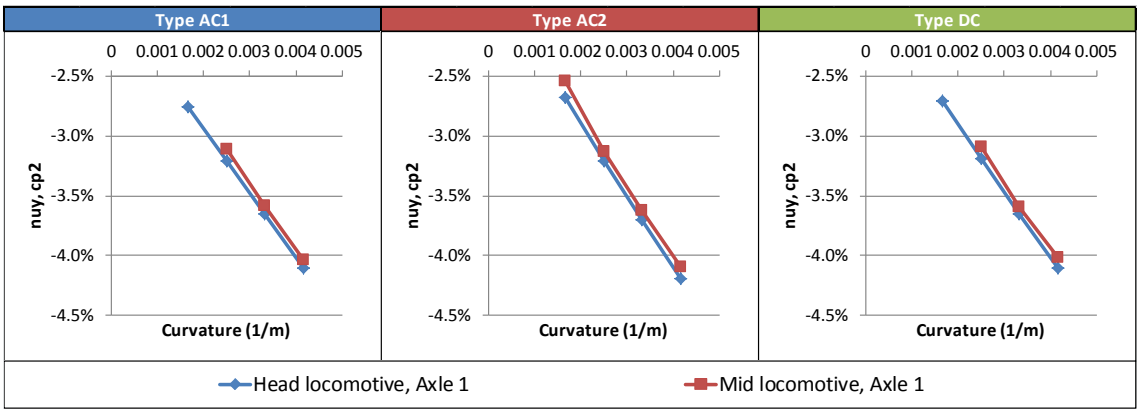

Figure 87: Gauge corner contact patch lateral creepages nuy, cp2 (high rail, dry track)

Figure 87 shows lateral creepages nuy, cp2 for the gauge corner contact patch. Those varied in a similar manner as nuy, cp1 for Axle 1, but the magnitude of nuy, cp2 was approximately four times higher. For all locomotive model types, nuy, cp2 increased with increasing curvature, while an increase in lateral coupler forces (from head to mid locomotives) reduced them slightly.

6.4.1.3. Low (right) rail forces

As previously discussed in Sections 6.4.1.1 and 6.4.1.2, wheelsets in the tested locomotive models were typically pushed toward the low rail as a result of low speeds, high traction forces, high in-train coupler forces and low radii curves. Because of this, two-point contact usually occurred for low rail wheels whilst in curves. Across all tested combinations of curvature, locomotive type and in-train locomotive positions, the Axles 3-6 were always in two-point contact on the low rail. For mid locomotives, two-point contact for Axle 2 on the low rail occurred in the 600 and 240 m radius curves, with Type AC1 experiencing two-point contact in the 300 m radius curves. The Type DC mid locomotive also had two-point contact occur in the 600 m radius curve. Two-point contact occurred in curves for all low rail wheels in end locomotives.

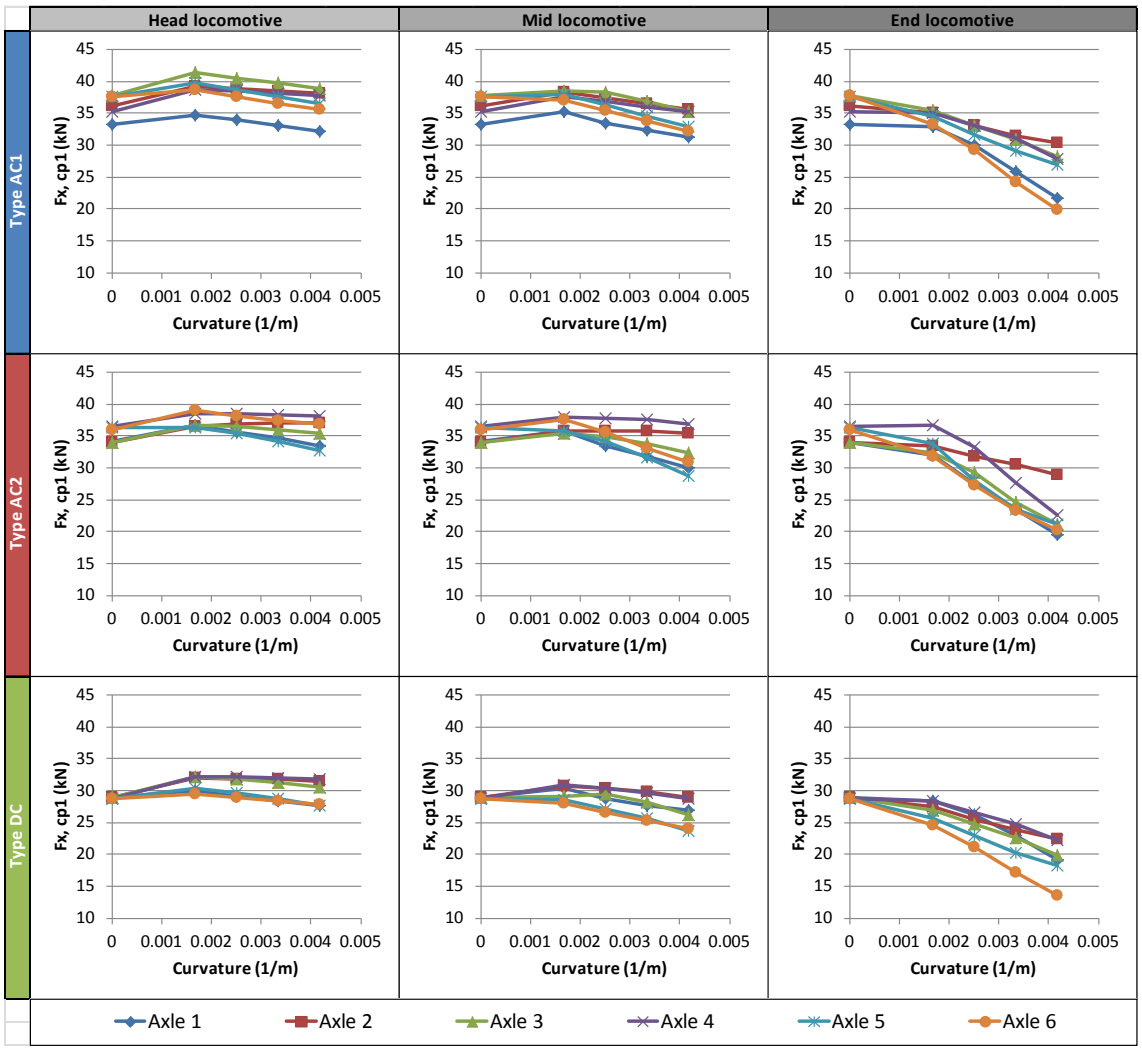

Figure 88: Rail head contact patch longitudinal forces Fx, cp1 (low rail, dry track)

Longitudinal forces within low rail head contact patches Fx, cp1 are shown in Figure 88, where forward acting forces are positive. For head and mid locomotives, there was generally an increase in Fx, cp1 from tangent track to the 600 m radius curve, which is the opposite of what happened for high rail wheels (Figure 76). For lower radii curves, Fx, cp1 for low rail wheels decreased, with the effect worsening as higher lateral coupler forces were applied to locomotives.

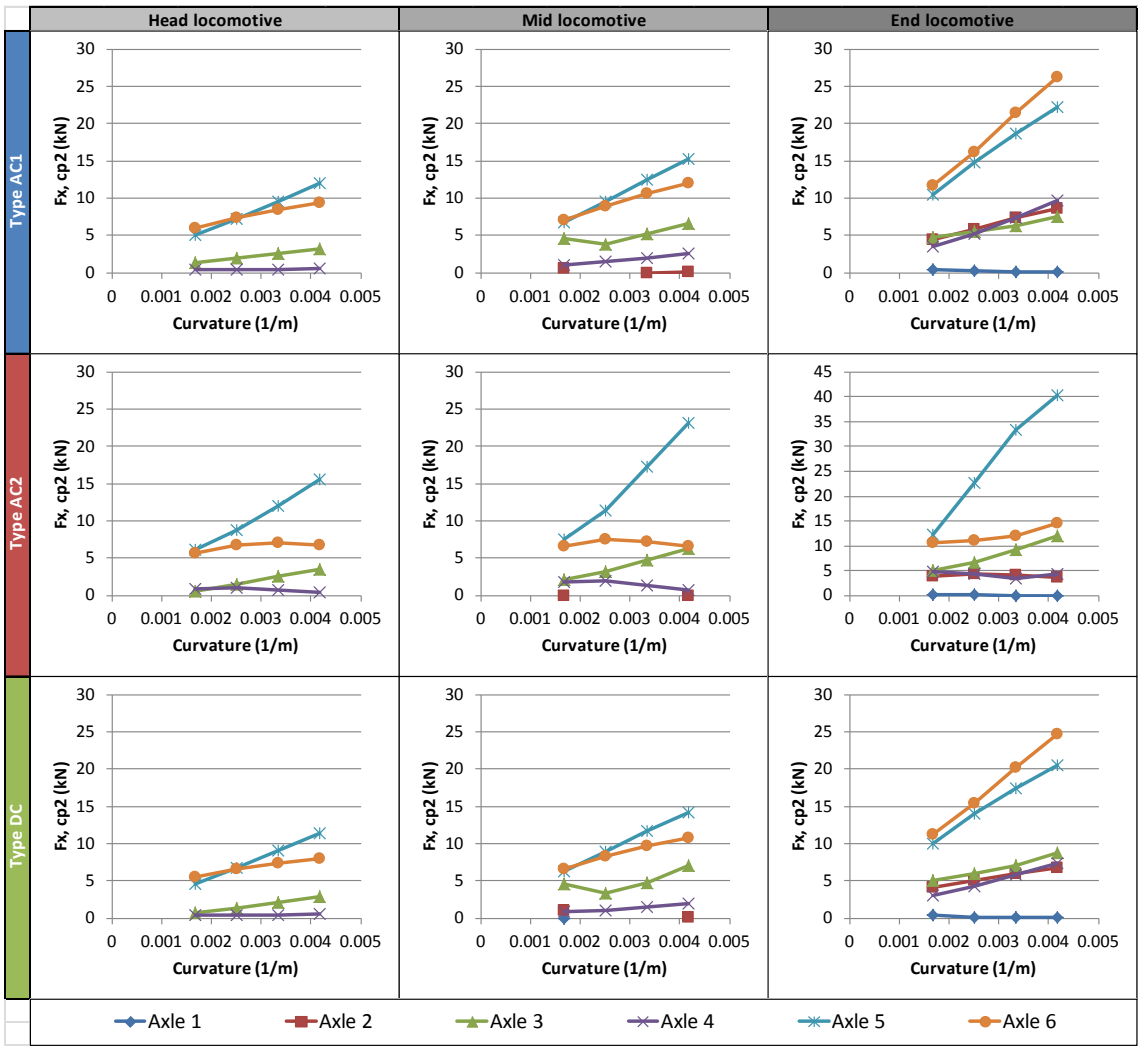

Figure 89: Gauge corner contact patch longitudinal forces Fx, cp2 (low rail, dry track)

Figure 89 shows the longitudinal forces Fx, cp2 within gauge corner contact patches. These typically increased in response to increase of both curvature and lateral coupler forces, although there were a few exceptions. In particular, Fx, cp2 for Axles 1-2 in mid locomotives, Axle 1 in the Type AC1 and DC end locomotives and Axles 1-2 in the Type AC2 end locomotive barely changed in response to increasing curvature. The rigid bogie Type AC1 and DC locomotive models behaved similarly, whilst for the semi-steering bogie Type AC2 there were high Fx, cp2 forces noted for Axle 5. Fx, cp2 for Axles 2, 4 and 6 in the Type AC2 end locomotive were also lower than for the Type AC1 and DC end locomotives. In general, it seems that, as curvature and lateral coupler forces increased, Fx, cp1 in the rail head contact patch decreased whilst Fx, cp2 in the gauge corner contact patch increased.

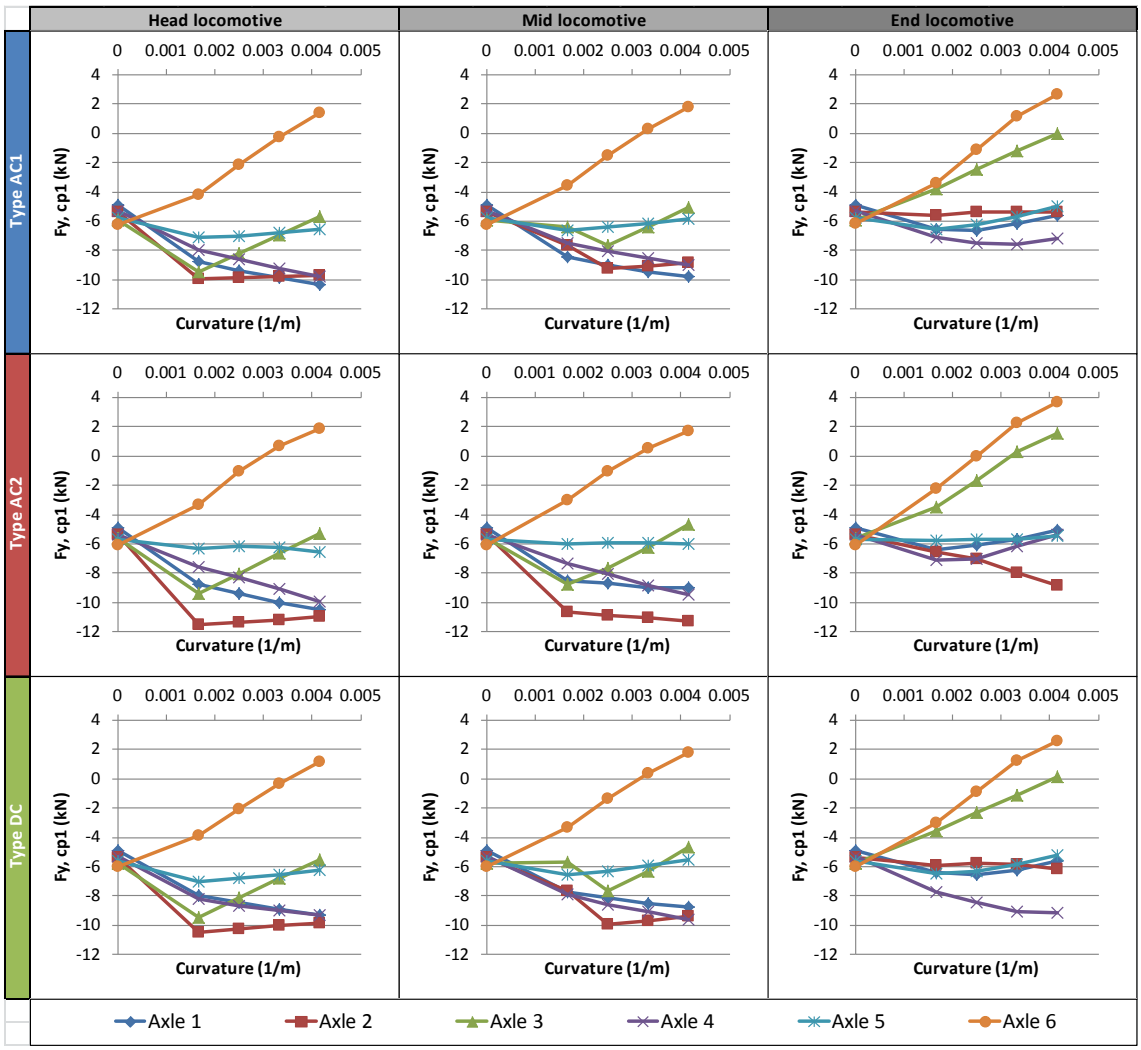

Figure 90: Rail head contact patch lateral forces Fy, cp1 (low rail, dry track)

Lateral forces Fy, cp1 within rail head contact patches are shown in Figure 90, where right acting forces are positive. Note that reaction forces between low rail wheels and rail are in the opposite direction to those for high rail wheels and rail. On tangent track, Fy, cp1 was ~5 – 6 kN for high rail wheels (see Figure 78) whereas, for low rail wheels, it was in the opposite direction, roughly between -5 and -6 kN. Fy, cp1 for low rail wheels more or less varied in the opposite manner to Fy, cp1 for high rail wheels, but the force magnitudes were lower. In contrast to the high rail results, Fy, cp1 for Axles 1, 2, 4 and 5 increased from tangent track to the 600 m radius curve, with increasing lateral coupler forces reducing this rise. For Axle 6 in all cases and Axle 3 for the end locomotives, Fy, cp1 decreased as curvature increased. Another notable difference is that Fy, cp1 for Axle 6 was barely affected by increasing lateral coupler forces across all locomotive types.

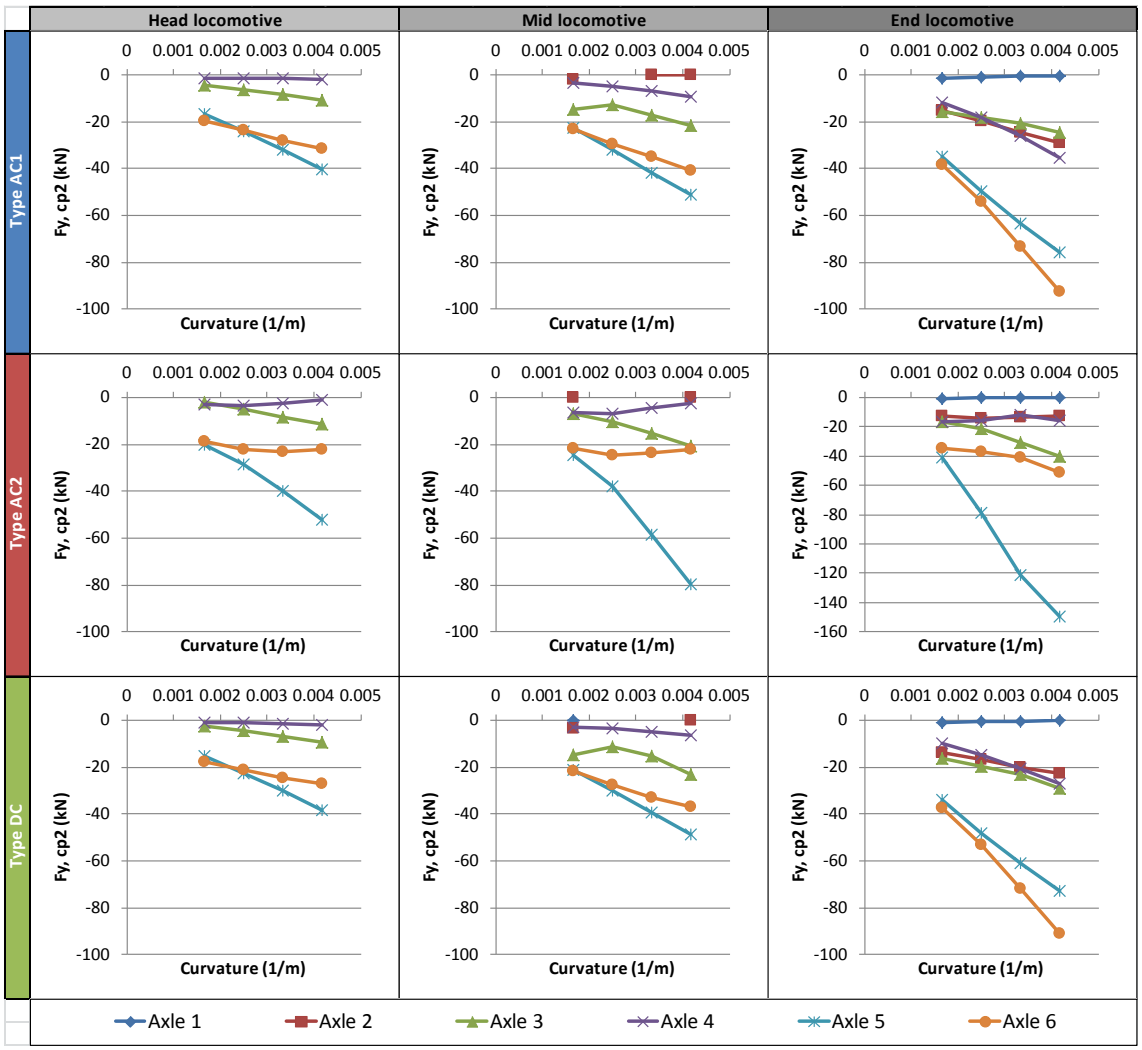

Figure 91: Gauge corner contact patch lateral forces Fy, cp2 (low rail, dry track)

Figure 91 shows gauge corner contact patch lateral forces Fy, cp2 for low rail wheels. These seemed to vary with curvature and lateral coupler force in a similar manner to Fx, cp2 (Figure 89), but the force magnitudes were much higher. This indicated that most of the force available within gauge corner contact patches was being used for steering as opposed to traction. As for Fx, cp2, Fy, cp2 typically increased with increase of both curvature and lateral coupler forces. In end locomotives, Axle 6 was pushed hardest toward the low rail for Types AC1 and DC, with Fy, cp2 equalling 96.2 kN and 90.8 kN respectively in the 240 m radius curve. Because of the bogie modelling fault in Type AC2, Fy, cp2 for the end locomotive in a 240 m radius curve was much higher at 149.2 kN.

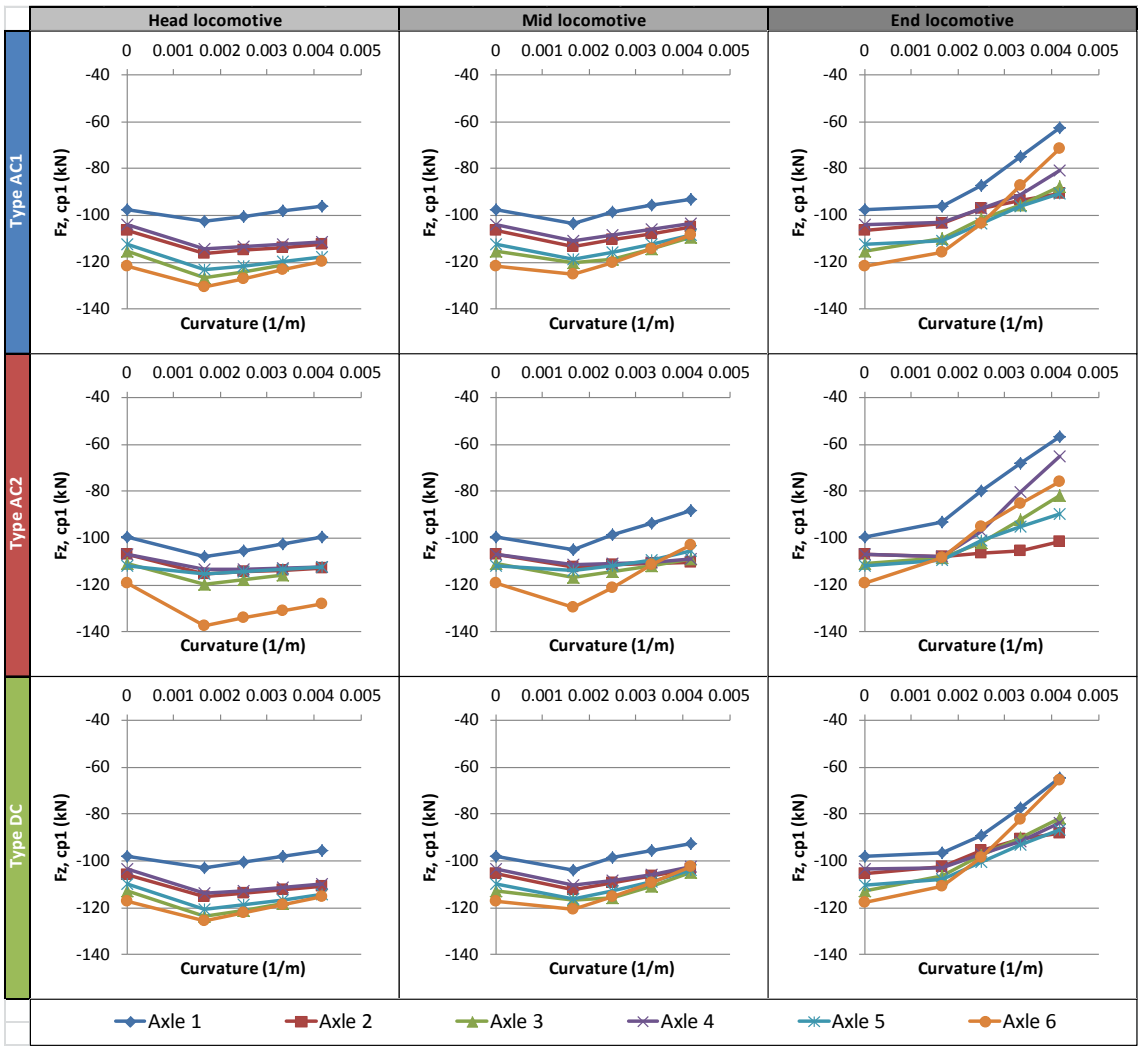

Figure 92: Rail head contact patch vertical forces Fz, cp1 (low rail, dry track)

Vertical forces for rail head contact patches Fz, cp1 on the low rail are shown in Figure 92, where downward acting forces are positive. In response to curvature and lateral coupler forces, Fz, cp1 for the low rail varied in the opposite manner to the high rail. Key differences include Fz, cp1 increasing from tangent track to the 600 m radius curve in head and mid locomotives, along with Fz, cp1 decreasing after that point as both curvature and lateral coupler forces increased.

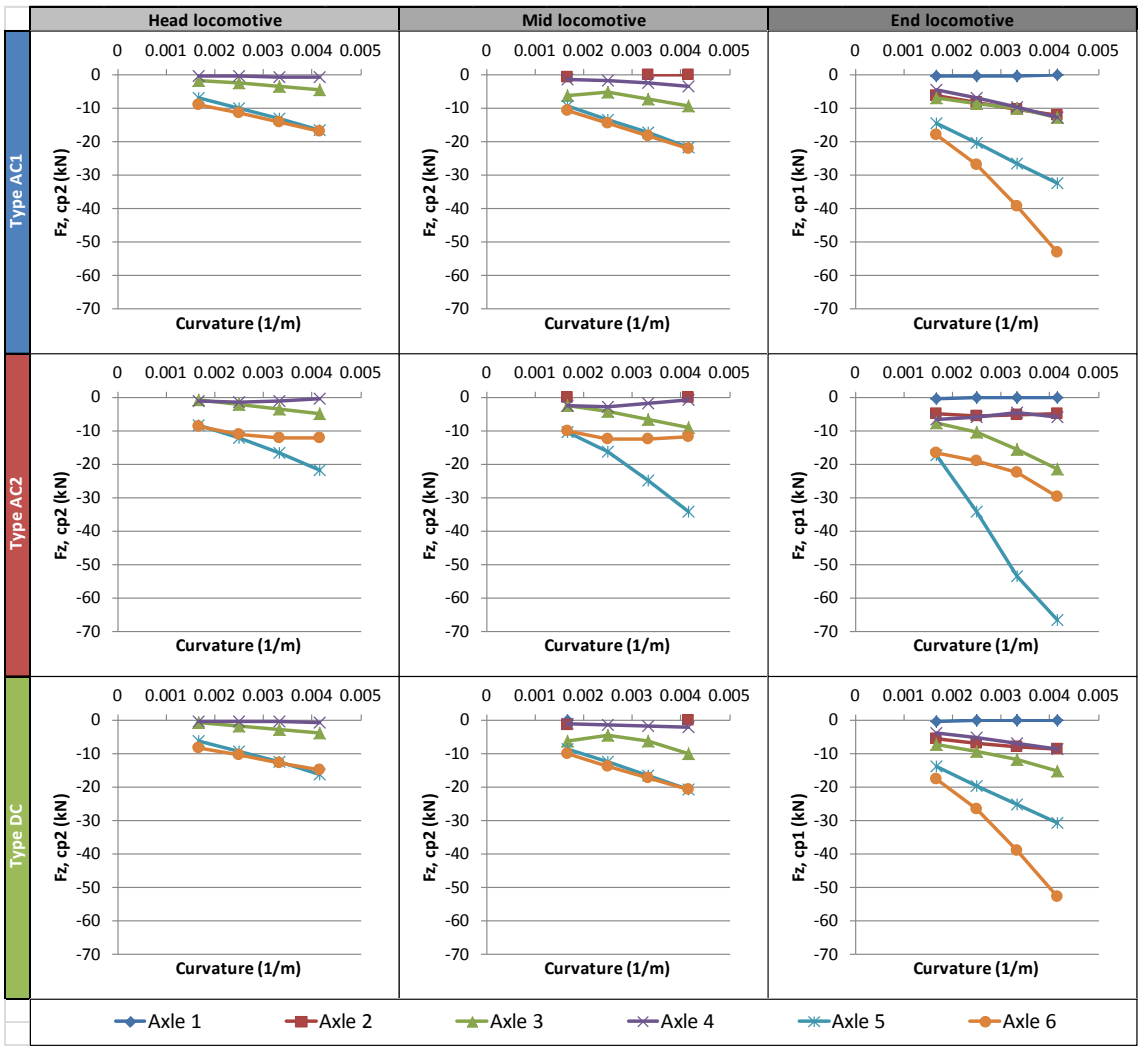

Figure 93: Gauge corner contact patch vertical forces Fz, cp2 (low rail, dry track)

Vertical forces for gauge corner contact patches Fz, cp2 are shown in Figure 93 for low rail wheels. Fz, cp2 varied with lateral coupler forces and curvature in a similar manner to both Fx, cp2 and Fy, cp2. High loadings for Axle 5 in the Type AC2 end locomotive may be the reason why loadings for Axles 4 and 6 were lower in comparison to the rigid bogie Type AC1 and DC locomotive models.

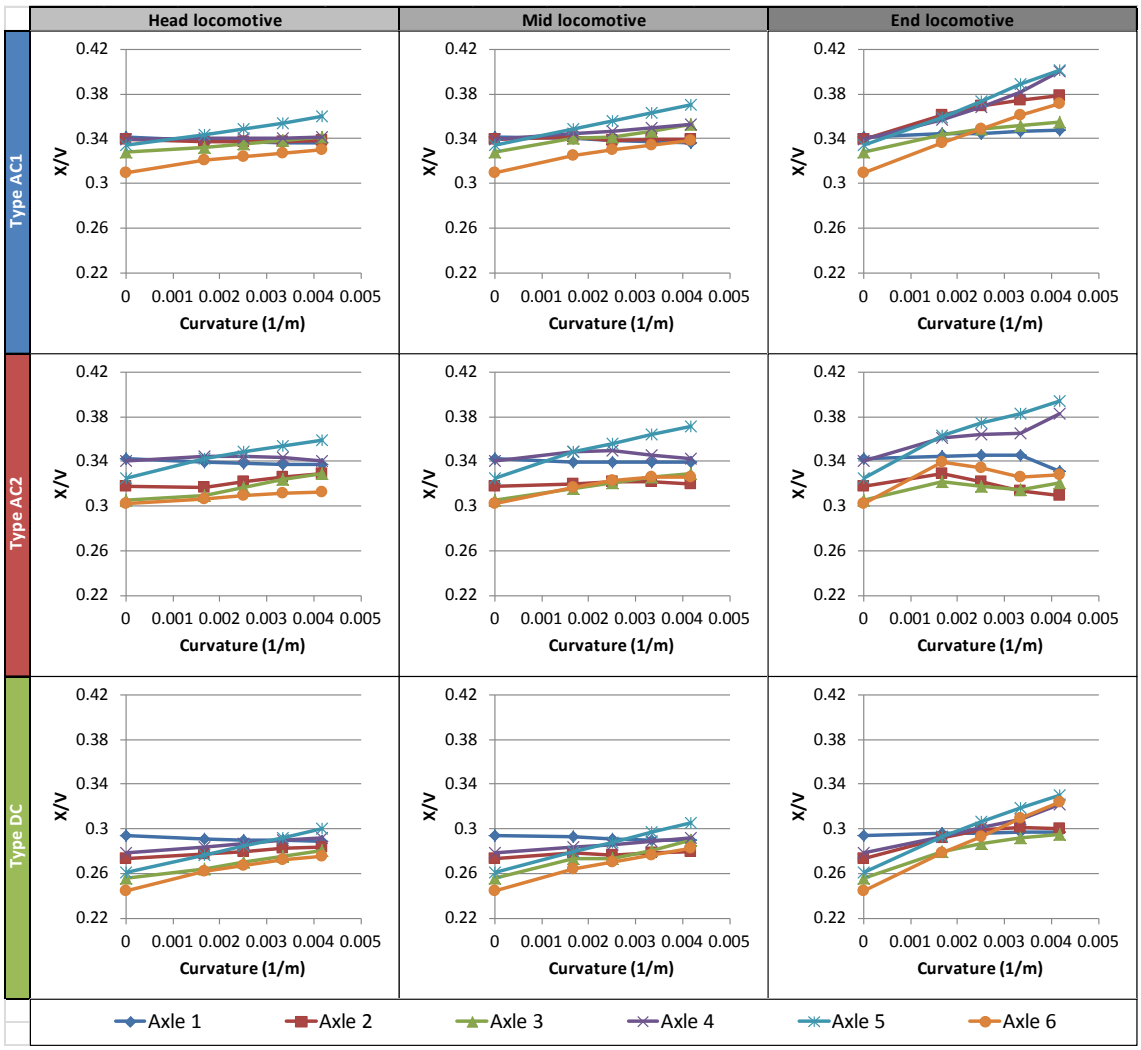

Figure 94: Approximate wheel adhesion coefficients X/V (low rail, dry track)

Approximate low rail wheel adhesion coefficients X/V are plotted in Figure 94. Adhesion coefficients for low rail wheels typically increased in response to increase of both curvature and lateral coupler forces. In broad terms this was the opposite of what happened to adhesion coefficients for high rail wheels.

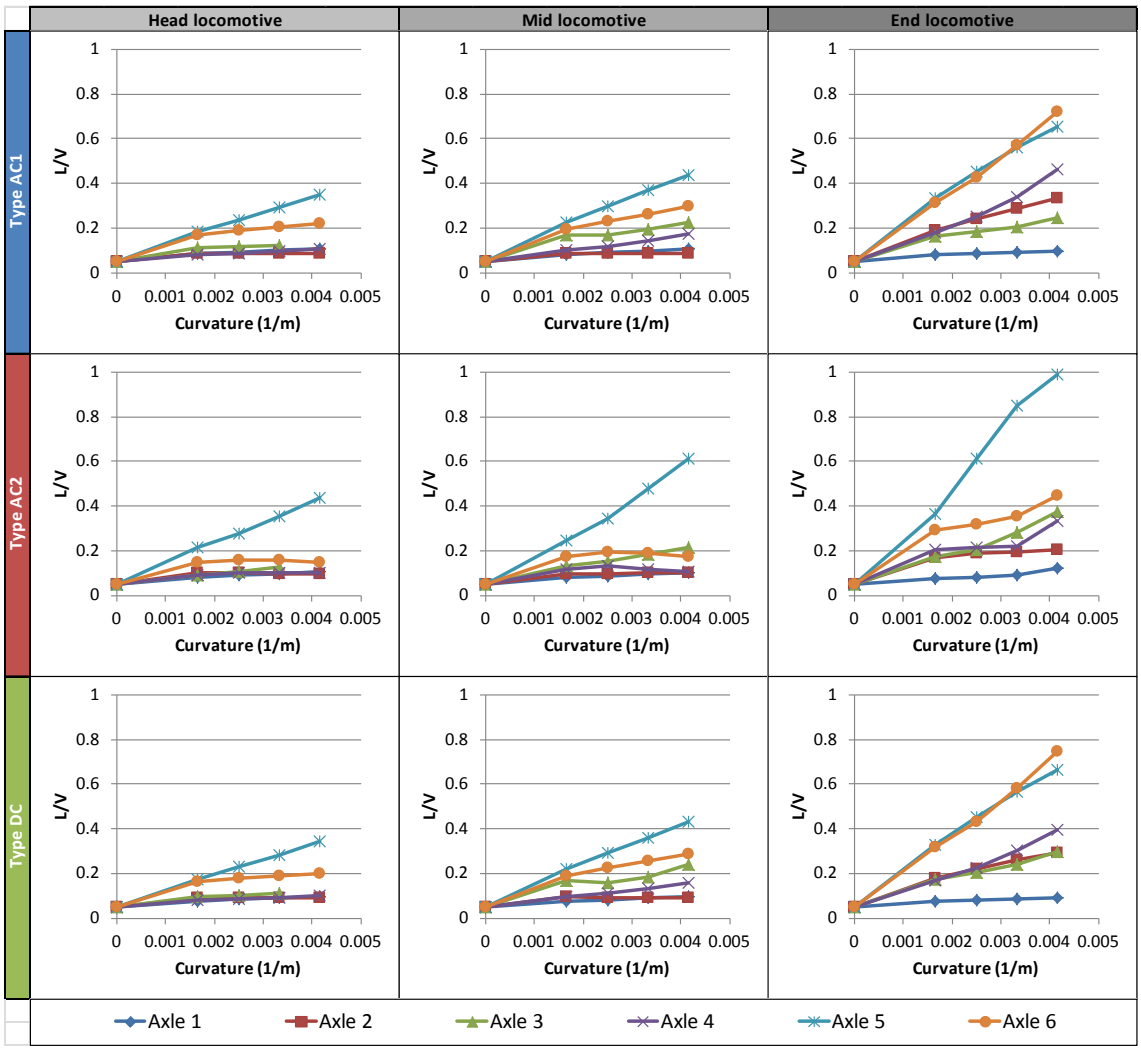

Figure 95: Wheel L/V ratios (low rail, dry track)

L/V ratios for low rail wheels are shown in Figure 95. These results were close to the sum wheelset L/V ratios described earlier in Figure 71, which means that the high rail wheel L/V ratios summarised in Figure 83 contributed little to the sum wheelset total. Low rail L/V ratios increased with increase of both curvature and lateral coupler forces. For the Type AC2 end locomotive, L/V for Axle 5's low rail wheel in the 240 m radius curve was 0.987, which was close to the maximum value of 1 recommended in AS 7509.1 [21]. For the same locomotive position and curve radius, Types AC1 and DC recorded maxima of 0.723 and 0.746 respectively for Axle 6. When earlier summarising results for low rail Fz, cp2 (Figure 93) for Type AC2, it was mentioned that Axle 5's high loadings on the low rail impacted forces on Axles 4 and 6. This can also be seen here, where low rail L/V ratios for Axles 4 and 6 were lower for the semi-

steering bogie Type AC2 model than the rigid bogie Types AC1 and DC models across all locomotive positions.

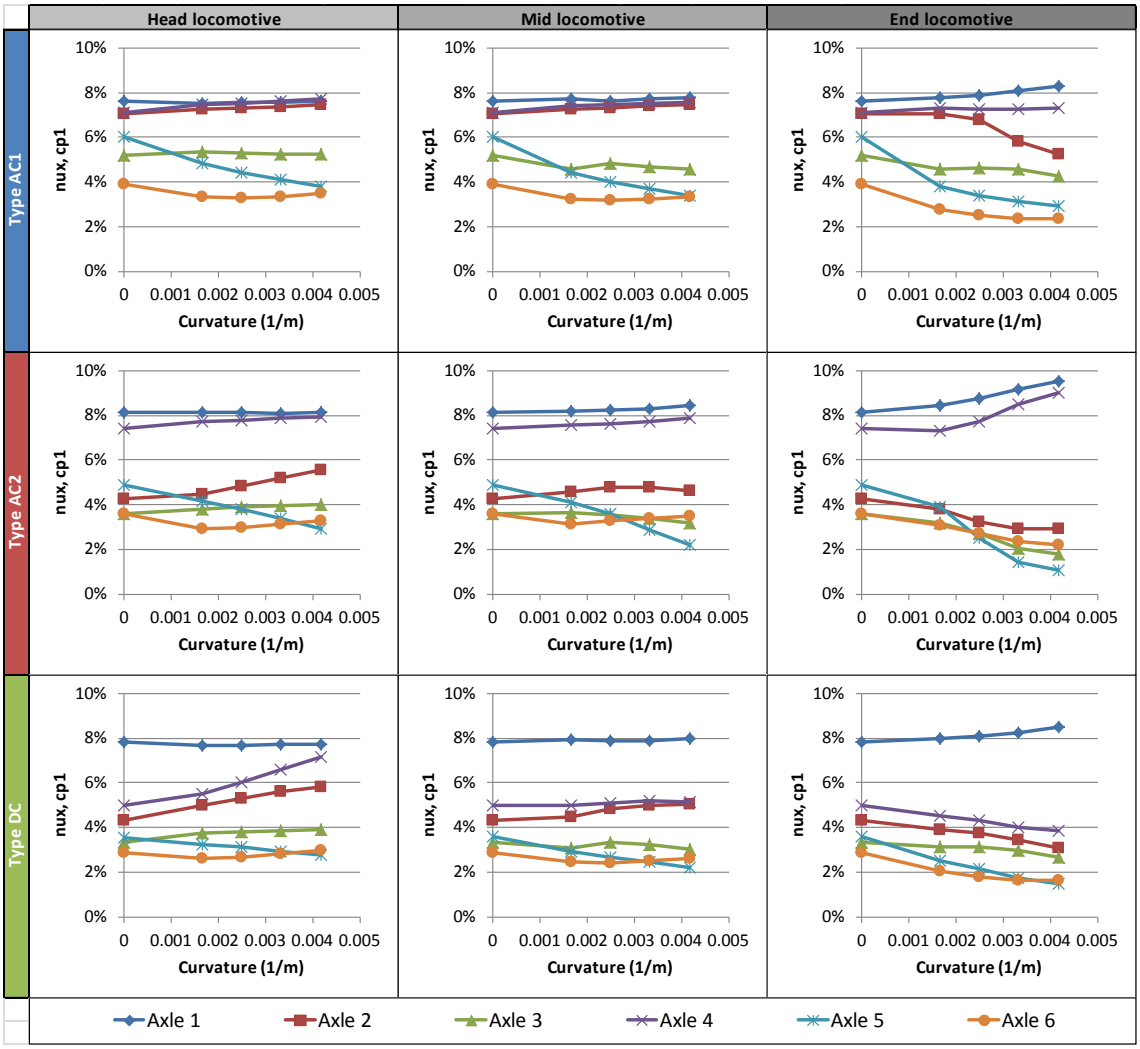

Figure 96: Rail head contact patch longitudinal creepages nux, cp1 (low rail, dry track)

Rail head contact patch longitudinal creepages nux, cp1 for the low rail are summarised in Figure 96. These results were very similar to nux, cp1 for the high rail as seen earlier in Figure 84.

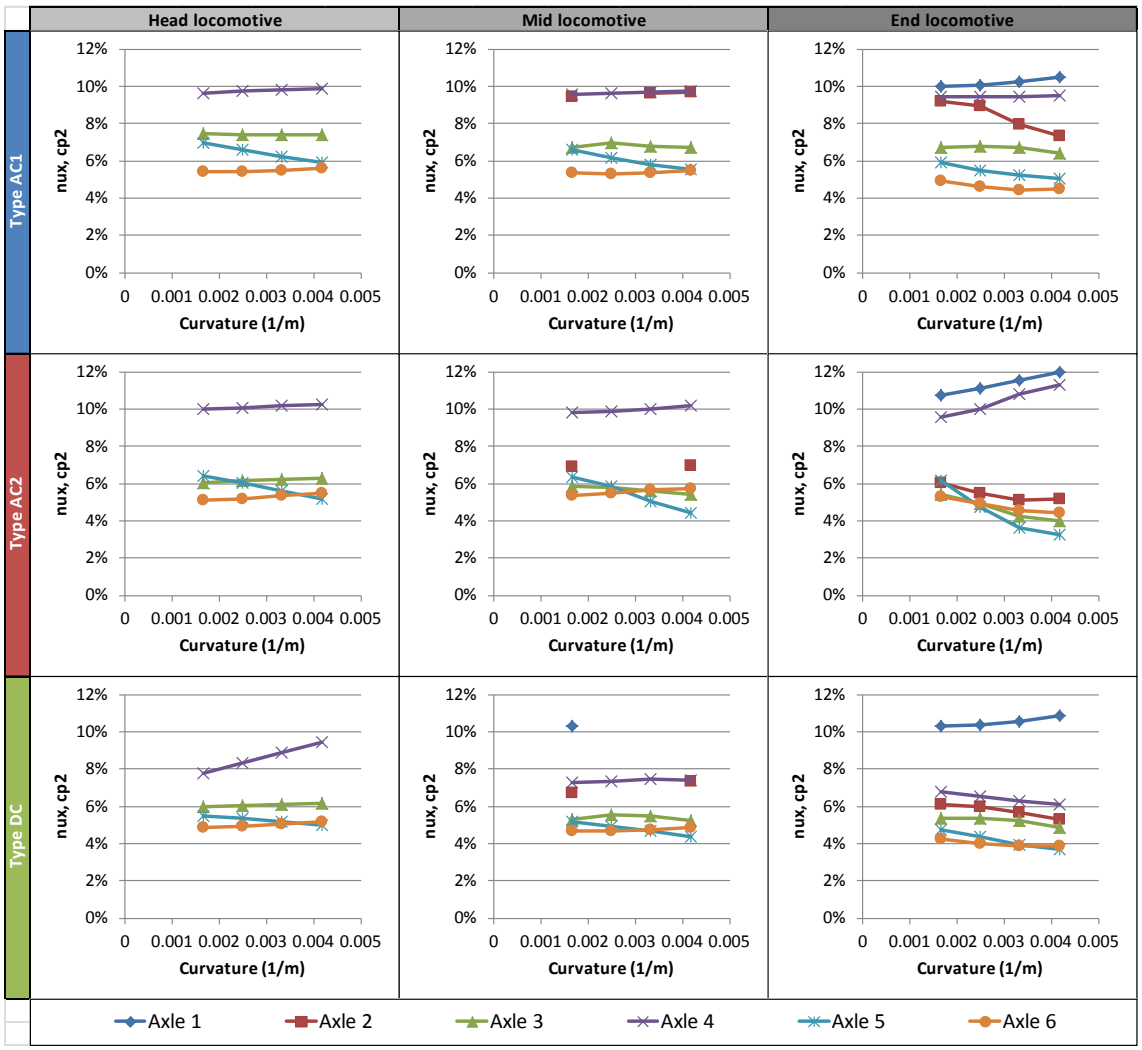

Figure 97: Gauge corner contact patch longitudinal creepages nux, cp2 (low rail, dry track)

Figure 97 shows longitudinal creepages nux, cp2 for gauge corner contact patches. At points where cp1 and cp2 contact occurred, nux, cp2 varied in a similar manner with coupler force and curvature as nux, cp1 but the corresponding nux, cp2 creepages were ~2% higher.

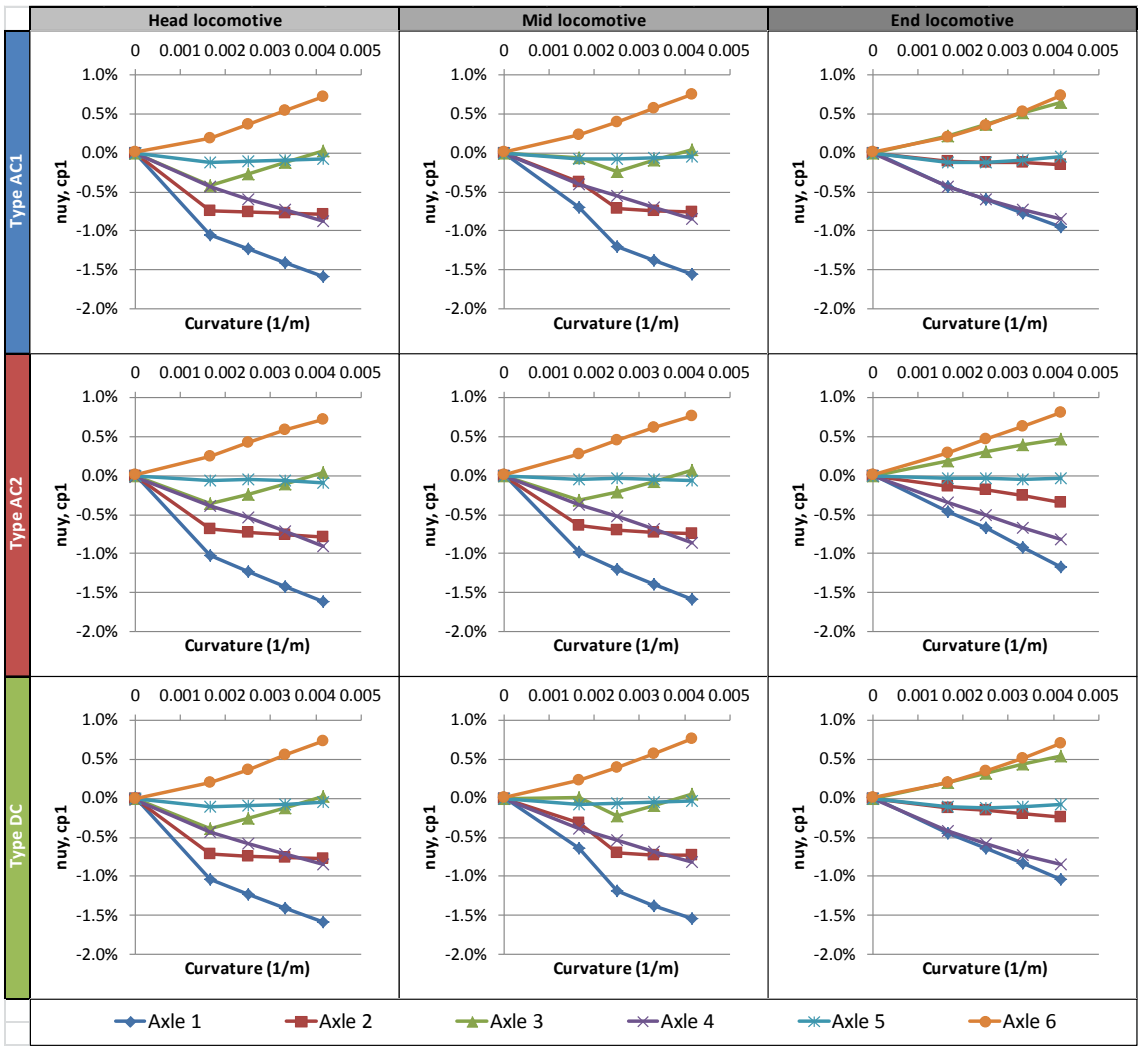

Figure 98: Rail head contact patch lateral creepages nuy, cp1 (low rail, dry track)

Figure 98 shows lateral creepages for rail head contact patches nuy, cp1. Results for nuy, cp1 on the low rail were just about identical to those for nuy, cp1 on the high rail seen earlier in Figure 87.

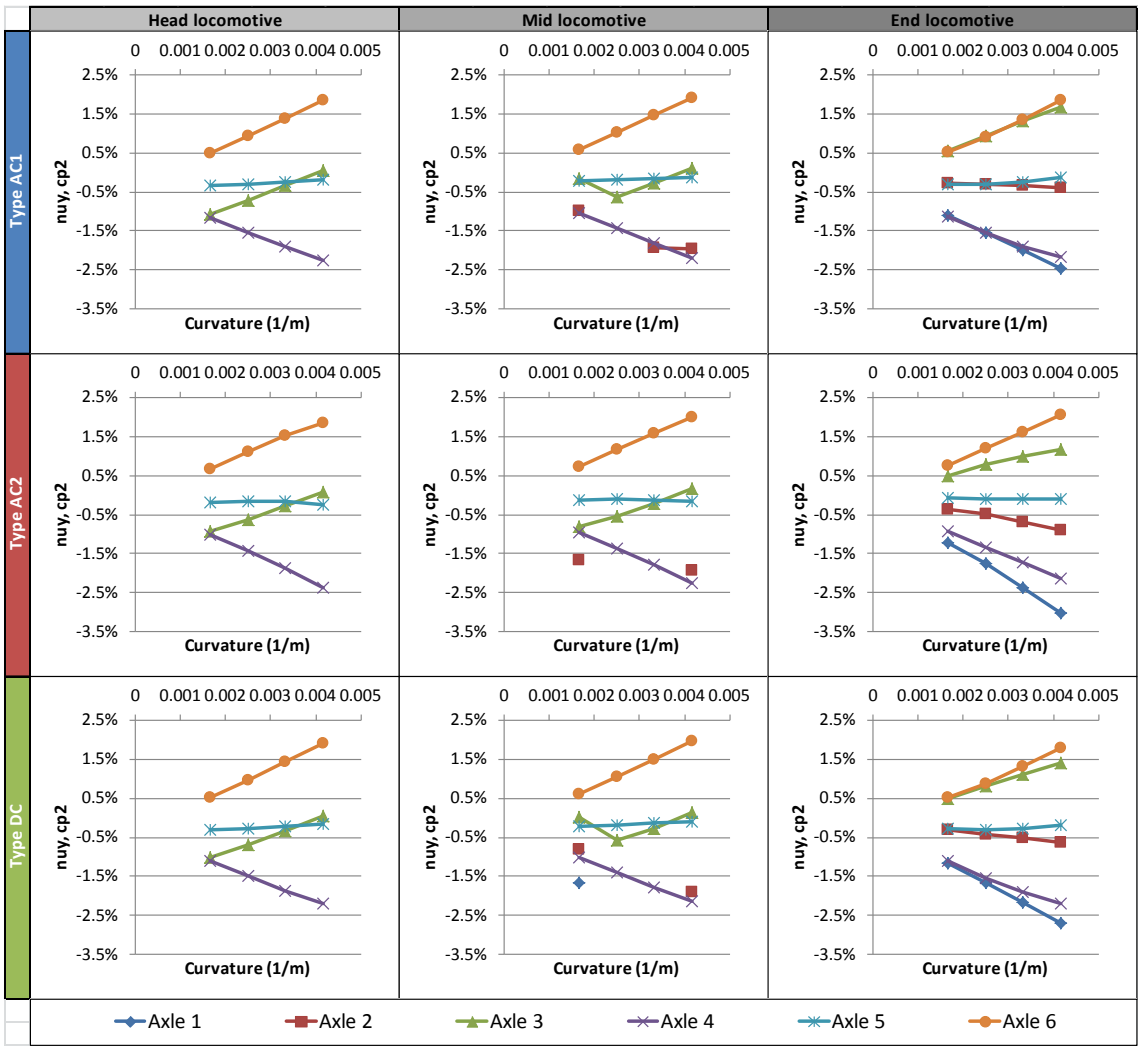

Figure 99: Gauge corner contact patch lateral creepages nuy, cp2 (low rail, dry track)

Lateral creepages for gauge corner contact patches nuy, cp1 are summarised in Figure 99. At points where cp1 and cp2 contact occurred, nuy, cp2 varied in a similar manner with curvature and coupler force as nuy, cp1 but the corresponding nuy, cp2 creepages were ~2.5 times higher.

6.4.2. Results for wet rail head conditions

Despite differing rail head friction coefficients in the wet track analyses, many basic trends were common to the dry track results detailed in Section 6.4.1. For the sake of brevity, only key differences between the wet and dry track results will be commented on in this section, so most trends common to both will not be repeated here.

6.4.2.1. Net wheelset forces

Figure 100 shows the simulated net longitudinal wheelset forces X for wet track, where forward acting forces are positive.

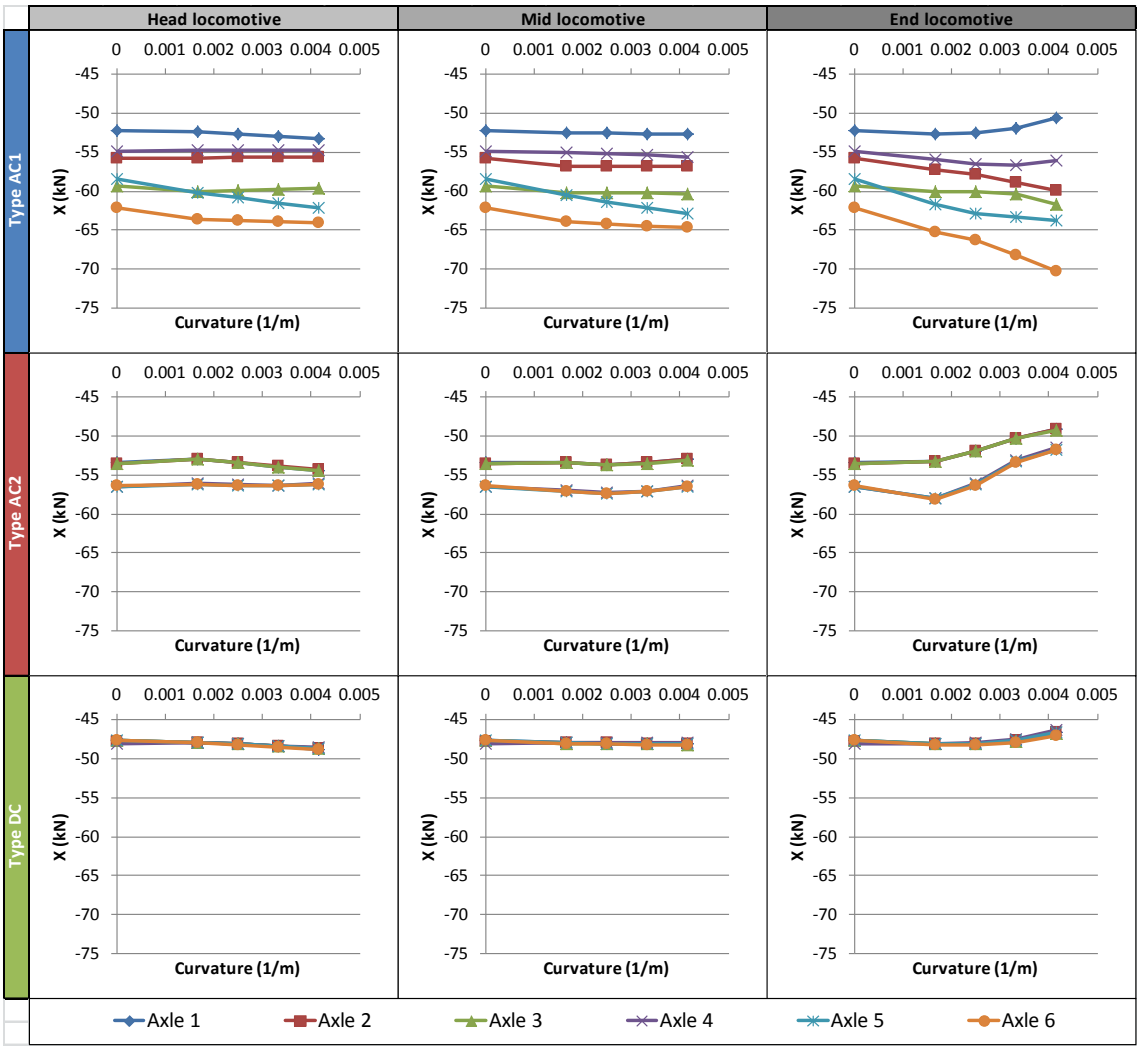

Figure 100: Longitudinal wheelset forces X (wet track)

Given the lower rail head friction coefficient of wet track in comparison to dry track, as summarised in Table 6, wheelset X generally dropped for locomotives on wet track. X forces for Types AC2 and DC varied with curvature and coupler forces in a similar manner as for dry track (Figure 67). For Type DC, X slightly improved with curvature in the head locomotive, remained relatively constant in the mid locomotive and slightly worsened in the end locomotive. Similar behaviour was noted for Type AC2, although wheelsets in Bogie 2 exerted more X than for Bogie 1 as seen on dry track. The biggest differences between wet and dry track conditions

occurred for Type AC1. Recalling the dry track data in Figure 67, X forces for Axles 3, 5 and 6 remained relatively constant with curvature and coupler forces, levelling out at ~75.5 kN. X forces for Axle 2 in the end locomotive also levelled out at this point. On wet track however, no such 'levelling out' occurred, with Type AC1's TC system able to exert more traction force for Axles 5-6 in all cases. X for Axle 3, which normally didn't vary much with curvature and coupler force, increased slightly for the end locomotive in the 240 m radius curve. Axle 6 in that case was exerting 70.3 kN, which is close to the maximum X forces exerted on dry track. In short, Type AC1, particularly its TC system, was able to adapt more effectively to, and produce more traction force in, wet track conditions compared to Types AC2 and DC.

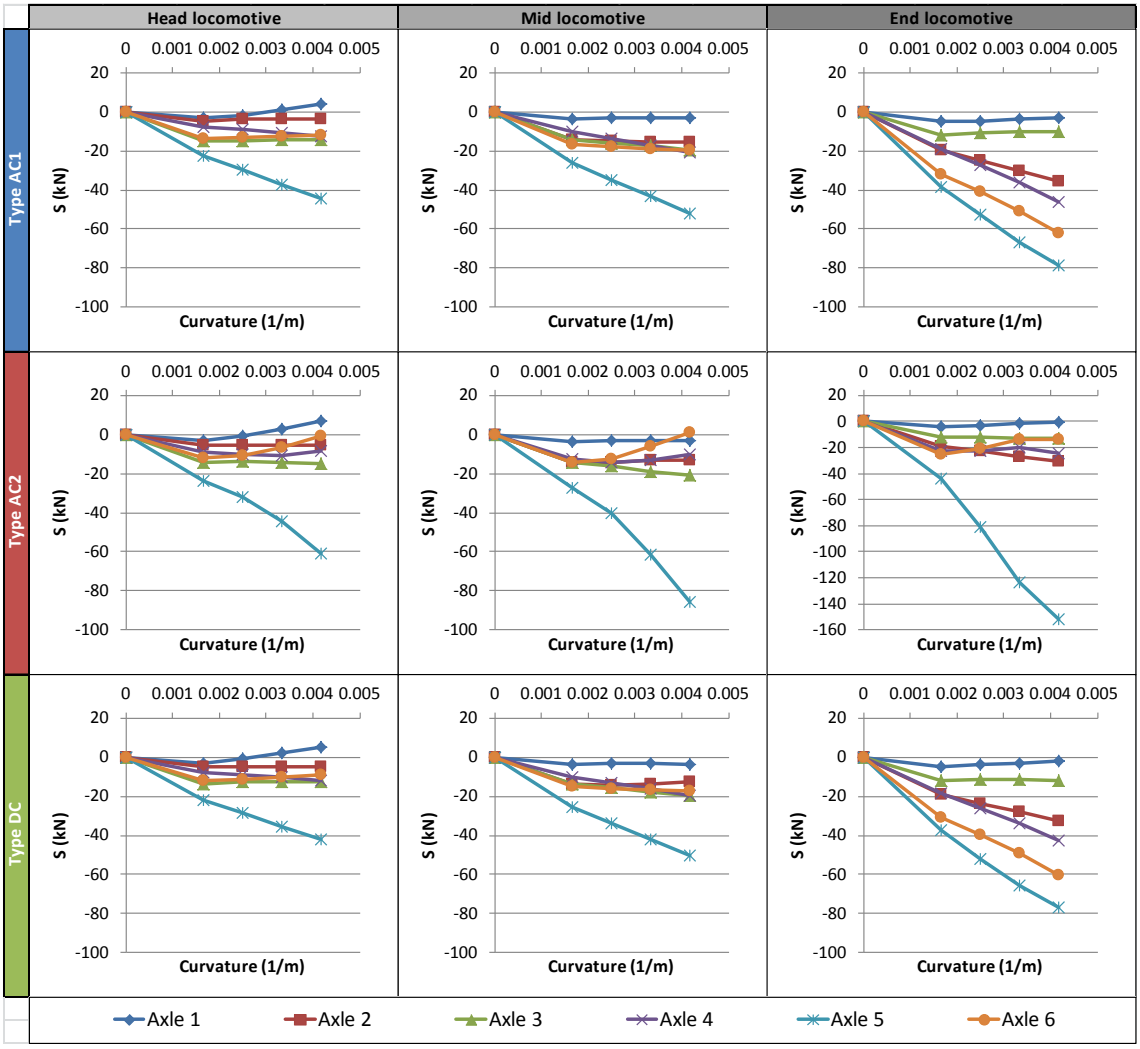

Figure 101: Lateral track-shifting forces S (wet track)

Lateral track-shifting forces S for each wheelset are shown in Figure 101, where negative S indicates that track is forced right of the centre line within curves. Although there were slight changes in wheelset S, particularly with small reductions for Axles 1 and 6, the force

magnitudes were similar to those for dry track (Figure 68). Axle 5 in Type AC2 was still producing high S forces, most likely because of the improperly-adjusted axle box lateral clearances mentioned earlier. It appears that having a wet rail head only deleteriously affected locomotive traction and not steering. This is most likely because the friction coefficients for gauge corner and flange contact zones were the same for both wet and dry track in this analysis (see Table 6), and that most of the lateral steering forces appear to be exerted by gauge corner contact patches on the low rail. Given that the locomotive models were travelling on wet track at the same speeds and with the same coupler forces applied as for dry track, the net lateral forces on the locomotive models wouldn't change much between the two rail head friction conditions. Differences in wheelset traction forces however would be responsible for some of these minor changes.

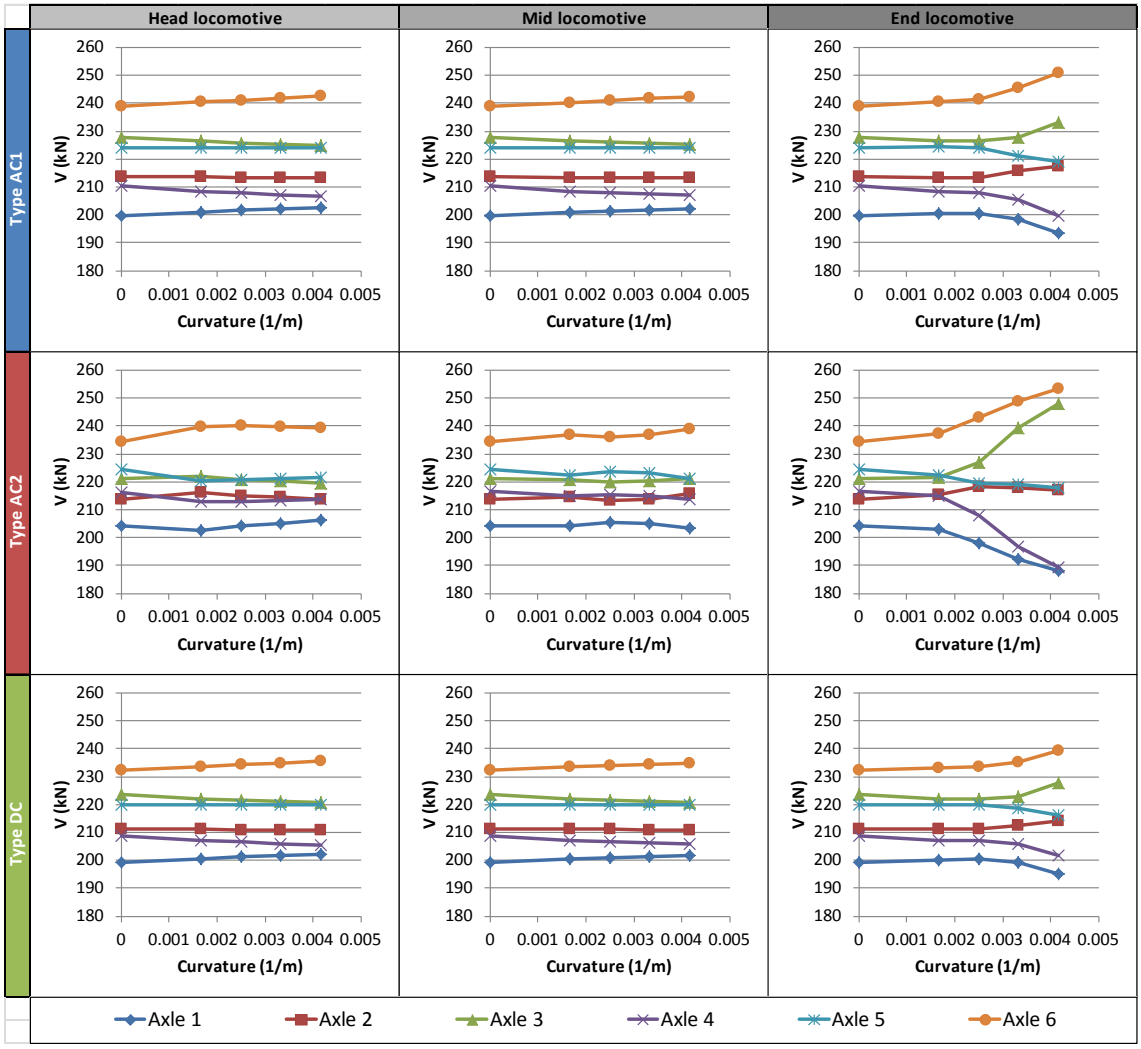

Figure 102: Vertical axle loads V (wet track)

Figure 102 shows vertical axle loads V, where downward acting forces are positive. With respect to locomotive type, position and curvature, axle loads on wet track varied in a similar manner as for dry track (Figure 69). Given that there was less traction-induced bogie and car-body pitching as indicated by the reduction in wheelset X forces (Figure 100), axle loads for locomotives on wet track deviated slightly less from their mean value. For Types AC1 and AC2, the mean axle load is 134 t / 6 axles = 22.3 t = 219.09 kN, whereas for Type DC it is 132 t / 6 axles = 22 t = 215.82 kN.

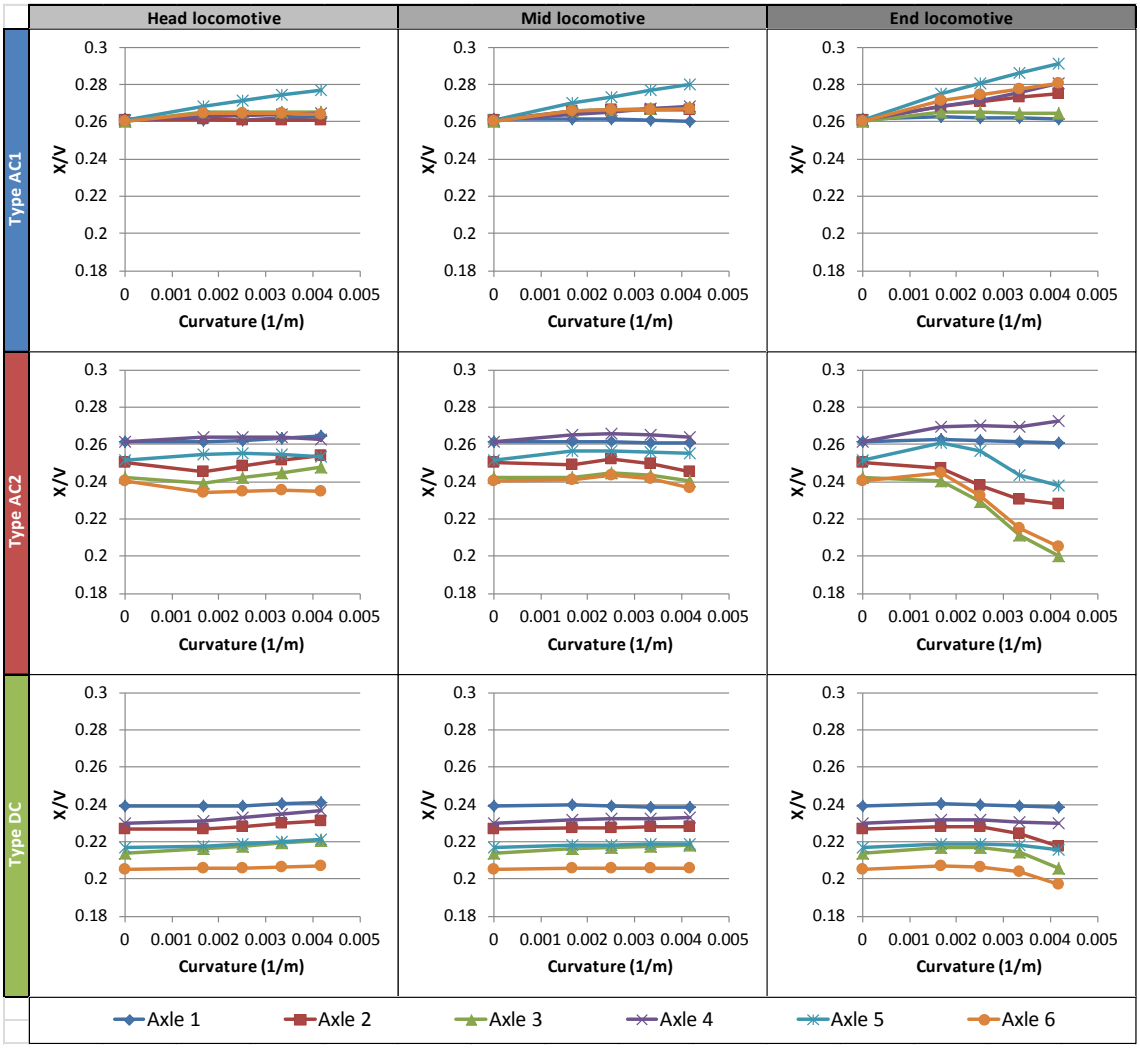

Figure 103: Approximate per-wheelset adhesion coefficients X/V (wet track)

Approximate per-wheelset adhesion coefficients X/V are given in Figure 103. Because axle loads V didn't vary much between wet and dry track data, longitudinal forces X had the most impact on per-wheelset adhesion coefficients for wet track. As a result, Types AC2 and DC wheelset X/V coefficients were lower for wet track, but they varied similarly in response to

increasing curvatures and coupler forces as for dry track (see Figure 70). Type AC1 was able to manage high adhesion coefficients on wet track, with a minimum of ~0.26 possible. In most cases, with an exception for Axle 1, X/V for wheelsets in Types AC1 improved as both coupler forces and curvatures increased.

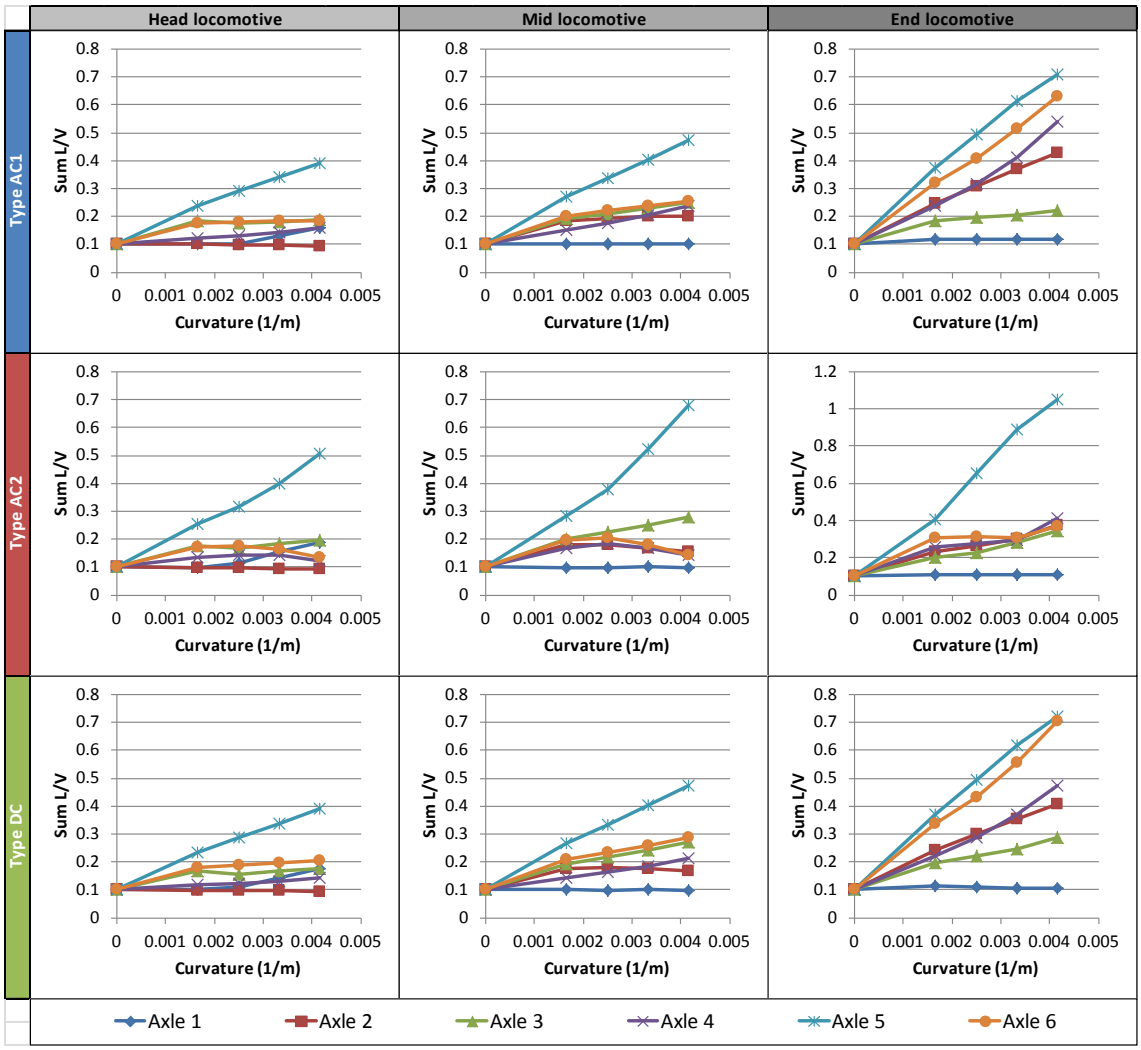

Figure 104: Sum wheelset L/V ratios (wet track)

None of the sum wheelset L/V ratios shown in Figure 104 exceeded the recommended limit of 1.5 in AS 7509.1 [21]. As for dry track, L/V ratios for locomotives on wet track increased with increase of both curvature and lateral coupler forces. Except for Axle 5, L/V ratios for all locomotives were generally lower on wet track, particularly Axle 6 on the rigid bogie Type AC1 and DC models.

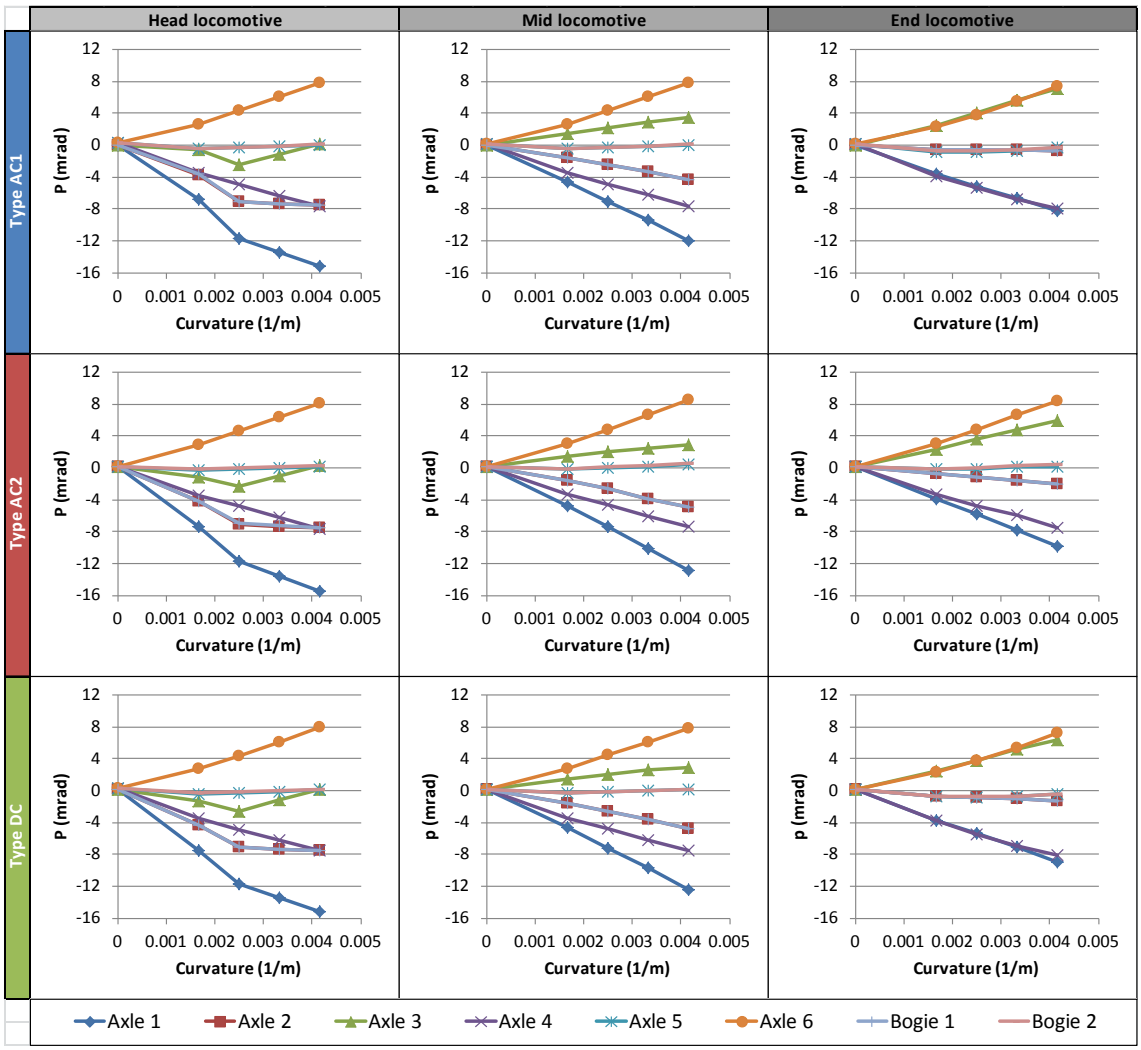

Figure 105: Wheelset and bogie Angles of Attack p (wet track)

Figure 105 shows AoAs for wheelsets and bogies, where positive AoAs denote clockwise wheelset/bogie rotation relative to the track. AoAs were near identical between all locomotive types for the head and mid locomotive positions. In Type AC1 and DC end locomotives, AoAs for Bogie 1 and its wheelsets (1-3) were close to Bogie 2 (wheelsets 4-6), whereas in the Type AC2 end locomotive, Bogie 1 was rotated ~2 mrad further clockwise than Bogie 2. Compared to the dry track results in Figure 72, all head locomotives produced lower AoAs in the 600 m radius curve. For mid locomotives, Types AC1 and DC produced better AoAs in curves of ≤400 m radii, whilst for Type AC2, improvements were noted in curves of ≤600 m radii. In general, it appeared for all locomotive types that Bogie 1 was able to steer better on wet track, whereas Bogie 2 AoAs didn't seem to be affected much by either lateral coupler forces, locomotive types or rail head friction conditions.

6.4.2.2. High (left) rail forces

Two-point contact on the high rail occurred less often for wet rail head conditions as opposed to completely dry track. For wet rail head conditions, gauge corner contact was only present at Axle 1, limited to ≤400 m curve radii for all head locomotives and the 240 m radius curve for the Type DC mid locomotive.

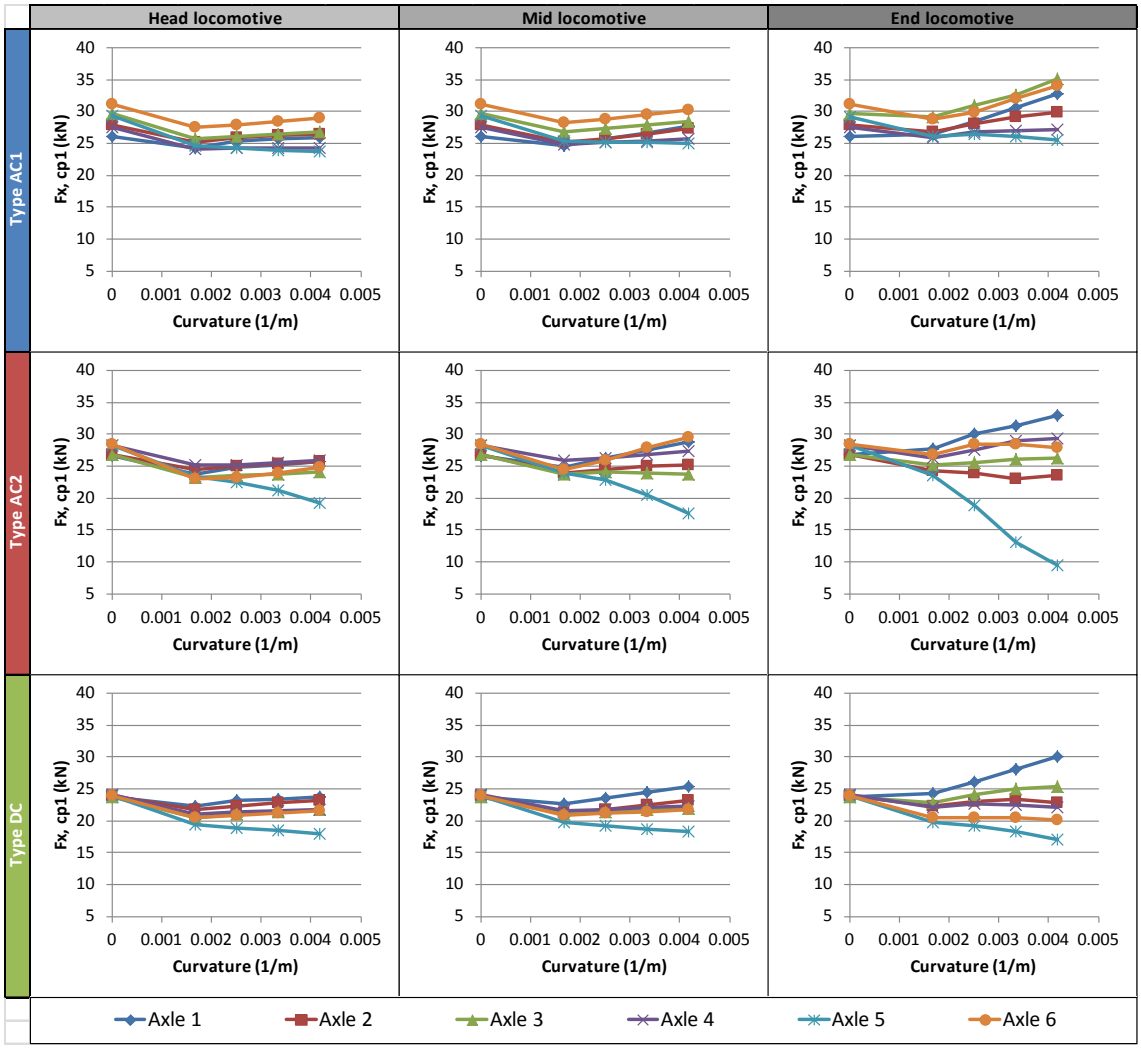

Figure 106: Rail head contact patch longitudinal forces Fx, cp1 (high rail, wet track)

Figure 106 shows longitudinal contact patch forces Fx, cp1 within rail head contact patches, where forward acting forces are positive. High rail Fx, cp1 forces simulated for wet track were basically similar to the dry track results (Figure 76), insofar as having Fx,cp1 generally drop from tangent track to the 600 m radius curve and then diverging greatly amongst wheelsets as lateral coupler forces and curvature further increased. The reduced rail head friction coefficient

had a more significant effect, where Fx, cp1 for high rail wheels on wet track was lower than for dry track.

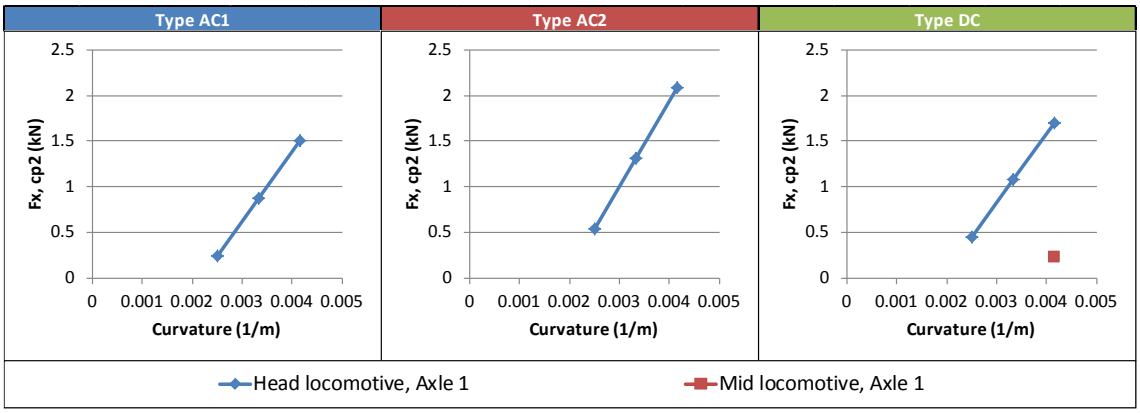

Figure 107: Gauge corner contact patch longitudinal forces Fx, cp2 (high rail, wet track)

Gauge corner contact patch longitudinal forces Fx, cp2 are summarised in Figure 107. Compared to dry track conditions (Figure 77), high rail Fx, cp2 forces for wet rail head conditions were much lower. Similarities included Fx, cp2 increasing with increase of curvature and decreasing as lateral coupler forces increased.

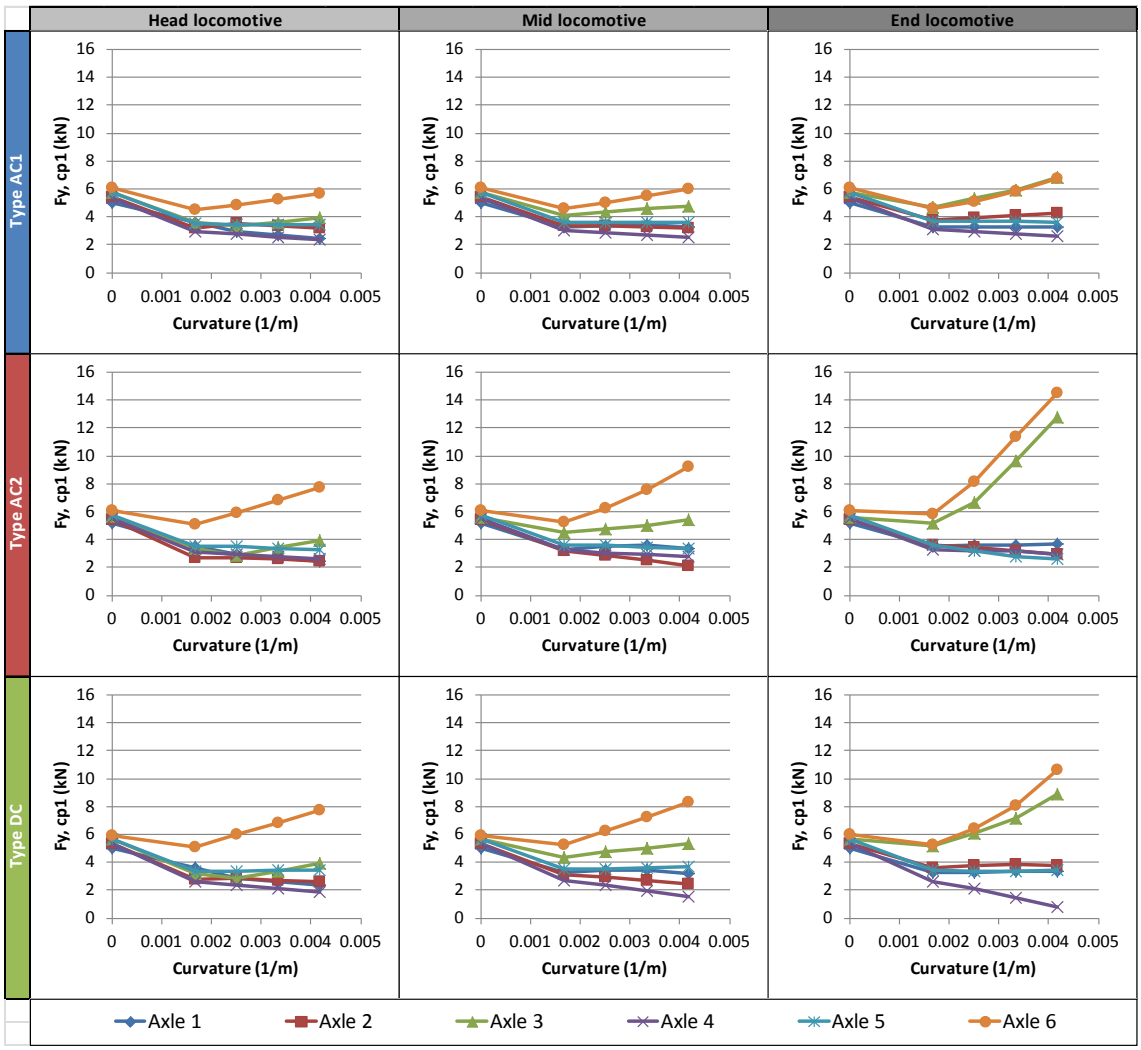

Figure 108: Rail head contact patch lateral forces Fy, cp1 (high rail, wet track)

Rail head contact patch lateral forces Fy, cp1 for high rail wheels on wet track are shown in Figure 108, where right acting forces are positive. Compared to the equivalent dry track data in Figure 78, Fy, cp1 in curves was closer to the tangent track value. For Type AC1, Fy, cp1 for Axle 6 was considerably reduced in comparison to Types AC2 and DC, along with such reductions in Axle 3 in the mid and end locomotives.

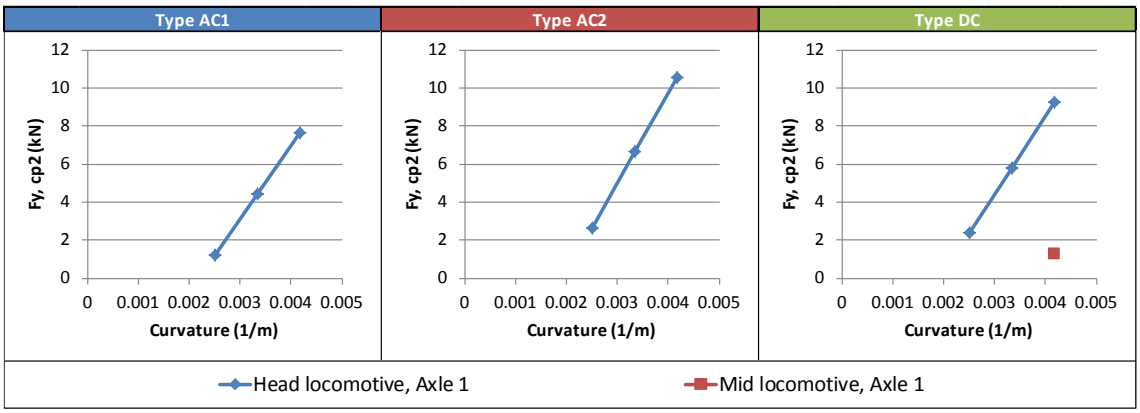

Figure 109: Gauge corner contact patch lateral forces Fy, cp2 (high rail, wet track)

Figure 109 shows lateral forces Fy, cp2 for gauge corner contact patches. Their magnitudes were roughly half that compared to the dry track conditions plotted in Figure 79 and they varied with curvature and lateral coupler forces in the same manner as Fx, cp2 forces (see Figure 107).

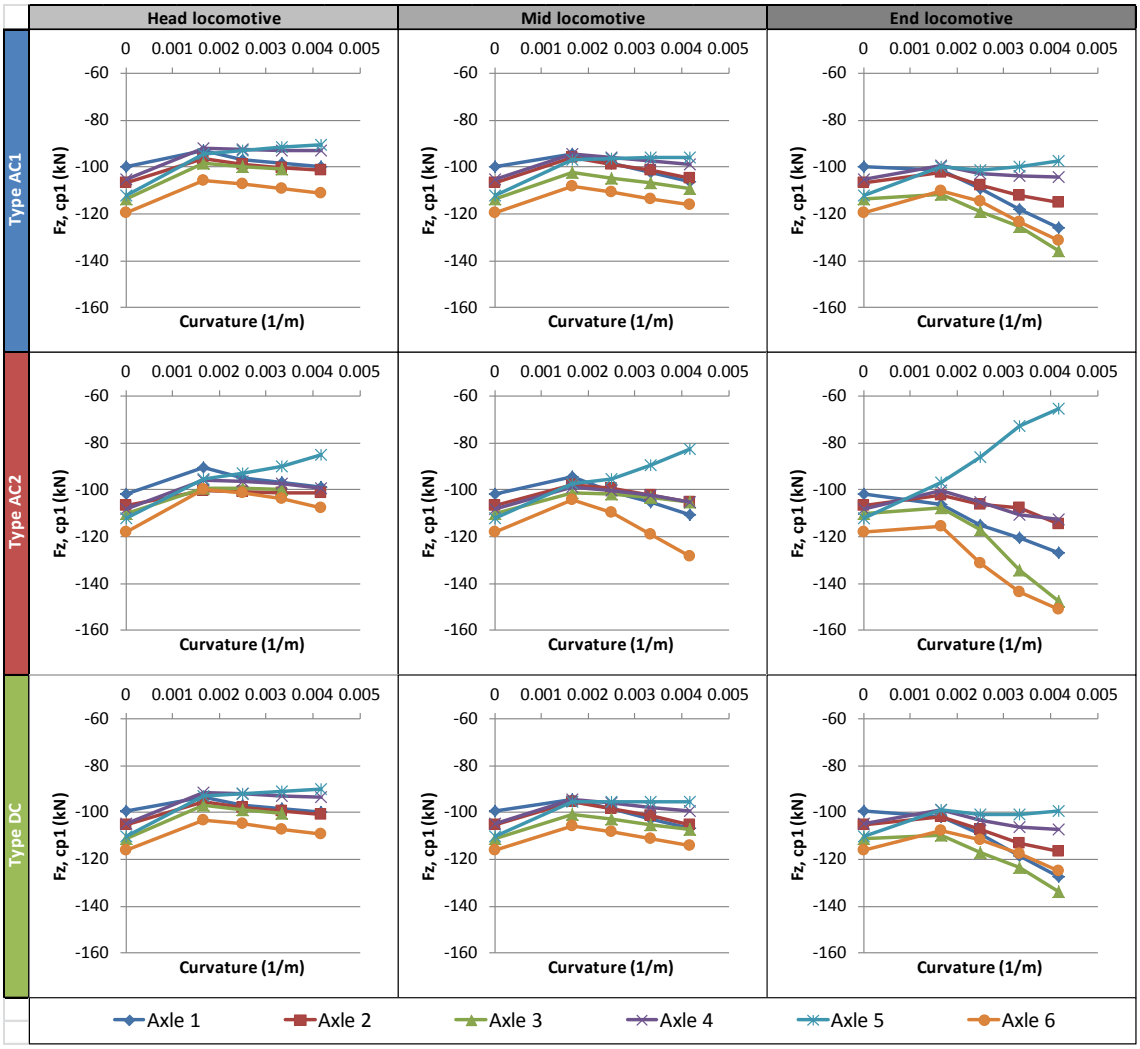

Figure 110: Rail head contact patch vertical forces Fz, cp1 (high rail, wet track)

Vertical forces Fz, cp1 for rail head contact patches are shown in Figure 110, where downward acting forces are positive. There was not much change between the wet and dry rail head conditions. High unloading still occurred for Axle 5's high rail wheel, which most likely lead to the (corresponding) drop in Fx, cp1 visible in Figure 106.

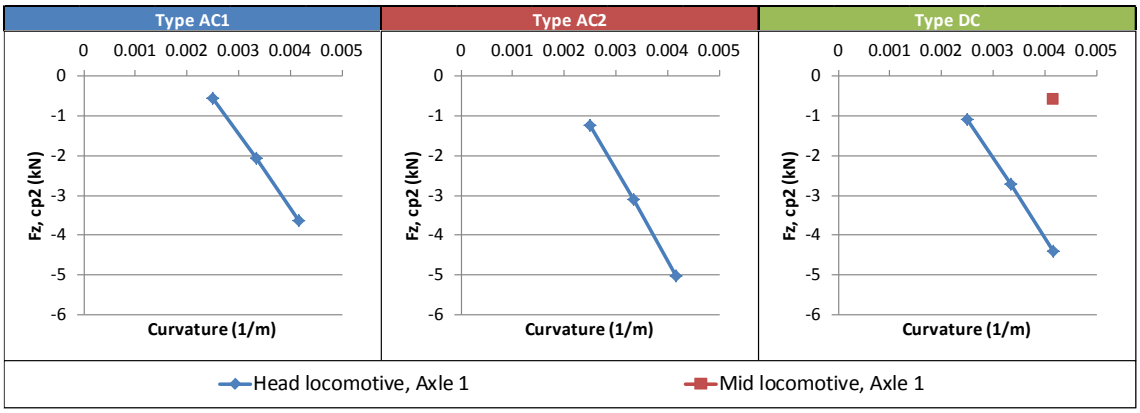

Figure 111: Gauge corner contact patch vertical forces Fz, cp2 (high rail, wet track)

Gauge corner contact patch vertical forces Fz, cp2 are displayed in Figure 111. For wet rail head conditions, Fz, cp2 was roughly halved in comparison to dry rail head conditions.

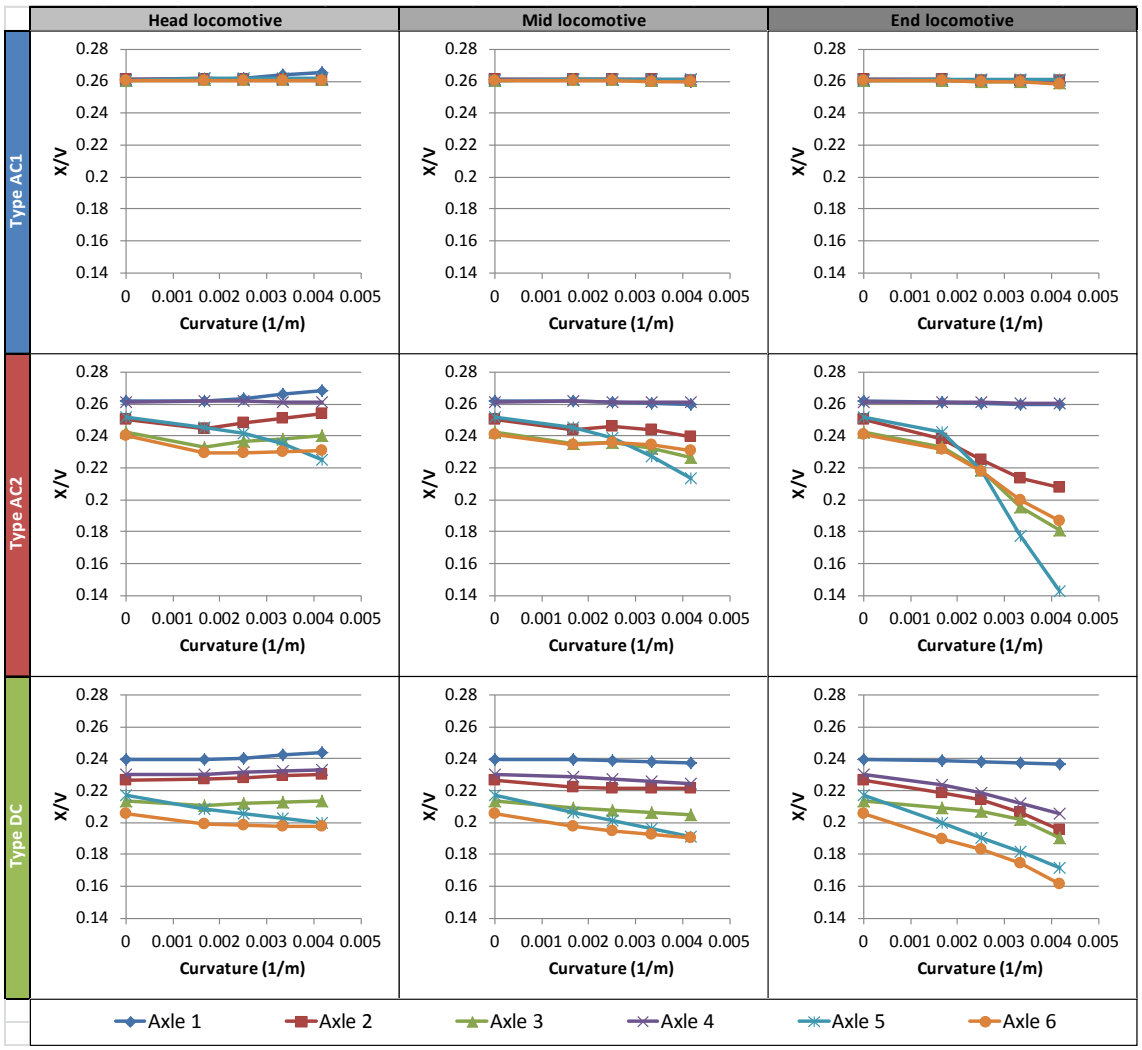

Figure 112: Approximate wheel adhesion coefficients X/V (high rail, wet track)

Figure 112 shows the approximate adhesion coefficients X/V simulated for high rail wheels on wet track. Lower adhesion coefficients were obtained for wet rail head conditions when compared to dry conditions. X/V coefficients for Types AC2 and DC were similarly affected by lateral coupler force and curvature variations for both dry and wet track. Type AC1's behaviour in this regard differed, with X/V almost constantly maintained at ~0.26.

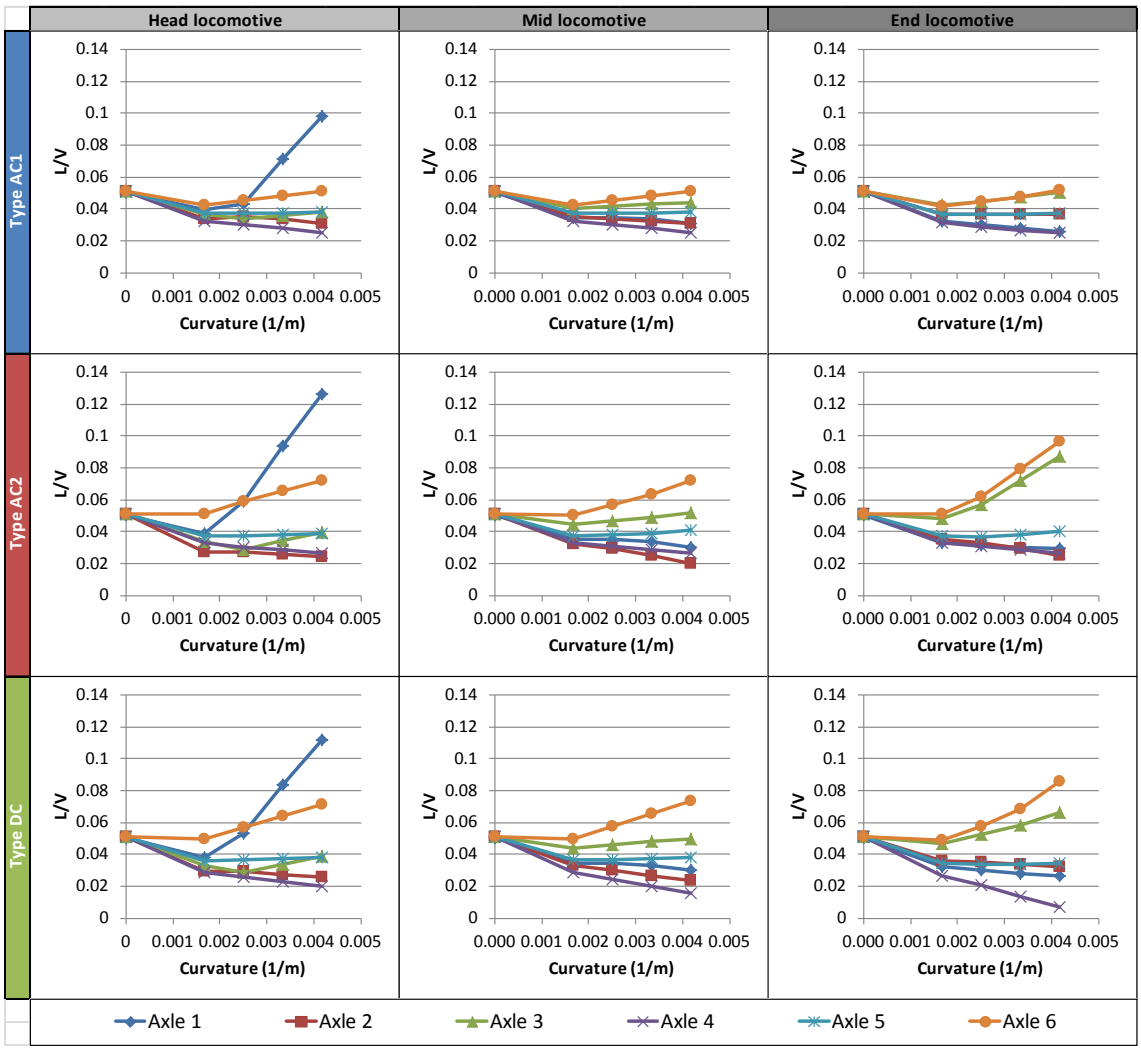

Figure 113: Wheel L/V ratios (high rail, wet track)

High rail wheel L/V ratios for wet track are shown in Figure 113. In common with the dry track simulations (Figure 83), high wheel L/V ratios for Axles 2-6 on wet track were similarly affected by curvature and locomotive position as their corresponding Fy, cp1 forces (Figure 108). On wet track, L/V ratios were reduced, particularly as lateral coupler forces increased down locomotive groups. In head locomotives, L/V for Axle 1 appeared to be more sensitive to increasing curvature.

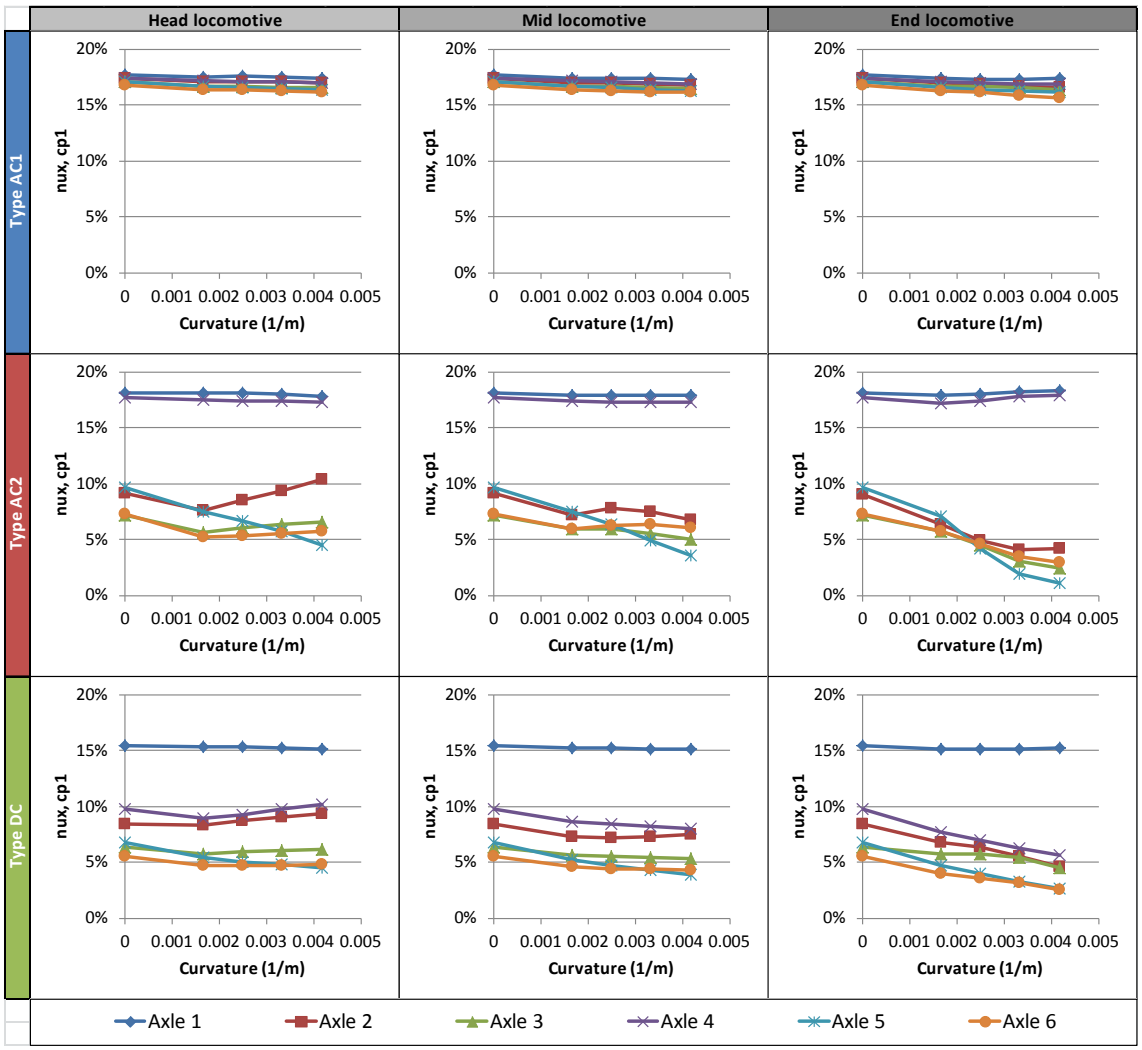

Figure 114: Rail head contact patch longitudinal creepages nux, cp1 (high rail, wet track)

Figure 114 shows longitudinal creepages for the rail head contact patch nux, cp1, where forward deflections are positive. When looking at Types AC2 and DC, nux, cp1 for all wheelsets was roughly doubled for wet track but varied with curvature and lateral coupler forces in a similar manner to nux, cp1 on dry track (Figure 84). Type AC1 was able to consistently maintain high creepages across wheelsets, with changes in curvature and lateral coupler forces having little effect.

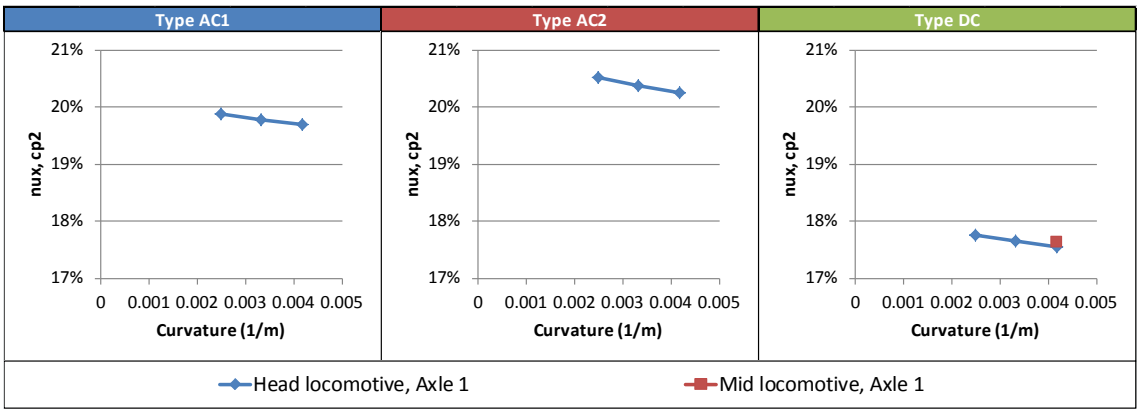

Figure 115: Gauge corner contact patch longitudinal creepages nux, cp2 (high rail, wet track)

Longitudinal creepages for the rail head contact patch nux, cp2 are shown in Figure 115. Although nux, cp2 for wet track was roughly twice that for dry track (Figure 87), similar variations with respect to lateral coupler forces and curvature were visible. Increasing curvature tended to lower nux, cp2 whilst increasing coupler forces resulted in a slight nux, cp2 increase.

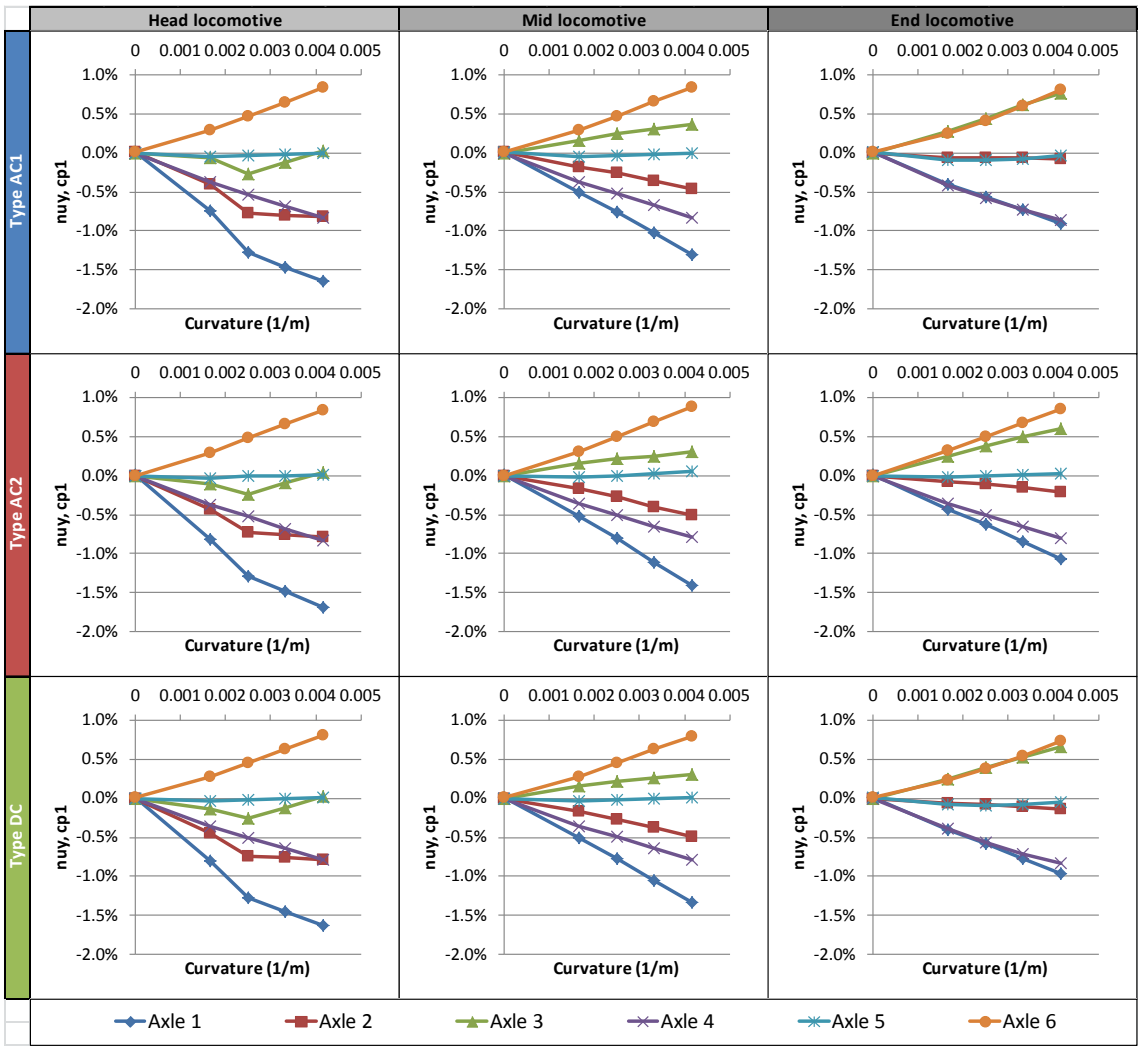

Figure 116: Rail head contact patch lateral creepages nuy, cp1 (high rail, wet track)

Lateral creepages nuy, cp1 for rail head contact patches are shown in Figure 116. As for dry track (Figure 86), the variation of nuy, cp1 with curvature, locomotive type and locomotive position was just about identical to that for Angle of Attack p (Figure 105). The magnitudes of nuy, cp1 for both dry and wet track were also close.

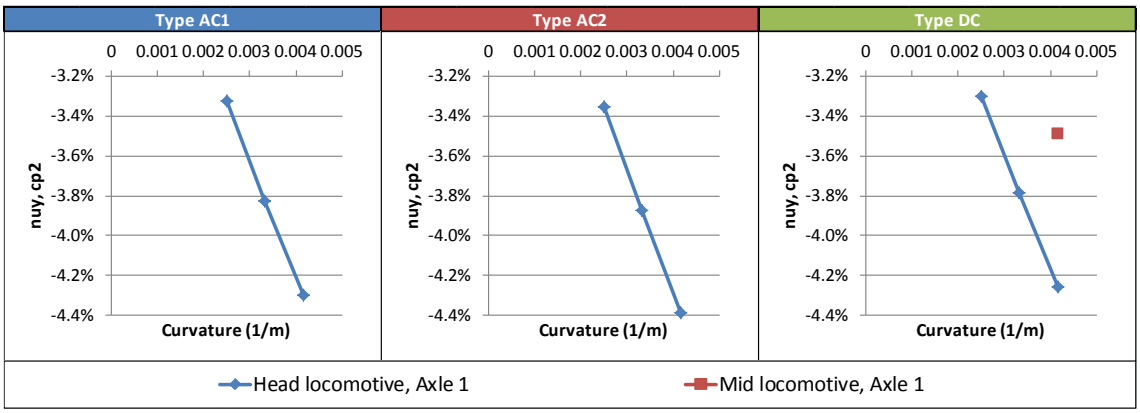

Figure 117: Gauge corner contact patch lateral creepages nuy, cp2 (high rail, wet track)

Figure 117 shows lateral creepages nuy, cp2 for gauge corner contact patches. Compared to dry track (Figure 87), nuy, cp2 seemed to be more sensitive to increase of both curvature and lateral coupler forces. In other words, nuy, cp2 was larger for head locomotives on wet track but there was a significant drop for the Type DC mid locomotive.

6.4.2.3. Low (right) rail forces

When running the locomotive models on wet track, two-point contact at the rail head (cp1) and gauge corner (cp2) occurred more often than for dry track. Mid and end locomotives always experienced such two-point contact in all curve radii. As for head locomotives, cp2 contact never occurred for Axle 1. Axle 2 meanwhile was in cp2 contact for all locomotive types in the 400 m and 300 m radii curves, with Type DC also in cp2 contact for the 600 m radius curve. In wet rail head conditions, it appears that locomotives may be riding more on the low rail when compared to dry rail head conditions, given that there was less two-point contact on the high rail and more on the low rail.

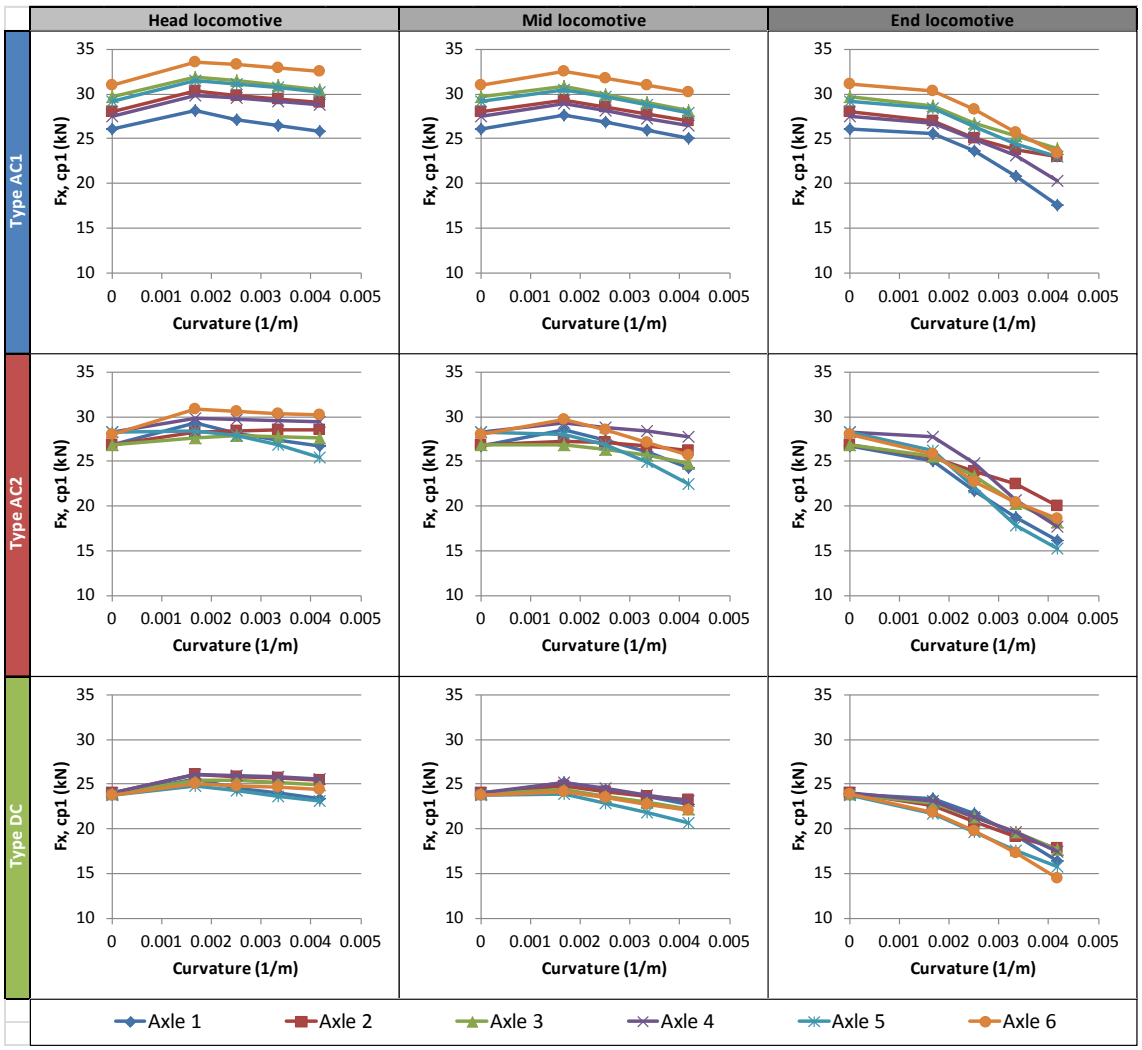

Figure 118: Rail head contact patch longitudinal forces Fx, cp1 (low rail, wet track)

Figure 118 shows longitudinal forces within rail head contact patches Fx, cp1, where forward acting forces are positive. In common with the dry track results (Figure 84), Fx, cp1 increased from tangent track to the 600 m radius curve, at least for the head and mid locomotives, then decreased as curvature increased. Increasing lateral coupler forces also resulted in worse Fx, cp1 for curved track sections. For wet rail head conditions, Fx, cp1 forces were reduced, but Fx, cp1 amongst low rail wheels varied less for all locomotive models in comparison to dry rail conditions. Axles 5 and 6 in Type AC1 were found to produce higher Fx, cp1, at least in proportion to other axles, than for dry track.

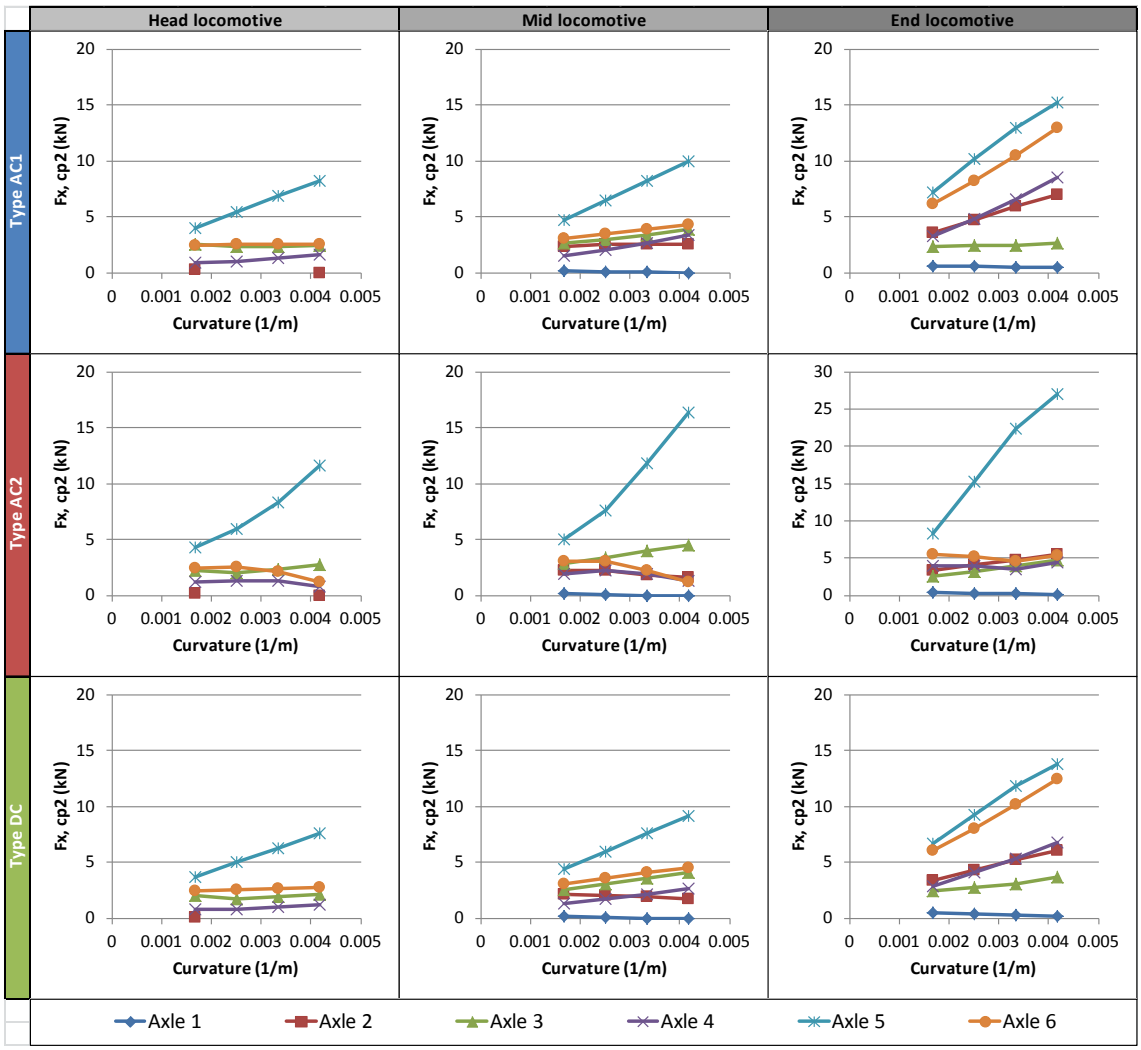

Figure 119: Gauge corner contact patch longitudinal forces Fx, cp2 (low rail, wet track)

Longitudinal forces for gauge corner contact patches Fx, cp2 are shown in Figure 119. As expected, lower Fx, cp2 was obtained for wet track than for dry track. Forces for low rail wheels on Axles 2-4 and 6 changed with curvature and lateral coupler forces in a differing manner to those on dry track (Figure 89), with Axle 6 in particular exerting lower Fx, cp2. Once again, Axle 5 in Type AC2 was exerting high Fx, cp2 forces due to its high loading on the low rail.

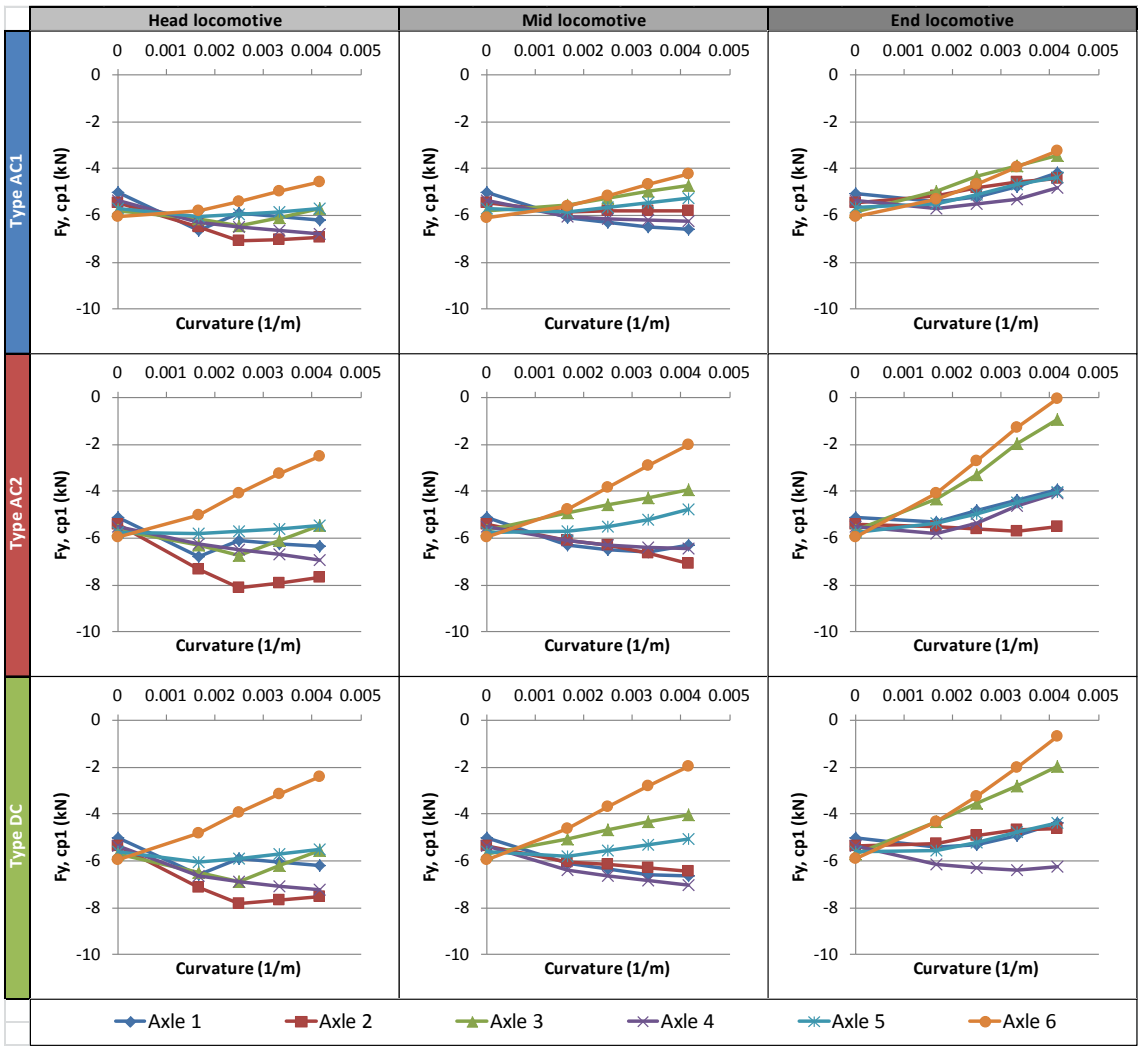

Figure 120: Rail head contact patch lateral forces Fy, cp1 (low rail, wet track)

Figure 120 shows lateral rail head contact patch forces Fy, cp1, where right acting forces are positive. In general, Fy, cp1 across wheelsets in curves deviated less from tangent track readings in comparison to the equivalent dry track data in Figure 90. As lateral coupler forces increased, Fy, cp1 for high rail wheels increased more with increase of curvature; hence, for high lateral coupler forces and low radii curves, high rail wheels (and their wheelsets) were forced more toward the low rail.

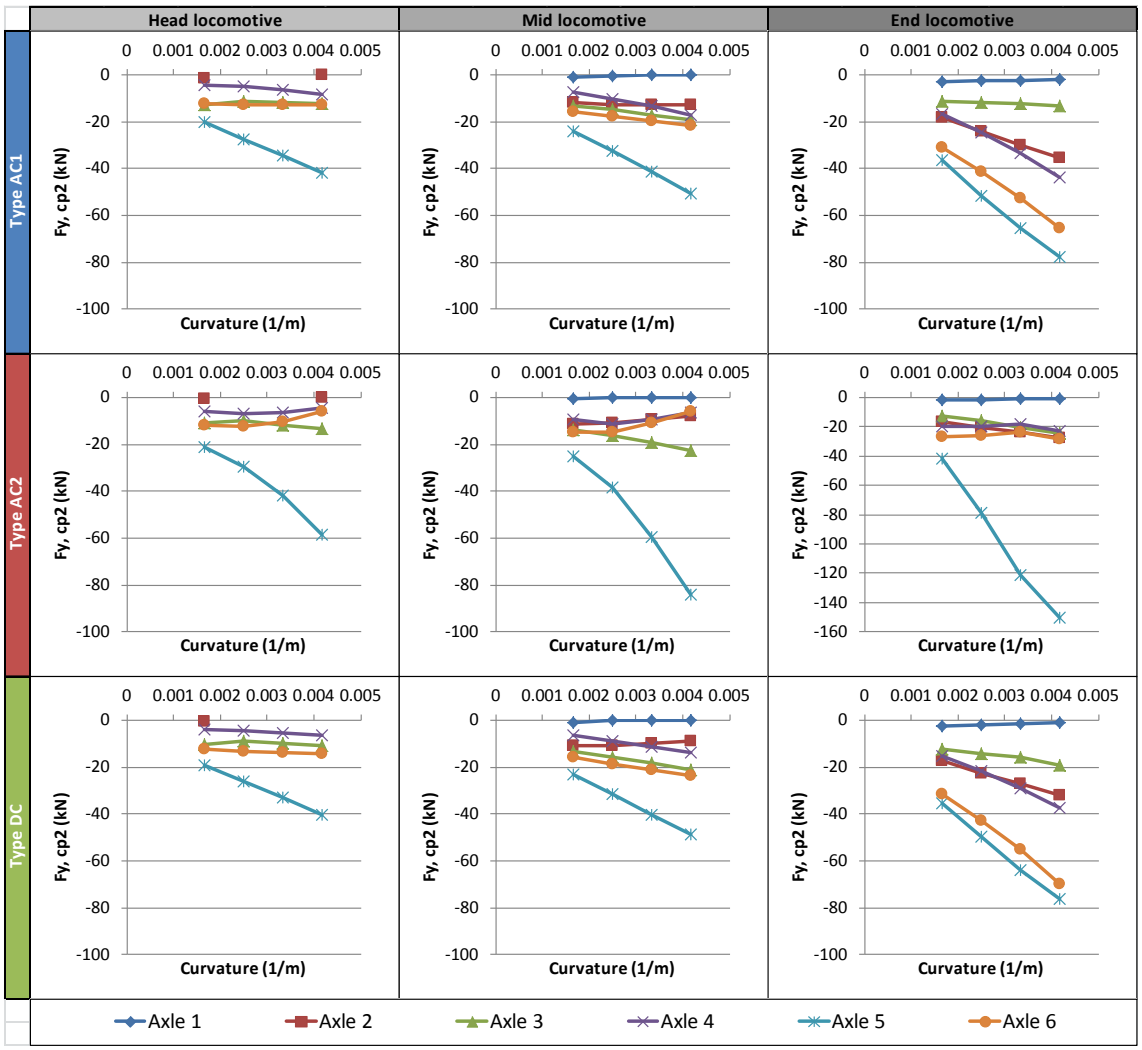

Figure 121: Gauge corner contact patch lateral forces Fy, cp2 (low rail, wet track)

Lateral gauge corner contact patch forces Fy, cp2 are shown in Figure 121. As was the case in dry rail head conditions (Figure 91), Fy, cp2 across wheelsets varied in much the same manner as Fx, cp2 in response to curvature, locomotive type and locomotive position. Fy, cp2 for Axles 1 and 5 on wet track were close to dry track values, with Axle 5 in the Type AC2 locomotive model still producing much higher Fy, cp2 than for Types AC1 and DC. A suspension fault, most likely due to improperly-adjusted axle box lateral clearances (at least on the mid-axles in the semi-steering bogie model), forced Axle 5 hard toward the low rail in curves.

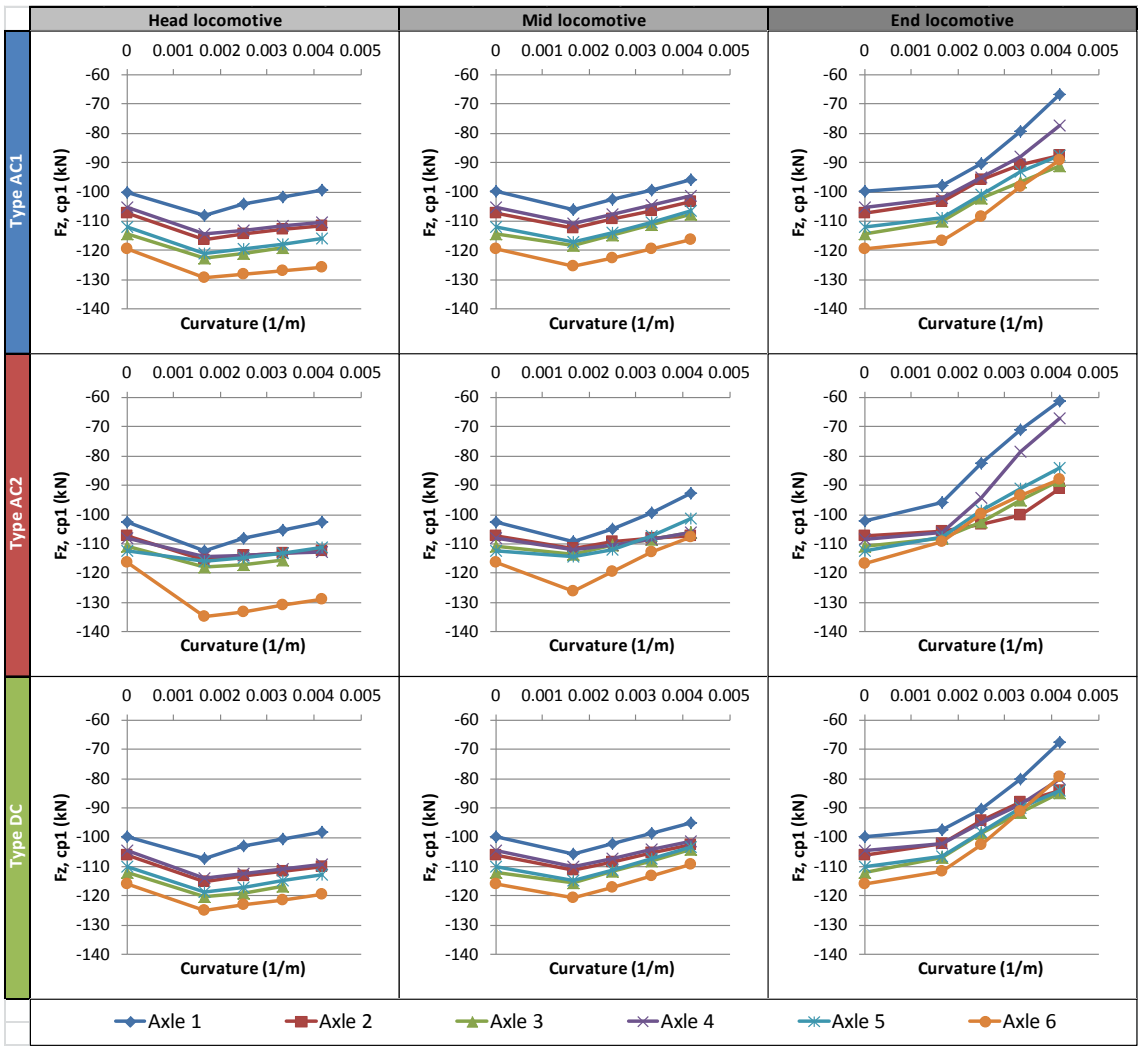

Figure 122: Rail head contact patch vertical forces Fz, cp1 (low rail, wet track)

Figure 122 shows vertical forces Fz, cp1 for rail head contact patches on the low rail, where downward acting forces are positive. In general, Fz, cp1 varied with curvature and lateral coupler force on wet track in much the same manner as for dry track, whilst overall force magnitudes are also close. Looking at Axle 6 in the rigid bogie models Type AC1 and DC, Fz, cp1 was slightly higher for wet rail head conditions than for dry conditions.

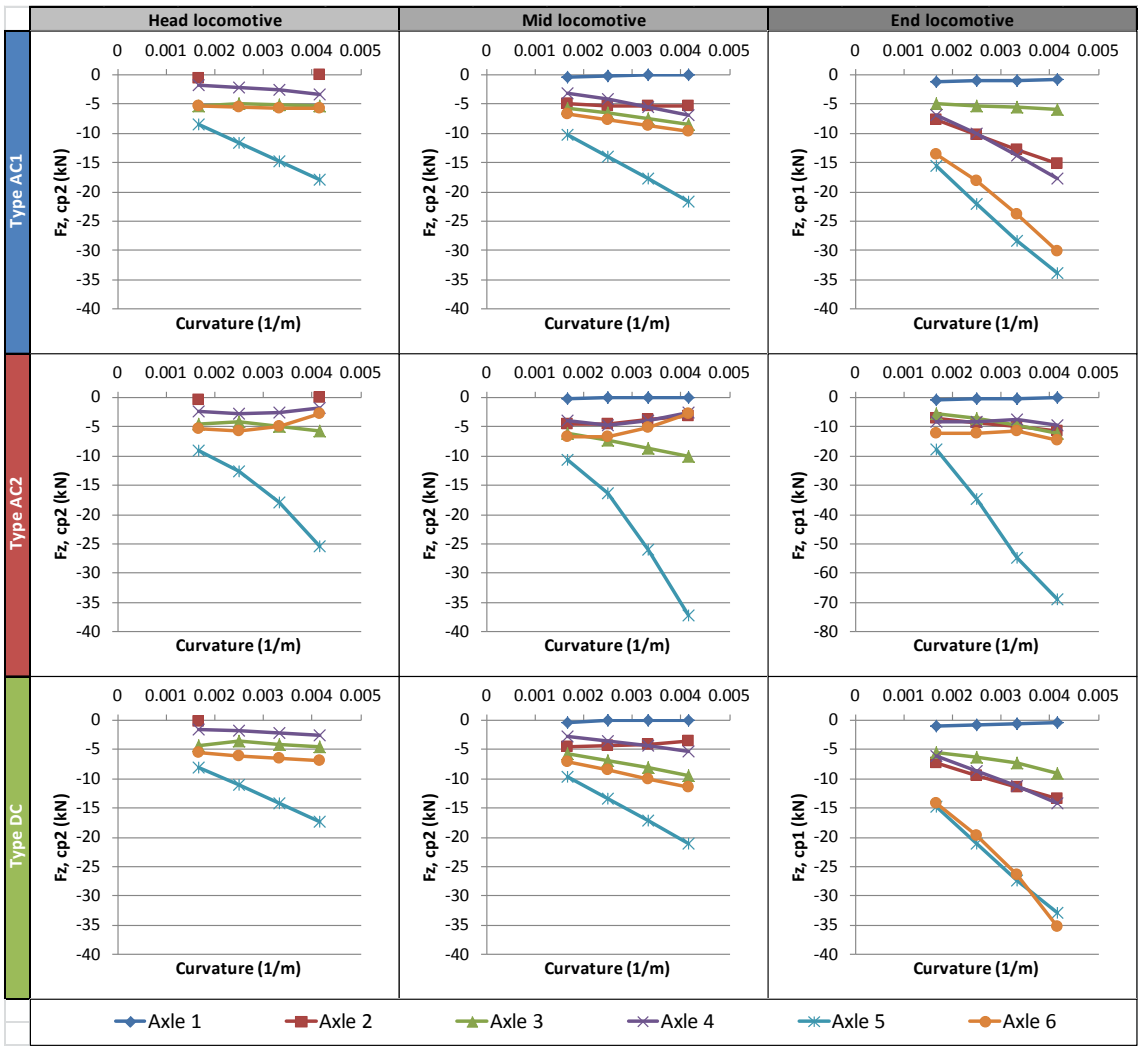

Figure 123: Gauge corner contact patch vertical forces Fz, cp2 (low rail, wet track)

Figure 123 shows vertical forces Fz, cp2 for rail head contact patches on the low rail, which varied with curvature and locomotive position in a similar manner to Fx, cp2 and Fy, cp2. Compared to dry track, Axles 1 and 5 on wet track exerted similar Fz, cp2 forces, with differences visible for Axles 2-4 and 6.

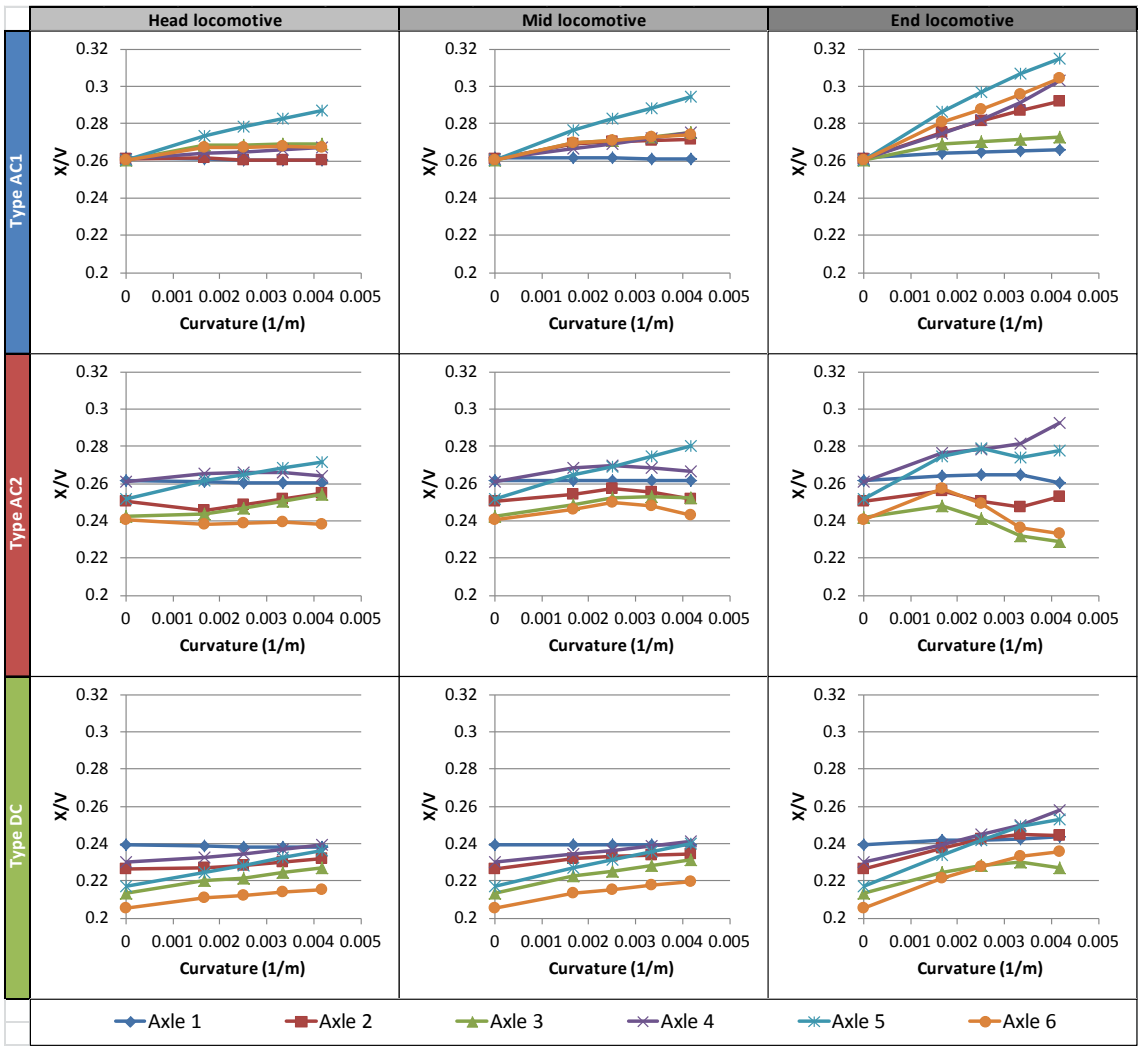

Figure 124: Approximate wheel adhesion coefficients X/V (low rail, wet track)

Approximate low rail wheel adhesion coefficients X/V for wet track are plotted in Figure 124. Compared to dry track, X/V coefficients were lower because less longitudinal force Fx could be exerted on wet track. X/V across low rail wheels for Types AC2 and DC on wet track varied in a similar manner with curvature and lateral coupler forces, whereas proportionally higher adhesion coefficients were realised for Axles 3, 5 and 6 for Type AC1.

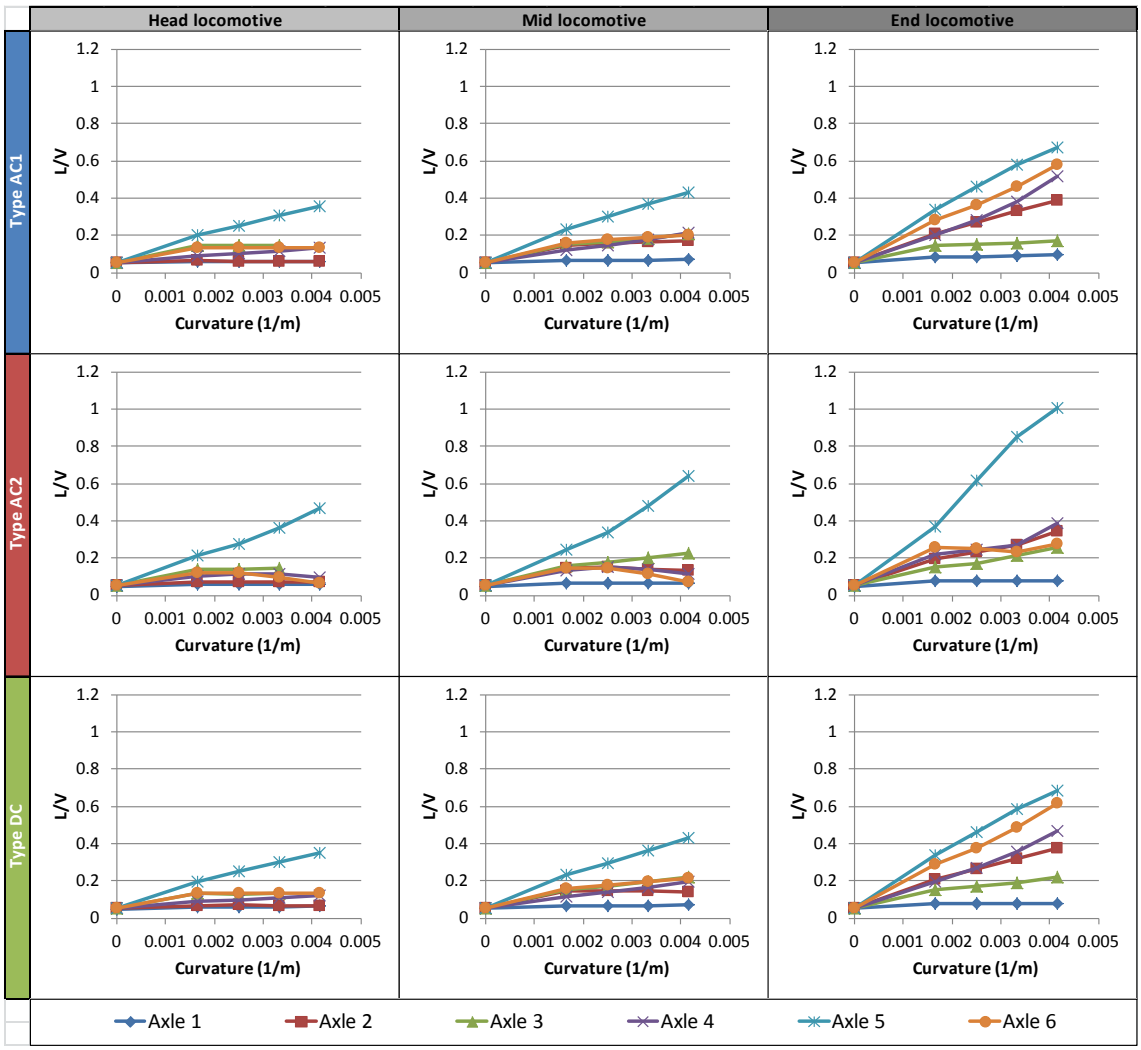

Figure 125: Wheel L/V ratios (low rail, wet track)

Figure 125 shows L/V ratios for low rail wheels on wet track, which were largely similar to the dry track results in Figure 95. A key difference occurred for Axle 6 in the rigid bogie Type AC1 and DC locomotive models, where L/V was reduced slightly because of the increased wheel loads Fz noted earlier. For the Type AC2 end locomotive, L/V for Axle 5 reached a maximum of 1.010 in the 240 m radius curve, slightly exceeding the maximum value of 1 recommended in AS 7509.1 [21].

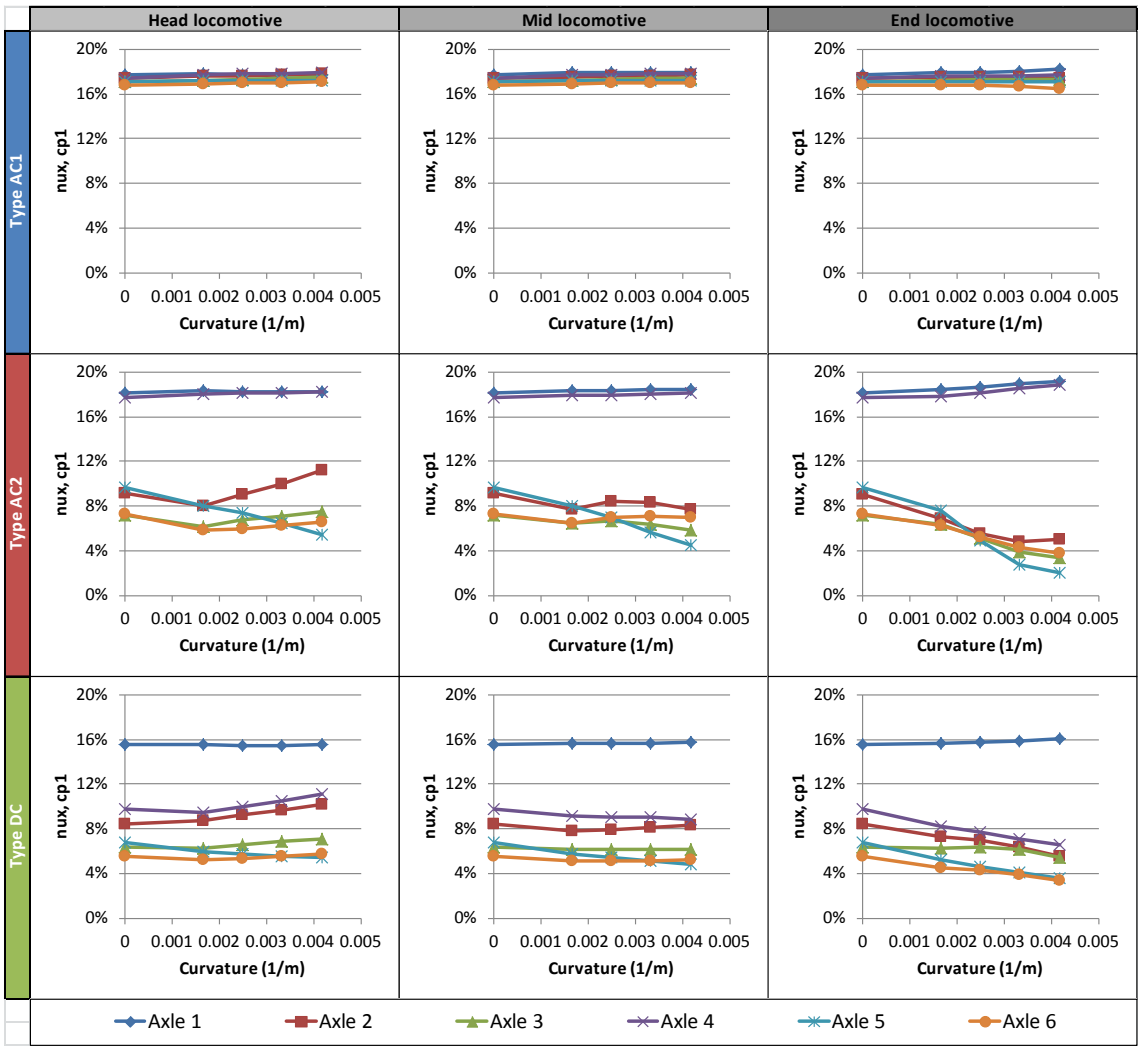

Figure 126: Rail head contact patch longitudinal creepages nux, cp1 (low rail, wet track)

Rail head contact patch longitudinal creepages for the low rail nux, cp1 are plotted in Figure 126. These results were very similar to nux, cp1 for the high rail seen earlier in Figure 114. The same phenomenon occurred for dry track where nux, cp1 for both high and low rail wheels were much the same.

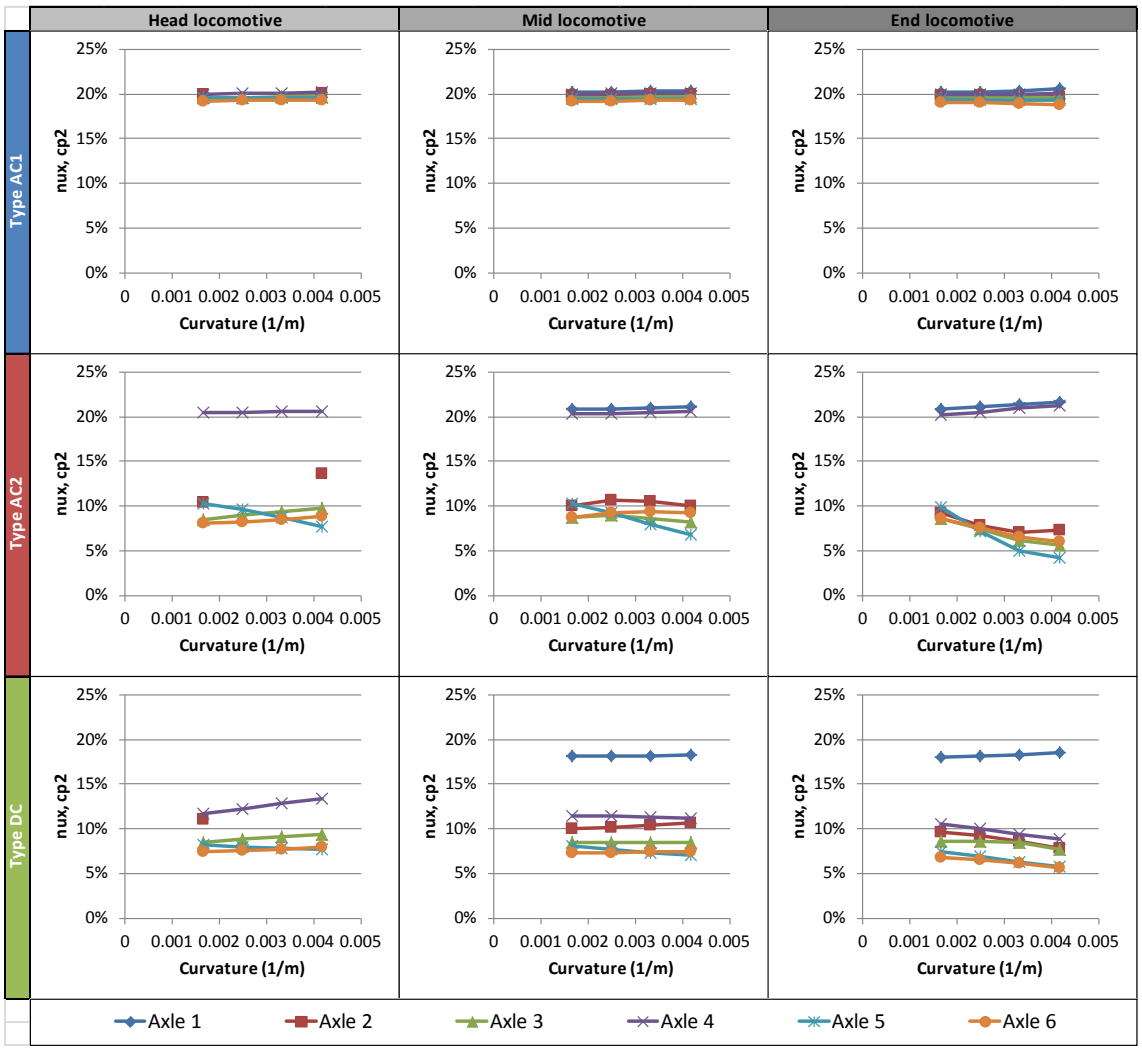

Figure 127: Gauge corner contact patch longitudinal creepages nux, cp2 (low rail, wet track)

Figure 127 shows longitudinal creepages nux, cp2 for gauge corner contact patches. At points where cp1 and cp2 contact occurred, nux, cp2 varied in a similar manner with coupler force and curvature as nux, cp1 but the corresponding nux, cp2 creepages were ~1-2% higher.

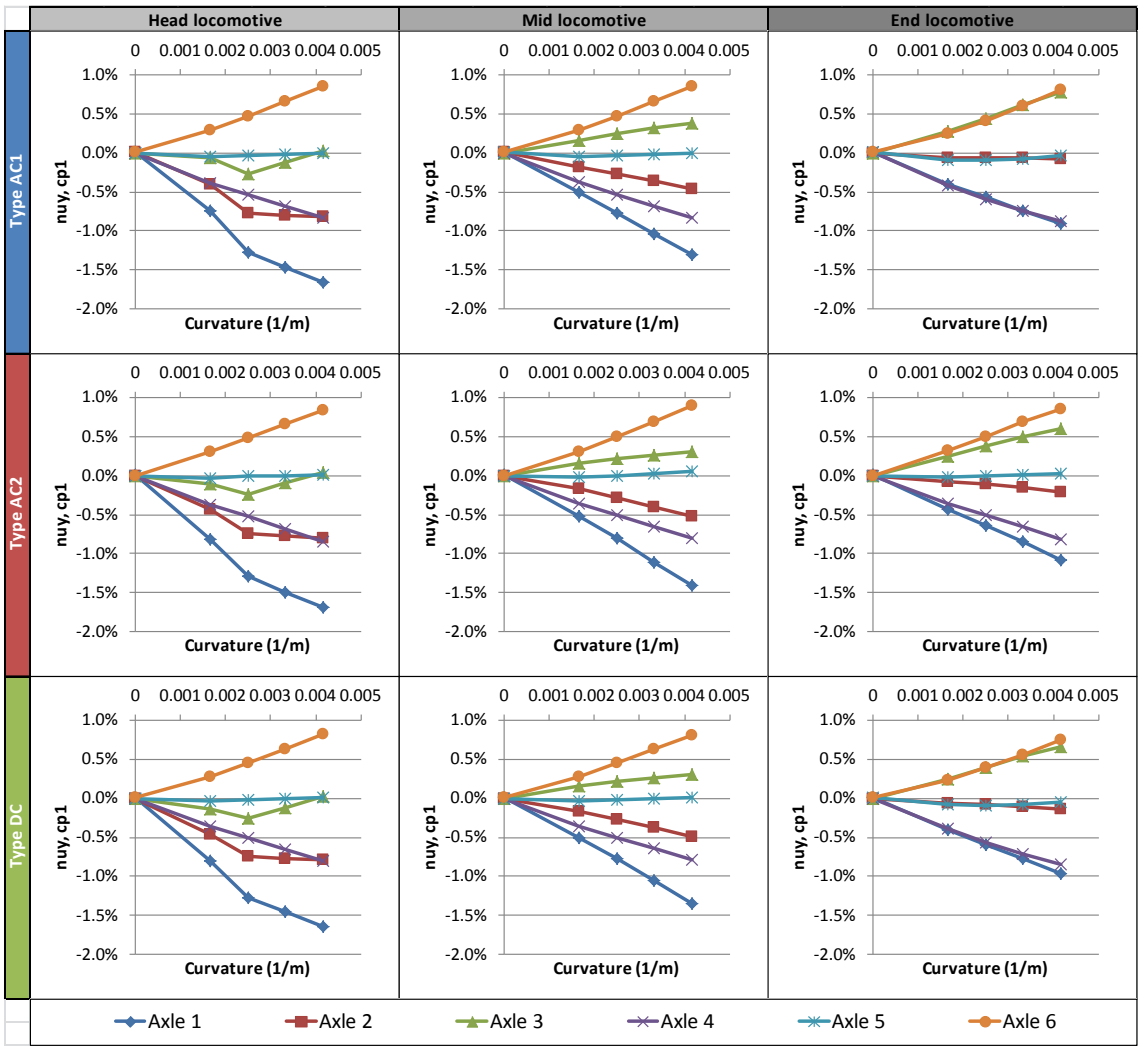

Figure 128: Rail head contact patch lateral creepages nuy, cp1 (low rail, wet track)

Lateral creepages nuy, cp1 for rail head contact patches on the low rail are shown in Figure 128. Results for nuy, cp1 on the low rail are just about identical to those for nuy, cp1 on the high rail seen earlier in Figure 116. The same phenomenon occurred for dry track where nuy, cp1 for both high and low rail wheels were practically identical.

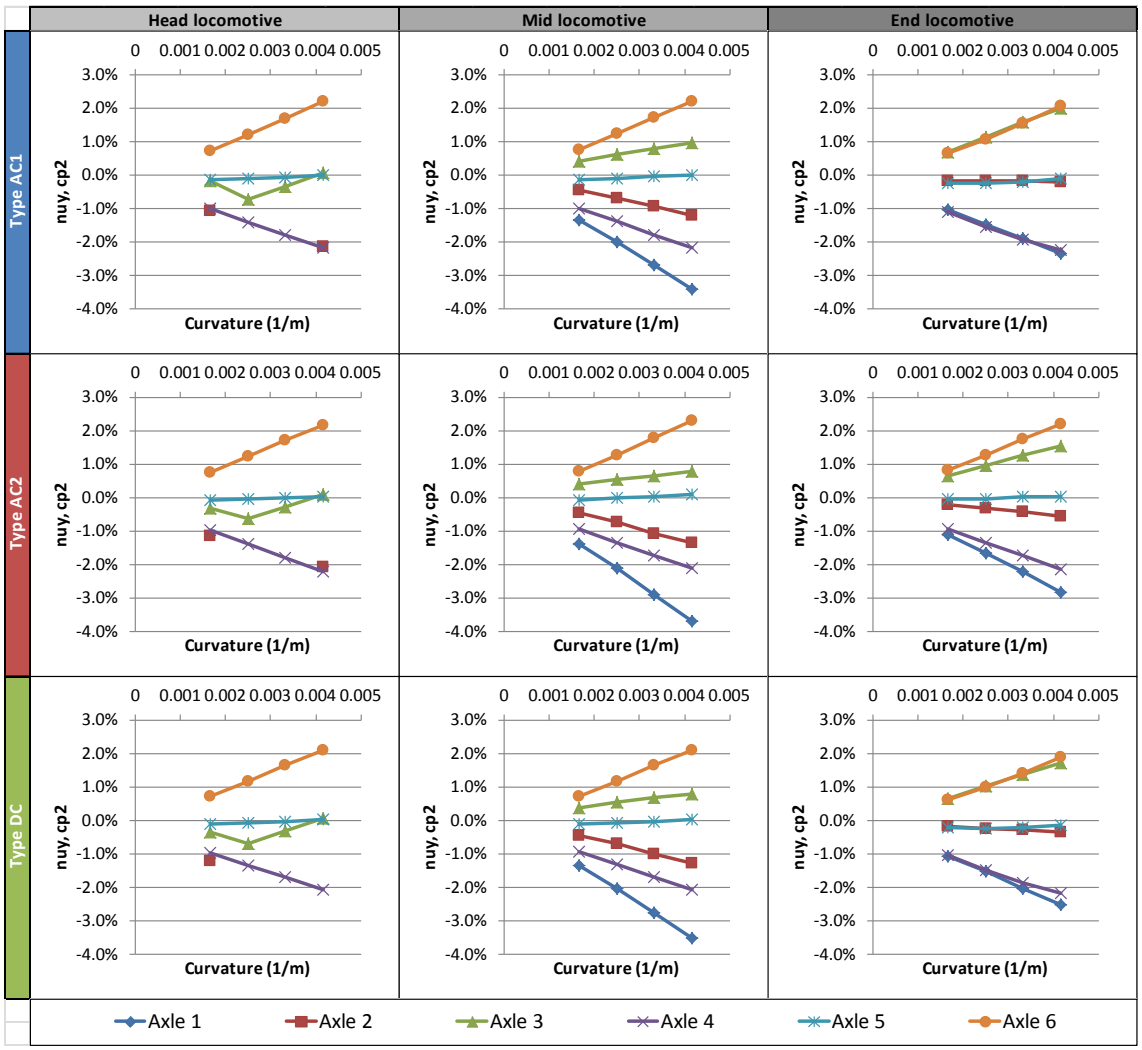

Figure 129: Gauge corner contact patch lateral creepages nuy, cp2 (low rail, wet track)

Figure 129 shows lateral creepages for gauge corner contact patches nuy, cp2. As for nuy on dry track, nuy, cp2 for wet track varied in a similar manner with curvature and coupler force as nuy, cp1 but the corresponding nuy, cp2 creepages were ~2.5 times higher.

6.5. Discussion

In this section, a detailed analysis was undertaken to determine how a wide range of input parameters affected locomotive dynamics and wheel-rail forces. Recall that, in all cases, groups of three locomotives, all of the same type, powered at the head end of 55 wagon trains whilst exerting maximum continuous tractive effort at minimum constant speeds. Because the AC drive locomotives could exert greater tractive effort, their trains were more heavily loaded to bring them down to minimum speed [3]. To simulate wheel-rail forces in detail, a simulation

methodology was developed [109] that allowed input from traction control models and approximated lateral coupler force data from longitudinal train simulation.

After analysing the various wheel-rail forces and other output parameters detailed in Section 6.4, it is possible to identify how changes in the input parameters generally affected locomotive dynamics. Recall that the following input parameters were considered in these simulations:

- Locomotive model types (3) = AC1, AC2 and DC
    - Traction Control systems = Per wheelset (Type AC1), Per bogie (Type AC2) and per locomotive (Type DC)
    - Bogie model types = Rigid (Types AC1 and DC), semi-steering (Type AC2)
- In-train locomotive positions (3)= Head, mid (middle) and end of locomotive group
- Curve radii (4) = 240, 300, 400 and 600 m (tangent track was also considered)
- Friction conditions (2) = Dry and wet rail heads (friction coefficients in the gauge corner and flange contact zones were the same in both cases)

Longitudinal wheel-rail forces, and consequently adhesion coefficients, were most affected by the traction control (TC) systems modelled. The more wheelsets that were monitored in a locomotive model's TC system, the better it was able to maintain high traction forces in response to:

- Car-body and bogie frame pitching when locomotive models were under traction
- Increasing lateral coupler forces applied to locomotive models
- A reduction in rail head friction (from dry to wet track)

Because of this, Type AC1's per-wheelset TC system was consistently able to exert the most traction force, followed by Type AC2 (per bogie control) and Type DC (per locomotive control). On wet track, Type AC1 was far better able to achieve high traction forces and adhesion coefficients than Types AC2 and DC.

After completing these simulations, it was noticed that the semi-steering bogie models used in Type AC2 need further development work. The most obvious fault occurred in Axle 5 (the

middle axle in the second bogie), where it was forced hard toward the low rail in curves, generating high track-shifting forces and L/V ratios. This increased vertical load on low rail wheels with a corresponding decrease on the high rail. As a result, longitudinal forces for each wheel were affected. Improperly adjusted lateral clearances in the axle-boxes are the most likely source of this problem. When comparing the semi-steering and rigid bogie models, the semi-steering bogie model was found to more susceptible to traction-induced car-body and bogie frame pitching, especially as curvature and lateral coupler forces on the locomotives increased. Wheelset Angles of Attack generated by the rigid and semi-steering bogie models were close, but Bogie 1 in Type AC2 was found to steer less effectively in some cases, particularly on dry track. Lateral track-shifting forces for Axles 1-4 and 6 in the semi-steering bogie model were lower in comparison to the rigid bogie model, but it's presently unclear how much of this is attributable to the axle-box fault in Axle 5. Notwithstanding any modelling errors, the rigid and semi-steering models steered in a similar manner when under traction, echoing earlier findings by Grassie & Elkins [6, 7].

Increasing curvatures were found to impact wheelset lateral forces and Angles of Attack. Recall that, for head locomotives on dry track, Axles 3-6 were forced hard enough onto the low rail that two-point contact occurred on the wheel tread / rail head and gauge corner zones. Axle 1 meanwhile was in two-point contact on the high rail, whereas Axle 2 was always only in single-point rail head contact on the high rail. As curvatures increased, Axles 3-6 were forced more toward the low rail and Axle 1 more toward the high rail. In those cases, more force was being exerted by the gauge corner contact patches, leading to a corresponding reduction in forces exerted by the rail head contact patches. As curvature increased, so did wheelset Angles of Attack, because insufficient lateral forces could be generated to properly steer the wheelsets [20, 23, 25, 29]. Since high traction forces were applied to wheelsets, most of the available slip area in contact patches was being used to transmit longitudinal force, with little left over for lateral steering forces [6, 7]

Coupler forces were found to increase from the head to end locomotives along locomotive groups [5]. As lateral coupler forces increased, locomotives were pulled harder toward the low

rail [1], causing wheelsets to ride harder on the low rail. In end locomotives, all wheelsets were in two-point contact on the low rail because of this, and in single-point rail head contact on the high rail. Increasing lateral coupler forces saw reductions in wheel-rail forces on high rail wheels, whilst for low rail wheels, wheel-rail forces were reduced in the rail head contact zone as they increased in the gauge contact zone. For high curvatures and lateral coupler forces, most wheel-rail forces were transmitted through gauge corner contact on the low rail. Increasing coupler forces were also found to worsen traction-induced car-body and bogie frame pitching, especially in end locomotives.

In wet rail head conditions, lower traction forces could be exerted, although Type AC1's TC system proved particularly effective with maximising the available adhesion. Longitudinal contact patch creepages nux were also ~2 – 2.5 times higher for wet track. Lateral forces and wheelset steering were largely unaffected because:

- Only rail head friction differed between dry and wet track in this analysis, where friction coefficients in the gauge corner and flange contact zones were identical
- Most of the lateral steering forces were exerted by gauge corner contact patches on the low rail
- Net lateral forces on the locomotive models wouldn't have changed much as they were travelling at the same speeds and with the same applied coupler forces regardless of rail head friction conditions

In Section 6.4.1.1 a comparison was made between the locomotive models under traction and coupler forces on dry track in this analysis, and the rolling locomotive tests in Section 5.3.1. This comparison wasn't ideal because, even though the curve radii were close (240 m versus 233 m), the rolling locomotive models travelled much faster through curves (20-23 km/h versus 39.7 km/h). That said, steering performance of Bogie 1 was similar for head and mid locomotives of the same type under both rolling and powering conditions, whilst Bogie 2 steered worse for rolling locomotives in comparison to those under traction and coupler forces. For tests under traction, Bogie 2's steering (and Axles 4-6 within) was found to be largely unaffected by either lateral coupler forces or changes in rail head friction.

One last point to make is that only new wheel and rail profiles were used in these simulations, owing to the lack of publically available worn wheel/rail profiles. Contact between worn wheels and rail is expected to differ significantly in comparison to new profiles, with a corresponding impact on the resulting wheel-rail forces. Additional research will be required to analyse the effects of worn rail profiles should any be made available in future.

7. Conclusions

In this thesis, a detailed simulation methodology was developed to allow the calculation of wheel-rail contact forces for locomotives under traction within trains. This methodology allowed a theoretical and numerical investigation on aggregate locomotive traction forces to be performed for a wide variety of scenarios that were relevant to Australian freight rail practices.

Some tests contained within the Locomotive Model Acceptance Procedure (LMAP) were performed to help identify any major sources of error within the locomotive models. Most undesirable behaviour was mitigated in the rigid bogie Type AC1 and Type DC models. However, by the time wheel-rail force analyses commenced, there were still a few faults present within the semi-steering bogie Type AC2 model. Compared to previous LMAP applications [108, 110], the methodology was capable of being adapted to test multiple locomotive model types and basic traction force modelling. Since the LMAP was not the main focus of this thesis, plenty of opportunities remain for future research.

Supplementary tests were also conducted to validate the steering performances of locomotive bogie models in this thesis by comparing them to an existing analysis [4] for free rolling locomotives (i.e., with no traction forces applied). Angles of Attack (AoAs) were similar between the two rigid bogie models, whilst the semi-steering bogie model produced AoAs that were closer to that of rigid bogies in comparison to the semi-steering bogie described in [4]. In this thesis, the semi-steering bogie model produced slightly better AoAs than the rigid bogie model, but only between 1-2 mrad in most cases.

The methodology used in the wheel-rail force analysis was first presented in [109], whereas a far wider array of input and output parameters was considered in this thesis. As in the related CRE-LTS analysis [3], there were three locomotives of each type powering at the head of 55 wagon trains through various (right-handed) curve radii. Lateral coupler forces were found to increase down the length of the group of locomotives hauling the train [5], particularly where the trailing locomotive was coupled to the leading wagon as a result of varying coupler centre lengths between that locomotive and the wagon [3]. As applied lateral coupler forces increased,

locomotives were pulled harder toward the low rail [1], resulting in the trailing locomotive having all low rail wheels in two-point contact at the rail head and gauge corner zones. Less wheel-rail forces were produced for high rail wheels, while most of the wheel-rail forces for low rail wheels were transmitted via gauge corner contact. This imbalance worsened further as track curvature increased in addition to higher lateral forces, where increased traction-induced car-body and bogie pitching was also noted.

Longitudinal wheel-rail forces and adhesion coefficients were influenced most by the Traction Control (TC) systems adopted. Type AC1's per-wheelset TC system was able to maintain the highest traction forces in response to traction-induced car-body and bogie frame pitching, increasing lateral coupler forces and reduced rail-head friction, followed by Type AC2's per-bogie TC system and Type DC's per-locomotive TC system.

Wet rail head conditions were found to deleteriously affect longitudinal wheel-rail forces and adhesion ratios, but lateral wheel-rail forces were largely unaffected. This occurred because a) only changes in rail head friction were considered in this analysis (where gauge corner and flanging zone friction coefficients were unchanged), b) most lateral forces were exerted through gauge corner contact, and c) locomotives were run through test tracks at the same speeds and with the same applied coupler forces regardless of rail head friction conditions.

During the analysis, a fault was found for Axle 5 in Type AC2's semi-steering bogies, where lateral track-shifting forces toward the low rail were far higher than for the rigid bogie Type AC1 and DC models. This is most likely the fault of improperly adjusted lateral clearances in the axle-boxes that need to be remedied in future research. Lateral track-shifting forces generated by other axles in Type AC2 were lower than for Types AC1 and DC, especially for higher degrees of curvature and lateral coupler forces, but it's presently unknown how this is influenced by the faulty axle. The semi-steering bogie model was found to be more susceptible to traction-induced car-body and bogie frame pitching (which affected axle loads), whilst Type AC2's lead bogie was found to steer slightly worse than was the case for the rigid bogie models. That said, AoAs for all locomotive types were similar as curvature and lateral coupler forces

varied, indicating that the steering performance of semi-steering bogies deteriorated to the level of rigid bogies as found in earlier research [6, 7].

References

1. CRC for Rail Innovation, *Project details, Project code R3.119, Short project title: Locomotive adhesion*, 2010, Brisbane, Australia.
2. DEsolver, *The GENSYS Homepage*, 2011 [Accessed 3 November 2011]; Available from: http://www.gensys.se/.
3. Sun, Y.Q, Cole, C.R and Spiryagin, M, *Longitudinal Train Simulation (CRE-LTS) Models and Results for CRC Project R3.119 – High Adhesive Traction*, 2012, Central Queensland University, Rockhampton, Australia.
4. Ahmadian, M, *On the virtues of steerable locomotive bogies*, in *ASME Rail Transportation Division, 1997 ASME International Congress and Exposition*, 1997, Dallas, Texas.
5. Cole, C.R, *Longitudinal train dynamics*, in *Handbook of railway vehicle dynamics*, S. Iwnicki, Editor. 2006, Taylor & Francis Group, Boca Raton, FL. pp. 239-277.
6. Grassie, S.L and J.A Elkins, *Traction and curving behaviour of a railway bogie*, Vehicle System Dynamics, 2006. **44** (1 supp 1): pp. 883 - 891.
7. Grassie, S.L and J.A. Elkins, *Tractive effort, curving and surface damage of rails; Part 1. Forces exerted on the rails*, Wear, 2005. **258**: pp. 1235-1244.
8. Ramsey, N, Szanto, F and Hewison, P, *Introducing the next generation locomotive to the Australian rail network*, in *Conference On Railway Engineering (CORE) 2008*, 2008, Perth, Australia.
9. Simson, S and Cole, C.R, *Wheel rail contact damage from high adhesion locomotives, and damage mitigation from steering bogies*, in *Conference On Railway Engineering (CORE) 2010*, 2010, Wellington, New Zealand.
10. Centre for Railway Engineering, *CRE-LTS reference manual*, 2001, Central Queensland University, Rockhampton, Australia.
11. DEsolver, *GENSYS in short*, The GENSYS Homepage, 2011 [Accessed 19 July 2011]; Available from: http://www.gensys.se/GENSYS_in_short/index.html.
12. Duncan, I.B and Webb, P.A, *The longitudinal behaviour of heavy haul trains using remote locomotives*, in *Fourth International Heavy Haul Conference*, 1989, Brisbane, Australia. pp. 587-590.
13. Wagner, S, *Derailment risk assessment*, in *Centre for Railway Engineering*, 2004, Master of Engineering Thesis, Central Queensland University, Rockhampton, Australia.
14. Association of American Railroads, *Chapter 11*, in *Manual of standards and recommended practices*, 1993, Association of American Railroads: Washington, DC.
15. McClanachan, M, Cole, C.R, Roach, D and Scown, B, *An investigation of the effect of bogie and wagon pitch associated with longitudinal train dynamics*, The Dynamics of Vehicles on Roads and on Tracks - Vehicle System Dynamics, 1999, Supplement 33, Swets & Zeitlinger, Amsterdam. pp. 374-385.
16. Wolf, G.P. and Kieres, K.C, *Innovative engineering concepts for unit train service: the slackless drawbar train and continuous center sill trough train*, in *The Fourth International Heavy Haul Railway Conference* 1989: Brisbane, Australia. pp. 124-128.
17. Hay, W.W, *Railroad engineering*. 2nd ed., 1982, Wiley, New York, NY.
18. Parker, C.W, *Design and operation of remote controlled locomotives in freight trains*, Railway Engineering Journal, 1974. pp. 29-38
19. Polach, O, Berg, M and Iwnicki, S.D, *Simulation*, in *Handbook of railway vehicle dynamics*, S. Iwnicki, Editor. 2006, Taylor & Francis Group, Boca Raton, FL. pp. 359-421.
20. Evans, J and Iwnicki, S.D, *Vehicle Dynamics and the Wheel/Rail Interface*, Proceedings of the Institution of Mechanical Engineers, Seminar 'Wheels on Rails - An update', 2002.
21. Standards Australia and Rail Industry Safety & Standards Board, *AS7509.1: Railway Rolling Stock - Dynamic Behaviour - Part 1: Locomotive Rolling Stock*, 2009, Sydney, Australia.
22. Kufver, B, *Optimisation of horizontal alignments for railways*, 2000, PhD Thesis, Royal Institute of Technology, Stockholm, Sweden.

23. Shabana, A.A, Zaazaa, K.E and Sugiyama, H, *Railroad vehicle dynamics: A computational approach*, 2008, CRC Press, Boca Raton, FL.
24. DEsolver, *Users manual for program CALC*, The GENSYS Homepage, 2011 [Accessed 17 January 2012]; Available from: http://www.gensys.se/doc_html/calc.html#jLocalCoordinateSystems.
25. Ayasse, J-B and Chollet, H, *Wheel-rail contact*, in *Handbook of railway vehicle dynamics*, S. Iwnicki, Editor. 2006, Taylor & Francis Group, Boca Raton, FL. pp. 85-120.
26. Hertz, H, *Über die berührung fester elastische Körper und über die Harte*, in *Verhandlungen des Vereins zur Beförderung des Gewerbefleisses*, 1882: Leipzig.
27. Olofsson, U and Lewis, R, *Tribology of the wheel-rail contact*, in *Handbook of railway vehicle dynamics*, S. Iwnicki, Editor. 2006, Taylor & Francis Group, Boca Raton, FL. pp. 121-141.
28. Wickens, AH, *A history of railway vehicle dynamics*, in *Handbook of railway vehicle dynamics*, S. Iwnicki, Editor. 2006, Taylor & Francis Group, Boca Raton, FL. pp. 5-38.
29. Kalker, J.J, *On the rolling contact of two elastic bodies in the presence of dry friction*, in *Department of Mechanical Engineering*, 1973, Delft University of Technology, The Netherlands.
30. Carter, F.W, *On the action of a locomotive driving wheel*, Proceedings of the Royal Society of London, Series A, Mathematical and Physical Sciences, 1926. **112**: pp. 151-157.
31. Kalker, J.J, *Rolling contact phenomena: linear elasticity*, 2000, Delft University of Technology, The Netherlands.
32. Kalker, J.J, *A fast algorithm for the simplified theory of rolling contact*, Vehicle System Dynamics, 1982. **11**: pp. 1-13.
33. Thompson, D.J, Monk-Steel, A.D, Jones, C.J.C, Allen, P.D, Hsu, S.S and Iwnicki, S.D, *Railway noise: curve squeal, roughness growth, friction and wear*, Rail Research UK Report RRUK/A3/1, 2003.
34. Zaazaa, K.E and A.L. Schwab, *Review of Joost Kalker's wheel-rail contact theories and their implementation in multibody codes*, in *ASME 2009 International Design Engineering Technical Conferences (IDETC) & Computers and Information in Engineering Conference (CIE)*, 2009, San Diego, CA. pp. 1-11.
35. Quost, X, Sebes, M, Eddhahak, A, Ayasse, J.B, Chollet, H, Gautier, P-E and Thouverez, F, *Assessment of a semi-Hertzian method for determination of wheel-rail contact patch.* Vehicle System Dynamics, 2006. **44**(10): pp. 789-814.
36. Piotrowski, J and H Chollet, *Wheel-rail contact models for vehicle system dynamics including multi-point contact*, Vehicle System Dynamics, 2005. **43**(6-7): pp. 455-483.
37. Piotrowski, J and Kik, W, *A simplified model of wheel/rail contact mechanics for non-Hertzian problems and its application in rail vehicle dynamic simulations*, Vehicle System Dynamics, 2008. **46**(1-2): pp. 27-48.
38. Cain, B.S, *Stresses and deflections of cylindrical bodies in contact, with application to contact of gears and locomotive wheels*, Journal of Applied Mechanics, 1950: p. 465.
39. Kalker, J.J, *Wheel-rail contact theory*, Wear, 1991. **144**: p. 243-261.
40. Kalker, J.J, *Three-dimensional elastic bodies in rolling contact*, 1990: Kluwer Academic Publishers.
41. Johnson, K.L, *The effect of spin upon the rolling motion of an elastic sphere upon a plane*, ASME Journal of Applied Mechanics, 1958. **25**: pp. 332-338.
42. Johnson, K.L, *The effect of a tangential contact force upon the rolling motion of an elastic sphere on a plane*, ASME Journal of Applied Mechanics, 1958. **25**: pp. 339-346.
43. Vermeulen, P.J, and Johnson, K.L, *Contact of nonspherical bodies transmitting tangential forces*, ASME Journal of Applied Mechanics, 1964. **31**: pp. 338-340.
44. Kalker, J.J and Piotrowski, J, *Some new results in rolling contact*, Vehicle System Dynamics, 1989. **18**: pp. 223-242.
45. Alonso, A, Giménez, J.G and Martín, L.M, *Spin moment calculation and its importance in railway dynamics*, Journal of Rail and Rapid Transit, 2009. **223**: pp. 453-460.
46. Elkins, J.A, *Prediction of wheel/rail interaction: the state of the art*, Vehicle System Dynamics, 1992. **20**(sup1): pp. 1-27.

47. Kalker, J.J, *Book of tables for the Hertzian creep force,* in *Second Mini Conference on Contact Mechanics and Wear of Rail/Wheel Systems,* 1996, TU Budapest.
48. White, R.C, Limbert, J.K, Hedrick, J.K and Copperrider, N.K, *Guideway-suspension tradeoffs in rail vehicle systems*, in *Report DOT-OS-50107,* 1978, U.S. Department of Transportation: Washington D.C.
49. Shen, Z.Y, Hedrick, J.K, and Elkins, J.A, *A comparison of alternative creep-force models for rail vehicle dynamic analysis,* Vehicle System Dynamics, 1983. **12**: pp. 79-87.
50. Polach, O, *A fast wheel-rail forces calculation computer code*, in *16th IAVSD Symposium* 1999: Pretoria, South Africa. pp. 9-21.
51. Polach, O, *Influence of locomotive tractive effort of the forces between wheel and rail,* Vehicle System Dynamics, 2001. **35**: pp. 7-22.
52. Pombo, J. and Ambrósio, J, *A New Approach to Study the Wheel-Rail Contact Problem in Railway Dynamics,* n.d., IDMEC/Instituto Superior Técnico: Lisbon.
53. Knothe, K, Wille, R, and Zastrau, B.W, *Advanced contact mechanics - road and rail,* Vehicle System Dynamics, 2001. **35**(4-5): pp. 361-407.
54. Li, L.Z and Kalker, J.J. *The computation of wheel-rail conformal contact*. in *4th World Conference on Computational Mechanics,* 1998, Buenos Aires, Argentina.
55. Li, L.Z. and Kalker, J.J, *The computation of wheel-rail conformal contact,* in *Computational mechanics, new trends and applications*, I. Idelsohm, E. Onate, and E. Dvorkin, Editors. 1998, CIMME: Barcelona.
56. Li, L.Z, *Wheel-rail rolling contact and its application to wear simulation*, 2002, Delft University.
57. Kalker, J.J, *Users Manual of the Fortran IV program CONTACT*, 1986, Delft University of Technology.
58. Pascal, J.P, *The railway dynamics codes "VOCO",* Vehicle System Dynamics, 1993. **22**(suppl.): pp. 137-139.
59. Pascal, J.P, *Benchmark to test wheel/rail contact forces,* Vehicle System Dynamics, 1993. **22**(Suppl.): pp. 169-173.
60. Aknin, P, Ayasse, J-B, Chollet, H, Maupu, J.L, Gautier, B and Paradinas, M, *Quasi-static derailment of a railway vehicle, comparison between experimental and simulation results*, Vehicle System Dynamics, 1993. **23**(Suppl.).
61. Kik, W and Piotrowski, J. *A fast, approximate method to calculate normal load at contact between wheel and rail and creep forces during rolling*. in *Second Mini Conference on Contact Mechanics and Wear of Rail/Wheel Systems,* 1996, Budapest, Hungary.
62. Iwnicki, S, *The Manchester benchmark for vehicle simulation,* Vehicle System Dynamics, 1999. **31**(Suppl.): pp. 1-48.
63. Ayasse, J.-B and Chollet, H, *Determination of the wheel rail contact patch in semi-Hertzian conditions*, Vehicle System Dynamics, 2005. **43**(3): pp. 161-172.
64. Giancoli, D.C, *Physics for scientists and engineers,* 3rd ed. Vol. 1. 2000, New Jersey: Prentice Hall.
65. Olofsson, U, *Adhesion and friction modification*, in *Wheel-rail interface handbook*, R. Lewis and U. Olofsson, Editors. 2009, Woodhead Publishing Limited: Padstow.
66. Tomberger, C, Dietmaier, P, Sextro, W and Six, K, *Friction in wheel-rail contact: A model comprising interfacial fluids, surface roughness and temperature,* Wear, 2011. **271**(1-2): pp. 2-12.
67. Zhang, W.H, Chen, J, Wu, W and Jin, X.S, *Wheel/rail adhesion and analysis by using full scale roller rig,* Wear, 2002. **253**: pp. 82-88.
68. Lang, W and Roth, G, *Optimale kraftschluûausnutzung bei hochleistungs-schienenfahrzeugen,* Eisenbahntechnische Rundschau, 1993. **42**: pp. 61-66.
69. Polach, O, *Creep forces in simulations of traction vehicles running on adhesion limit,* Wear, 2005. **258**: pp. 992-1000.
70. Jin, X.S, Zhang, W.H, Zeng, J, Zhou, Z.R, Liu, Q.Y and Wen, Z.F, *Adhesion experiment on a wheel/rail system and its numerical analysis,* Proceedings of the Institution of Mechanical Engineers, Part J: Journal of Engineering Tribology, 2004. **218**(4): pp. 293-304.

71. Baek, K-S, Kyogoku, K and Nakahara, T, *An experimental investigation of transient traction characteristics in rolling–sliding wheel/rail contacts under dry–wet conditions*, Wear, 2007. **263**: pp. 169-179.
72. Chen, H, Ban, T, Ishida, M and Nakahara, T, *Experimental investigation of influential factors on adhesion between wheel and rail under wet conditions*, Wear, 2008.
73. Arias-Cuveas, O, Li, Z, Lewis, R and Gallardo-Hernández, E.A, *Rolling–sliding laboratory tests of friction modifiers in dry and wet wheel–rail contacts*, Wear, 2010. **268**: pp. 543-551.
74. Niccolini, E and Berthier, Y, *Wheel–rail adhesion: laboratory study of "natural" third body role on locomotives wheels and rails*, Wear, 2004(258): pp. 1172-1178.
75. Bochet, B, *Nouvelles recherches experimentals sur le frottement de glissement*, Annls Mines, 1861. **19**(38): pp. 27-31.
76. Chen, H, Ban, T, Ishida, M and Nakahara, T, *Adhesion between rail/wheel under water lubricated contact*, Wear, 2002. **253**: pp. 75-81.
77. Chen, H, Ohyama, T and Yoahimura, A, *Numerical analysis for the influence of water film on adhesion between rail and wheel*, Journal of Engineering Tribology, 1998. **212**: pp. 359-368.
78. Greenwood, J.A and Tripp, T.H, *The contact of two nominally rough surfaces*, Proceedings of the Institution of Mechanical Engineers, 1975. **185**: pp. 623-633.
79. Greenwood, J.A. and Williamson, J.B.P, *Contact of nominally flat surfaces*, Proceedings of the Royal Society of London, Series A, Mathematical and Physical Science, 1966. **295**: pp. 300-319.
80. Zhao, Z, Maietta, D and Chang, L, *An asperity microcontact model incorporating the transition from elastic deformation to fully plastic flow*, Journal of Tribology, 2000. **122**: pp. 86-93.
81. VICSIG, *Locomotives*, 2011 [Accessed 24 July 2011]; Available from: http://www.vicsig.net/index.php?page=locomotives.
82. Railway Technical Web Pages, *Diesel locomotive technology*, 2011 [Accessed 9 September 2011]; Available from: http://www.railway-technical.com/diesel.shtml.
83. Railway Technical Web Pages, *Electronic power for trains*, 2011 [Accessed 9 May 2013]; Available from: http://www.railway-technical.com/tract-02.shtml.
84. Matthews, C, *Development of the Cv43ACi locomotive*, in *Conference On Railway Engineering (CORE) 2008*, 2008. Perth, Australia.
85. DeLorenzo, M, *NUCARS modelling of a freight locomotive with steerable trucks*, in *Department of Mechanical Engineering*, 1997, Virginia Polytechnic Institute and State University: Blacksburg, Virginia.
86. Yamashita, M and Soeda, T, *Development of re-adhesion control method considering axle-weight transfer of electric locomotive*, Quarterly reports of Railway Technical Research Institute, 2011. **52**(1): pp. 7-12.
87. Pfleger, E, *Parameter-excited vibrations in rail vehicle drives*, in *Simpack User Meeting 2007*, 2007: Bonn-Bad Godesberg.
88. Electro-Motive Diesel Inc., *Patented radial truck*, 2011 [Accessed 28 July 2011]; Available from: http://www.emdiesels.com/emdweb/products/radial_truck.jsp.
89. Walters, C and Baker, B *Just ACe - SCT's new GT46C-ACe locomotives*, Railway Digest, 2008. pp. 5-11.
90. Semple, J.D, Butcher, C.F and Wiwatowski, K. *An innovative steering bogie for heavy haul diesel locomotives*, in *Conference On Railway Engineering (CORE) 1998*, 1998, Rockhampton, Australia. pp. 325-328.
91. Goding, D.J, Handley, J.H and Rassaian, M, *Enhancements in the curving performance of locomotives equipped with three-axle radial steering bogies*, in *The Fourth International Heavy Haul Railway Conference 1989*, 1989, Brisbane, Australia.
92. General Electric (GE) Transportation, *Earlier locomotive models*, 2010 [Accessed 28 July 2011]; Available from: http://www.getransportation.com/rail/rail-products/locomotives/earlier-locomotive-models.html.
93. Frylmark, D and Johnsson, S, *Automatic slip control for railway vehicles*, in *Dept. of Electrical Engineering*, 2003, Masters Thesis, Linköpings universitet: Linköping, Sweeden.

94. Yasuoka, I, Henmi, T, Nakazawa, Y and Aoyama, I, *Improvement of re-adhesion for commuter trains with vector control traction inverter*, in *proceedings of the Power Conversion Conference - Nagaoka*, 1997.
95. Solomon, B, *EMD locomotives*, ed. D. Pernu and L. Noel. 2006, St. Paul: MBI Publishing Company, St. Paul, MN.
96. Q-Tron, *QES-III locomotive performance enhancement system*, 2007.
97. ABB, *Technical guide No. 1 - Direct torque control - the world's most advanced AC drive technology*, 2002.
98. Spiryagin, M, Lee, K.S, and Yoo, H.L, *Control system for maximum use of adhesive forces of a railway vehicle in a tractive mode*, Mechanical Systems and Signal Processing, 2008(22): pp. 709-720.
99. Simson, S.A, *Three Axle Locomotive Bogie Steering, Simulation of Powered Curving Performance Passive and Active Steering Bogies*, in *Faculty of Sciences, Engineering and* Health, 2009, Doctor of Philosophy Thesis, Central Queensland University, Rockhampton, Australia.
100. Simson, S and Cole, C.R, *An active steering bogie for heavy haul diesel locomotives*, in *Conference On Railway Engineering (CORE) 2008*, 2008, Perth, Australia.
101. Simson, S and Cole, C.R, *Simulation of traction and curving for passive steering hauling locomotives*, Journal of Rail and Rapid Transit, 2008. **222**: pp. 117-127.
102. Simson, S and Cole, C.R, *Parametric simulation study of traction curving of three axle steering bogie designs*, Vehicle System Dynamics, 2008. **46**: pp. 717-728.
103. Simson, S and Cole, C.R, *Simulation of curving at low speed under high traction for passive steering hauling locomotives*, Vehicle System Dynamics, 2008. **46**(12): pp. 1107-1121.
104. Simson, S and Cole, C.R, *Idealized steering for hauling locomotives*, Journal of Rail and Rapid Transit, 2007. **221**: pp. 227-235.
105. Spiryagin, M, Sun, Y.Q, Cole, C.R, Simson, S and Persson, I, *Development of Traction Control for Hauling Locomotives*, Journal of System Design and Dynamics, 2011. **5**(6): pp. 1214-1225.
106. Spiryagin, M, Simson, S, Cole, C.R and Persson, I, *Co-simulation of a mechatronic system using Gensys and Simulink.* Vehicle System Dynamics, 2012. **50**(3): pp. 495-507.
107. Spiryagin, M, Sun, Y.Q, Cole, C.R, McSweeney, T, Simson, S and Persson, I, *Development of a real-time bogie test rig model based on railway specialised multibody software*, Vehicle System Dynamics, 2012. **51**(2): pp. 236-250.
108. Spiryagin, M, George, A.L, Sun, Y.Q and Cole, C.R, *Locomotive Model Acceptance Procedure Based on International Standards*, in *The 2nd Joint International Conference on Multibody System Dynamics*. 2012. Stuttgart, Germany.
109. Spiryagin, M., et al. *Influence of Lateral Components of Coupler Forces on The Wheel-Rail Contact Forces for Hauling Locomotives Under Traction*. in *VSDIA 2012 - The 13th Mini Conference on Vehicle System Dynamics, Identification and Anomalies.* November 5-7 2012. Budapest, Hungary.
110. Spiryagin, M, Sun, Y.Q, Cole, C.R, George, A.L, Simson, S and Persson, I, *Investigation of locomotive multibody modelling issues and results assessment based on the locomotive model acceptance procedure*, Journal of Rail and Rapid Transit, 2013. **227**(5): pp. 453-468.
111. DEsolver, *A model of three wheels subjected to pure creep in longitudinal, lateral and spin direction*, The GENSYS Homepage, 2013 [Accessed 25 February 2013]; Available from: http://www.gensys.se/doc_html/calc/example_creep_lookuptable_1.html.
112. DEsolver, *The CALC Coupl manual*, The GENSYS Homepage, 2015 [Accessed 4 June 2015]; Available from: http://www.gensys.se/doc_html/calc_coupl.html.
113. DEsolver, *The CALC Func Manual*, The GENSYS Homepage, 2013 [Accessed 25 February 2013]; Available from: http://www.gensys.se/doc_html/calc_func.html.
114. Cole, C.R, Spiryagin, M, Sun, Y.Q, Vo, K.D, Tieu, K.A, Zhu, H and Meehan, P, *R3.119: Locomotive Adhesion, Final Report 2013*, 2013, CRC for Rail Innovation: Brisbane, Australia.

115. DEsolver, *Example of a rail road vehicle input data model*, The GENSYS Homepage 2013 [Accessed 30 April 2013]; Available from: http://www.gensys.se/doc_html/analyse_r_vehicle.html.
116. Logston, C.F Jr. and Itami, G.S, *Locomotive Friction-Creep Studies*, Journal of Engineering for Industry, 1980. **102**(3): pp. 275-281.
117. Spiryagin, M, Wolfs, P, Szanto, F and Cole C.R, *Simplified and advanced modelling of traction control systems of heavy-haul locomotives*, Vehicle System Dynamics, 2015. **53**(5): pp. 672-691.
118. Bosso, N, Gugliotta, A and Somá, A, *Dynamic behavior of a railway wheelset on a roller rig versus tangent track*, Shock and Vibration, 2004. **9**.
119. Jordan, L.B Jr., *Locomotive traction conrol system using fuzzy logic*, U.S.P. Office, Editor 1995, General Motors Corporation: United States of America.
120. Shuard, M, *National Rail "NR" Class Locomotives*, in *IRSE AGM*. 1998. Adelaide, Australia.
121. A. Goninan & Co. Limited, *Cv40-9i diesel electric locomotive* [pamphlet].
122. Orlova, A and Boronenko, Y, *The anatomy of railway vehicle running gear*, in *Handbook of railway vehicle dynamics*, S. Iwnicki, Editor. 2006, Taylor & Francis Group, Boca Raton, FL. pp. 39-83.
123. Electro-Motive Division, G.M.C, *GT46MAC Indian State Railways Locomotive Service Manual*, 1999.
124. Electro-Motive Diesel Inc., *The Merits of AC vs DC Locomotives*, 2008 [slide show].
125. Standards Australia and Rail Industry Safety & Standards Board, *AS7507.1: Railway Rolling Stock - Rolling Stock Outlines - Part 1: Locomotive Rolling Stock*, 2009, Sydney, Australia.
126. Standards Australia and Rail Industry Safety & Standards Board, *AS7508.1: Railway Rolling Stock - Track Forces and Stresses - Part 1: Locomotive Rolling Stock*, 2009, Sydney, Australia.
127. Spiryagin, M, George, A.L, Ahmad, S.S.N, Rathakrishnan, K, Sun, Y.Q and Cole, C.R, *Wagon model acceptance procedure using Australian Standards*, in *Conference on Railway Engineering (CORE) 2012*, 2012. Brisbane, Australia: Railway Technical Society of Australasia (RTSA). pp. 343-350.
128. AEA Technology plc, *VAMPIRE (Version 4.32) User Manual*, L. Rawlings, Editor 2004.
129. British Standards, *BS EN 14363:2005, Railway applications - Testing for the acceptance of running characteristics of railway vehicles - Testing of running behaviour and stationary tests*, 2006.
130. International Union of Railways (UIC), *Leaflet 518:2005, Testing and approval of railway vehicles from the point of view of their dynamic behaviour - Safety - Track fatigue - Ride quality*, 2005.
131. RailCorp. *Rolling Stock - Minimum Operating Standards for Rolling Stock*. 2012; Available from: http://engineering.railcorp.nsw.gov.au/InternetStandards.asp?discipline=RollingStock&standards=Minimum%20Operating%20Standards%20for%20Rolling%20Stock.
132. RailCorp. *Rolling Stock Procedures*. 2012; Available from: http://engineering.railcorp.nsw.gov.au/RollingStocks_Procedures.asp.
133. Railways of Australia, *ROA Manual of Engineering Standards and Practices Section 13 - locomotives*, 1992.
134. *Section 601 - Testing - General*, in *Diesel-electric locomotives*, 2007, Virginia Railway Express.
135. Iwnicki, S.D, *Manchester benchmarks for rail vehicle simulation*, Vehicle System Dynamics, 1998. **30**: pp. 295-313.
136. *The Manchester Benchmarks for rail vehicle simulation*, 1998, Manchester Metropolitan University.
137. *Manchester Benchmarks for Rail Vehicle Simulation*, in *Universal Mechanism 5.0 Users Manual*, 2009.
138. Pérez, J, Allen, P, and Uem, B.V, *Use of simulation in railway vehicle acceptance procedures*, in *SIMPACK User Meeting*, 2004.

139. Gansekow, R, *Using SIMPACK at Siemens TS Trains*, in *SIMPACK User Meeting*, 2004.
140. Tillmetz, K and Kossmann, C, *Using SIMPACK Wheel/Rail for Model Verification and Optimization at STADLER RAIL*, in *Simpack User Meeting*, 2006.
141. Goldney, I and Church, D, *Validation of dynamic performance of a railway vehicle by simulation*, in *Conference on Railway Engineering (CORE) 2012*, M. Dhanasekar, T. Constable, and D. Schonfield, Editors. 2012, Railway Technical Society of Australasia (RTSA): Brisbane, Australia. pp. 351-358.
142. Sperry, B and Dick, M, *VAMPIRE SD70MAC Locomotive Model and Validation*, in *2011 VAMPIRE User Day*, 2011.
143. Jönsson, L-O, Nilstam, N, and Persson, I, *Using simulations for approval of railway vehicles: a comparison between measured and simulated track forces*, Vehicle System Dynamics, 2008. **46**(Supplement): pp. 869-881.
144. Polach, O and Evans, J, *Simulations of Running Dynamics for Vehicle Acceptance: Application and Validation*. in *Railways 2014 - The Second International Conference on Railway Technology: Research, Development and Maintenance*, 2014. Ajaccio, Corsica, France: Civil-Comp Press.
145. Association of American Railroads, *Manual of Standards and Recommended Practices Section C - Part II - Design, fabrication and construction of freight cars*, in *Safety and Operations*, 2011, Association of American Railroads.
146. DEsolver, *Users Manual for Program RUNF_INFO*, The GENSYS Homepage, 2010 [Accessed 16 October 2011]; Available from: http://www.gensys.se/doc_html/misc_runf_info.html.
147. DEsolver, *Debugging a vehicle model*, The GENSYS Homepage, 2010 [Accessed 16 October 2011]; Available from: http://www.gensys.se/doc_html/analyse_check.html#Mainmenu.
148. RailCorp, *RSU 100 series - Miminum operating standards for rolling stock - General interface standards*, in *Engineering Standard - Rolling Stock*, 2011.
149. RailCorp, *RSU 200 series - Mimimum operating standards for rolling stock - Common interface requirements*, in *Engineering Standard - Rolling Stock*, 2011.
150. RailCorp, *EPR 0026 - Static vehicle weigh test*, in *Engineering Procedure - Rolling Stock*, 2011.
151. RailCorp, *RSU 300 series - Railcorp mimimum operating standards for rolling stock - Locomotive specific interface requirements*, in *Engineering Standard - Rolling Stock*, 2011.
152. RailCorp, *RSU Appendix A1 - Locomotive vehicle information pack*, in *Engineering Standard - Rolling Stock*, 2011.
153. RailCorp, *Testing of locomotive all weather adhesion*, in *Engineering Procedure - Rolling Stock*, 2009.
154. RailCorp, *Measurement of brake performance*, in *Engineering Procedure - Rolling Stock*, 2009.
155. RailCorp, *Measurement of brake performance (stopping distances)*, in *Engineering Procedure - Rolling Stock*, 2009.
156. RailCorp, *Measurement of locomotive brake block forces*, in *Engineering Procedure - Rolling Stock*, 2009.
157. DEsolver, *Error in a vehicle model*, The GENSYS Homepage, 2010 [Accessed 16 October 2011]; Available from: http://www.gensys.se/doc_html/analyse_error.html.
158. True, H, *Multiple attractors and critical parameters and how to find them numerically: the right, the wrong and the gambling way*, Vehicle System Dynamics, 2013. **51**(3): pp. 443-459.
159. Railways of Australia, *ROA Manual of Engineering Standards and Practices Section 3 - Road worthiness acceptance standards for rail freight vehicles*, 1991.
160. DEsolver, *Users Manual for Program CALC*, The GENSYS Homepage, 2011 [Accessed 17 January 2012]; Available from: http://www.gensys.se/doc_html/calc.html.
161. DEsolver, *RUNF_INFO - Creating an input data file*, The GENSYS Homepage, 2010 [Accessed 17 January 2012]; Available

from: http://www.gensys.se/tutorial/intro_tutor_3_bobo_pe3/README_files/create_runf_infof.html.
162. DEsolver, *Tutorial Bo-Bo vehicle using wheel/rail-coupling function wr_coupl_pe3*, The GENSYS Homepage, 2011 [Accessed 28 July 2011]; Available from: http://www.gensys.se/tutorial/intro_tutor_3_bobo_pe3/README.html#.
163. Federal Railroad Administration, *Track Safety Standards Compliance Manual*, in *Chapter 6 - Track Safety Standards - Classes 6 Through 9*, 2002.
164. Pastorino, R, *Experimental Validation of a Multibody Model for a Vehicle Prototype and its Application to Automotive State Observers*, in *Departamento de Ingenieria Industrial II*, 2012, Doctoral Thesis, University of La Coruna, Spain.
165. Ahmadian, M, Gray, L.W, McGrew, D.Z, Kurtzhals, W.A, Whitehill, J.H and Jaramillo, J.L, *Self-steering railway truck*, 1997, General Electric Company: U.S.A.
166. Federal Railroad Administration, *Track Safety Standards Compliance Manual*, in *Chapter 5 - Track Safety Standards - Classes 1 Through 5*, 2007.

Appendix A: Output parameter descriptions

When defining the simulation output parameters analysed in Section 6.4, it is best to start at the contact patch level. Contact patch forces and creepages follow the wheel-rail contact patch co-ordinate system described in Figure 9 [25]. A sample contact patch on the rail head is shown below, showing the forces and creepages exerted by the rail onto a wheel.

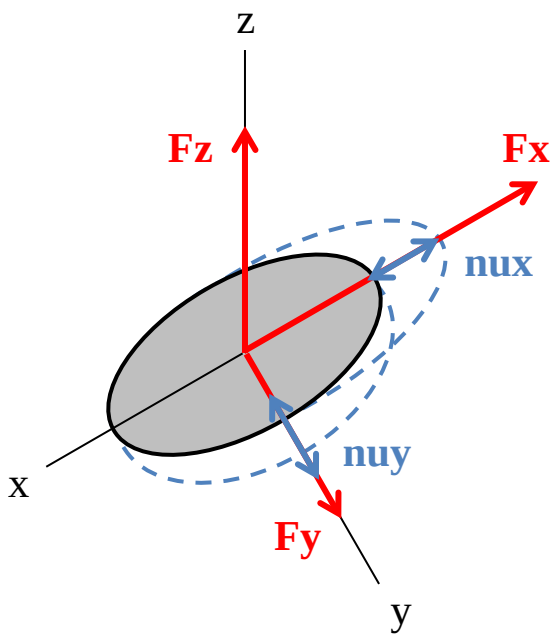

Where: Fx = Longitudinal contact patch force
Fy = Lateral contact patch force
Fz = Vertical contact patch force
nux = Longitudinal contact patch creepage
nuy = Lateral contact patch creepage

Net wheel forces consist of the sum of all wheel-rail contact patch forces in a wheel-rail contact pair. They describe the forces exerted by wheels onto a rail and follow the vehicle body co-ordinate system shown in Figure 7 [22]. The locomotive models used in this thesis could model up to three contact patches for the wheel tread / rail head (CP1), gauge corner (CP2) and flange contact (CP3) zones.

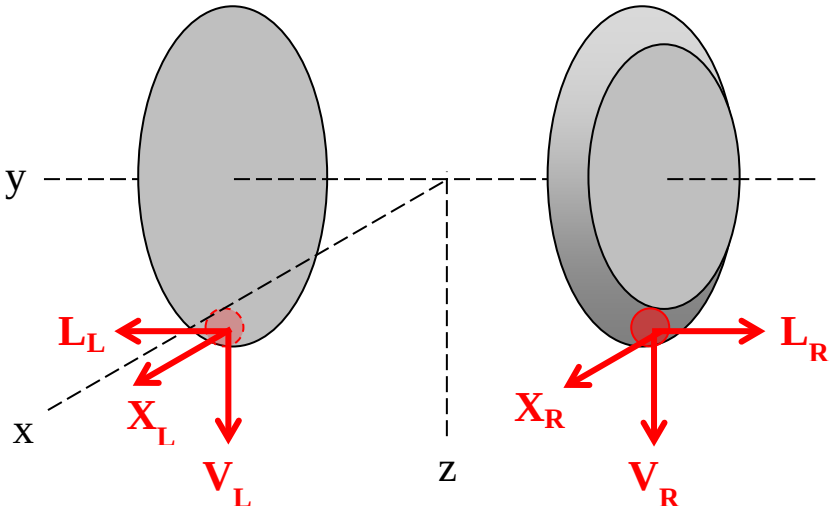

$$X_L = -\Sigma Fx_L = -Fx_{L,CP1} - Fx_{L,CP2} - Fx_{L,CP3}$$

$$X_R = -\Sigma Fx_R = -Fx_{R,CP1} - Fx_{R,CP2} - Fx_{R,CP3}$$

$$L_L = \Sigma Fy_L = Fy_{L,CP1} + Fy_{L,CP2} + Fy_{L,CP3}$$

$$L_R = -\Sigma Fy_R = -Fy_{R,CP1} - Fy_{R,CP2} - Fy_{R,CP3}$$

$$V_L = -\Sigma Fz_L = -Fz_{L,CP1} - Fz_{L,CP2} - Fz_{L,CP3}$$

$$V_R = -\Sigma Fz_R = -Fz_{R,CP1} - Fz_{R,CP2} - Fz_{R,CP3}$$

Where: X = Net longitudinal wheel force

L = Net lateral wheel force

V = Net vertical wheel force

$_R$ = Right wheel subscript

$_L$ = Left wheel subscript

Note that L_L points in the opposite direction to L_R. Approximate adhesion coefficients X/V and L/V ratios can now be defined for wheels.

$$X/V_L = X_L/V_L, \qquad X/V_R = X_R/V_R, \qquad L/V_L = L_L/V_L, \qquad L/V_R = L_R/V_R$$

Net wheel forces can now be summed to form net wheelset forces.

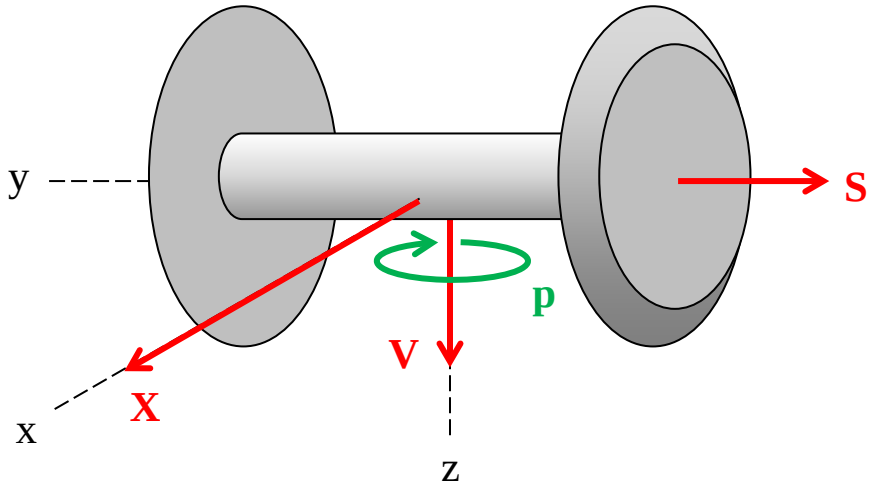

$$X = X_L + X_R, \qquad S = L_L - L_R, \qquad V = V_L + V_R$$

Where: X = Net longitudinal wheelset force

S = Lateral track-shifting force

V = Axle load

p = Angle of Attack = Wheelset yaw rotation relative to track

These allow approximate adhesion coefficients X/V and sum L/V ratios to be defined for wheelsets.

$$X/V = X/V_L + X/V_R, \qquad L/V = L/V_L + L/V_R$$